Structural degradation in Ni-rich NCM cathodes:
A high-resolution scanning transmission electron microscopy study

Von der Fakultät für Georessourcen und Materialtechnik der
Rheinisch-Westfälischen Technischen Hochschule Aachen

zur Erlangung des akademischen Grades einer

Doktorin der Naturwissenschaften

genehmigte Dissertation

vorgelegt von

Lara Ahrens, M.Sc.

Berichter: **Univ.-Prof. Dr. rer. nat. Joachim Mayer**
Univ.-Prof. Dr. rer. nat. Egbert Figgemeier
Prof. Dr. Anja Henss

Tag der mündlichen Prüfung: 04.07.2025

Diese Dissertation ist auf den Internetseiten der Universitätsbibliothek online verfügbar

Abstract

Ni-rich nickel cobalt manganese oxide (NCM) cathode active materials are commercially used in high-energy lithium-ion batteries, e.g. in electric vehicles, due to their high capacity. However, structural and thermal degradation at high voltages prevent the usage of the total theoretical capacity. For targeted and resource-efficient material solutions, a deep understanding of the structural degradation phenomena is urgently needed. This work focuses on three specific aspects: (i) Time-dependent structural surface degradation at high potential holds, (ii) thermally induced structural degradation of protonated NCM, and (iii) Al_2O_3 coatings and their behavior during cycling. Scanning transmission electron microscopy (STEM), energy-dispersive X-ray spectroscopy, electron energy loss spectroscopy and *in situ* transmission electron microscopy were applied to investigate these structural degradation phenomena.

The analysis of high-resolution STEM images and electron energy loss spectra in (i) confirmed an anisotropic surface degradation at high potential holds of 4.5 V, which deviates from the often proposed homogeneous core-shell model. A gradual transition boundary was observed between the intact layered structure and the rock salt structure, which formed epitaxially and coherently on the surface. Furthermore, we introduced a new image processing method that highlights the structural differences of the intact layered structure, the gradual transition boundary, and the rock salt layer immediately. The STEM investigations and energy-dispersive X-ray spectroscopy analysis of protonated and heated Ni-rich NCM in (ii) showed strong rock salt formation on the surface. Furthermore, nanopore formation with oxygen-depleted surfaces was observed at the particle surfaces, along defects, and in the core of particles, which was confirmed by *in situ* heating experiments. The observation of nanopore formation offers new insights into structural degradation caused by washing and subsequent heating. The STEM and energy-dispersive X-ray spectroscopy analysis in (iii) of Al_2O_3 coated polycrystalline NCM particles revealed a change in the coating layer from a homogeneously confined layer before to a more diffusive layer after cycling. Finally, we presented the first building block of *in situ* biasing transmission electron microscopy, which aims to study the dynamics of coating behavior during cycling.

The results of the investigations in (i) and (ii) showed that the extent of structural degradation is more complex and pronounced than initially assumed. The results in (iii) highlight the need to investigate coatings at the nanoscale with high spatial resolution and provide ideas for an improved *in situ* biasing transmission electron microscopy approach to investigate the dynamics of Al_2O_3 coatings on polycrystalline NCM during cycling. The (high-resolution) STEM investigations have yielded a deeper understanding of the structural degradation behavior in Ni-rich NCM, which

is essential for tailored material development and the optimization of commercial high-energy NCM cathodes.

Zusammenfassung

Ni-reiche Lithium-Nickel-Mangan-Cobalt-Oxid (NCM) Kathodenmaterialien werden aufgrund ihrer hohen Kapazität in hochenergetischen Lithium-Ionen-Batterien, z. B. in Elektrofahrzeugen mit großer Reichweite, verwendet. Allerdings verhindern strukturelle und thermische Degradation, die vor allem bei hohen Spannungen auftreten, die vollständige Nutzung der theoretisch verfügbaren Kapazität. Daher ist für gezielte und ressourceneffiziente Materiallösungen ein tieferes Verständnis dieser Degradationsphänomene dringend erforderlich. Diese Arbeit konzentriert sich auf drei spezifische Aspekte: (i) die zeitabhängige Phasenumwandlung an der Oberfläche während des Haltens bei hohem Potential, (ii) die thermisch induzierte strukturelle Degradation von protoniertem NCM und (iii) die Beschaffenheit von Al_2O_3-Beschichtungen und das Verhalten dieser während des Zyklisierens. Rastertransmissionselektronenmikroskopie (STEM), energiedispersive Röntgenspektroskopie, Elektronenenergieverlustspektroskopie und *in situ* Transmissionselektronenmikroskopie wurden angewandt, um die Phänomene der strukturellen Degradation genauer zu untersuchen.

Die Analyse hochauflösender STEM-Bilder und Elektronenenergieverlustspektren in (i) bestätigte eine anisotrope Oberflächendegradation während des Haltens bei einem Potential von $4,5\,\mathrm{V}$, die vom häufig vorgeschlagenen homogenen Kern-Schalen-Modell abweicht. Ein gradueller Übergang zwischen der intakten Schichtstruktur und der Steinsalzstruktur, die sich epitaktisch und kohärent an der Oberfläche gebildet hat, wurde beobachtet. Darüber hinaus wurde im Rahmen dieser Arbeit eine neue Bildverarbeitungsmethode entwickelt, die Fourier-Koeffizientenkarte, die die strukturellen Unterschiede an der Oberfläche zwischen der intakten Schichtstruktur, dem graduellen Übergang und der Steinsalzschicht hervorhebt. Die STEM- und energiedispersive Röntgenspektroskopie-Untersuchungen von protoniertem und erhitztem Ni-reichen NCM in (ii) zeigten einen ausgeprägten Phasenübergang von der Lagenstruktur zur Steinsalzphase an der Oberfläche. Darüber hinaus wurde die Bildung von Nanoporen mit sauerstoffarmen Oberflächen an den Partikeloberflächen, entlang von Defekten und im Inneren der Partikel beobachtet, was durch *in situ* Heizexperimente bestätigt wurde. Die Beobachtung der Nanoporenbildung bietet neue Erkenntnisse über die strukturelle Degradation, die durch Waschen und anschließendes Aufheizen verursacht wird. Die STEM-Untersuchungen und die energiedispersive Röntgenspektroskopie-Analyse in (iii) von Al_2O_3-beschichteten polykristallinen NCM-Partikeln zeigte eine Veränderung der Beschichtungen von einer homogenen Schicht vor dem Zyklieren zu einer diffusen Schicht nach dem Zyklieren. Abschließend wurde ein erster Baustein für *in situ* Spannungsversuche vorgestellt, der darauf abzielt, das dynamische Verhalten der Beschichtung während des Zyklisierens zu untersuchen.

Die Ergebnisse der Untersuchungen in (i) und (ii) zeigten, dass das Ausmaß der strukturellen Degradation komplexer und ausgeprägter ist als zunächst angenommen. Die Ergebnisse in (iii) unterstreichen die Notwendigkeit, Beschichtungen im Nanomaßstab mit hoher räumlicher Auflösung zu untersuchen, und liefern Ideen für einen verbesserten Ansatz für einen *in situ* Spannungsversuch, um die Dynamik der Al_2O_3-Beschichtungen auf polykrystallinem NCM während des Zyklisierens zu untersuchen. Die (hochauflösenden) STEM-Untersuchungen haben zu einem tieferen Verständnis des strukturellen Degradationsverhaltens in Ni-reichem NCM geführt, was für die maßgeschneiderte Materialentwicklung und Optimierung kommerzieller hochenergetischer NCM-Kathoden von entscheidender Bedeutung ist.

Acknowledgements

I would like to express my deepest gratitude to all those who have supported me throughout my PhD journey.

First and foremost, I would like to thank Prof. Dr. Joachim Mayer for giving me the opportunity to conduct my research at the Central Facility for Electron Microscopy (GFE) at RWTH Aachen University and the Ernst-Ruska Centre for Microscopy and Spectroscopy with Electrons (ER-C) at Forschungszentrum Jülich. I am especially grateful for the chance to use the new Spectra from its installation onward. I also appreciate the freedom you gave me in my work, which, though at times challenging, contributed greatly to my growth as a researcher. I value that you were consistently available for discussions whenever I sought your guidance. Your support in facilitating my research stay in Korea significantly enriched my PhD experience.

I would also like to thank Prof. Dr. Anja Henß for her excellent coordination of the AQua-POp project. I am also grateful for her role as the second reviewer of my dissertation.

My sincere appreciation goes to Prof. Dr. Egbert Figgemeier for serving as the third reviewer of my dissertation.

I gratefully acknowledge Dr. Juri Barthel, who has been an important mentor since the early stages of my PhD journey. He introduced me to aberration-corrected TEM and provided invaluable support on the microscope during difficult times of the COVID-19 pandemic. Juri was always available when I had specific questions about microscopy and became an key person to discuss my dissertation with. He taught me a lot about TEM, image simulation and scientific writing. Thank you for our long and fruitful discussions and your critical yet encouraging feedback.

I am grateful to Dr. Maria Meledina for being a supervisor during the first year of my PhD before she left for Thermo Fisher. She shared extensive knowledge about batteries and how to study them using TEM.

Dr. Shibabrata (Shiv) Basak deserves special mention as a supervisor and mentor during the years of my PhD after Maria's departure from the institute. Our regular meetings, especially during the pandemic when exchanges between colleague were limited, were important for me. He taught me a lot about *in situ* TEM and always provided valuable feedback.

Helen (Stefi) Valencia has not only been a wonderful colleague but also good friend over the years. She was always someone I could turn to with questions, whether

they were related to microscopy or personal matters, and offered an open ear during both good times and challenging moments. Thank you for the many hours spent together at the microscope conducting *in situ* biasing battery experiments!

I extend my gratitude to Dr. Junbeom Park for his support in arranging my research stay at the Korea Institute of Science and Technology (KIST). This invaluable opportunity not only introduced me to a new lab but also immersed me in a different culture, broadening my horizons through exchanges with fellow researchers.

I would also like to thank Dr. Janghyun Jo for teaching me how to use *in situ* TEM holders and for the opportunity to visit his former lab at Seoul National University in Korea, an experience that was very enriching for me.

To my project partners, Rebecca Wilhelm, Kilian Vettori, and Steffen Schröder, thank you for making our monthly Jour Fix enjoyable with great exchanges in a positive atmosphere. It was reassuring to know I could reach out with questions about electrochemistry or other topics.

I would like to thank Shriya Agarwal, our dedicated master student, for her valuable assistance with the coating study.

I would also like to thank Kevin Kistermann and Martina Schiffers from GFE, and Lea Risters and Lidia Kibkalo from ER-C for introducing me to TEM sample preparation using focused ion beam and for always being there when I sought advice on improving my lamella preparation. Many thanks to Sebastian Zischke for introducing me to conventional TEM, and to Gudrun Nitziger, Wilma Sybertz, and Melanie Keil for their guidance in conventional preparation and their technical assistance.

I thank all my current and former colleagues at GFE and ER-C for the pleasant working environment and the refreshing conversations during lunch breaks.

I am deeply grateful to my parents for their unconditional support, encouragement, and belief in me. I also thank my brother Leon for always being there for me.

A heartfelt thank you to my beloved boyfriend, Tobi Pankert, for being my emotional anchor and encouraging me to take breaks when needed. Thank you also for every hug and for the time spent outdoors, climbing, hiking, or riding our bikes. Your support has greatly enriched both my personal life and academic journey!

Finally, I am grateful to my friends for always being there and helping me clear my head. Thank you for the evenings, climbing sessions, bike tours, and outdoor adventures that helped me through my PhD journey.

Aachen, March 2025

Contents

Acronyms **xv**

1. Introduction **1**
1.1. Research strategy . . . 3

2. Literature review **7**
2.1. Ni-rich NCM - the materials system . . . 7
2.1.1. Crystal structure . . . 7
2.1.2. Role of transition metals . . . 9
2.1.3. Synthesis and particle morphology . . . 11
2.2. Degradation mechanisms . . . 12
2.2.1. Cracking . . . 12
2.2.2. Cation mixing . . . 13
2.2.3. Phase transition . . . 14
2.2.4. Electrolyte decomposition . . . 16
2.2.5. CEI Formation . . . 18
2.2.6. Transition metal dissolution . . . 18
2.3. Washing of Ni-rich NCM and induced thermal instability . . . 19
2.4. Mitigation strategies . . . 20
2.4.1. Optimizing synthesis protocols . . . 21
2.4.2. Coating . . . 21
2.4.3. Doping . . . 22

3. Instrumentation and methods **23**
3.1. Transmission electron microscopy . . . 24
3.1.1. Setup . . . 24
3.1.2. Image formation . . . 25
3.2. Scanning transmission electron microscopy . . . 29
3.2.1. Setup . . . 29
3.2.2. Image formation . . . 30
3.2.3. High-resolution scanning transmission electron microscopy . . . 32
3.3. Analytical transmission electron microscopy . . . 35
3.3.1. Electron energy loss spectroscopy . . . 35
3.3.2. Energy-dispersive X-ray spectroscopy . . . 37
3.4. Beam-induced damage effects . . . 39
3.5. *In situ* transmission electron microscopy . . . 40
3.5.1. *In situ* Heating . . . 41

3.5.2. *In situ* Biasing . . . 41
3.6. Scanning electron microscopy . . . 43
3.7. Focused ion beam . . . 45

4. TEM Sample Preparation **47**
4.1. Sample storage and handling . . . 48
4.2. FIB sample preparation . . . 50
4.2.1. Preliminary steps . . . 50
4.2.2. Standard protocol . . . 51
4.2.3. Challenges and improvements of FIB sample preparation for NCM . . . 55
4.2.4. *In situ* chip preparation . . . 60
4.3. Conventional sample preparation: Drop casting . . . 61

5. Results **63**
5.1. Ni-rich NCM - the material system . . . 63
5.1.1. Overview used materials: Structure and chemistry . . . 63
5.1.2. Morphology and particle size . . . 63
5.1.3. Structural properties of Ni-rich NCM visualized by STEM . . . 65
5.1.4. Discussion of phase transitions in Ni-rich NCM . . . 67
5.2. Time-dependent surface degradation of SC-NCM at high potential . . . 70
5.2.1. Qualitative observations of the surface structure . . . 71
5.2.2. Data processing of HR-STEM images . . . 75
5.2.3. EELS analysis . . . 84
5.2.4. Discussion of the results . . . 85
5.3. Thermal instability of protonated NCM . . . 90
5.3.1. Nanostructural analysis . . . 92
5.3.2. HR-STEM analysis . . . 95
5.3.3. *In situ* heating experiments . . . 99
5.3.4. Discussion of the results . . . 103
5.4. Al_2O_3 surface coating to prevent degradation . . . 107
5.4.1. Verifying the quality and thickness of the Al_2O_3 coating . . . 107
5.4.2. Studying of coating before and after cycling . . . 108
5.4.3. *In situ* biasing experiments of coated PC-NCM . . . 110

6. Discussion **115**
6.1. Phase transition on the particle surface in Ni-rich NCM at high potential holds . . . 115
6.2. Impact of protonated Ni-rich NCM on the structural and thermal stability . . . 116
6.3. Experimental limitations . . . 118
6.3.1. HAADF-STEM imaging and other imaging techniques . . . 118
6.3.2. *In situ* transmission electron microscopy . . . 121

7. Conclusion **123**

Bibliography **127**

List of Figures **144**

List of Tables **147**

A. Synthesis protocols **149**
A.1. PC-NCM coated with Al_2O_3 149

B. Python scripts **151**
B.1. EELS analysis 151
B.2. Fourier coefficient mapping 159

Acronyms

ABF annular bright-field

ADF annular dark-field

ALD atomic layer deposition

AQua analytics and quality assurance

AQua-POp Oberflächen- und Grenzflächenanalytik von Aktivmaterialien mittels hochaufgelöster Analytischer Verfahren (von *Post mortem*- zu *in situ*- und *Operando*-Methoden)

BF bright-field

bfp back focal plane

BSE back scattered electron

CAM cathode active material

CBED convergent beam electron diffraction

CEI cathode-electrolyte interface

EC ethylene carbonate

EDX energy-dispersive X-ray spectroscopy

EEL electron energy loss

EELS electron energy loss spectroscopy

EIS electrochemical impedance spectroscopy

ELNEFS electron loss near edge fine structure

EV electric vehicle

FEG field emission gun

FIB focused ion beam

FT Fourier transform

GIS gas injection system

HAADF high-angle annular dark-field

HF hydrofluoric acid

HR-STEM high-resolution scanning transmission electron microscopy

HR-TEM high-resolution transmission electron microscopy

iDPC integrated differential phase contrast

LCO lithium cobalt oxide

LFP lithium iron phosphate oxides

LIB lithium-ion battery

LNO lithium nickel oxide

MEMS micro-electro-mechanical system

NCM nickel cobalt manganese oxide

OCV open circuit voltage

PC polycrystalline

SAED selected area electron diffraction

SC single crystalline

SE secondary electron

SEI solid-electrolyte interface

SEM scanning electron microscopy

SOC state of charge

STEM scanning transmission electron microscopy

TEM transmission electron microscopy

TGA thermogravimetric analysis

TM transition metal

ToF-SIMS time-of-flight secondary ion mass sepctroscopy

XPS X-ray photoelectron spectroscopy

XRD X-ray powder diffraction

1. Introduction

The global climate crisis has become one of the most urgent challenges of our time. Greenhouse gas emissions are the primary driver of global warming and have more than doubled compared to the pre-industrial level [1]. 2024 was the warmest year on record at 1.55 °C [2]. Global warming increases sea levels and amplifies extreme weather events such as heat waves, floods, or hurricanes. The changing climate has far-reaching consequences for the integrity of ecosystems, human societies, and economics. To mitigate global warming and its consequences, the long-term increase in global temperature should be kept below 1.5 °C. [3]

To meet the 1.5 °C target, decarbonization is needed in the areas of energy generation, industry, and agriculture, among others. Battery solutions have become a key technology for the transformation towards a decarbonized planet. The sector of passenger transport has a large savings potential, including cars, motorcycles and buses, which accounts for approximately 10 % of the greenhouse gas emissions worldwide [4]. A combustion engine consuming fossil fuels produces up to three times more greenhouse gas emissions than an electric vehicle (EV) powered by renewable energies over a lifetime of 15 years or 200000 km [4]. Moreover, batteries are used not only in the transportation sector. They are also needed for grid storage systems to save the energy produced by solar, wind, or water power, ensuring a stable electrical network throughout the day [5].

In recent decades, various types of batteries have been developed [6–8]. In 1991, Sony commercialized the first lithium-ion battery (LIB), representing a significant advancement in battery technology [9]. Layered lithium cobalt oxide (LCO) was used as cathode material. Carbon-based materials were used as anode. Since then, LIBs have been steadily optimized and dominated the battery market by approximately 44 % percent in 2024 [10], reflecting the diverse application fields of LIBs and their good performance in terms of high capacity, energy density and lifetime [11].

Working principle of lithium-ion batteries

A lithium-ion battery comprises four principal components: anode, cathode, electrolyte, and separator, as illustrated in the schematic in Figure 1.1. The anode typically consists of graphite or silicon, while the cathode is composed of lithium-based transition metal oxides such as LCO, lithium iron phosphate oxides (LFP) or nickel cobalt manganese oxide (NCM). The electrolyte, usually a lithium salt (e.g. $LiFP_6$), facilitates the movement of lithium-ions between the anode and the cathode.

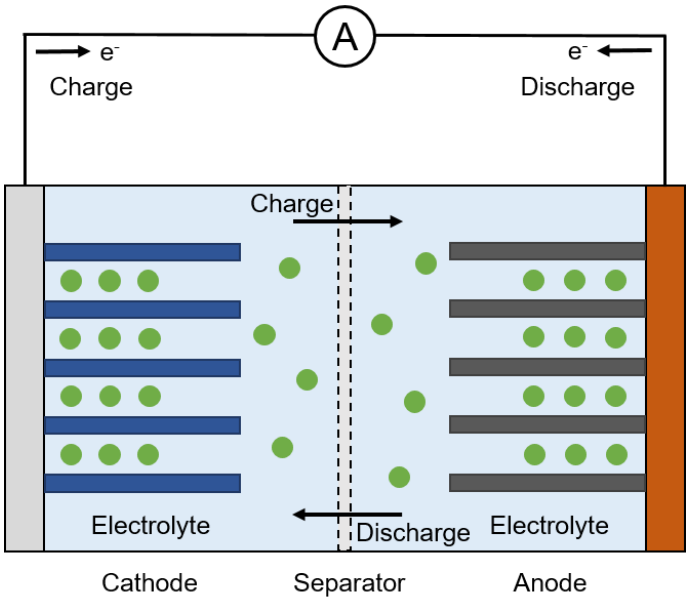

Figure 1.1.: The working principle of a lithium-ion battery illustrating the flow of electrons via an external circuit and the flow of lithium-ions (green circles) within the electrolyte.

During discharge, lithium-ions migrate from the anode to the cathode through the electrolyte, generating a flow of electrons in an external circuit. Conversely, during charging, an external power source drives the lithium-ions from the cathode back to the anode, where they intercalate into the anode structure. The separator, a porous membrane, allows lithium-ion transfer while simultaneously inhibiting direct contact between the two electrodes. This function is essential for safety, as it prevents short circuits.

Cathode active materials

The cathode of a battery significantly influences the performance of LIBs in terms of capacity, energy density, lifespan, safety and costs. The requirements for LIBs depend on their field of application. For EVs, long mileage, fast charging, low weight, and safety under various conditions, such as crashes and extreme temperatures, are desired [12, 13]. For grid storage systems, on the other hand, weight and fast charging are less critical. However, they require a very long lifespan, often more than 20 years, low costs as a significant number of battery modules are used, and high safety standards over thousands of cycles [14].

Various cathode materials have been developed over the years; yet currently, two stand out and dominate the market: LFP and NCM [15]. Both materials are used for EVs and grid storage systems. LFP cathodes are cost-effective, environmentally friendly, resistant to thermal runaway, and have a long lifespan. Although they

operate efficiently over a large temperature range, they do not perform well in cold conditions. In comparison to LFP, NCM offers a high capacity and energy density, which optimize the weight and space of the battery packages, making it attractive for EVs and small devices such as portable electronics and applications in micro and nano devices. Furthermore, NCM has a well-balanced battery performance over a wide range of temperatures. However, the lifespan is shorter than that of LFP and it is more expensive due to the raw materials used. Overall, NCMs are attractive materials for solutions which require high-energy-density battery materials such as for EVs aiming for long mileage [15].

Ni-rich NCM cathode active materials

NCM are state-of-the-art cathode active materials (CAMs) due to their high capacity, good capacity retention and structural and thermal stability. In recent years, Ni-rich NCM such as NCM811 ($Li_1Ni_{0.8}Co_{0.1}Mn_{0.1}O_2$) has gained growing attention due to its high theoretical capacity of approximately $275\,mAhg^{-1}$ [16] (LFP $\sim$$170\,mAhg^{-1}$ [17]), which is particularly interesting for EVs aiming for long distances. Furthermore, an increase in nickel content reduces the cost compared to that of cobalt-rich layered oxides. Beyond technological and economic reasons, eliminating cobalt in battery cathodes is essential. Cobalt is toxic and is mined largely under inhumane conditions involving child labor in the Democratic Republic of the Congo [18].

Despite the high theoretical capacity of Ni-rich NCM, it cannot be reached in practice because Ni-rich NCM suffers from structural and thermal instabilities at high state of charge (SOC), e.g. due to the release of lattice oxygen. The increased nickel content leads to greater destabilization of the structure at high SOC than NCM cathodes with lower nickel content. Nonetheless, the capacity that can be delivered within a stable voltage window is still higher for NCM811 ($200\,mAhg^{-1}$) than for NCM111 ($160\,mAhg^{-1}$) [19]. In particular, degradation of the surface structure is a common issue in Ni-rich NCM. A prominent degradation mechanism is the phase transition from the layered to the rock salt structure on the surface. In the rock salt structure, transition metals (TMs) occupy lithium-ion positions and thus hinder lithium diffusion, which causes kinetic hindrance and eventually leads to capacity fading. Furthermore, Ni-rich NCMs can suffer from cracking, electrolyte degradation, and formation of potentially harmful cathode-electrolyte interface (CEI) among other phenomena [20].

1.1. Research strategy

In recent years, numerous studies have been conducted to understand the degradation phenomena in Ni-rich NCMs and address the identified structural and thermal instability [20–24]. Despite extensive research and progress in stabilizing Ni-rich

NCM structures, structural degradation remains a key point of discussion, with some details still not fully understood. Several factors contribute to a lack of knowledge. First, degradation processes in Ni-rich NCM LIBs are complex, as they are not isolated but are mutually interconnected and can amplify each other. Therefore, extensive research is needed that sheds light on various aspects. Second, sample history has a great influence on the properties and performance of a battery. Therefore, comparing the results of materials with the same stoichiometry can be misleading. Third, the observed degradation phenomena can have different origins. They may originate from synthesis steps, manufacturing or cyclic processes, but can lead to the same behavior.

In order to refine the scope of this thesis, we concentrate on the following three specific research gaps:

- The shift to a higher nickel concentration in NCM requires a re-examination of the structural degradation because the results previously observed for other NCM compositions are not necessarily valid anymore. While it is widely agreed that a rock salt layer forms on the surface when the cathode is exposed to high potentials, the question of a stable intermediate spinel phase, as observed in NCM with lower nickel content, remains ambiguous [23, 25–32]. Furthermore, the time-dependent formation of a rock salt layer at high potentials and its impact on the electrochemical impedance compared to the formation of a CEI remain unanswered. A better understanding of the dominant degradation process can, for example, help prioritize mitigation strategies.

- High-quality Ni-rich NCM requires a slight lithium excess during the synthesis, and residual lithium components can remain on the surface. To enhance the processability and avoid gassing during battery operation, Ni-rich NCM powders are typically washed in water to remove surface contamination. Washing leads to a lithium/proton exchange which destabilizes the layered NCM structure and eventually leads to rock salt formation. However, the exact phase transition mechanisms and the migration of protons within the particles remain unclear [33, 34]. A better understanding is needed to develop specific solutions to stabilize the structure.

- Mitigation strategies, such as coating, have been successfully applied [20, 35–39]. Although many coatings have been investigated and extensive electrochemical studies have been carried out, limited characterization data are available on the structural evolution of coatings during cycling. To optimize coatings in the future, a better understanding of their behavior during cycling is needed.

Answering these research questions is of great scientific and industrial interest, as the targeted development of material solutions can save resources, including costs, time, and energy, and ideally lead to significantly better battery performance.

The analytics and quality assurance (AQua) cluster, funded by the German Federal Ministry of Education and Research (BMBF), followed a multi-scale approach to address complex degradation phenomena in Ni-rich NCM. The purpose of the cluster was to gain a thorough understanding of the relationships between structure, manufacturing processes, and electrochemical characteristics. The project Oberflächen- und Grenzflächenanalytik von Aktivmaterialien mittels hochaufgelöster Analytischer Verfahren (von *Post mortem-* zu *in situ-* und *Operando*-Methoden) (AQua-POp) was embedded in the AQua-cluster and focused on the analysis of fundamental degradation and aging processes from microscale to nanoscale by combining structural, chemical and electrochemical analysis. The AQua-POp project involved collaboration between three partners from JLU Gießen (Institute of Physical Chemistry), TU Munich (Chair of Technical Electrochemistry), and RWTH Aachen University (Central Facility for Electron Microscopy). This dissertation was written within the framework of the AQua-POp project and presents new insights into the structural changes of Ni-rich NCM during fabrication and cycling through the application of (high-resolution) transmission electron microscopy (TEM) techniques and analytical TEM.

TEM is a versatile technique used in materials science which offers a local analysis of the atomic crystal structure of materials. Therefore, TEM is suitable for studying structural degradation in Ni-rich NCM locally, which is highly needed to answer the aforementioned research questions. High-angle annular dark-field (HAADF)-STEM was the primary imaging technique employed in this work. This imaging technique provides contrast which strongly increases with the atomic number Z, allowing direct interpretation and study the atom positions of the used TM. In combination with spectroscopy, information about the local elemental composition and electronic structure can be analyzed. An *in situ* biasing setup was tested to investigate the dynamics of a coating material during cycling.

Ni-rich NCM can be synthesized as polycrystalline (PC) powders of spherical secondary particles consisting of many primary particles or as single crystalline (SC) particles. SC-particles were chosen because the main focus in the first two research topics was on phase transitions expected to occur on the surface. The use of SC-particles has the great advantage that lithium diffusion along grain boundaries and cracking due to anisotropic volume changes, which would make it difficult to study surface degradation, were absent. The samples investigated were provided by the company BASF (Ludwigshafen, Germany) and the collaborators from JLU Gießen.

2. Literature review

This chapter reviews the material system, common degradation mechanisms, effects of washing, and mitigation strategies in layered Ni-rich NCM cathodes. The literature review focuses mainly on the structural properties and changes of NCM because this knowledge is the basis for a later classification and discussion of the results. The emphasis is on Ni-rich NCM with a nickel content of at least 80 %, which is the type of NCM used later in the experiments. Although some observations and descriptions are valid for NCM with a lower nickel content, this is not always the case. In particular, structural instabilities and the associated degradation mechanisms are exacerbated by a high nickel concentration.

2.1. Ni-rich NCM - the materials system

In general, Ni-rich NCM refers to $Li_1Ni_xCo_yMn_zO_2$, and $x + y + z = 1$ with a Ni-content above 80 %. Common material combinations include $Li_1Ni_{0.8}Co_{0.1}Mn_{0.1}O_2$, $Li_1Ni_{0.83}Co_{0.11}Mn_{0.06}O_2$ or $Li_1Ni_{0.9}Co_{0.05}Mn_{0.05}O_2$, abbreviated as NCM811, NCM83 and NCM90, respectively.

2.1.1. Crystal structure

NCM forms a characteristic layered structure in which the atomic planes of lithium-ions and TM ions alternate. These atomic planes are separated by layers of oxygen atoms, as illustrated in Figure 2.1. Each TM is coordinated by six oxygen atoms, which form an octahedron. The crystallographic structure of NCM is described by the space group R-3m with number 166, corresponding to the trigonal crystal system [40, 41]. Therefore, the crystal structure can be displayed in the rhombohedral or hexagonal lattice, with the latter being the more common choice. For the hexagonal lattice of NCM811, the lattice constants are approximately 2.8 Å for the a- and b-axis and approximately 14.2 Å for the c-axis. Moreover, the layered structure is isostructural with the α-$NaFeO_2$ structure type.

During charging of the battery, lithium-ions deintercalate from the layered structure, resulting in an alteration of the lattice configuration as a function of the state of charge (SOC). The a-axis lattice parameter shrinks monotonically as a consequence of the contraction of the NiO_6 octahedra due to the oxidation of nickel from Ni^{3+} to Ni^{4+}. With increasing SOC, the repulsion between oxygen layers becomes stronger due to the missing lithium-ions, which leads to an elongation of the c-axis lattice

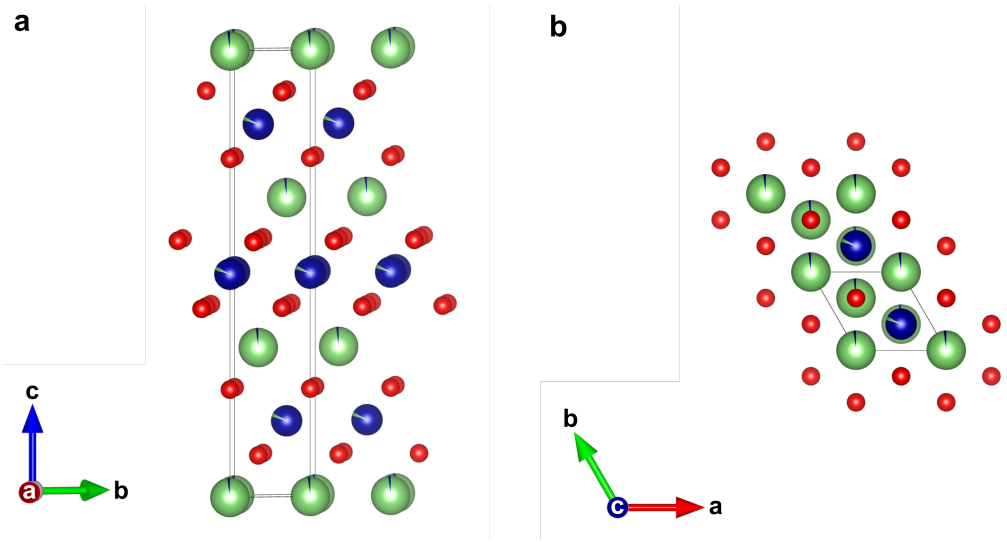

Figure 2.1.: Crystal structure model of layered NCM with alternating atomic planes of Li-ions (green) and TM-ions (blue) which are separated by oxygen (red) layers [41] along the (a) [100] direction and (b) along the [001] direction. The material shows an intrinsic cation mixing of lithium-ions and TM ions. The structure model was generated using Vesta [42].

parameter in the hexagonal lattice [41, 43, 44]. At high SOC, the lattice parameter decreases again, involving mixing of nickel cations at lithium positions or hybridization of the Ni 3d orbital and O 2p orbital [44, 45], reducing the negative charge of oxygen ions.

The study by Xu *et al.* [44] offers a detailed analysis of the various crystallographic states of lithium nickel oxide (LNO) as a function of the SOC, as demonstrated in Figure 2.2. The phase terminologies (O3-O1 and H1-H3) are prevalent in the literature; thus, a concise explanation is provided herein. Upon delithiation, the following phases are observed as a function of the SOC: H1(O3) $\rightarrow$ M(monoclinic) $\rightarrow$ H2 $\rightarrow$ H3 $\rightarrow$ O1. The terms O3 and O1 are less frequently used and describe the fully lithiated and fully delithiated states, respectively, in which the layered structure is retained. The numbers correspond to the number of TMO_2 planes in the unit cell. Phases H1 to H3 describe hybrid phases of the hexagonal arrangement in which their lattice parameters change with increasing SOC (see also Section 2.2.1 and Section 2.2.3).

Typically, the different hexagonal states are correlated with the electrochemical cyclic voltammetry (CV) curves [22, 23, 26, 44, 46]. CV curves display redox reactions occurring in the material indicated by peaks. Although it is common practice to directly correlate electrochemical data with structural data, researchers recently challenged this approach, arguing that the correlation is too simplistic and that CV curves are not sufficient evidence for structural analysis [44]. For example, they

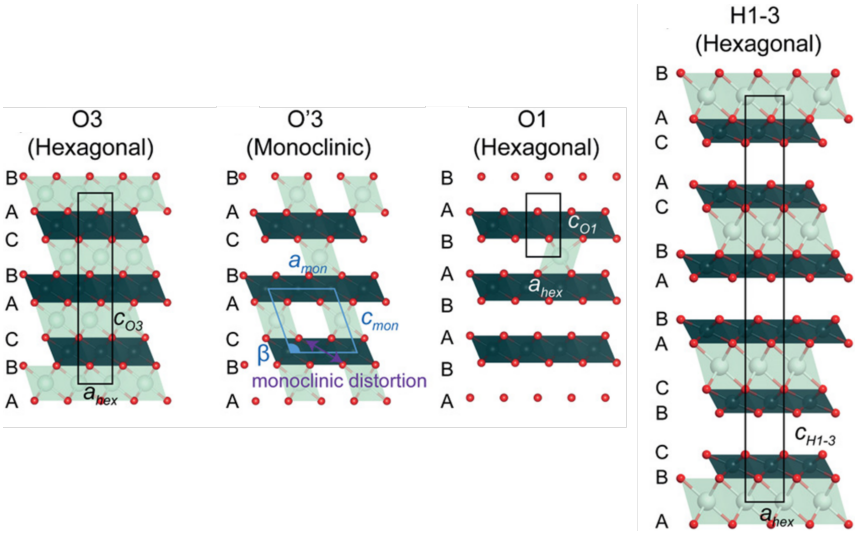

Figure 2.2.: Illustration of the different crystal structure states that can occur in Ni-rich cathodes depending on the SOC. The structure models show a parallel view of the layered structure and highlight the stacking sequences within the corresponding structures. The H1-H3 structures differ in their lattice parameters a and c. The figure was modified from [44].

claim that such a strict phase transition, as they have observed in LNO does not exist in Ni-rich NCM because the lattice parameters change continuously instead of abruptly, as is the case with LNO. However, the electrochemical phase transition from H2 to H3 is typically used to explain the structural degradation of Ni-rich NCM.

2.1.2. Role of transition metals

To gain a deeper understanding of the material properties in Ni-rich NCM, it is imperative to delve into the electronic band structure of the TMs nickel, cobalt, and manganese. Extensive information is available in the review articles authored by Jung *et al.* [47], Manthiram [48], Lu *et al.* [49], and Dai *et al.* [45], and a brief summary is given here. The configuration of the band structure of the TMs is presented in Figure 2.3. Nickel is the primary TM in Ni-rich NCM cathode material, offering more stable valence states than cobalt and manganese. In its ionic form, nickel can exist in three different valence states: Ni^{2+}, Ni^{3+} and Ni^{4+}. In the fully lithiated state, nickel is present in the valence state Ni^{2+} or Ni^{3+}. Upon charging, nickel is oxidized to Ni^{3+}/Ni^{4+}, resulting in a higher capacity than in LCO for example, because more lithium-ions can be extracted. Furthermore, the redox pairs of nickel (Ni^{2+}/Ni^{3+} and Ni^{3+}/Ni^{4+}) are at higher band energies than, for example, the band of the cobalt redox pair Co^{3+}/Co^{4+}. Consequently, nickel requires less charge voltage than cobalt to achieve the same capacity because extracting electrons from its e_g-orbitals is energetically more favorable than from the lower t_{2g}-orbitals. In

summary, the capability of high lithium extraction from Ni-rich NCM at a given potential leads to a high energy density within reasonable voltage windows [16].

Although Ni^{2+} is chemically less reactive, as no energetically higher e_g-orbitals are occupied, it does not lead to a more stable structure overall. The ion radii of Ni^{2+} and Li^+ are nearly identical to 0.69 Å and 0.76 Å, respectively. In a highly depleted Li^+-state at the cathode site, Ni^{2+} tends to occupy Li^+-positions due to a reduced migration energy barrier for nickel. Consequently, lithium channels are partially, or in extreme cases, fully blocked, which hinders lithium solid-state diffusion. This kinetic hindrance results in overpotentials causing capacity fading. Furthermore, the Ni^{3+} valence state is susceptible to Jahn-Teller distortion due to the unpaired electron in the e_g-band, causing structural instability [50, 51].

In Ni-rich NCM, cobalt and manganese serve as stabilizers. Cobalt plays a crucial role in electronic conductivity. The hybridization of the O 2p band with the Co^{3+}/Co^{4+} redox pair band results in more delocalized electrons, enhancing electronic conductivity. Furthermore, cobalt reinforces the layered structure by mitigating antisite defects between lithium and nickel, thus preserving the rate capability. Cobalt provides additional capacity, as it can undergo redox reactions from Co^{3+} to Co^{4+}. In comparison, manganese does not undergo any redox reactions and remains electrochemically inactive in the Mn^{4+} valence state. It mainly stabilizes the layered structure by preventing oxygen release, since the Mn^{4+} and O 2p bands do not overlap.

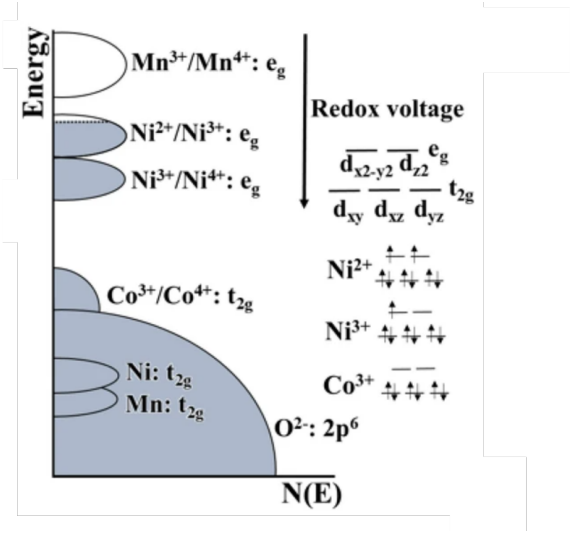

Figure 2.3.: Schematic of the electronic band structure in Ni-rich NCM layered oxide with TM 3d orbital occupancy. Copied from [47].

2.1.3. Synthesis and particle morphology

The synthesis route and parameters greatly affect the quality of Ni-rich NCMs and, subsequently, the battery performance. Therefore, a magnitude of parameters, such as temperature and atmosphere, needs to be controlled carefully during the synthesis process because they determine the structure at the micro- and nanoscale. Various synthesis routes and parameters have been explored in recent years. An overview of the most common synthesis routes is given in a review by Saaid *et al.* [52]. The most widely used synthesis method is co-precipitation based on TM hydroxide precursors or TM oxide precursors [53].

There are two types of NCM morphology: polycrystalline (PC) and single crystalline (SC) particles, as schematically shown in Figure 2.4. PC-NCM consists of spherical, micrometer-sized secondary particles with many nanometer-sized primary particles inside, which are often oriented randomly. SC-NCM describes particles ranging from sub-micrometer size up to a few micrometers, with a single crystalline domain. While PC-NCM cathodes remain widely used, SC-NCM has recently gained popularity. PC-NCM is likely to crack during the anisotropic volume change of randomly oriented primary particles during cycling [54, 55] (see also Section 2.1.1 and Section 2.2.1), which introduces a cascade of degradation mechanisms. SC-NCM exhibits a higher mechanical strength and is unlikely to crack during cycling, which enhances the long-term performance of the cathode. However, SC-NCM suffers from slow lithium diffusion in the large bulk and a slow rate capability due to long diffusion pathways [55, 56]. Trevisanello *et al.* [55] advocated for further optimization of the morphology and size of the particles to meet the demands of fast charging and long-lasting cathode materials.

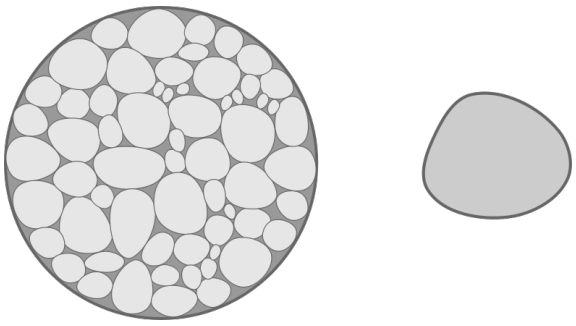

Figure 2.4.: Schematic of a secondary polycrystalline particle with many primary particles (left) and a single crystalline particle (right).

2.2. Degradation mechanisms

Degradation of Ni-rich NCM arises during synthesis, storage, and operation and is generally caused by any type of chemical, thermal, or structural instability. Typical degradation processes include cracking, rock salt formation on the surface, and disorder of TMs. The formation of a CEI is discussed as a degradation process in Ni-rich NCM, which, however, can also have a positive effect on the electrochemistry [20]. An overview of degradation mechanisms occurring in Ni-rich NCM is presented in Figure 2.5. Importantly, degradation mechanisms cannot be considered independently; they are mutually interconnected [20]. This section aims to give an overview of the main degradation mechanisms and to describe their key characteristics, as well as to highlight controversial findings in the literature.

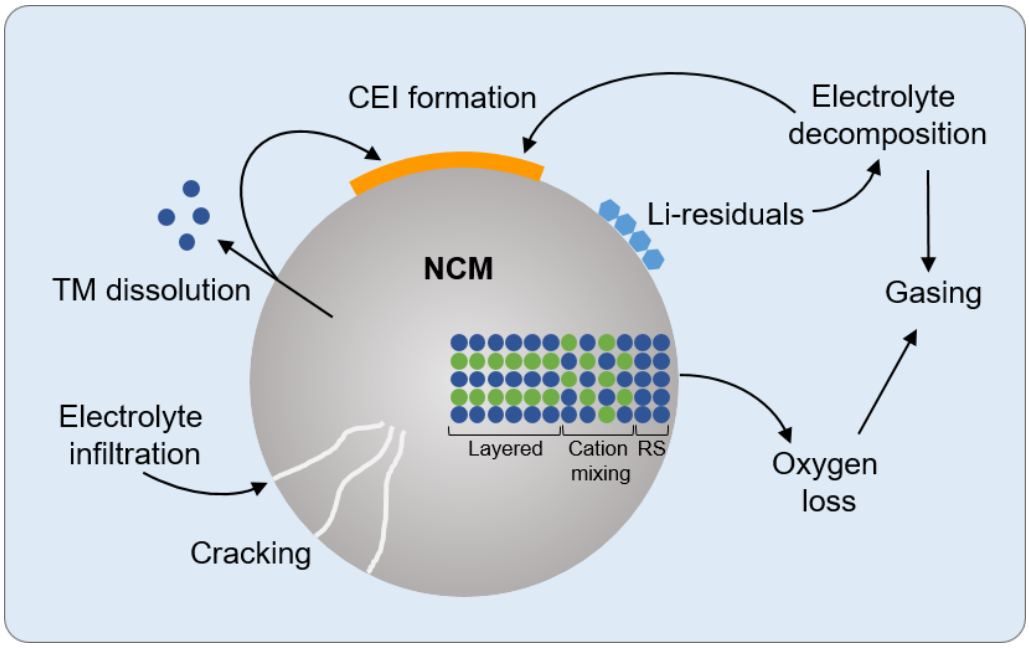

Figure 2.5.: Schematic overview of degradation mechanisms occurring in Ni-rich NCM and the cross linking between them. The blue dots represent TMs and the green dots represent lithium-ions.

2.2.1. Cracking

Cracking is a commonly observed degradation phenomenon in Ni-rich NCM materials. There are two types of cracking: intergranular and intragranular cracking. Intergranular cracking only occurs in polycrystalline NCM [54, 57, 58] and can have different origins. First, intergranular cracks can form during the fabrication of the electrode. This type of cracking results directly from mechanical effects during calendering processes [59]. Second, intergranular cracks occur during cycling. At a high

SOC, Ni-rich NCM undergoes an anisotropic lattice change, as described above in Section 2.1.1. The significant volume change is described by the H2 to H3 transition. The anisotropic volume change causes mechanical stress between the often randomly oriented primary particles, leading to cracking at the grain boundaries. The detachment of the particles results in reduced electronic conductivity. Furthermore, cracks increase the surface area. An increased surface area enhances lithium diffusion but also increases side reactions, which can promote CEI formation, rock salt formation, and loss of active material [60]; thus, negatively affecting battery performance.

Intragranular cracks can occur in single crystalline and polycrystalline NCM in the form of nanopores, voids, or cracks within a primary particle or single crystalline particle. As found in previous studies [61–63], intragranular cracks impair electrochemical performance. The origin of intragranular cracking in Ni-rich NCM is multifaceted [64]. Again, high SOC, leads to structural instabilities and oxygen loss, which can lead to pore formation also in the core of particles [65]. Furthermore, structural inhomogeneities such as Ni/Li antisite defects, commonly referred to as cation mixing, can cause internal stress and cracking. Yan *et al.* [62] identified dislocation-based crack incubation, occurring in the core of a particle at high voltages, as a further mechanism responsible for the formation of intragranular cracks.

2.2.2. Cation mixing

Cation mixing or cation disorder describes the phenomenon in which nickel ions migrate to lithium-ion positions, with significant consequences for electrochemical performance. The origin and consequences of cation mixing were analyzed in comprehensive detail in the reviews published by Li *et al.* [66], Wei *et al.* [67], and Cho *et al.* [68]. Thus, the most essential findings will be briefly summarized here. The main reason for cation mixing was found to be the similar ionic radii of Ni^{2+} and Li^{+}. Therefore, cation mixing is particularly an issue in layered CAMs with a high nickel concentration. During synthesis, cation mixing can be controlled by optimizing the amount of lithium sources, the sintering temperature, and the oxygen partial pressure. During cycling, cation mixing occurs, particularly at high SOC, because it is energetically favorable for nickel ions to move to vacant lithium-ion positions. With an increasing concentration of lithium vacancies and oxygen vacancies, the energy barrier for Ni^{2+} migration decreases further. The nickel ions at the lithium-ion positions block the lithium diffusion channels, reducing the overall Li^{+} diffusion coefficient and ultimately the battery capacity. Furthermore, the stronger O-TM-O bonds, compared to the O-Li-O bonds, reduce the interplanar lattice spacing and contribute to lithium diffusion hindrance. However, it was found that a specific low amount of cation mixing can improve structural stability.

2.2.3. Phase transition

The phase transition on the particle surface from the layered structure (space group R-3m) to the cubic rock salt structure (space group Fm-3m) with NiO-structure type, which is often referred to as surface reconstruction in the literature, is a commonly observed degradation phenomenon in NCM-CAMs leading to capacity fading [58, 69–72]. The rock salt phase is deficient in lithium-ions and TMs occupy the former lithium channels, as indicated in the schematic in Figure 2.6. The driving forces for this phase transition are lithium extraction from the layered structure and oxygen release, which are favored at high SOC or elevated temperatures. As Ni^{2+} has an ionic radius similar to Li^{+}, Ni^{2+} tends to migrate to empty lithium positions. At high SOC, the highly reactive Ni^{4+} is present. As it is energetically favorable, Ni^{4+} is reduced to Ni^{2+} under oxygen release. A further source of rock salt formation is the high nickel content itself, which induces structural instability during synthesis due to Ni/Li disorder [73]. In addition, contact of the surface with the electrolyte or other impurities can lead to oxygen loss and, consequently, to the formation of a rock salt surface layer. Finally, protons, which are incorporated into the layered structure during washing, were found to be another source of destabilization of the layered structure and to increase the likelihood of rock salt formation (see Section 2.3) [33, 34].

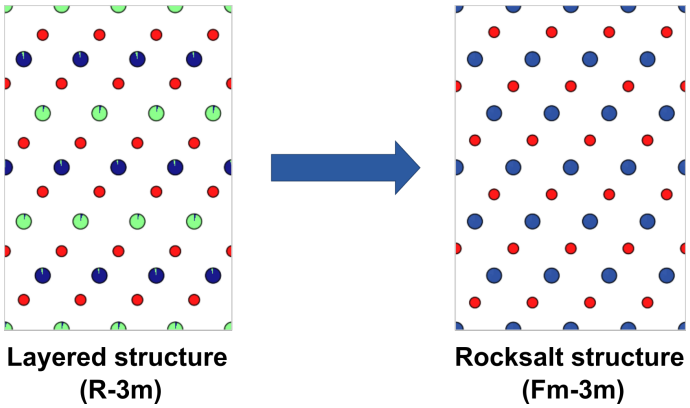

Figure 2.6.: Phase transition from the layered NCM structure with layers of the TMs nickel, cobalt, manganese (blue), oxygen (red) and lithium (green) to the NiO rock salt structure which is often accompanied by release of lattice oxygen. The structures were generated with Dr. Probe [74] using crystallographic structure information from [41, 75].

It is widely agreed that rock salt formation on the surface can occur in Ni-rich NCM. However, the exact transition mechanism from the layered to the rock salt phase, including potential intermediate phases, is not yet fully understood. The literature on phase transition mechanisms is sometimes inconsistent, as outlined below. Chemists [41] proposed that the phase transition from the layered structure to the

rock salt structure can occur directly or via an intermediate spinel phase (M_3O_4). Several review papers have claimed that an intermediate spinel phase appears, accompanied by oxygen release, in Ni-rich NCM [23, 25, 26]. However, the referenced articles did not discuss Ni-rich NCM with a nickel content of 80 % or above. Instead, they focused on NCM phases and other cathode oxides with elevated concentrations of cobalt and/or manganese.

A review of the existing literature containing TEM measurements revealed that the atomic structure at the surface of NCM811 did not usually show any clear indications of an intermediate spinel phase. Instead, a mixed cation layer was observed as a transition layer between the layer and the rock salt phases [27–30]. Nevertheless, two examples were found in which the transition region was marked as spinel phase [31, 32].

Studies that did not present TEM data but used alternative structural analysis methods, such as X-ray powder diffraction (XRD), showed controversial results regarding an intermediate spinel phase (M_3O_4). While Bak *et al.* identified an intermediate spinel phase [76], other researchers [34] found no evidence of spinel formation. In their study of various NCMs, including NCM811, Bak *et al.* [76] attributed spinel formation to the migration of cobalt-ions to 8a tetrahedral sites during thermal decomposition. They admitted that in NCM811 the temperature range for a LiM_2O_4 spinel phase is very narrow and mostly M_3O_4 occurs in NCM811.

In contrast to Ni-rich NCM, NCM with a high manganese content tends to form a spinel phase upon electrochemical cycling or thermal treatment. In these cases, a well-ordered spinel phase can be clearly recognized in the corresponding TEM images [77, 78]. Pure lithium manganese oxide ($LiMn_2O_4$) crystallizes in a spinel structure (space group Fd-3m) with a cubic close-packed oxygen sublattice [79, 80]. Overall, there is no convincing evidence that an ordered spinel phase generally occurs as an intermediate phase in Ni-rich NCM. Instead, numerous studies have shown a layered structure with strong cation mixing in the lithium channels.

The literature agrees that a phase transition, which eventually forms a rock salt layer, emerges at the particle surface under conditions of high SOC, elevated temperature, or other factors that induce structural destabilization. However, the reported results sometimes present contradictory findings regarding the thickness of the rock salt layer, its impact on the electrochemical performance, and the onset point of the phase transition. To shed some light on ongoing discussions, a literature overview is presented in Table 2.1. The overview offers insight into the controversial discussion and does not claim to be complete.

In most studies, the thickness of the transformed surface layer was found to be between 3 - 10 nm. However, Abraham *et al.* [81] found a transformed surface layer thickness of 30 - 40 nm after a voltage hold at 3.92 V. Lin *et al.* [82] observed a gradual

increase in the thickness of the transformed surface layer from 2 - 18 nm with increasing numbers of cycles, with an upper cut-off voltage of 4.5 V. Li *et al.* [83] and Dose *et al.* [28] noted that electrolytes and electrolyte additives have a significant impact on the transformed surface layer thickness. All of the studies mentioned so far used TEM to examine the layer thickness. In contrast, Friedrich *et al.* [41] calculated a rock salt layer thickness of approximately 15 nm after 1000 cycles to 4.5 V based on XPD data. However, the calculation results were not directly confirmed by TEM data.

In conclusion, the exact stoichiometry, the synthesis route, coatings or dopants, as well as further treatments and cycling protocols have a significant impact on the structure and structural evolution, including rock salt layer formation at the surface, and thus on the electrochemical properties of the cathode material. Therefore, it is essential to ensure that the materials being compared are accurately defined and that the presented structures are unambiguously determined.

2.2.4. Electrolyte decomposition

When studying the degradation mechanisms of NCM cathode materials, it is necessary to consider the role of the electrolyte, as electrolyte decomposition is directly linked to the degradation processes occurring at both electrodes. The electrolyte is a key component in LIBs that facilitates lithium-ion diffusion between the anode and the cathode. For LIBs, an electrolyte typically consists of a lithium-containing salt dissolved in a non-aqueous, carbonate-based solvent such as ethylene carbonate (EC) or ethyl methyl carbonate [28]. For example, remaining moisture in a cell can trigger the decomposition of lithium hexafluorophosphate ($LiPF_6$), an often used lithium salt, into hydrofluoric acid (HF) among other degradation products [86]. The consumption of active lithium inventory can lead to capacity fading. HF can attack the cathode surface, prompting further degradation such as TM dissolution or structural changes. Furthermore, at a high state of charge (SOC $>$ 80 %), NCM is prone to release reactive singlet oxygen [87], which initiates a series of subsequent degradation processes. The release of lattice oxygen is closely related to the stoichiometry of the NCM material; as with higher nickel content, the onset potential for oxygen release decreases [88]. It has been proposed that the released lattice oxygen interacts with the organic solvent, resulting in the generation of H_2O, CO_2, and CO [89]. Gas formation in battery cells poses a serious safety risk. A detailed report on electrolyte decomposition pathways is beyond the scope of this thesis. For further information, see recent publications by Rinkel *et al.* [90] and Dose *et al.* [28].

Another aspect to consider is that different organic solvents are beneficial for both the anode and the cathode. As observed by Dose *et al.* [28], the combination of EC-based electrolytes with Ni-rich NCM resulted in substantial degradation of the battery. While EC-free electrolytes seemed beneficial for the cathode, EC-based electrolytes play a pivotal role in the formation and repair of the solid-electrolyte

Material	Treatment	Transformed surface layer thickness	Observations	Method	Reference
NCM811	150 cycles to 4.5 V	2-18 nm	gradual increase with increasing # cycles; transitional region	HAADF-STEM and diffraction	[82]
NCM811	83 cycle to 4.1 V and 4.3 V	3-10.5 nm	Electroyte additives have a great impact on the layer thickness	HAADF-STEM + image processing (summation of line scans to average out the thickness variations)	[83]
NCM811	1 cycle between to 4.6 V with 60 h potentiostat hold at 4.6 V	3-5 nm	Electrolyte has a significant impact	HR-TEM	[28]
NCM811	500 cycles to 4.3 V	3-7 nm RS plus >20 nm cation mixed layer	1-2 nm in pristine and cation mixing in bulk	HAADF-STEM	[46]
NCM811	1000 cycles to 4.5 V	15 nm		Calculation of O-depleted surface layer based on XRD data, TEM measurements were not successful	[41]
LNCO82	voltage hold at 3.92 V	30-40 nm	RS was confirmed by diffraction	TEM	[81]
NCM900505	100 cyles to 4.3 V	5 nm RS + amorphous layer	4.5 V more amorphous layer	TEM	[84]
NCM523	50 cycles to 4.5 V and 4.8 V	15-20 nm	Higher cut-off voltages lead to thicker RS layer	HAADF-STEM + diffraction (see spinel spots in DP)	[85]

Table 2.1.: Literature overview about phase transition on the surface in Ni-rich NCM.

interface (SEI) at the anode site, thereby preventing gassing due to lithium plating. Finding a suitable compromise that meets the requirements of both electrodes remains a challenge in the development of high-performance LIBs.

2.2.5. CEI Formation

The cathode-electrolyte interface (CEI) is a layer that forms between the cathode surface and the electrolyte due to electrolyte decomposition. Typical species contributing to CEI formation are lithium residuals and degradation products (Li_2O, LiOH, Li_2CO_3, LiF), TM fluorides formed by the reaction of NCM with HF and electrolyte decomposition products such as polycarbonates and lithium hexafluorophosphate products ($Li_xPF_yO_z$). The exact reaction mechanisms of the individual redox reactions are described in [20, 22]. The formation of CEI is significantly influenced by the composition of the cathode material, the electrolyte, and the operational parameters, including the temperature and applied voltage. These factors control, for instance, the dissolution kinetics of TM and the electrolyte degradation. As numerous factors influence CEI formation, it has not yet been possible to define a universal mechanism.

CEI formation can be seen as a degradation mechanism that implies a detrimental influence on battery performance due to the loss of lithium and active cathode material which leads to capacity fading [20]. A thicker CEI layer impedes lithium diffusion, resulting in an increased interfacial impedance. However, the presence of a CEI can also yield positive effects because a stable CEI can serve as a passivation layer, protecting the cathode surface from side reactions with the electrolyte and mitigating structural surface degradation. The type of electrolyte and the salt concentration are key factors for a stable CEI layer [91, 92].

2.2.6. Transition metal dissolution

The dissolution of TMs from the cathode is another significant degradation mechanism that occurs in NCM and can be caused by different factors such as elevated temperatures, high voltages, and HF attack [93, 94]. Cracked particles are especially prone to TM dissolution due to their enlarged surface area, which results in a greater contact surface with the electrolyte [94]. TM dissolution results in the loss of active material, and thus in an increase in impedance and capacity fading. Furthermore, TM dissolution can lead to the formation of fluoridic TM species MF_x, which can contribute to CEI formation [22]. Moreover, TM dissolution has a detrimental impact on the anode. For example, dissolved TMs from the cathode site can deposit on the SEI and can initiate several severe degradation processes, such as SEI growth [93, 95].

2.3. Washing of Ni-rich NCM and induced thermal instability

Washing of Ni-rich NCM after synthesis is a crucial step in industrial manufacturing to remove surface contaminants such as lithium and TM hydroxides, carbonates, and bicarbonates. Surface contaminants originate, for example, from residual lithium salts [21, 34]. These salts are used to generate a slight lithium excess during synthesis, which is necessary for the synthesis of Ni-rich NCM [96]. Additionally, contaminants form during the storage of NCM in an ambient atmosphere containing water vapor and CO_2 [97–100]. The presence of surface contaminants adversely affects electrode manufacturing, cell performance, and battery safety for the following reasons: (1) gelation of the electrode slurry during mixing due to an elevated pH value [101], (2) reduction in the cycling life of a battery [34], and (3) gas formation during the initial cycles due to CO_2 evolution driven by the chemical decomposition of carbonate species [102, 103]. Washing NCM in H_2O effectively eliminates surface contaminants and thus mitigates gassing and increases processability, making it a necessary step despite the added cost [34].

Although washing is inevitable, the washing process is associated with a lithium / proton (Li^+/H^+) ion exchange, resulting in a layered NCM with a protonated surface (H_xLi_{1-x} TMO_2, where TM represents Ni, Co, Mn) and the formation of LiOH, as illustrated in Figure 2.7. Based on the work of Pritzl *et al.* [33] and Oswald *et al.* [34] the protons intercalate in the near-surface lattice leading to reduced thermal stability. This effect was also observed by researchers who investigated NCM storage in an ambient atmosphere [104, 105]. Upon heating to 450 °C, H_2O and O_2 [33] are released, leading to an oxygen-depleted surface layer comparable to the situation of highly delithiated NCM [19, 76]. Non-protonated NCM also forms a rock salt layer when heated, but the process starts at significantly higher temperatures above 550 °C. Furthermore, washing and subsequent heating above 180 °C or 300 °C prevents or reduces oxygen-release during cycling and thus minimizes the electrolyte oxidation reaction [33], which appears advantageous. However, the formation of an oxygen-depleted surface was found to yield an impedance increase of about 10 times, reducing overall performance [33]. An effective but cost-intensive approach to regenerate the oxygen-depleted surface is to recalcinate the NCM powder at a high temperature (e.g. 800 °C) under constant oxygen flow [104]. However, the reduced lithium inventory due to washing cannot be restored without adding new lithium salts which would negate all efforts made.

The kinetics of ion-exchange processes are not yet fully understood. Washing of CAMs became more relevant with the recently increasing interest in Ni-rich NCM with a nickel content above 80,%, which is known for its structural instability [19]. While most studies have focused on degradation mechanisms and mitigation strategies [20, 22], the effects of washing and the accompanied ion-exchange kinetics

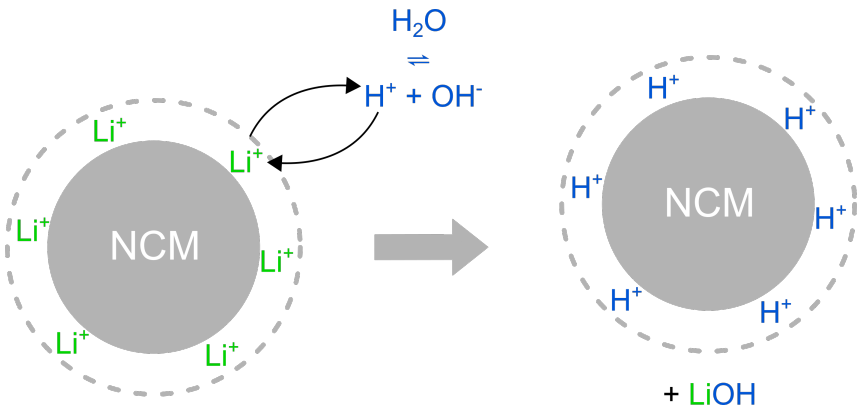

Figure 2.7.: Schematic illustrating the Li^+/H^+ cation exchange mechanism which is assumed to occur at the NCM particle surface (dashed lines) during the washing of NCM.

have not been studied extensively yet, and there are relatively few studies on the subject [33, 34, 106, 107]. Researchers have shown that, for example, the pH value and the lithium hydroxide concentration of the washing solution highly depend on the amount of water and washing time [34].

Although it is undisputed that ion-exchange kinetics scale with the amount of nickel [99], and the washing of Ni-rich NCM leads to a phase transformation from a layered structure to the rock salt structure, possible intermediate phases and the kinetic behavior of the intercalated protons remain unclear. Pritzl *et al.* [33] proposed the formation of a spinel phase (M_3O_4) as an intermediate phase under the release of mainly H_2O and a small amount of O_2, followed by the formation of a rock salt phase (MO) under oxygen release. In contrast to this, Oswald *et al.* [34] did not find any evidence for the proposed formation of a spinel phase upon heating, but they could confirm rock salt formation. Investigating the ion-exchange kinetics and the accompanied phase transition mechanism is a central subject of this work. The findings from the study by Oswald *et al.*, which was conducted within the AQua-POp project, are therefore relevant for the TEM study presented in Section 5.3. More detailed information relevant for the TEM study will be provided there.

2.4. Mitigation strategies

After different degradation mechanisms were introduced in Section 2.2, this section discusses common mitigation strategies to prevent or at least impede degradation processes in Ni-rich NCM. The three main concepts are: improving the microstructure to reduce cracking during cycling, applying a physical protection layer between the CAM and the electrolyte to avoid direct contact between both of them, and stabilizing the atomic structure to prevent TM migration. These concepts can be realized by adjusting the synthesis protocols of CAMs, coating, or doping. To address

the complex and mutually influencing degradation mechanisms of Ni-rich NCM, different mitigation strategies are often combined [20].

2.4.1. Optimizing synthesis protocols

Optimizing synthesis parameters such as calcination time, temperature, and atmosphere can greatly enhance the properties of the NCM powder, as summarized in the review by Saaid *et al.* [52]. An alternative approach is to induce a nickel concentration gradient from the surface to the bulk to stabilize the particle surface and prevent structural degradation [20]. By changing the synthesis conditions, a Mn-rich surface layer followed by a smooth transition to a nickel-rich core can greatly reduce capacity fading during cycling [108]. The Mn-rich surface layer offers good thermal and structural stability, while the nickel-rich bulk provides high capacity. More recently, Lin *et al.* [109] designed an NMC811 powder with a nickel valence gradient without a change in stoichiometry. The outer surface contains Ni^{2+} ions and is oxygen depleted , while the inner part consists of the less stable but more capacitive Ni^{3+}. Therefore, surface degradation is reduced. To achieve an appropriate nickel valence gradient, it is essential to adjust the partial oxygen pressure during calcination.

2.4.2. Coating

Coating of NCM particles is a widely used technique to mitigate structural and chemical degradation, thus maintaining capacity and extending cycling life. A coating layer on the cathode surface acts as a physical barrier between the CAM and the electrolyte, thus preventing decomposition or oxidation of the electrolyte. Although the coating should resist the electrolyte, it should ideally be permeable to Li^+ ions and electrons to preserve charge transfer, which is challenging to achieve. Furthermore, mechanically strong coatings, such as amorphous Al_2O_3, can improve structural integrity and prevent cracking [20]. The primary factors determining the quality of the coating are coating material, thickness, uniformity, density, and conductivity. In recent years, great effort has been put into investigating new coatings and understanding the underlying mechanisms. Several comprehensive reviews provide an extensive overview of surface coatings [35, 36, 110].

Al_2O_3 is commonly used as a coating material, which is briefly presented here as an example, as it was used in one of the subsequent experiments (Section 5.4). Al_2O_3 is a typical coating material for NCM due to its mechanical strength and chemical resistance. However, Al_2O_3 is considered a non-conductive coating, which is particularly true for thicker layers. Nevertheless, lithiation through the reaction of Al_2O_3 with LiOH and Li_2CO_3 at high temperatures ($600 - 800\,°C$) results in the formation of $LiAlO_2$, exhibiting enhanced ion conductivity. Consequently, a uniform coating layer with a thickness of only a few atomic layers, $Al_2O_3/LiAlO_2$, can substantially improve cycling performance [111].

2.4.3. Doping

Doping is a common approach to improve the stability of CAMs by introducing one or several elements into a target structure. Thereby, the dopants change the defect structure of the material and thus alter its properties. In NCM, it is very common to dope the TM site. Doping at the TM site influences grain growth at the microstructural level and/or stabilizes the structure at the atomic level. For example, Park et al. [39] observed that boron ions altered the surface energies of the primary particles, leading to a textured microstructure with radially-symmetrically oriented, elongated primary particles. The modified microstructure generated less internal stress during cycling; therefore, less cracking occurred. For stabilizing the atomic structure of NCM, materials are chosen that, for example, overlap more with the oxygen orbital. In previous studies, researchers showed that a stronger bonding between the dopant element, like aluminum, and oxygen reduced the *c*-axis extension during charging, and thus enhanced the long-term cyclability of the NCM [112–114]. An extensive overview of dopants and their impact on Ni-rich cathodes is provided in the review paper by Cho *et al.* [68].

3. Instrumentation and methods

TEM is used for analyzing the structure and composition of materials at the nanoscale, making it a powerful tool for materials scientists. In a TEM, a high-energy electron beam guided by electromagnetic lenses passes through an electron-transparent sample. The beam-sample interaction leads to a change of the electron beam, which then carries information about the sample. This information is used to form a magnified image. The basic principles of a TEM follow the laws of geometric optics. Using electrons instead of visible light has two key advantages. First, the short wavelength of the electrons shifts the resolution limit d_0, into the Ångström-regime, allowing diffraction at atomic structures. The resolution limit of the optics is given by the Rayleigh limit

$$d_0 \approx 0.61 \frac{\lambda}{\beta}\,, \tag{3.0.1}$$

where λ is the wavelength and β the maximal aperture angle in which the lens works perfectly. Since electron-optical lenses are only perfect within a very small angular range of approximately 10 mrad, the electrons are accelerated to shorten their wavelength. Second, the beam-sample interaction is strong compared to other forms of radiation, which enables the investigation of material structures at the atomic scale. The mean free path for fast electron scattering is typically between 10 nm and 100 nm. Therefore, samples should be sufficiently thinned to minimize multiple scattering and thus allow straightforward and local interpretation of the signals.

Electrons are emitted by an electron gun, which has a small tip from which the electrons are extracted. A field emission gun (FEG) is the state-of-the-art electron source, providing high brightness and low energy spread (< 1 eV), which improves resolution compared to a traditional thermionic emitter. The electrons are extracted by a positive voltage of a few kV and then further accelerated by 100 kV to 300 kV in an ultra-high vacuum. The vacuum prevents collisions with other particles and reduces positive charge impact on the tip. For the further propagation of the beam through the rest of the up to 4 m long microscope column, a high vacuum is generally sufficient to reduce unintended beam scattering. Electron-optical lenses are inhomogeneous magnetic fields. They are used to guide and shape the beam through the microscope, for example, to form a sharp probe and scan it across the sample or to magnify an image onto a detector. The strongest lens is the objective lens with a magnetic field of about 1 T strength. Magnetic fields are generated by currents through coils, and as a result of the strong currents, the coils have to be permanently

cooled by water.

The interaction of the incident electron beam and the sample generates various types of signals, yielding spatially resolved and chemical information about the material. It should be noted that only one beam electron is interacting with the sample at a time. Scattering processes are essentially due to Coulomb interactions and can be elastic or inelastic. In elastic scattering processes, the electron does not lose energy, and in inelastic scattering processes, energy is transferred from the electron to the sample or vise versa. Electron scattering at the atomic core charge is essentially elastic. Exceptions are phonon excitations, where the electron energy can change in a range of a few 100 meV. Inelastic scattering occurs mainly due to the interaction of the incident electron with the electron charges in the shells of the atoms. In these processes, the electron mostly loses energy and may also lead to the emission of secondary electrons (Auger) or X-rays. Back scattering also takes place but is mainly used for imaging in scanning electron microscopy (SEM) with slower electrons and bulk samples.

Essentially, two different setups can be distinguished in TEM: (1) a TEM, in which a parallel electron beam illuminates the sample and the magnified image is recorded on a pixelated detector. (2) a STEM, in which a focused electron probe scans in a raster pattern over the sample and the scattered intensity is recorded on an integrating detector. Both setups were utilized in this work; however, STEM was the primary method to study the degradation mechanisms of Ni-rich NCM cathodes. The relevant setups and principles of image formation for both techniques will be explained in Section 3.1 and Section 3.2, respectively. For sample preparation, a SEM combined with a focused ion beam (FIB) was used and is introduced in Section 3.6 and Section 3.7. The descriptions of the applied methods focus on the experimental setups and provide the basis for interpreting the materials science investigation in this work. For further details and explanations, we refer the reader to the following comprehensive literature [115–120].

3.1. Transmission electron microscopy

Even though high-resolution transmission electron microscopy (HR-TEM) was not used in the conducted experiments, the basic principles will be briefly explained here, as it provides a solid understanding of TEM and can be described more intuitively than in the STEM mode.

3.1.1. Setup

In a transmission electron microscopy (TEM) setup, the sample is illuminated with a parallel beam and a magnified image is recorded with a pixelated detector. The electron beam is emitted from the electron source and is accelerated by a positive

high voltage. A two-lens condenser system is used to form a parallel electron beam incident on the sample. The first condenser lens determines the size of the electron source, the spot size. The condenser aperture limits the divergence and intensity of the electron beam. The second condenser lens spreads the electron beam over the sample. An almost parallel illumination is achieved only for larger spreads of the electron beam. Assuming parallel illumination, Figure 3.1 schematically shows the ray diagram of an ideal microscope, in which electrons are transmitted from top to bottom. After the beam has passed through the sample, the objective lens applies the strongest magnification step and forms the first intermediate image or provides a diffraction image in the back focal plane (bfp). Two different operation modes are possible: (a) diffraction mode, magnifying the back focal plane, and (b) image mode, magnifying the first intermediate image onto the detector. In a TEM, it is possible to switch between the two modes by changing the strength of the intermediate lens, which sits below the objective lens. In addition, when switching from diffraction mode to image mode, the selected area electron diffraction (SAED) aperture is retracted and the objective aperture is inserted, and vice versa. The SAED aperture is used to select a specific sample area to produce a diffraction image. The objective aperture limits the angular range for imaging to produce absorption contrast or to avoid the effects of strong aberrations in phase-contrast imaging for real microscopes. The intermediate and projection lenses, of which only one is shown in the figure, magnify the image before it is displayed on a fluorescence screen or a digital electron detector.

3.1.2. Image formation

Amplitude contrast

Amplitude contrast is the primary contrast mechanism at medium resolution and depends on the mass, thickness and crystallographic orientation of the sample. The principle is illustrated in Figure 3.2. An incident electron beam is weakly scattered by a thin or light sample and therefore just a few electrons are diffracted. In contrast, an incident electron beam is strongly scattered by a thick or heavy sample, which causes diffraction of many electrons. In the example, the strongly diffracted electrons are excluded from the image formation due to the insertion of the objective aperture in the back focal plane. Only the unscattered beam is transmitted and forms the image. The image intensity, which is the squared amplitude of the unscattered beam, is high where the object is thin or weakly scattering, and it is low where the object is thick or strongly scattering. This mode is called bright-field imaging. The complementary mode is called dark-field imaging in which only strongly scattered beams are detected.

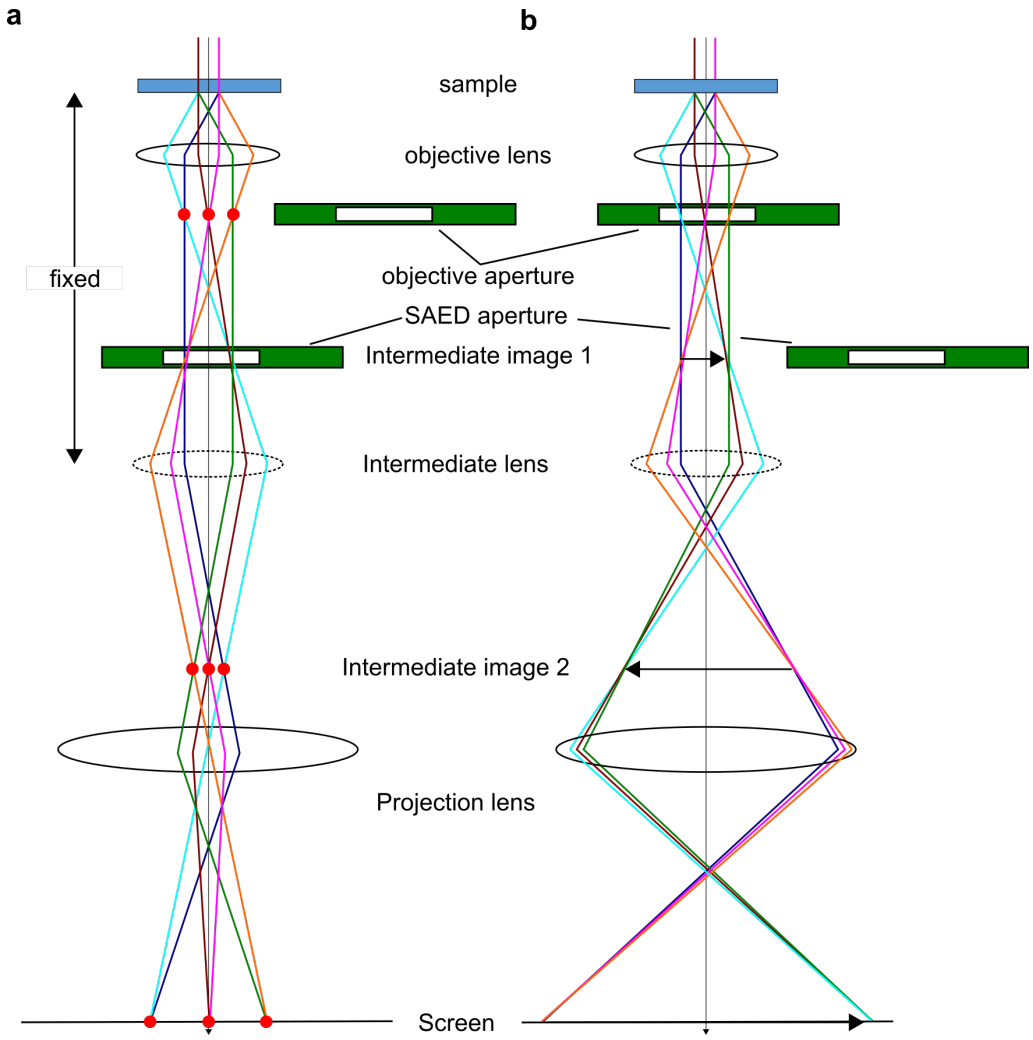

Figure 3.1.: Simplified ray diagram of the two TEM modes (a) diffraction and (b) image mode of an idealized microscope post illumination by a parallel electron beam. The objective lens provides the highest step of magnification into the first intermediate image. To switch from diffraction mode, magnifying the diffraction pattern in the back focal plane (bfp) on the screen, to image mode, magnifying the first intermediate image on the screen, the strength of the intermediate lens has to be changed (indicated by dashed lines). In diffraction mode, the objective aperture is retracted and the selected area electron diffraction (SAED) aperture is inserted and vise versa for the image mode. The intermediate lens and projection lens, of which only one is shown here, magnify the image before it is displayed on a screen.

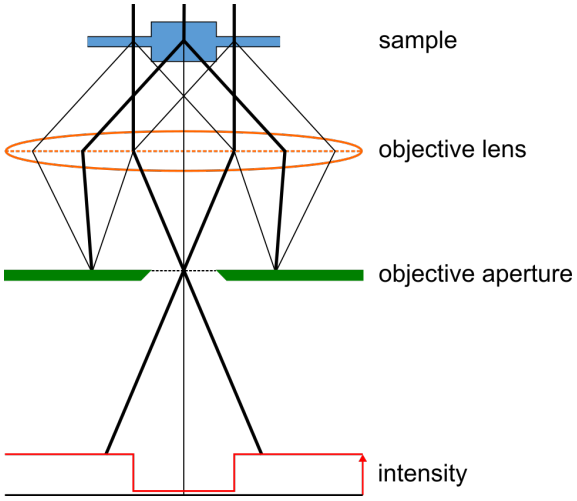

Figure 3.2.: Amplitude contrast: In thin or light samples, few electrons are diffracted; in thick or heavy samples, most electrons are scattered. In bright-field imaging (illustrated here), non-diffracted beams contribute to high intensity in the image plane as diffracted beams are blocked by the objective aperture. In dark-field imaging, diffracted beams produce high intensities while unscattered beams are blocked.

HR-TEM: Phase contrast imaging

Modern HR-TEMs allows for the visualization of atomic structures. The basic concept of HR-TEM is described below in a compact form. Elastic scattering mainly contributes to high-resolution information in TEM. HR-TEM utilizes the wave nature of electrons. In HR-TEM imaging, the intrinsic phase shift between the direct beam and the scattered beams is used to generate contrast in the image. To resolve atomic structures, a very thin sample is required that is usually oriented with a highly symmetric crystal direction parallel to the beam so that the atoms are aligned in columns along the beam direction, as shown schematically in Figure 3.3a. The parallel electron beam can be described as a plane wave Ψ_0 with a wave front visualized by straight lines striking the crystal. The electron wave propagates through the crystal and interacts with the atomic nuclei, thereby picking up structure information. The interaction can approximately be described as a phase shift of the wave function that is strong at the positions of the atoms and weaker elsewhere. The change of the wave function is indicated by Ψ_s and the resulting exit-plane wave function Ψ_e is modulated according to the projected atomic structure. The exit-plane wave function of thin samples is mathematically described as:

$$\Psi_e(\boldsymbol{r}) \approx \Psi_0(\boldsymbol{r}) e^{i\sigma V_p(\boldsymbol{r})}\,, \tag{3.1.1}$$

where $\boldsymbol{r} = (x, y)$ is a two-dimensional real-space vector in the exit plane, σ the interaction constant, and V_p the projected crystal potential. For very thin samples,

the phase shift is very small and the weak phase objective approximation can be applied by neglecting square and higher-order terms of $\sigma V_p(\boldsymbol{r})$, yielding

$$\Psi_e(\boldsymbol{r}) \approx \Psi_0(\boldsymbol{r})[1 + i\sigma V_p(\boldsymbol{r})]\,. \tag{3.1.2}$$

For simplicity the incident plane wave function at the entrance plane can be set to one, i.e., $\Psi_0(\boldsymbol{r}) = 1$. In the schematic example of Figure 3.3a, three different interaction scenarios of a plane wave with the crystal are considered: interaction with a heavy atom column, interaction with a light atom column, and no interaction. The phase shift is larger for interactions with heavier atoms than for interactions with lighter atoms. The third case does not modulated the wave function.

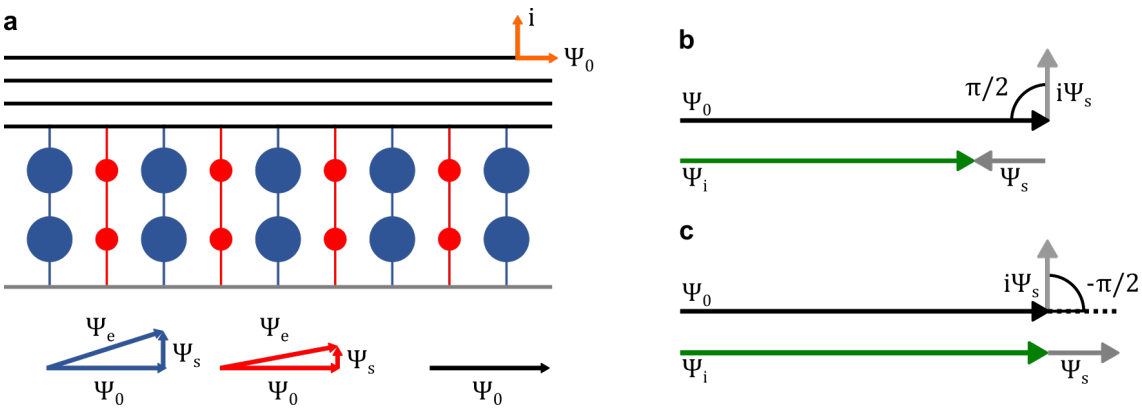

Figure 3.3.: (a) An incident electron beam described as plane wave Ψ_0 (black lines) strike the crystal and interact with light (red) and heavy (blue) atoms, which modulates the wave function to Ψ_e. The propagation of the wave function is accelerated in the atom which leads to a phase shift expressed by Ψ_s. A phase shift of $\pm\frac{\pi}{2}$ has to be applied to create a contrast in the image-plane. (b) positive phase contrast, (c) negative phase contrast.

The following describes the image formation and how the structure information, that is contained in the wave function, becomes visible in an image. For simplicity, we start by assuming an ideal microscope in which the exit-plane wave function Ψ_e is equivalent to the image-plane wave function Ψ_i. The intensity observed in a real-space image is given by the modulus square of the image-plane wave function, with

$$|\Psi_i|^2 = |\Psi_e|^2 \approx |1 + i\sigma V_p(\boldsymbol{r})|^2 = 1 + \sigma^2 V^2 \;\approx 1\,. \tag{3.1.3}$$

Again, the weak object phase approximation has been applied, in which the term $\sigma^2 V^2$ is set to zero. Consequently, the intensity is constant and no image contrast is observed.

To achieve phase contrast, the change in the wave function Ψ_s must be rotated by $\pm\frac{\pi}{2}$. This leads to a positive or negative phase contrast, as shown in Figure 3.3b and

c. A phase shift of $-\frac{\pi}{2}$ can be applied by adjusting the strength of the objective lens to compensate for the positive spherical aberration by a negative defocus. However, this situation can only be achieved approximately and over a limited range of spatial frequencies. An optimum defocus for phase contrast was proposed by Scherzer [121]. More details on these conditions can be found in the literature [115, 117].

3.2. Scanning transmission electron microscopy

In a scanning transmission electron microscopy (STEM) a convergent electron probe is focused on the sample and scanned across the sample in a raster pattern. The image is generated by recording the intensity of the electron beam within a defined scattering angle range as a function of the probe position. STEM is very flexible and a wide variety of detector geometries can be used to record the generated signals at different scattering angles, which will be described later in Section 3.2.2. Prior to that, we start with the setup and the ray diagram of a scanning transmission electron microscope from the source to the detector.

3.2.1. Setup

A STEM setup consists of similar components as a TEM with the key difference that a set of scan coils is added, which enable scanning of the probe. Figure 3.4 shows schematically a simplified ray diagram of a STEM. The condenser and upper pole of the objective lens create a demagnified image of the source in the sample plane. The C_2-aperture confines the convergence angle, which determines the smallest diameter of the probe possible and thus defines the resolution limit of the microscope. The intensity of the probe can be adjusted by changing the excitation of the C_1-lens, thereby determining the electron beam current passing through the C_2-aperture. A set of scan coils deflects the electron probe to raster over the sample. The effect of scan and descan deflections, which generate a shifted probe image, is indicated in the ray diagram. The objective lens applies the final and strongest step of demagnification and focuses the electron probe to approximately a diameter of 1 Å on the sample, assuming aberration correction (see Section 3.2.3).

The actual magnification of a STEM image is effectively defined by the scan area and the step size. A higher magnification is achieved by decreasing the step size. For modern microscopes it is often possible to switch between TEM and STEM mode on the same device by changing the lens excitations. This is the case with the Spectra 300 (Thermo Fisher Scientific, the Netherlands), which was primarily used in STEM mode in this thesis.

Multiple detectors are placed below the sample to record the intensity of the scattered beam covering specific angular ranges. Ring detectors are usually used, as indicated in the ray diagram, which can be divided into segments in the azimuth direction.

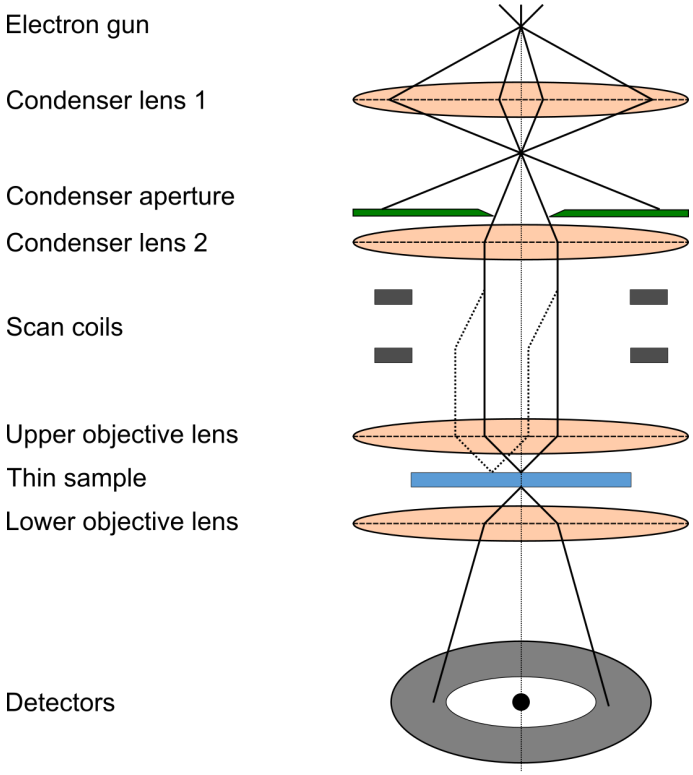

Figure 3.4.: Schematic of a ray diagram of a fully coherent STEM setup. A convergent electron probe, which size is limited by the C_2-aperture, is focused on the sample by the upper objective aperture. The resolution is limited by the diameter of the probe. Magnification is achieved solely by the scan area and the scan rate.

For energy loss measurements, a spectrometer is placed at the bottom of the electron column. Spectrometers for detecting secondary X-ray emissions are placed above the sample.

3.2.2. Image formation

STEM is quite flexible regarding imaging techniques, essentially by changing the detection geometry. Three important imaging modes are: annular dark-field (ADF), annular bright-field (ABF), and bright-field (BF), as shown schematically in Figure 3.5a. For ADF, a large ring detector is used, which collects electrons that were scattered outside the convergence angle of the probe. BF-STEM images are recorded with a disk or point-like detector placed within the convergence angle of the probe. For a point-like detector, this generates images equivalent to high-resolution TEM, an equivalence also described as reciprocity [122].

The most frequently used imaging technique, also used predominantly in this work, is HAADF-STEM imaging, where a ring detector is placed at very high angles,

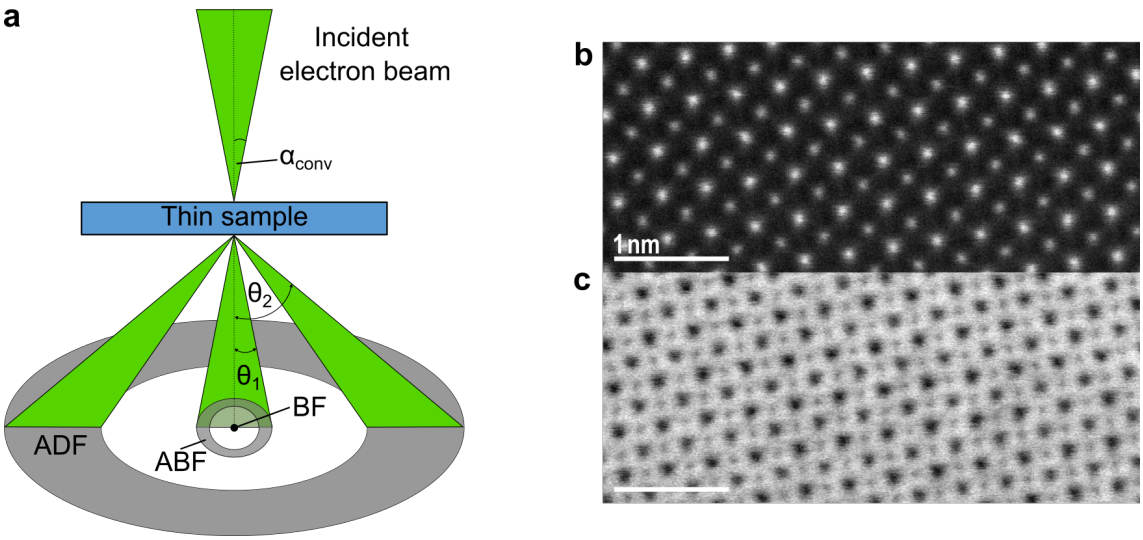

Figure 3.5.: (a) Schematic of STEM detector setup for ADF, ABF and BF imaging. The incident convergent electron beam with a convergence angle α_{conv} interacts with the sample leading to elastically and inelastically scattered electrons. Scattering into a small collection angle θ_1 or a large collection angle θ_2 is detected by ABF or ADF, respectively. Scattering into the forward direction and unscattered electrons are detected with a bright-field detector. (b) shows an image of strontium titanium oxide ($SrTiO_3$) which was acquired at 300 kV in the HAADF showing Z-contrast of the sample. (c) presents an ABF image of the same area as (b), exhibiting an inverse contrast relative to the HAADF-image and including contrast due to light oxygen atoms in vicinity to the heavier Ti and Sr atoms.

collecting mainly inelastically scattered electrons. The inner-angle collection angle is usually about three to five times larger than the convergence angle. This method provides Z-contrast in images, where the intensity increases with the atomic number Z in an atomic column [123]. Heavier atoms produce high intensities and lighter atoms produce lower intensities, as shown in (Figure 3.5b). The intensity I in an HAADF-image can be expressed in a simplified form by assuming a very thin sample with a small periodic scattering potential as

$$I(\boldsymbol{x_p}) = |P(\boldsymbol{x}, \boldsymbol{x_p})|^2 * |O(\boldsymbol{x})|^2 \,, \tag{3.2.1}$$

where $\boldsymbol{x}$ and $\boldsymbol{x_p}$ represent two-dimensional vectors that denote the position of the crystal and the probe, respectively. In other words, the image intensity is the object function smeared out by the probe shape. At the surface of the sample, the probe is sharp and spreads as it propagates further through the crystal. Therefore, the structure information in HAADF-STEM images originates mainly from the upper atomic layers, depending on the thickness of the sample. Increasing sample thickness or strong defocus blur the image but do not alternate the contrast,

which enables straightforward interpretation of the Z-contrast. The disadvantage of HAADF-STEM imaging is that light elements such as oxygen are not visible when heavy elements such as TMs are present.

For ABF-imaging [124], an annular detector with an angular range of $\frac{\alpha}{2}$-α is used, where α is the convergence angle. The ABF-mode provides simultaneous imaging of light and heavy elements, which appear dark on a bright background (e.g. in Figure 3.5c). ABF-imaging is generally a robust technique against focus and sample thickness, enabling direct interpretation across diverse sample thicknesses and moderate defocus levels; however, it is more sensitive to thickness and focus changes than ADF-imaging [125]. In general, samples for ABF-imaging have to be considerably thinner than for HAADF-imaging.

Advances in detector technology and computer performance have enabled further and more complex STEM imaging techniques, including integrated differential phase contrast (iDPC) and 4D-STEM. The iDPC technique allows direct linear mapping of the electrostatic potential field in thin samples and thus facilitates the simultaneous visualization of both light and heavy elements. IDPC provides a high signal-to-noise ratio and thus requires less dose, which is particularly interesting for beam-sensitive materials such as NCM. However, the derivation of the iDPC method is valid only for very thin samples of a few atomic layers [126]. In 4D-STEM, for example, a 2D diffraction pattern is measured for each probe position of a 2D scan pattern [127]. The simulated convergent beam electron diffraction (CBED) pattern of NCM in Figure 3.6 visualize the field of view of the different detectors, including an HAADF-STEM detector as a reference. For iDPC, the signals are recorded by a segmented ring detector as visualized in Figure 3.6b, which takes into account the angle range of ABF and partially also of ADF. The HAADF angle range is not reached, as shown by comparison with Figure 3.6a, allowing simultaneous use of both detectors. For 4D-STEM a pixelated detector is used, as illustrated in Figure 3.6c.

Moreover, it should be mentioned that sample drift and scanning noise influence image formation and can lead to distortions or artifacts in the image [128]. Reasons for this include electronic noise, superimposition of external fields with the field of the scanning coils, or the process of moving the probe from the end of a row to the beginning of the next row, which is slower than scanning from right to left. However, the implementation of shielding, drift compensation, and advanced scanning routines mitigates many of these factors.

3.2.3. High-resolution scanning transmission electron microscopy

High-resolution scanning transmission electron microscopy (HR-STEM) requires an electron probe with a very small probe diameter close to or below 1 Å diameter. However, the probe size is limited by the imperfections of the lenses as well as by the finite size and energy spread of the electron source. The most important im-

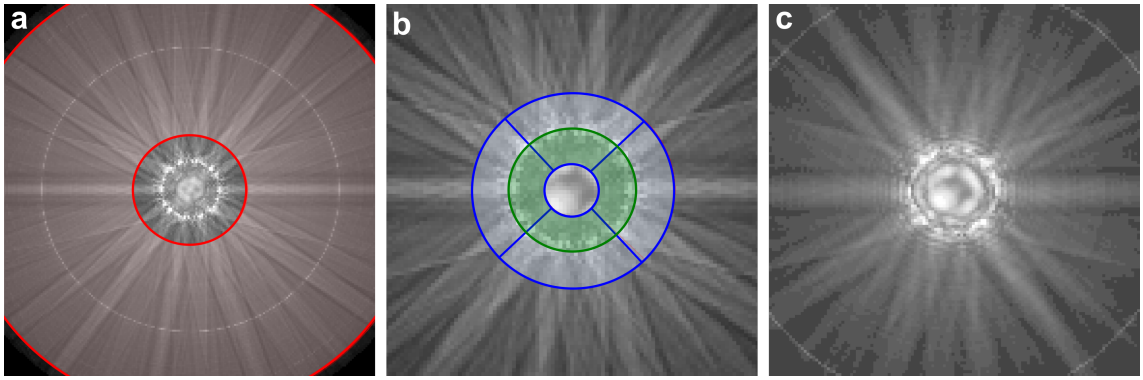

Figure 3.6.: Example of a simulated CBED pattern of NCM at a nickel column for (a) HAADF detector (red), (b) ABF detector (green) and segmented iDPC detector (blue) and (c) pixelated 4D-STEM detector. The CBED pattern were simulated with Dr. Probe [74] at 200 kV, 115 mm camera length and a convergence angle of 25.4 mrad.

perfection of the lenses is the spherical aberration, which is schematically shown in Figure 3.7. A point P, located in the sample plane for TEM and in the source plane for STEM, is imaged into a point P' on a detector. The example shown illustrates the case for magnifying lenses, but the principle also applies for demagnifying lenses. The spherical aberration causes off-axis beams to deflect more strongly than on-axis beams, resulting in a shorter focal length for off-axis beams. The smallest width for an image of a point in the object plane is therefore no longer in the Gaussian image plane, but rather in the plane of least confusion. The image in the Gaussian is plane blurred. In an uncorrected microscope, the highest resolution is obtained in underfocus ($\Delta z < 0$), where the effect of the positive spherical aberration is partially compensated up to a certain scattering angle. The energy spread of the electron source leads to chromatic aberration, which causes a fluctuation of the focal length. However, a field-emission gun as used in this work possesses a very small energy spread at high accelerating voltages; therefore the influence of chromatic aberration is negligible and will not be described in further detail.

In optical microscopy, the problem of spherical aberration is solved by the interaction of converging lenses, which have a focusing effect, and diverging lenses, which have a defocusing effect. All electron-optical lenses used for imaging are rotationally symmetric. The Scherzer theorem states that all rotationally symmetric magnetic lenses are converging lenses with a positive spherical aberration, and it is not possible to introduce a negative spherical aberration of another round lens to compensate for it [129]. It was Scherzer again, who proposed that the combination of multipole lenses allows to create a negative C_S and compensate the spherical aberration in TEMs [130]. The aberration-corrected Spectra 300 has a probe C_S-corrector (and an image C_S-corrector) based on a double-hexapole, described by Rose [131, 132]. The realization of a spherical aberration corrector, which yielded a significant im-

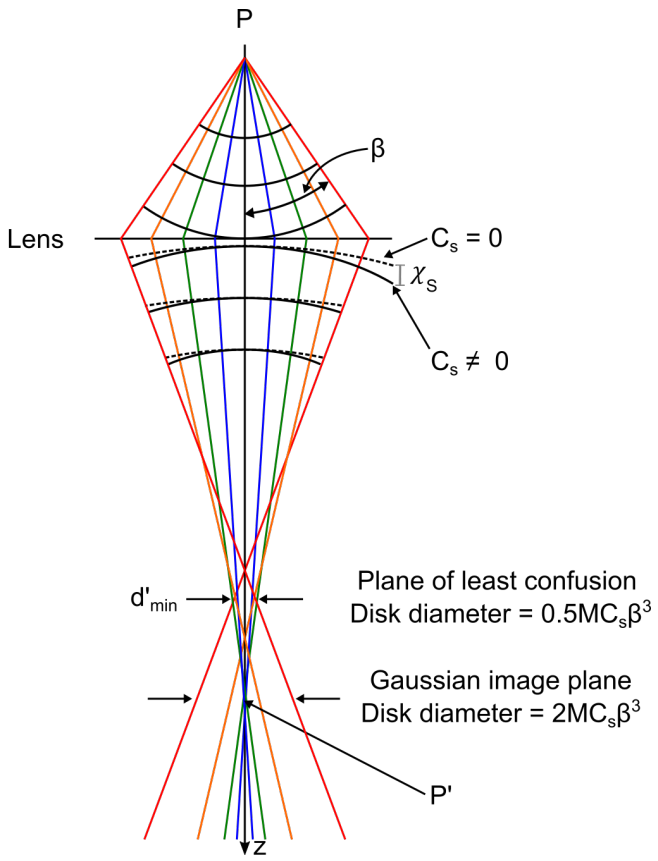

Figure 3.7.: Schematic ray diagram and wavefronts originating from the point source which are focused by a lens with a spherical aberration C_s into the point P' on a detector. The wave aberration is indicated by χ_s. Spherical aberration causes the wave fronts at the outer parts of the lens to diffracted more strongly than those closer to the optical axis, resulting in a shorter focal length for off-axis beams. The plane of least confusion is above the Gaussian image plane, suggesting that the STEM should be operated in underfocus for higher image resolution. A larger opening angle β leads to a strong effect of the spherical aberration. The factor M indicates the magnification. Figure adapted from [115].

provement in resolution was achieved by Haider *et al.* [133] based on the theoretical considerations of Rose [131]. Spherical aberration correction in STEM has improved the resolution limit by a factor of two, down to the sub-Ångström regime [134].

3.3. Analytical transmission electron microscopy

As shown in the introduction of this chapter, the interaction between a fast electron beam and a sample results in forward elastic and inelastic scattering processes. Inelastic scattering originates mostly from electron-electron interactions. Consequently, inelastically scattered electrons provide information about the chemical composition, band structure, and valence states. Figure 3.8 shows schematically the primary and secondary inelastic scattering processes for inner-shell excitation. The incident electron ejects an electron in the inner shell and excites it to a higher state above the Fermi level. Thereby, the incident electron loses energy and changes its trajectory, leaving the atom in an excited state (mostly ionized). The electron energy loss can be measured by a dedicated spectrometer. This method is called electron energy loss spectroscopy (EELS) (Section 3.3.1). In a secondary process, the electron vacancy in an inner shell is filled by an electron emitted from an outer shell to an energetically more favorable state. To compensate for the energy difference between the inner and the outer shell states, two different secondary emission processes compete with each other: characteristic X-ray emission and Auger electron emission. X-ray emission dominates for heavy elements and is detected by energy-dispersive X-ray spectroscopy (EDX) detectors (Section 3.3.2). Auger electrons are emitted particularly from light elements, and due to their very small escape depth, they are used for surface chemical and bonding analysis. However, specialized secondary electron (SE) detectors, which are not standard in a TEM, are required and thus not discussed further.

3.3.1. Electron energy loss spectroscopy

Electron energy loss spectroscopy (EELS) provides information on the chemical composition, the electronic structure, valance states and shifts as well as the thickness of a sample. Besides the broad information gain, EELS is more sensitive than EDX to detect very light elements (Li, Be and B). However, for a good lateral resolution, very thin samples are required to achieve a good signal-to-noise ratio due to reduced multiple scattering. For thicker samples multiple scattering leads to an increased background while the edge signal remains the same or can be reduced. The electron energy loss can be measured with an imaging filter, which is mounted at the bottom of the electron column. The working principle is schematically depicted in Figure 3.9. After the electron beam has been transmitted through the sample, the entrance aperture controls which electrons are used for the electron energy loss (EEL) spectrum. A magnetic prism bents the electron beam by 90 °C and thereby dispersing the electrons according to their energies. The zero-loss electrons carry

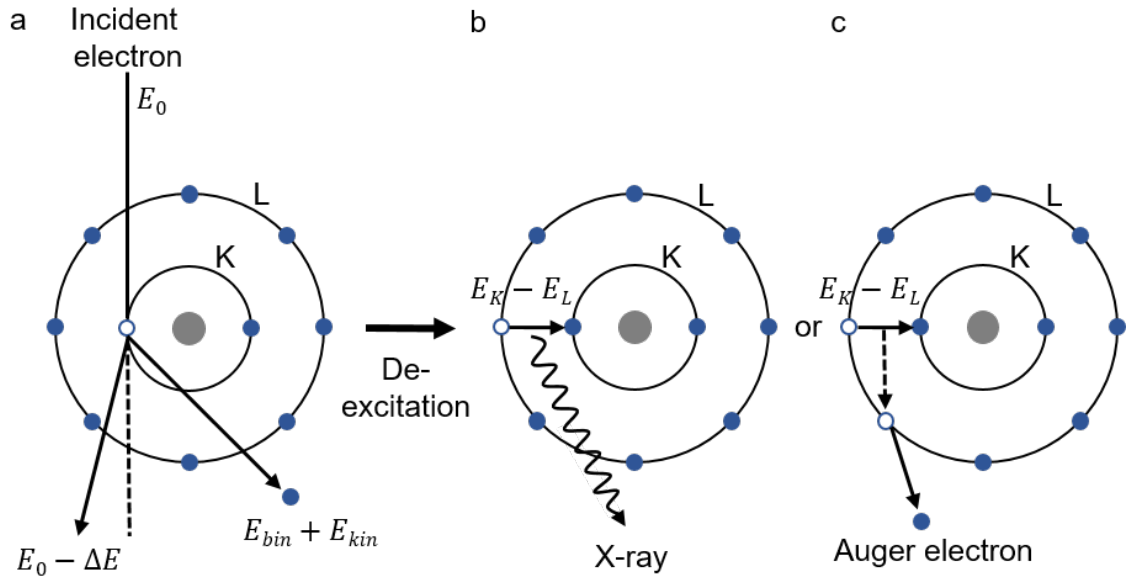

Figure 3.8.: Schematic of inelastic scattering and secondary processes showing (a) electron loss, (b) deexcitation through the emission of an X-ray and (c) deexcitation through the emission of a SE.

the highest energy and are bent the least. Electrons with lower energy, indicating higher energy loss, are bent more. The energy resolution in EELS is usually limited by the energy distribution of the source. For sources with a higher energy spread, the energy resolution in spectroscopy can be improved by applying a monochromator. Nowadays, energy resolution $< 10\,\text{meV}$ can be achieved while preserving atomic resolution with STEM instruments specialized for that purpose [135].
Figure 3.10 shows an EEL spectrum of Ni-rich NCM, in which the different regions, properties and ionization edges are indicated. The low-loss region ranges from 0 eV to approximately 50 eV. It encloses the zero loss peak, which is the most intense feature in the entire spectrum, and the plasmon loss region, which contains contributions from plasmon and outer-shell excitations. The full width at half maximum (FWHM) of the zero loss peak indicates the energy resolution of an EEL spectrum. The energy loss intensity increases with increasing thickness, which is often used to measure sample thickness. The log-ratio method provides the relative sample thickness t/λ by

$$\frac{t}{\lambda} = ln(\frac{I_{\text{tot}}}{I_{\text{zlp}}}) \tag{3.3.1}$$

where λ is the mean free path for inelastic scattering specific to the material, I_{tot} the intensity of the entire spectrum and I_{zlp} the intensity of the the zero-loss peak. The core-loss region shows characteristic ionization edges of the material which allows to determine the elemental composition. The intensities of the ionization edges contain information about the stoichiometry of the material which can be accessed with a suitable reference, such as scattering cross sections or reference spectra. Considering

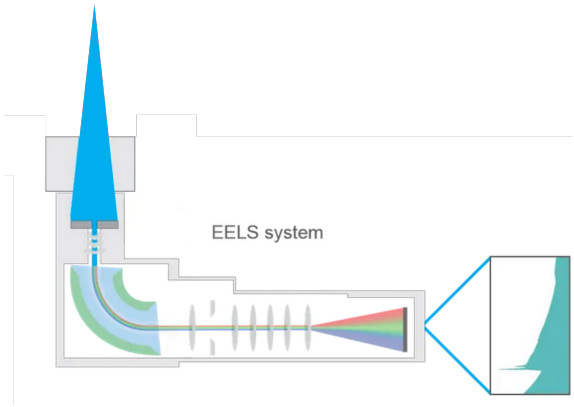

Figure 3.9.: Spectrometer with a magnetic prism, which bends the electron beam by 90 °C and disperses the electrons according to their energies. Electrons with higher energies are bent less than electrons with lower energies. At the end of the spectrometer, the dispersed electron energies are recorded giving the typical EEL spectrum with a low-loss and a core-loss region. The figure was adapted from [136].

the simplified Bohr model of the atom, an ionization edge would be a vertical line with a right-hand edge which decays exponentially, corresponding to the binding energy and the kinetic energy, respectively. However, the band structure of materials is more complex. Instead of a vertical edge, electron loss near edge fine structure (ELNEFS) is observed in an EEL spectrum, providing information about the bonding and oxidation states. For example, a shift of the ionization edge towards higher energies corresponds to an increased oxidation of the element.

For data acquisition, the Continuum 1066 energy filter (Gatan) was used without monochromation, thus providing EELS with an energy resolution of approximately 1 eV. Data analysis, including background estimation and subtraction, was performed using the open-source, python-based HyperSpy library [137,138]. The script used, annotated with further details, is shown in Appendix B.1.

3.3.2. Energy-dispersive X-ray spectroscopy

Energy-dispersive X-ray spectroscopy (EDX) exploits element specific secondary X-ray emission energies offering another way to determine the elemental distribution of a material. In contrast to EELS, EDX still performs well with relatively thick samples because multiple scattering has little influence on signal quality. EDX offers a significantly better signal-to-background ratio than EELS, where the signal is concentrated in usually well-separated peaks over a weak background. The detection limit is reached by boron ($Z = 5$). Only very specialized EDX detectors can detect lithium.

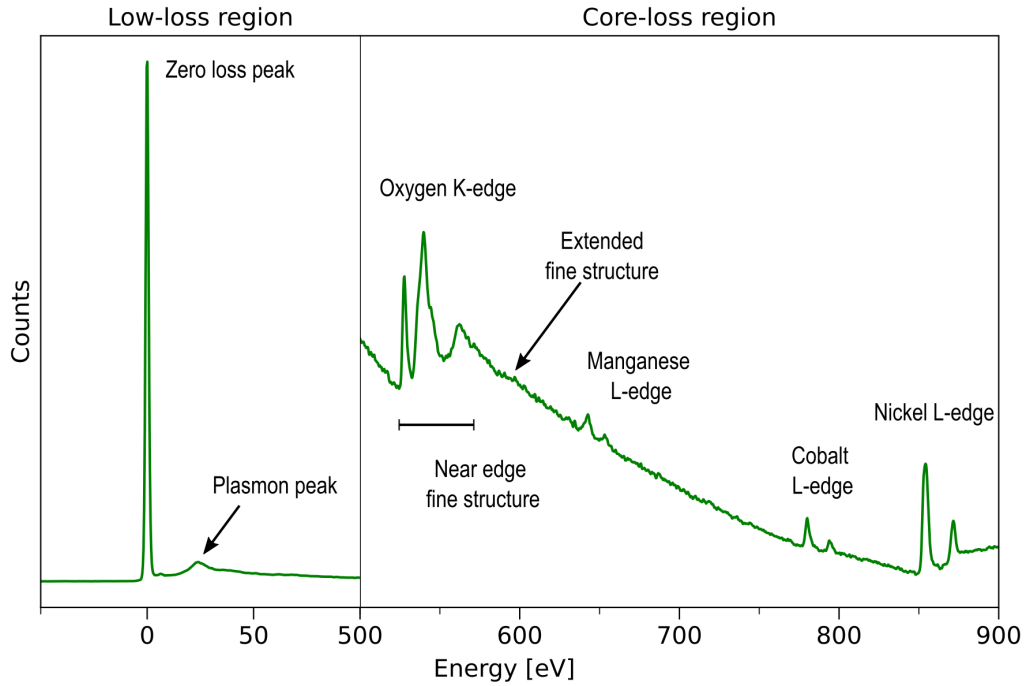

Figure 3.10.: ELL spectrum of Ni-rich NCM oxide. The spectrum is divided in a low-loss region and a core-loss region. The zero loss peak contains electrons that have not been scattered and those that have been scattered elastically. Low energy losses are attributed to plasmon and outer-shell excitations. Edge-like features for high energy losses are due to inner shell excitation and ionization. The near edge fine structure can provide information about bonding and oxidation states.

Figure 3.11 shows a EDX spectrum of Ni-rich NCM. An EDX spectrum consists of the continuous bremsstrahlung background and the characteristic X-ray peaks at discrete energies. Bremsstrahlung is produced when the beam electrons are slowed down. Electrons can lose a portion or all of their kinetic energy, which is converted into electromagnetic radiation and emitted in the form of X-rays. Each element has a unique set of peaks at energies corresponding to its electronic structure. The energy of a characteristic peak is equivalent to the energy transition between two electron shells when an electron from a higher shell takes the vacant place in a lower shell. For example, K_α describes the transition to the vacant position in the K shell from the next higher shell, which is indicated by the Greek letter α. An electron transitioning from the next-highest shell is labeled with a β. In the M and L series, a numerical index is also given to indicate the splitting of the energy levels. The intensities of the peaks in a spectrum contain information about the concentrations of elements in a material. A copper signal is usually present in a STEM-EDX spectrum originating from the TEM grid.

The EDX analysis carried out at Spectra utilized the ThermoFisher Super X sys-

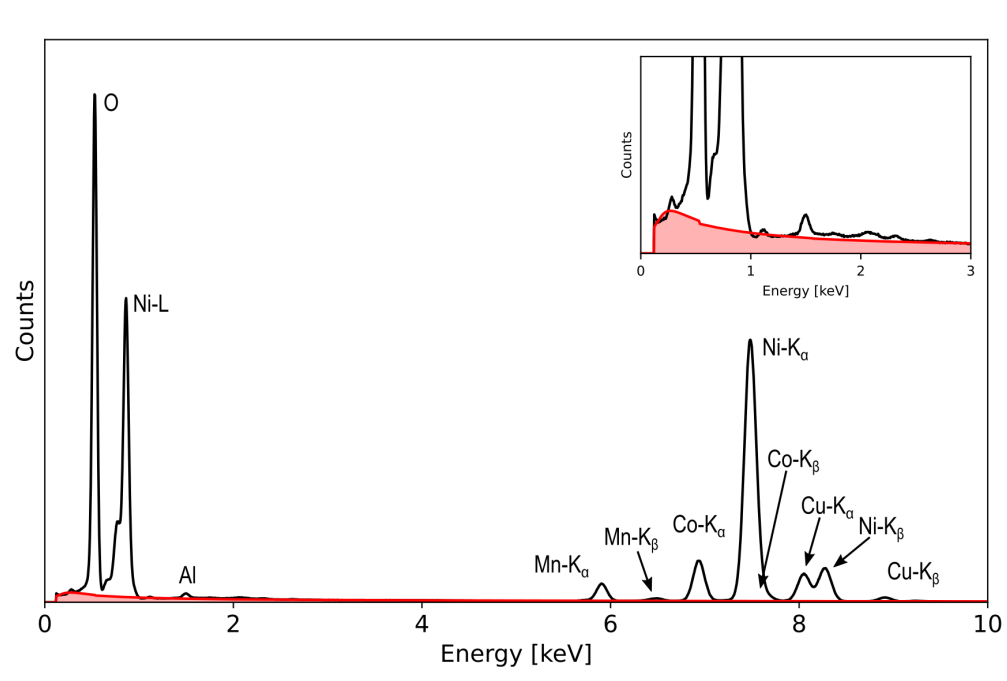

Figure 3.11.: EDX spectrum of Ni-rich NCM with a background (red) arising from the continuous bremsstrahlung and the characteristic spectrum with discrete peaks (black). The inset shows a zoom of the low energy range, which visualizes the typical decay of the background and some smaller peaks. In the lower energy range, the peaks of the L- and M-series of the transition metals are very close and overlap, and are therefore not labeled individually. However, in the higher energy range the individual peaks are resolved and the individual transitions are indicated. The copper and aluminum peaks arise from the TEM holder.

tem, which consists of four detectors operating in conjunction with Velox software. Conversely, the Hitachi HF5000 was equipped with two Oxford Instruments Ultra 100 detectors employing AzTec software. A low-background holder was used to optimize the signal-to-noise ratio. Both software have drift compensation implemented which was utilized during acquisition. For data analysis, background estimation and subtraction were performed before elemental maps were generated from the spectra.

3.4. Beam-induced damage effects

Typical beam-induced damage effects in TEM include ionization, knock-on damage, thermal effects, and contamination [117]. Ionization is caused by inelastic scattering due to electron-electron scattering leading to breaking of bonds and chemical reactions. Knock-on damage causes atomic displacement and creates point defects and interstitials. When knock-on damage occurs on the surface, it is called sput-

tering. Radiolysis prevails at lower acceleration voltages, whereas knock-on damage dominates at higher acceleration voltages. The electron beam radiation leads to generation of phonons, which leads to heating of the sample. Contamination with hydrocarbons on the surface of the sample is another issue, which can lead to charging effects and blurred images.

NCM is a beam-sensitive material which requires the selection of an appropriate set of parameters to spread the electron dose and mitigate beam-induced damage during a TEM experiment [139, 140]. All STEM experiments were conducted at 200 kV or 300 kV and a beam current between 20 pA and 30 pA was applied. A fast scan series was selected for high-resolution scanning transmission electron microscopy (HR-STEM) images with a dwell time of 200 ns and a maximum of 20 frames per series. The frames were integrated after rigid shift correction by applying the drift-corrected frame integration (DCFI) function in Velox (Thermo Fisher Scientific, the Netherlands). These settings allowed for good acquisition without any visible damage to the sample. In analytical TEM (Section 3.3), higher beam currents are necessary to produce a substantial number of inelastic scattering events and thus to achieve a good signal-to-noise ratio for these techniques. Due to the sensitivity of NCM to high doses of radiation, atomically resolved spectroscopy was not successful, because the structure was destroyed before sufficient signal could be recorded in EDX or EELS maps. Mostly, the crystal structure underwent a rapid transformation, shifting from its original layered structure to a rock salt-like structure.

3.5. *In situ* transmission electron microscopy

The previous sections of this chapter show the variety of powerful TEM methods that can be used to image atomic structures and to extract chemical information locally. However, *ex situ* TEM only offers a picture of a specific, fixed situation at room temperature under high vacuum. In the real world, materials are exposed to many stimuli and undergo dynamic changes. For example, batteries are constantly charged and discharged, experience temperature changes during operation and changes of environmental conditions and undergo electrochemical reactions between electrode and electrolyte. Understanding the atomic structure, chemical composition, transition mechanisms, and kinetics of a material is vital to obtain a complete picture.

An approach to investigate and visualize dynamic phenomena is *in situ* TEM. *In situ* TEM combines the application of external stimuli with simultaneous imaging. External stimuli can be thermal excitation, electric or magnetic fields, liquid or gaseous environments, and mechanical forces. The application of external stimuli inside a TEM requires a combination of a dedicated *in situ* holder and a micro-electro-mechanical system (MEMS). In addition, real-time observation (video speed) requires fast detection and quick data storage. In this thesis, two types of *in situ* experiments were conducted: heating and biasing. The experimental setups and

holders are presented in the following.

3.5.1. *In situ* Heating

Holder

Figure Figure 3.12a shows the tip of the Wildfire heating holder from DENSsolutions (Delft, the Netherlands) which was used for *in situ* TEM heating experiments. The holder has four electrical contacts to apply the heating current. In the center of the chip, several holes are manufactured in the silicon-nitride (SiN) membrane to place the FIB lamella. A detailed protocol describing lamella chip preparation is presented in Section 4.2.4.

Setup

The *in situ* heating setup consists of three main parts: heating holder, heating control unit and PC as shown in Fig. 3.12b. The heating holder is connected to the TEM to enable the β-tilt and to the heating control unit to control the applied current, which determines the temperature of the heating chip. The PC allows the user to set a temperature or a temperature ramp using the software digiheater (DENSsolutions, the Netherlands). The heating control unit converts the set temperature into a current, which is applied to the heating holder. To keep temperature fluctuations in the heating spiral of the chip to a minimum, a sensor records the temperature and constantly sends the information to the heating control unit. A temperature accuracy of above 95 % is achieved.

3.5.2. *In situ* Biasing

Holder

Fig. 3.13a illustrates the tip of the single-tilt *in situ* biasing holder from Nanofactory (Gothenburg, Sweden). On the left hand site, a sharp needle is mounted, which can be made of gold or tungsten depending on the requirements of the experiment. To form a sharp needle with a tip diameter smaller than 100 nm, an electrochemical etching process is applied. The needle sits tightly in a piezo-hat and is fixed with a small screw. The piezo-hat itself, which sits on a metal sphere, has six electrical contacts and enables precise movements in x-, y-, and z-directions within the nanometer range. On the right-hand site, the sample is mounted, which can be a lamella on an omniprobe grid or a powder distributed on a half lacey carbon grid. Before the sample is attached to the holder, the grid must be fixed to a tungsten rod using conductive glue.

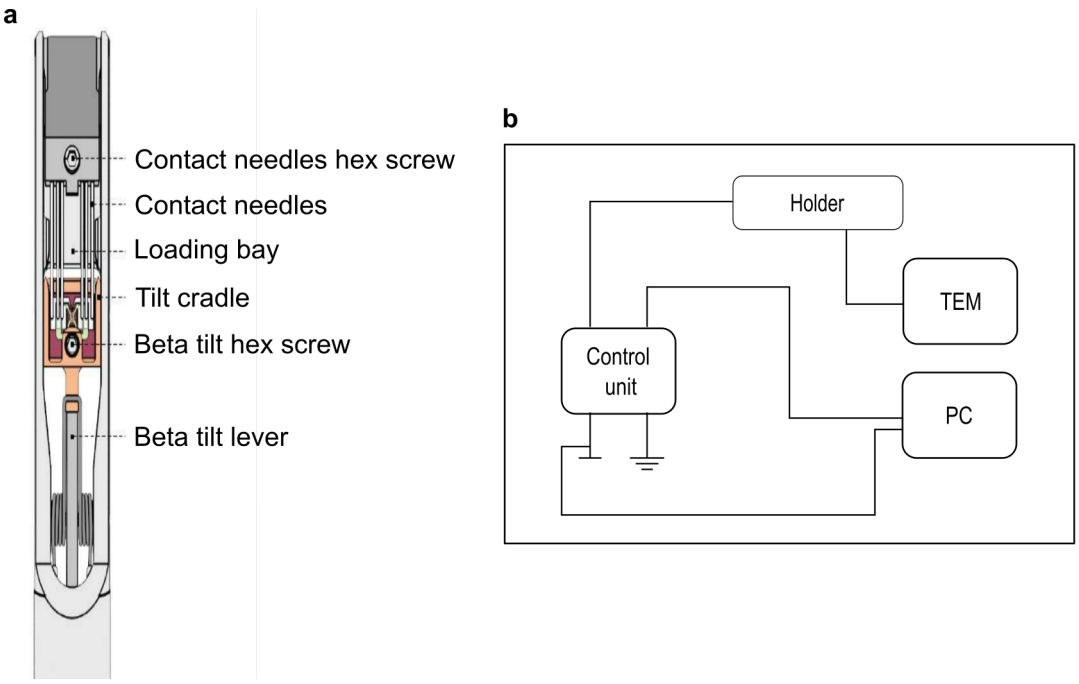

Figure 3.12.: (a) Tip of *in situ* heating holder. Figure copied from [141]. (b) *In situ* heating setup. The temperature is controlled via a heating control unit that is connected to a PC and to the TEM holder.

Setup

The biasing *in situ* setup (Figure 3.13b) contains four main parts: biasing holder, biasing control unit and piezo-movement control unit, and PCs as depicted in Figure Figure 3.13b. The biasing holder is connected to the biasing control unit and to the piezo-movement control unit. The biasing holder has an α-tilt option. A voltage is applied and current is measured using the potentiostat (Keithley 2636A system SourceMaker, USA). The IV-curve is recorded with the software LabVIEW 2013 (Version 13, National Instruments).

Work flow

For biasing experiments with cathode materials of Li-ion batteries, two additional preparation steps are needed. First, another electrode and a lithium-based electrolyte are needed to properly cycle the cathode. The simplest way to create a lithium-based electrolyte is to carefully scratch a sharp needle over a fresh lithium foil. Because lithium oxidizes immediately when it is exposed to air, this preparation step must be conducted in a glovebox under an inert gas atmosphere. Once the sharp tip of the tungsten needle is covered with lithium, it can be placed back in the holder and aligned in the desired direction toward the sample. Second, the holder must be kept under an inert gas atmosphere until it is inserted into the TEM. Therefore, it is placed into a holder tube, which should prevent oxidation while the

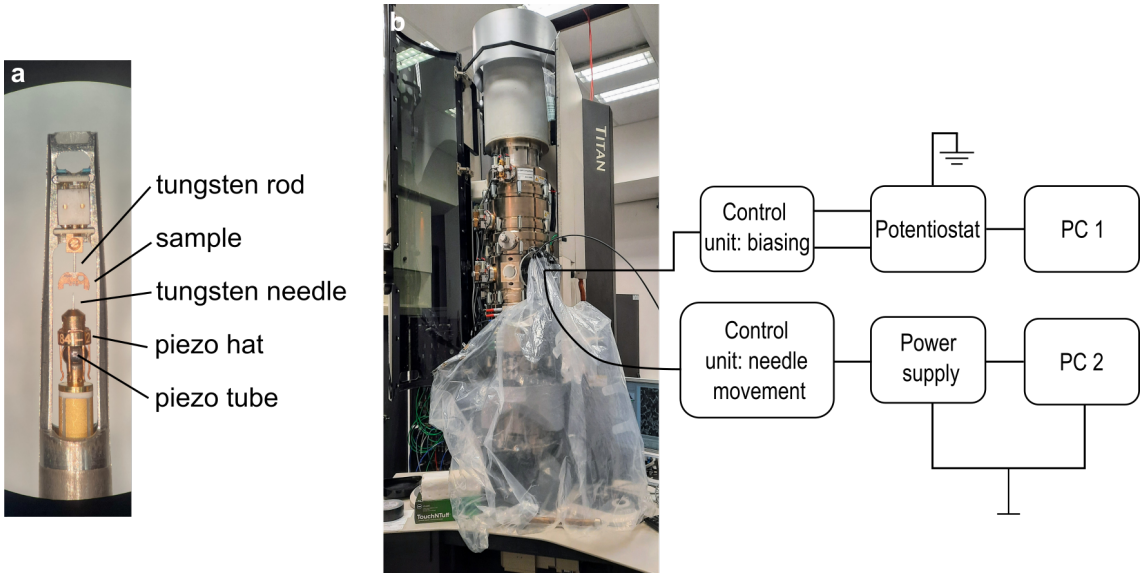

Figure 3.13.: (a) Tip of *in situ* biasing holder []. (b) *In situ* biasing setup. The voltage is applied via a potentiostat that is connected to a control unit which is connected with the TEM holder. The movement of the tungsten needle is controlled separately via another control unit that is also connected to the TEM holder.

holder is transferred from the glovebox to the microscope. A glove bag is attached to the load lock of the TEM. After the holder tube is transferred to the glove bag, it is pumped and squeezed four times to remove air from the glove bag. In addition, a gas tube is mounted on top of the load lock to flush the region around it with argon. After the last pump with Argon, the holder is pulled out and inserted into the TEM as usual. A detailed overview of the preparation steps is presented in a video recorded by Basak *et al.* [142].

3.6. Scanning electron microscopy

Scanning electron microscopy (SEM) is widely used to image the microstructure of bulk samples in materials science. Similarly to STEM, an electron beam scans the sample in a raster pattern. Figure 3.14 introduces the working principle of an SEM. Electrons are generated by the electron gun mounted on the top of the instrument. Electrons are extracted from a cathode and then accelerated by a voltage of 0.1 to 50 keV. A system of magnetic lenses including one or two condenser lenses, scan coils, and objective lens guides the electron beam through the column within a vacuum. The objective lens focuses the beam on the sample. The diameter of the electron probe, that strikes the sample, limits the resolution of a SEM. A lateral resolution of less than 1 nm can be achieved with modern SEMs.

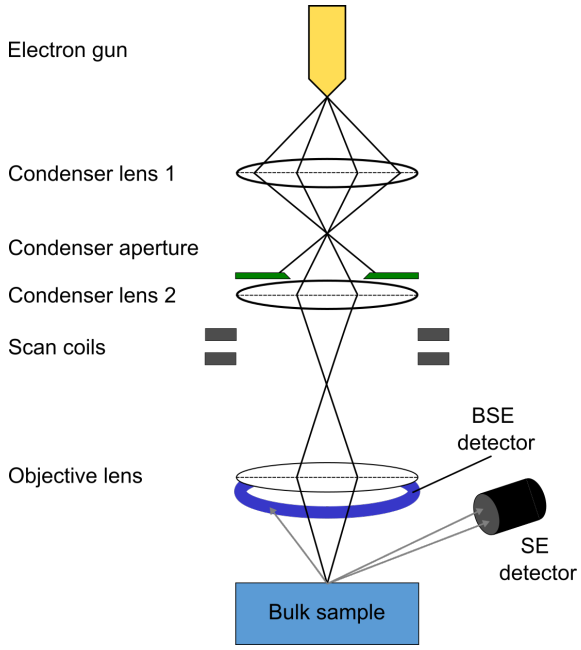

Figure 3.14.: Schematic drawing showing the setup of a SEM. Secondary electrons (SE) and back scattered electrons (BSEs) are the primary signals forming SEM images.

Electron-sample interaction causes elastic and inelastic scattering, resulting in the emission of SEs, back scattered electrons (BSEs), Auger electrons, and X-rays. SEs and BSEs are the most important signals for imaging in a SEM. SEs are knocked out outer-shell electrons or conduction band electrons, and can therefore be generated everywhere in the sample. However, because of their relatively low energy of 1-5 eV, SEs can only escape from a thin surface region of a few nanometers depth and be detected from a positively biased Everhart-Thornley detector, which is mounted on the side. SEs mainly contribute to topography and volume contrast. BSEs are primary electrons that undergo many scattering processes within the sample before exiting the sample in the backwards direction. Compared with SEs, BSEs are from the primary beam and have penetrated deeper in the material and have more kinetic energy. A ring detector is used to detect the BSE signal. This detector is positioned under the objective lens. The main contribution to the BSE signal is the elemental contrast because the detected signal depends on the atomic number Z. In addition, BSEs provide orientation contrast which is obtained by recording an electron backscattering diffraction (EBSD) pattern with a pixelated detector.

3.7. Focused ion beam

Focused ion beam machine is usually combined with an electron microscope (FIB-SEM), also known as a dual-beam mill. FIB-SEMs are used for preparing TEM samples by cutting very thin, electron-transparent lamellae from a bulk sample. While the focused ion beam mills the material, the main function of the SEM is to identify an area of interest and to gently monitor the milling process without seriously damaging the sample. A schematic of a FIB-SEM is shown in Figure 3.15. The electron source is mounted at the top of the instrument. The ion source is positioned at a 52° angle relative to the electron source. A gas injection system (GIS) can be inserted to deposit a protective layer on top of the sample or to glue a lamella to a grid. At the side, detectors are placed to capture signals from electron and ion radiation. The sample itself is attached to a stub that is fixed on the stage. The applied voltage at the ion source determines the beam energy, while the beam currents are confined by mechanical apertures, a disk with several holes that rotates according to the desired current. A detailed description of the FIB processing steps, pitfalls, and tips is summarized in the following chapter.

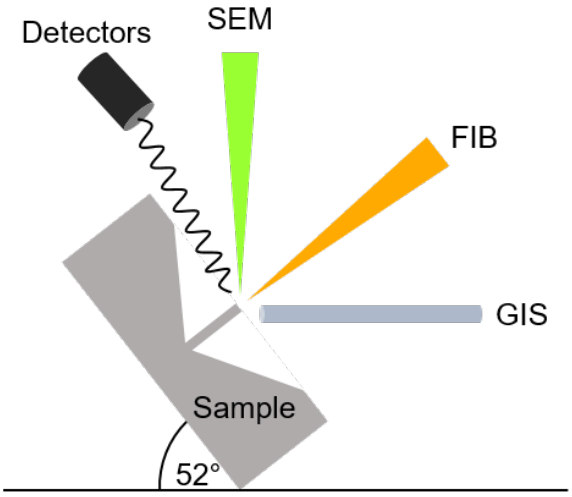

Figure 3.15.: Schematic of a focused ion beam (FIB) combined with an SEM.

4. TEM Sample Preparation

The preparation of suitable samples for TEM experiments was a critical step as the sample quality greatly influences the outcome of the experiments. Each TEM method has slightly different requirements for an ideal sample. The following considerations focus on the application of high-resolution HAADF-STEM imaging, EDX, and EELS experiments on NCM samples. The NCM samples were supplied either as powders or as electrode sheets. Given that most of the studies concentrated on degradation processes or coatings on the surface, it was necessary to fulfill the following requirements for high-quality TEM samples:

- **Geometrical requirements:** First, a cross-sectional sample of the particles was required to facilitate analysis via transmission. Second, the particle surfaces had to be oriented edge-on to avoid an overlap of the surface and the bulk structure in the images.

- **Sample thickness:** The TEM samples should be very thin to reduce the signal-to-noise ratio for HR-STEM imaging, EELS and EDX and to minimize projection artifacts caused by the particle's curvature during imaging, thus enabling edge-on condition. Conversely, the sample thickness should not be too thin to avoid damage and instability. We observed that a thickness between 50 nm and 100 nm nm is beneficial since this still provides visual information to check whether the edge-on condition is sufficiently met.

- **Contamination:** The sample should be free of any surface contamination in particular on the cross section surface, which is aligned perpendicular to the electron beam.

- **High-resolution imaging:** Particles should be close to a low-indexed zone axis ($\pm 10\,^\circ$ tilt).

Figure 4.1 illustrates schematically the necessity to achieve an edge-on condition. The particle shown has an intact layered NCM core and a rock salt surface layer. The rock salt structure contains nearly twice as many TMs within the same volume as the intact layered structure [41, 75]. This results in a higher HAADF-STEM image intensity. On the left site, an edge-on situation is realized with sharp interfaces of the reconstructed surface along the projection direction, yielding a clear image intensity. In contrast, on the right site, no edge-on conditions of the surface are met. Instead, a smooth transition is observable in the image intensity, which results

from overlapping information of the dense rock salt structure and the layered structure. Thin cross sections considerably reduce the information overlap of the surface structures when the particle is not aligned edge-on.

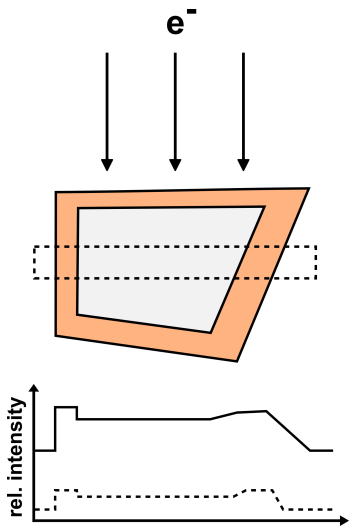

Figure 4.1.: Schematic of a NCM particle in projection, illustrating a layered structure at the core (gray) and a rock salt layer at the surface (orange). A cross-sectional area through the particle is indicated (dashed line). The corresponding relative HAADF-STEM intensity profiles of the entire particle (solid curve) and the cross-sectional sample (dashed curve) of the projection are shown below. The view along the projection direction of the left surface is edge on, leading to a sharp transition of the image intensity at the interface, while the transition is smooth on the right, where the edge-on condition is not met.

In the following, sample storage, handling of NCM, and different preparation methods are described. The preparation methods include both conventional and advanced approaches, namely drop casting and FIB, respectively. Ultimately, we chose FIB as sample preparation method because it best met the stated requirements, which could not be fulfilled by drop casting. Therefore, this chapter is primarily dedicated to FIB preparation. The standard FIB protocol is described in detail, along with the challenges that arise when preparing NCM samples. Where possible, appropriate solutions are presented. Nonetheless, Section 4.3 shortly presents drop casting and explains why it was inappropriate as a sample preparation method to study surface degradation in Ni-rich NCM.

4.1. Sample storage and handling

NCM oxides are air-sensitive materials due to their lithium content, which requires careful handling. All samples were received in double-sealed aluminum bags that

were filled with argon and stored in a glovebox (Jakomex) under an argon atmosphere until they were needed for an experiment. The glovebox was equipped with a sealing unit (Wusing 200-500 mm), which allowed resealing of the opened aluminum bags and sealing of the removed samples; thus ensuring safe transport to the designated sample preparation location.

Since all samples were lithiated, which stabilizes the layered structure, a short exposure to air of less than 30 min was acceptable before serious oxidation damage occurred. Air exposure of the sample was minimized. The prepared TEM samples were stored in a vacuum cabinet or vacuumed in a plastic bag until the experiment. The TEM experiments were conducted on the same day or the day after sample preparation. Repeating an HR-STEM experiment with a sample stored in a vacuum cabinet for two weeks did not show significant changes of the TM lattice structure. Ideally, the entire sample preparation procedure would be carried out under an inert gas atmosphere; however, a suitable TEM holder for inert gas transfer was not available at the beginning of the project. For safety reasons, NCM powders should be handled in a glovebox or under a fume hood. Inhalation of NCM particles is strongly discouraged due to their toxicity.

Embedding NCM-particles in epoxy

Handling powder samples for TEM preparation is challenging, especially in the case of SC-NCM particles ranging in size from a few hundred nanometers to 5 µm. Most of the used SC-NCM particles were too large for simple drop casting, as they were not electron transparent, and too small for FIB preparation, which required a size of at least 4 µm. Embedding the powders in an epoxy matrix created bulk-like samples suitable for dimpling or FIB preparation.

Epoxy G1 (Gatan, Germany) was chosen because it is stable under the electron beam and has a curing temperature below 100 °C below the temperature at which Ni-rich NCM changes are expected. The embedding process was carried out under a fume hood to avoid inhaling hazardous NCM powder. First, the resin and the hardener were mixed in a 10:1 ratio according to the instructions using a flat Petri dish and a wooden toothpick. The NCM powder was added to the mixture. The Petri dish was placed on a heating plate set to 40 °C to keep the mixture viscous. The mixture was transferred, using a toothpick, to a small brass tube, which contained a brass inset with a 300 µm wide slit, as shown in Figure 4.2. The brass tube was placed on a heat-resistant plastic holder on the heating plate. The powder-epoxy mixture was carefully inserted into the brass tube, drop by drop, through the narrow slit. A time span of two to three minutes between each step was beneficial to prevent bubble formation. Once the brass tube was filled, it was placed in a furnace and kept at 65 °C for 120 min to cure the powder-epoxy mixture.
Once the powder-epoxy mixture was cured, the brass tube was cut into thin slices of approximately 250 µm using a diamond-wire saw. Prior to FIB or dimpling, the

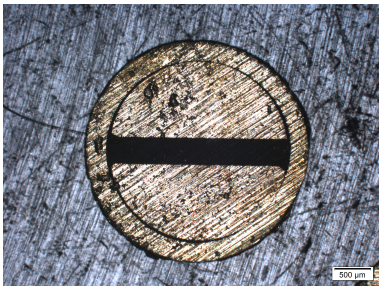

Figure 4.2.: Slice of brass tube with a slit in the middle filled with an epoxy powder mixture.

thin slabs were polished using fine grinding paper with grain size 4000. Achieving a high particle density within the epoxy matrix required much more powder than for sample preparation without embedding. Because the amount of powder within the project was very limited, the approach of embedding samples could not be pursued beyond the initial trials.

4.2. FIB sample preparation

FIB is an advanced technique for precise cutting of electron transparent samples. The working principle of FIB is introduced in the method chapter (Section 3.7). This section presents results from applying the standard lamella cutting protocol on NCM samples, highlights challenges in the preparation of powder samples or electrodes, and outlines strategies to address them. It also covers *in situ* chip preparation. More detailed information on FIB for TEM sample preparation can be found in the book by Giannuzzi and Stevie [120]. FIB preparation was performed with a Helios NanoLab 460F1 (FEI, the Netherlands).

4.2.1. Preliminary steps

For the FIB preparation, the sample had to be mounted on a SEM stub: (i) Powder particles were spread on a carbon pad which was glued to an SEM stub. This step was carried out in the glovebox to minimize air exposure time. (ii) A small piece of electrode sheets was cut off and glued to an SEM stub by applying conductive silver paste (G3692, Plano, Germany) or conductive carbon cement (Leit-C nach Göcke, Plano, Germany). Since no paste was available in the glovebox, this step was performed outside of the glovebox. After approximately 5 min, the conductive paste had dried. Lastly, the SEM stub was placed on a load-lock shuttle and inserted into the vacuum chamber of the FIB-SEM.

4.2.2. Standard protocol

The standard FIB process for the creation of a TEM lamella comprises the following steps: depositing a protection layer, digging trenches, lifting out, attaching the lamella to the grid, milling, and polishing. SEM images of these steps are shown in Figure 4.3. (a) Once a suitable area was identified, the initial protection layer was deposited by enabling the electron beam. (b) A second, thicker protection layer was applied using the ion beam. (c) Trenches were dug to prepare for the lift-out procedure. A triangular, stepwise cross-section pattern was used for efficient milling. For powder samples, digging trenches often involved cutting protruding areas of the particle or agglomerate, using a cleaning cross-section pattern (CCS). To prevent cutting into the protection layer due to drift of the sample, a safety distance of approximately 2 µm was maintained, especially at high currents like 21 nA. It is recommended to regularly acquire electron images to monitor the progression of the milling steps. (d) The trenches were cleaned using a lower current such as 2.5 nA and a CCS pattern. (e and f) An L-cut was preformed to prepare the sample for the lift out. (g) The manipulator was attached to the lamella and (h) welded together. The lamella was cut free and moved to the center pin of the omniprobe grid. (i and j) The lamella was welded to the omniprobe grid. Afterward, the manipulator was detached. (k) The neutral position of the lamella was checked, which is defined by the uniform appearance of the upper and lower cross-sections in the electron image. As shown in the example, the lamella was slightly tilted and deviated from the ideal neutral position at an angle of 52°. Therefore, the inclination of the stage was adjusted and a new neutral position was defined. (l-o) The lamella thickness was reduced by alternating milling on each side. A CCS was used and drawn across the entire bright-appearing area to the surface edge of the protection layer. The z-value of the milling pattern depends on the material and the height of the lamella. Therefore, it was adjusted until no material remained at the lower edge of the lamella due to an incomplete milling step. In the end, a polishing step is recommended. If the lamella is unstable, there is a high risk of loss, requiring careful consideration of whether the benefits of final polishing outweigh the risks. The use of a nanomill, a common method for further reducing the thickness of a lamella, was not employed; as in the case of electrode sheets, all particles except those directly beneath the protection layer were lost.

The FIB protocol for cutting a TEM lamella varies between materials depending on a number of factors, including electronic conductivity or resistance against the Ga^+-ion beam of a material. The protocol presented in Table 4.1 was tailored to the HELIOS 460F1 FIB (FEI, the Netherlands). The protocol presented could be considered as a good starting point for the preparation of FIB lamella. Modifications to the NCM-specific protocol are described in Section 4.2.3.
When a sample was stored in a vacuum cabinet overnight, it was plasma cleaned in an argon plasma cleaner (Model 1020, Fischione, USA) for three to five minutes. Plasma cleaning could reduce organic contamination at the cross-sectional surface

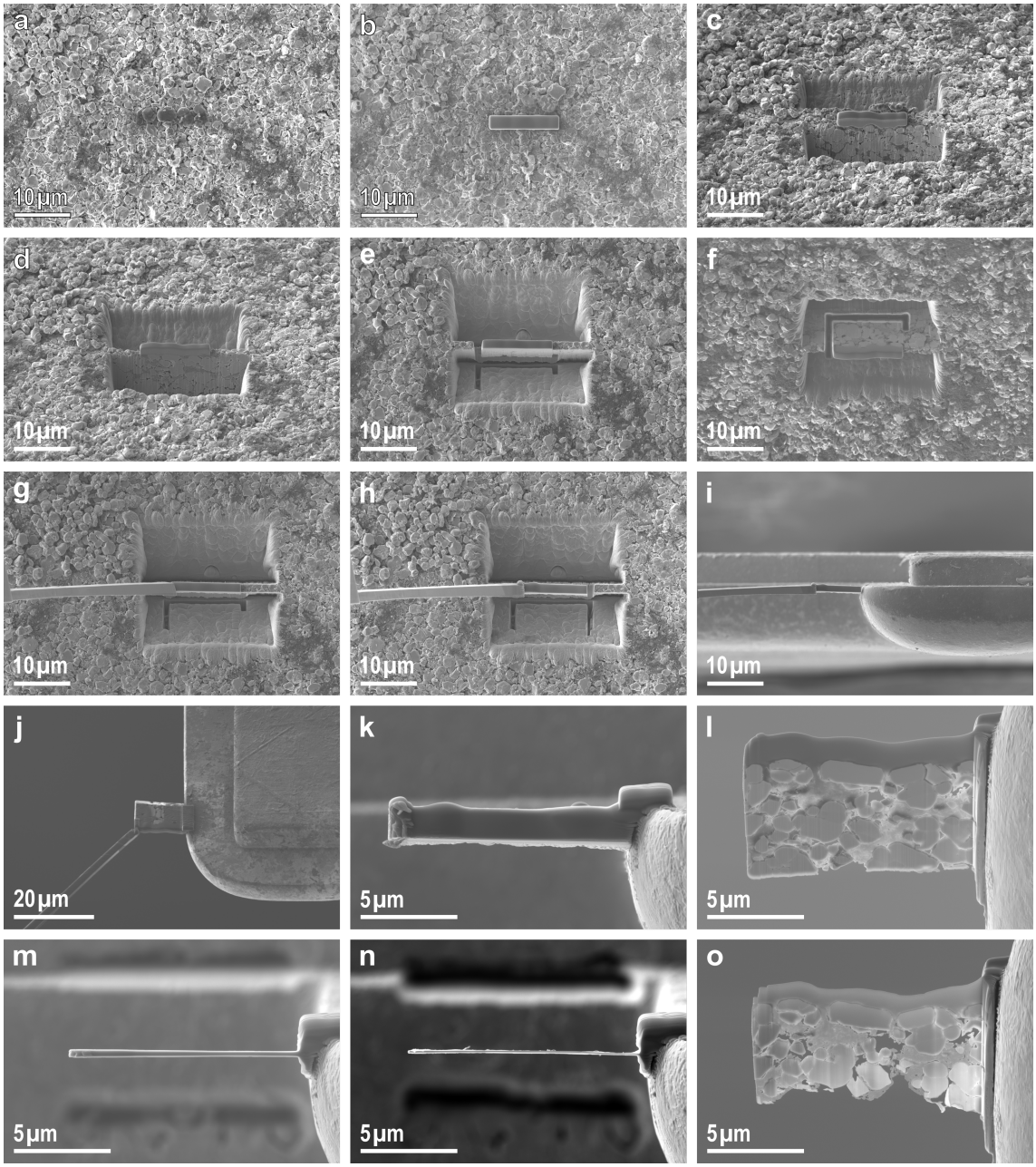

Figure 4.3.: SEM images illustrating the steps of the standard FIB procedure for a lamella preparation from an electrode sheet: (a) Protection layer deposited by the electron beam (carbon). (b) Protection layer deposited by the ion beam (carbon). (c) Trench milling. (d) Cleaning trenches. (e) L-cut (electron view). (f) L-cut (ion view). (g) Positioning of manipulator. (h) Manipulator connected to the lamella followed by the free cut of the lamella. (i) Positioning of lamella to grid. (j) Attachment of lamella to grid. (k) After detachment of manipulator and in position for milling. (l) Site-view of lamella after first milling step. (m) Lamella in neutral position during milling. (n) Top-view of lamella at the end after polishing. (o) Site-view of lamella at the end after polishing.

and thus enhance image quality.

Table 4.1.: FIB Process Steps

Step	Tilt	Beam	Beam parameters	Pattern	Pattern size (x,y,z) in µm	Notes
Electron protection layer	0°	E	5kV, 6.4nA	Rectangle (C, Pt)	(12,2,1)	Usually 100nm -200nm are deposit although z = 1µm is chosen
Ion protection layer	52°	I	30kV, 0.23nA	Rectangle (C, Pt)	(12,2,2)	
Trenches	52°	I	30kV, 9nA	Regular cross section (Si)	(24,8,10)	z depends on the material and works well here for NCM. Keep a distance of approx. 2µm between and protection layer to compensate for drift during the milling process.
Cleaning trenches	52° ± 2°	I	30kV, 2.5nA	Cleaning cross section (CCS) (Si)	(24,y,10)	For y: Draw the pattern over the bright appearing part up to the upper edge of the protection layer.
L-cut	7°	I	30kV, 2.5nA	Rectangle (Si)	z = 2	Check if lamella is free.
Connect to manipulator	0°	I	30kV, 40pA	Rectangle (C, Pt)	(0.7,1.8,1.3)	Bring manipulator in contact with needle and weld it together. The x- and y-values of the pattern size should be adjusted if necessary.
Cut free	0°	I	30kV, 0.43nA	Rectangle (Si)	z = 2	Cut lamella free and lift lamella off carefully using the manual control before moving manipulator to park position.
Attach lamella	0°	I	30kV, 40pA / 0.23nA	Rectangle (C, Pt)	(6,2,1.3)	If necessary, a second layer of weld can be deposit with a higher current.
Cut off manipulator	0°	I	30kV, 0.43nA	Rectangle (Si)	z = 2µm	Cut until free, retract manipulator
1. Milling step	52° ± 2°	I	30kV, 2.5nA	CCS (Si)	(11.8,y,15)	The pattern should cover the bright appearing part along y. The z-value depends on the material and the height of the lamella. z = 15µm was a good start value for NCM.
2. Milling step	52° ± 1.5°	I	30kV, 0.73nA	CCS (Si)	(11.8,y,15)	
3. Milling step	52° ± 1.5°	I	30kV, 0.4nA	CCS (Si)	(11.8,y,15)	
4. Milling step	52° ± 1.2°	I	30kV, 0.24nA	CCS (Si)	(11.8,y,15)	
5. Milling step	52° ± 1.2°	I	30kV, 80pA	CCS (Si)	(11.8,y,15)	Use these parameters until the lamella achieved the desired thickness. If necessary go down to I_{ion} = 40pA
Polishing	52° ± 5°	I	5kV, 40pA	Rectangle (Si)	x,y larger than entire lamella excluding weld, z = 0.1	Less than 1 minute. Watch the live image of the ion image carefully and check frequently the electron image.

4.2.3. Challenges and improvements of FIB sample preparation for NCM

FIB lamella preparation of Ni-rich CAM powders and electrode sheets needed some adjustments of the standard protocol, which were implemented step by step during the project. The major challenges of the sample preparation were as follows and are highlighted in Figure 4.4.

- **Structural instability:** The lamellae of NCM-samples exhibited increased instability compared to a bulk sample due to their heterogeneous morphology. In most samples, the particles broke off during the milling process (Figure 4.4a and b). Furthermore, the lamella often bent during milling when it was thinner than approximately 250 nm, making uniform and controlled milling challenging (Figure 4.4c). Agglomerated particles and electrode sheets exhibited numerous voids between particles, which contributed to an overall instability of the lamella. The organic binder utilized in the electrode sheets was less resistant to the ion beam than the NCM particles. Consequently, the organic binder gradually disappeared during the milling process, leading to further instability of the lamella.

- **Rough surfaces:** Very rough or highly curved particle surfaces led to an inhomogeneous deposition of the protection layer (Figure 4.4d). The inhomogeneous protection layer was particularly problematic when the lamella was thinner than approximately 300 nm due to reduced particle protection and decreased lamella stability.

- **Particle size of SC-NCM:** The maximal size of SC particles was approximately 5 µm which is smaller than that of a standard lamella with a width of 10 µm or more. Furthermore, orientation of a particle could not be determined based on the shape of these specific particles.

- **Beam damage:** The ion beam caused substantial damage to the milled surfaces, resulting in the formation of a thick amorphous layer on these surfaces or the amorphization of entire particles. The curtaining effect caused by the ion beam led to non-uniform milling (Figure 4.4e).

- **Surface contamination:** The redeposition of the protection layer material led to surface contamination (Figure 4.4f).

In conclusion, the issues were manifold. Not all of them were avoidable. For the issues where improvements were feasible, solutions are described in detail in the next sections and visualized in Figure 4.5.

Structural instability

The instability of lamellae comprising NCM powders or electrode sheets represented a significant challenge that could not be completely eliminated. However, strategies

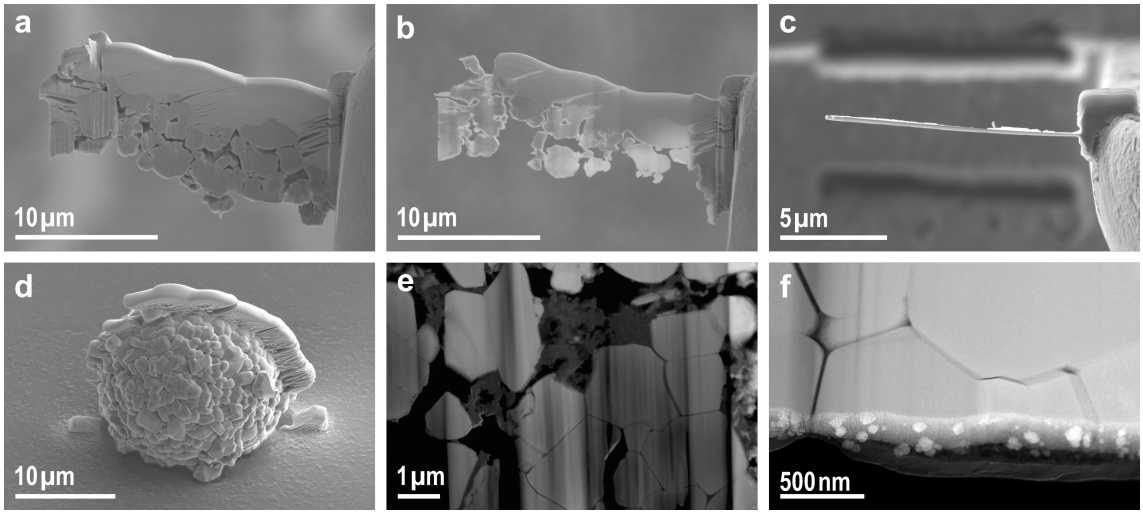

Figure 4.4.: SEM (a-d) and STEM-HAADF (e and f) images illustrate the challenges encountered during or caused by the FIB preparation. (a) and (b) Agglomerated SC-NCM particles falling off and voids appearing with progressive milling. (c) Bending of a lamella at the end of the milling process. (d) A PC-NCM particle with a highly curved surface exhibited an inhomogeneous platinum coating. (e) Lamella of an electrode sheet displayed non-uniform milling and the curtaining effect. (f) Material including the platinum of the protection layer was redeposited at the bottom of a lamella.

could be employed to preserve the material that remained intact. An issue was the breakage of particles (Figure 4.4a and b), leading to significant material loss. One resulting challenge encountered was the incomplete detachment of certain particles from the lamella. This phenomenon was particularly observable towards the end of the milling process, when the lamella had reached a few hundred nanometers in thickness. In this case, we recommend a controlled cut-off of the protruding particle to prevent it from folding onto the cross-sectional area and thereby complicating further milling.

Another issue was that the lamella frequently bent during the milling process if a thickness of less than 250 nm was reached (Figure 4.4c). The lamella bending was limited by adjusting the milling parameters, such as the tilt angle, milling time, and region. When the lamella bent, it was crucial to quickly switch milling sides, even if milling time remained. The decision to continue or stop thinning in the event of potential lamella loss must be made at each stage, which requires experience and expertise. Milling should be stopped at the latest when the lamella begins to twist. Bending of the lamella can be reduced by (i) choosing a shorter lamella length of 6 µm to 10 µm or (ii) fixing the lamella on two sides of the grid instead of one. To secure the lamella from two sides, the lamella can be positioned in the valley of an

M-shaped pin of a standard Omniprobe grid (Figure 4.5c). For EDX measurements, it should be emphasized that the copper grid can shield X-ray emission when the lamella is positioned in the M-valley. In this case, it is advisable to select and prepare the central pin tip to position the lamella there.

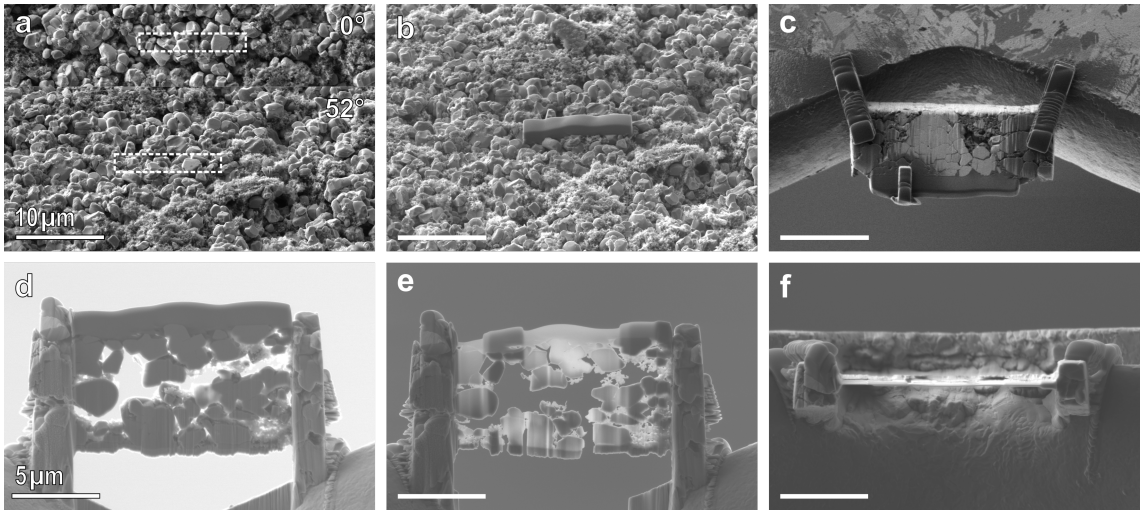

Figure 4.5.: SEM images demonstrate the improvements that were made to optimize the lamella quality. (a) Selection of a flat sample area (dashed rectangles). The view from the top (0°) and from the side (52°) helped to assess whether the surface was flat. (b) Relatively flat surface from (a) coated with the protection layer. (c) A lamella was placed in the valley of an M-pin attached to the grid at two sites (ion image). (d) and (e) illustrate the strategy of sequential milling of lamellae cut from electrode sheets containing binder and voids. (f) Site view of the lamella shown in (e), demonstrating how thin and hardly bent a lamella can be when an M-valley position is used to mount the lamella.

Both the agglomerated particles and electrode sheets showed numerous voids, increasing lamella instability. Voids in the electrode sheets were filled with an organic binder which was less resistant to the ion beam than the NCM, and therefore, it gradually disappeared during milling. The application of U-shaped milling is a common method for stabilizing a lamella when cutting extremely thin lamellae of a few tens of nanometers in thickness. A window is gradually milled into the lamella while a stable U-shaped frame is maintained. In the SC-NCM used, the voids were numerous and randomly placed. Therefore, a stable U-shaped frame could not be established. However, the idea of U-shape milling was adjusted and sequential milling was applied (Figure 4.5d-f). In sequential milling, specific lamella areas containing many particles are thinned, while void-rich regions are not thinned further. Sequential milling is particularly useful for lamellae thinner than 1 µm, as the voids and unstable areas become clearly visible, but the lamella is still stable due to its thick-

ness. Extending the lamella by 5 µm to 10 µm beyond the standard length provides flexibility during sequential milling. This was useful because when the lamella position was selected, it was not possible to see how the particles were arranged beneath the first particle layer and where voids were located. The application of sequential milling substantially improved stability and allowed sample areas to be thinned to 60 nm thickness.

Rough surfaces

The rough and highly curved sample surfaces posed a significant challenge. A uniform application of a protective layer was not feasible resulting in an inhomogeneous protective layer (Figure 4.4d). The inhomogeneous deposition of the protection layer was attributed to the position of the GIS nozzle, which was mounted at an angle to the ion column (Figure 3.15). When the sample is aligned perpendicular to the ion column, the protective layer is applied from the side. At the beginning of lamella milling, a porous protection layer was not a problem as long as the entire surface of the sample was covered. However, it became problematic when the lamella reached a thickness of approximately 300 nm for two reasons. First, a porous protection layer disappeared more quickly than a dense one, and the sample was no longer well protected from the ion beam. Second, the mechanical strength of the lamella, which originated from the protective layer, was weakened.

This problem could be countered by selecting a flat and even sample area (Figure 4.5a). In the case of PC-particles, which had a spherical shape, larger particles were better suited due to the lower relative curvature. In the case of agglomerated SC-particles and electrode sheets, an even surface area with well-connected particles was favorable. To check whether the surface is truly flat and even, it is beneficial to tilt the stage and look at it from the side. The selection of an appropriate sample location could take several minutes, but it is highly recommended to invest the time, as a suitable sample location greatly influences the results of the lamella preparation.

Particle size of SC-NCM

The received SC-particles exhibited a size range of several hundred nanometers to approximately 5 µm, which is smaller than a typical lamella size (standard > 10 µm). In principle, a lamella could be made from large particles by attaching a particle as a whole to the grid. However, these individual particles adhered to the carbon pad, making it difficult to lift them with the manipulator needle in order to transfer them to the grid. In addition, the morphology of the particles did not permit to estimate the crystallographic orientation, since the particles lacked pronounced faceting, such as described in [50]. Therefore, a targeted cut along a crystallographic direction was not feasible, which reduced the likelihood of producing a lamella aligned closely to a low index zone axis and thus would significantly increase the workload because many lamellae were required.

Cutting lamellae from agglomerated particles was more successful and efficient. These lamellae consisted of approximately ten to 25 particles, of which at least one or two were thin enough and closely aligned with a low-indexed zone axis (±5 °). In the case of electrode sheets containing both individual and agglomerated particles, no difference was observed between the two particle types regarding their surface structure as far as it could be assessed.

Reducing beam damage by adjusting the voltage of the ion beam

Milling at 30 kV resulted in damage of the lamella which manifested itself in the formation of an amorphous layer at the milled surfaces. In extreme cases, when the lamella was already quite thin (< 100 nm), entire particles became amorphous. To enhance the quality of the sample in terms of lamella thickness and clean surfaces, the ion beam voltage was reduced to 16 kV, when the lamella reached a thickness of approximately 1 µm. The ion beam current was automatically adjusted to the corresponding value for 16 kV and the milling was continued as normal. The lower voltage of the ion beam greatly improved the sample quality; however, the milling time increased and the resolution of the ion image became worse.

Curtaining

Curtaining is caused by irregular erosion caused by the ion beam. NCM-powder samples with voids and binder in between the particles were particularly prone to this phenomenon. Curtaining was not avoidable, but it was confined by limiting the height of a lamella. In case of high-resolution STEM imaging, curtaining may be beneficial. Although the overall thickness of a sample exceeded the favorable range of 50 nm to 100 nm, and therefore was rather stable, some areas exhibited a lower thickness, which was advantageous for HR-STEM because only a small area is captured in an image.

Redeposition

Redeposition of material which was previously removed by the ion-beam is a common issue in FIB-preparation [120]. The redeposited material deposit preferably at the bottom of the lamella or at other accessible particle surfaces located in between voids. For example, redeposition was observed coming from the protection layer (Figure 4.4f). Although in the beginning, platinum was used as a protection layer, carbon became the material of choice for two reasons. First, carbon is lighter than platinum and also lighter than NCM, which reduced the outshining effect that platinum showed in HAADF-STEM imaging. Second, carbon could be polished away more effectively from the cross-sectional surface of the lamella than platinum.

.

4.2.4. *In situ* chip preparation

In situ heating experiments were conducted using MEMS chips, which allow precise temperature control and heating of the sample. The preparation of a lamella on a chip was analogous to the preparation of a lamella on a grid in many respects; however, the mounting of the lamella on the chip and subsequent milling differed from the standard protocol. The various steps are outlined below and illustrated in Figure 4.6. The only difference from the standard protocol before the lift-out was the usage of dedicated chip sample holder. A 45° inclined sample holder was used and the chip was secured to it with a metal clamp (Figure 4.6a). Measuring the dimensions of the holes on the chip was essential to determine an appropriate size for the lamella (Figure 4.6b). To prevent charging of the chip due to its low conductivity, an electron beam of 10 kV was advantageous. In addition, the chip was moved to the eucentric height, and the position was stored for later.

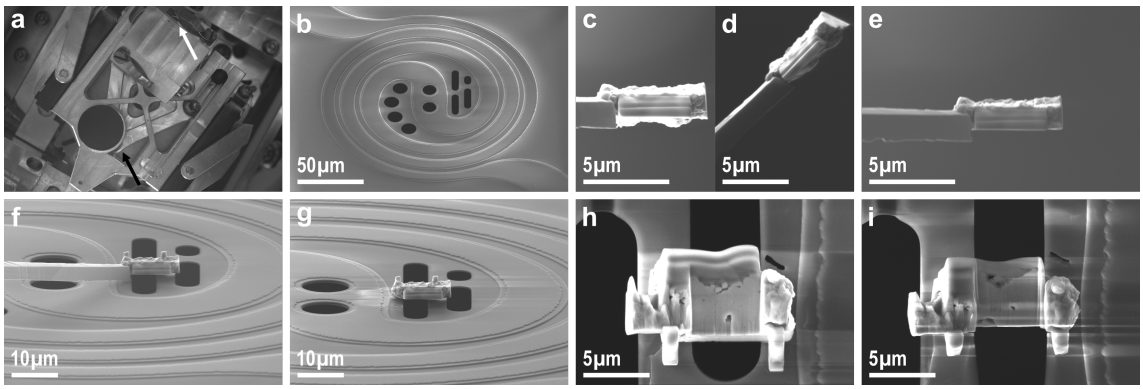

Figure 4.6.: SEM images and an ion image (noted under d) illustrating the key steps involved in lamella chip preparation via FIB, which diverge from the standard protocol. (a) overview of the 45° inclined sample holder on which the chip was mounted (white arrow) and the powder sample distributed on a carbon pad (black arrow). (b) heating chip. (c) lamella on manipulator after the lift out procedure. (d) manipulator rotated in a neutral position for cleaning the site which will be placed on the chip. (e) lamella with the cleaned lower site. (f) lamella with manipulator attached to chip. (g) lamella after the manipulator was detached. (h) lamella during the milling process. Milling of the lamella was only possible from one side, as tilting and milling from the lower side would have resulted in damage to the chip. (i) lamella after milling.

Subsequent to the lift-out, the site of the lamella that was placed on the chip in the next step required cleaning, as the chip setup only allowed milling of the upper site (Figure 4.6c). Therefore, the stage was lowered and the manipulator was relocated to its park position. The manipulator was moved into focus, first using the electron image and then the ion image, to monitor the movement and to adjust the height.

The manipulator was rotated so that the lamella was in a neutral position within the ion image to clean the bottom site (Figure 4.6d). After cleaning the bottom site, the manipulator was rotated back, relocated to the park position, and retracted (Figure 4.6e). Next, the chip was approached and the eucentric height was adjusted. The stage was tilted at an angle of 30° to place the lamella on the chip (Figure 4.6f). While working on the chip, the ion image should not be activated to avoid damaging the current lines. The GIS was then inserted and the manipulator was moved toward the chip first in y-direction, then in z-direction. As the lamella approached the chip, a shadow appeared. The shadow was used to check the distance between the chip and the needle. Finally, the lamella was placed on the chip by enabling the y-drive. The lamella was welded to the chip in two places (Figure 4.6g) and the manipulator was cut off and then removed. To properly view the upper lamella site, the chip was now rotated by 180° around the z-axis (as in Figure 4.6h and i) and rotated back for milling. After checking the eucentric height, the stage was tilted to 22°. If this was not the neutral position, the tilt angle had to be adjusted. The subsequent milling procedure followed the standard protocol described in Section 4.2.2, with the exception that only the upper site was milled to reach an appropriate thickness using a cleaning cross-section.

4.3. Conventional sample preparation: Drop casting

The easiest and fastest way to prepare powder samples for TEM experiments is to dissolve the powder in a solvent such as ethanol and to drop cast the dispersion on a 200 µm mesh copper grid covered with a carbon hole film (Plano GmbH, Germany). Two scenarios are described for particles smaller than 100 nm and larger than 100 nm. For particles smaller than 100 nm, the thickness requirement was met; however, the main issue was that the particle was not a cross-sectional sample and therefore the geometric requirements were not satisfied. Furthermore, orienting the smaller particles along a zone axis was not feasible. Therefore, particles oriented in low-index zone axes needed to be identified, which was a time-consuming task.

The larger particles were crushed to reduce their thickness. Therefore, the powder was dissolved in ethanol and pulverized using mortar and pestle. Although the crushing process created new surfaces, it was anticipated that this would occur uncontrolled, as described in Figure 4.7. It was not feasible to reconstruct whether the observed surfaces were original particle surfaces, nor were the fragments generally oriented edge-on (Figure 4.8). A surface showing alterations could be assumed to be an original particle surface. Surfaces of fragments that appear unchanged could be either an original particle surface or a surface generated by particle fracture. Consequently, a study involving inhomogeneous surface alteration would be biased. These cross-section and edge-on requirements were important for the surface degradation study. A potential shift in research focus could favor drop casting as the preparation method of choice, for example, if the target is to determine dopants in

a material.

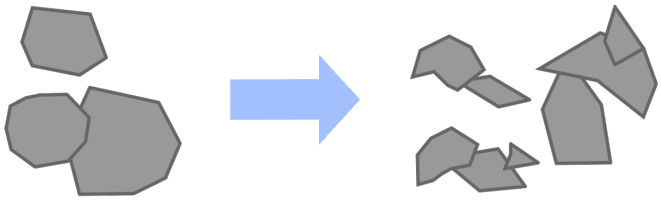

Figure 4.7.: Schematic representation of NCM particles (left) and after they were crushed with a mortar and pestle (right). The particles became smaller and the newly formed surfaces made it difficult to determine which surfaces were the original outer surfaces of interest.

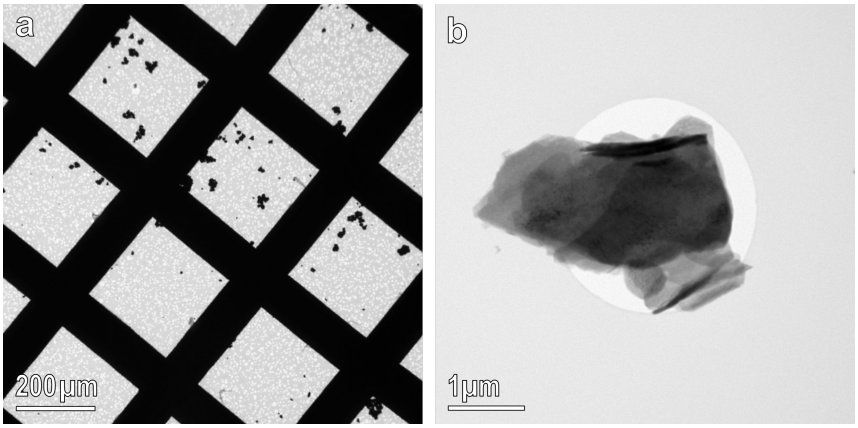

Figure 4.8.: STEM-BF images illustrating (a) the distribution of crushed particles on the carbon hole grid and (b) the arrangement of crushed particles over a hole. The image in (b) shows edges that cannot be clearly linked to an original or new surface. Furthermore, some fractures are too rough to meet the edge-on condition.

5. Results

5.1. Ni-rich NCM - the material system

The first part of this chapter introduces the NCM cathode materials used in the three subsequent experimental studies. The focus is on the chemical composition, particle morphology, and size. The second part of this chapter connects the structural properties of the materials used with the theoretical considerations presented in Section 3.2.

5.1.1. Overview used materials: Structure and chemistry

The materials investigated were all Ni-rich NCM cathodes or cathode powders with a layered structure. They differed in their chemical composition and particle morphology. In Section 5.2, which focuses on structural degradation at high potentials, commercially available SC powder was used (MSE Supplies LLC, Tucson, USA) with a stoichiometry of $LiNi_{0.83}Co_{0.11}Mn_{0.06}O_2$ (NCM831106). The samples were received from JLU Gießen as cathode sheets consisting of NCM powder blended with binder, which was calendered onto aluminum foil. A more detailed description of the cathode preparation and treatment can be found in [143]. In Section 5.3, reporting on the effects of washing on structural stability, single crystalline powder with a stoichiometry of $LiNi_{0.83}Co_{0.12}Mn_{0.05}O_2$ (NCM831205) was employed. The powder was provided by the industrial partner BASF (Ludwigshafen, Germany) and further treated by Rebecca Wilhelm (TU Munich). More detailed information on sample preparation is presented in [34]. In Section 5.4, focusing on coatings, a polycrystalline powder was used with a stoichiometry of NCM831106. The PC-powder was synthesized by Kilian Vettori (JLU Gießen) using commercially available precursor and coated with Al_2O_3 using atomic layer deposition. Further information on the material synthesis can be found in Appendix A.1. XRD analysis including Rietveld-refinement was conducted by the research partners. The XRD-data confirmed the layered structure (R-3m) in the pristine state of the materials used. Figure 5.1 exemplarily shows an XRD-spectrum of the pristine sample described in Section 5.3 with a goodness-of-fit of $\chi = 0.96$ [34].

5.1.2. Morphology and particle size

The SC-NCM powders studied showed spherical-like and cubic-shaped particles. The particle size varied substantially from approximately 100 nm to 3 µm. The

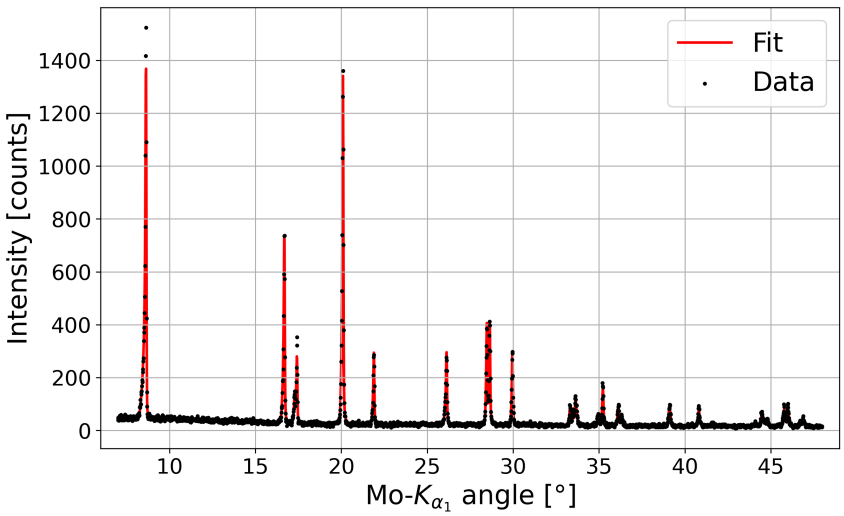

Figure 5.1.: XRD-spectrum of the as-received (pristine) sample used in Section 5.3 raw data (black dots) and the corresponding Rietveld-refinement (red curve) acquired using a molybdenum $K_{\alpha 1}$ X-ray source [34].

.

particles tended to agglomerate into chunks, measuring a few tens of micrometers as shown in Figure 5.2. The SC-particles which clustered in agglomerates formed grain boundaries between each other. Therefore, they were no longer single crystalline in a crystallographic sense. However, the term 'single crystalline' is still useful for describing Ni-rich NCM cathode materials because these materials differ substantially from polycrystalline particles as described in Section 2.1.3.

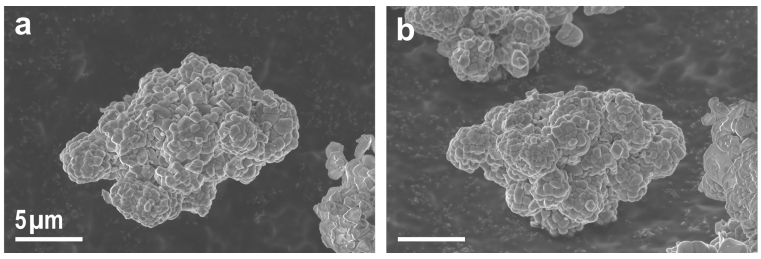

Figure 5.2.: SEM images showing the morphology and size of single crystalline Ni-NCM powder: (a) top view at 0 ° tilt angle and (b) site view at 52 ° tilt angle.

Figure 5.3a and b show a sample of the investigated PC-NCM powder which formed spherical-like secondary particles with particle sizes ranging from approximately 5 µm to 25 µm. A significant amount of particles did not form distinct spherical-shaped secondary particles, which were not chosen for lamella preparation. The cross section of a large secondary particle is depicted in Figure 5.3c. This FIB image provides insight into the arrangement of the primary particles, which are

numerous and exhibit a diverse range of shapes and sizes. A characteristic feature of PC-NCM is the radially symmetrical arrangement of the primary particles. The contrast between the primary particles is related to their orientation.

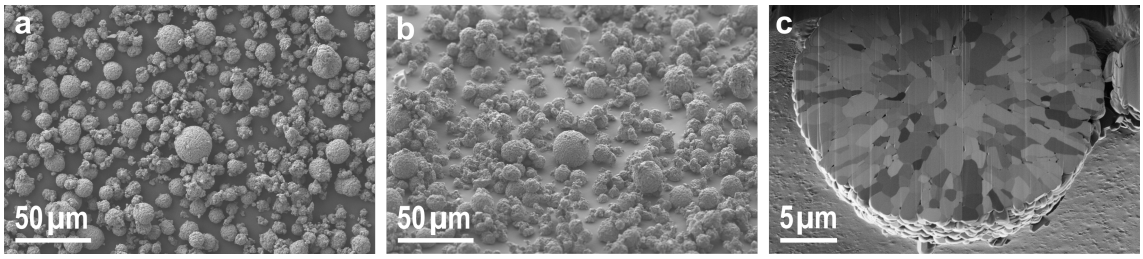

Figure 5.3.: SEM and FIB images showing the morphology of polycrystalline Ni-rich NCM powder: (a) top view at 0 ° tilt angle, (b) site view at 54 ° tilt angle and (c) FIB images showing a cross section of a PC-particle.

5.1.3. Structural properties of Ni-rich NCM visualized by STEM

Ni-rich NCM was analyzed by using high-resolution HAADF-STEM to resolve the atomic structure locally. This section aims to connect the theoretical consideration (Section 3.2) with the experiment, and shows how the structure of layered and degraded Ni-rich NCM is visualized in a high-resolution HAADF-STEM image. Before starting to explain the HR-STEM images, we should consider the following key aspects of HR-STEM imaging: A STEM image can be seen as a 2D-projection of the crystal along the incident beam direction. To obtain an atomically resolved image, the crystal must be oriented such that the beam electrons propagate essentially along a highly symmetric crystal axis, which is usually a low-index zone axis. Because the layered structure of the alternating TM planes and lithium channels plays a crucial role in the study of degradation mechanisms, it is recommended to select a zone axis in which the beam propagates in the layer planes. Zone axis orientations that realize this condition and were used primarily in this work are [100] and [210] for the layered phase, which are both perpendicular to the c-axis, and [110] and [211] for the corresponding rock salt phase.

Figure 5.4a presents an HAADF-STEM image showing the layered structure along the [100]-direction. In HAADF-STEM imaging, high-angle scattering is collected by a large ring detector, which leads to a contrast depending on the atomic number Z. The heavy TM atoms nickel, cobalt and manganese have higher atomic numbers of Z equal 28, 27 and 25 respectively, compared to oxygen ($Z = 8$) and lithium ($Z = 3$), and therefore contribute much stronger to the image intensity. Effectively, oxygen and lithium are not visible in the HAADF-STEM image. The atomic numbers Z of nickel, cobalt and manganese are very close, producing very similar large-angle scattering signals, so that these elements cannot be distinguished from each other in an HAADF-STEM image. The superimposed structure model [42] along the [100]

zone axis emphasizes that the contrast of the HAADF STEM image is dominated by scattering at the transition metal ions. The structure model suggests cation mixing of Li^{+}-ions and Ni^{2+}-ions. However, in the pristine state, the Ni^{2+} concentration on the Li^{+} site is so low that the corresponding signal disappears in the background.

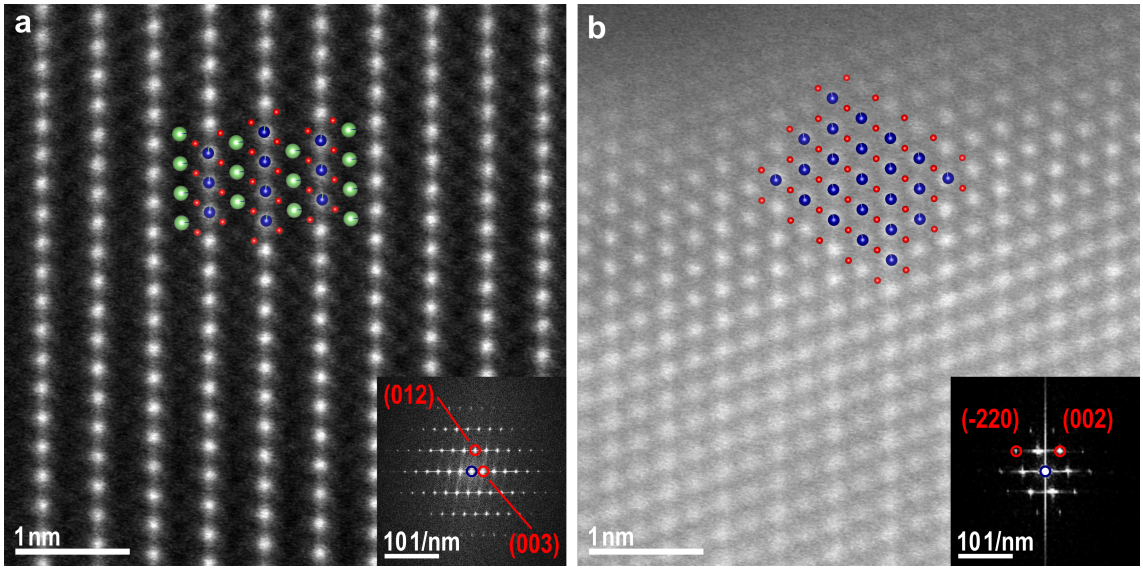

Figure 5.4.: High-resolution HAADF-STEM images of the (a) layered structure in [100] zone axis and (b) degraded material with a predominantly rock salt structure in [110] at the upper part of the image. The superimposed structure models, generated with Vesta [42], highlight that the bright intensities can be attributed to TM ions (blue) while oxygen ions (red) and lithium-ions (green) cannot be observed by HAADF-STEM imaging. The insets in (a) and (b) show the corresponding Fourier transforms of the images with the central spot circled in blue and two spots encircled in red indexing according to the corresponding reciprocal lattice planes.

The high nickel content ensures high capacity and energy density in the material. The lithium-ions diffuse rapidly along the lithium channels parallel to the TM plane, which enables fast charging and discharging. However, the high nickel content also leads to structural instabilities, which are, for example, induced by the application of high potentials. The layered structure gradually collapses and a rock salt layer forms on the surface of the particle as visualized in Figure 5.4b. In the upper part of the image, which was recorded on a surface of an NCM particle, a rock salt layer was formed. The structure is in the [110] zone axis orientation highlighted by the superimposed structure model.

The orientations of the zone axes were determined by applying a Fourier transform (FT) to the high-resolution HAADF-STEM images. The resulting FT pattern represents the dominant frequencies of the HAADF image by high Fourier coefficients

in reciprocal space such that their position corresponds to a reciprocal lattice spacing. A FT pattern looks similar to a diffraction pattern, but there are distinct differences. While a FT is only a computational transformation of a real-space image, diffraction patterns are the results of real scattering experiments. Diffraction pattern are more accurate to determine crystallographic structures because all elements are considered and the length and angle accuracy is higher assuming a well calibrated diffraction projection. In HAADF-STEM imaging sample drift and scan noise can distort the lengths and angles between the spots slightly and introduce artifact peaks. Nonetheless, for known structures, the FT pattern provides a useful representation of the periodic properties of the structure captured in an HAADF-STEM image. Therefore, Fourier spectra were produced using DigitialMicrograph (Gatan, version 3.60.4441.0) to determine the zone axes of the acquired images. First, the area of interest was selected and an fast Fourier transform was applied. A line scan was placed along a line of spots that goes through the central spot, which has the highest intensity. Second, the length d^* between the outermost spots on the line scan was measured in reciprocal nanometers. The lattice plane spacing d in real-space was calculated by

$$d = \frac{n-1}{d^*} \tag{5.1.1}$$

where n is the number of spots. The measurement was repeated in several directions starting with the brightest spots after the central spot. Third, the obtained d-values were compared with a list of d-values of the possible structures, which was generated by JEMS ([144]) after loading the crystallographic information file (cif). The structure with best agreement to rock salt, layered and spinel structure was chosen. The lattice spacing d is correlated with the lattice planes which are indexed by hkl. In a cubic system, the lattice spacing is described as

$$d = \frac{a}{\sqrt{h^2+k^2+l^2}}\,, \tag{5.1.2}$$

where a is the lattice constant and h, k, l the Miller indices. In a hexagonal system the lattice spacing is described as

$$d = \left(\frac{3(h^2+k^2+hk)}{4a^2} + \frac{l^2}{c^2}\right)^{-\frac{1}{2}}\,, \tag{5.1.3}$$

where a and c are the lattice constants, and again h, k, l the Miller indices. Last, the zone axis was determined by computing the cross product of two (hkl)-vectors to the measured lattice plane distances. Since some d-values were very close, leading to several options of (hkl)-triplets, the FT was matched with simulated diffraction patterns. This method reliably determined the zone axis in all cases.

5.1.4. Discussion of phase transitions in Ni-rich NCM

As visible in Figure 5.4b, the phase transition between the layered structure and the rock salt structure is not sharp but is characterized by a gradual transition. In

the existing literature, the phase transition in Ni-rich NCM has not been coherently characterized. On the one hand, spinel (space group Fd-3m, 227), which is typical for Mn-rich NCM structures [77,78], is discussed as a stable intermediate phase. Several TEM studies have identified an intermediate spinel phase [22, 31, 32, 85]. Most of the NCM materials investigated in these studies had a nickel content well below 80 %, but not exclusively. On the other hand, selected studies that analyze Ni-rich NCM with a nickel concentration of 80 % or greater did not detect the presence of an intermediate spinel phase [27–30]. In these studies, the transition between the layered and the rock salt structure is described as a defective region with a high degree of cation mixing. The acquired high-resolution HAADF-STEM images (see also Section 5.2 and Section 5.3) did not indicate spinel formation as a stable intermediate phase, but suggested strong cation mixing in the gradual transition regime.

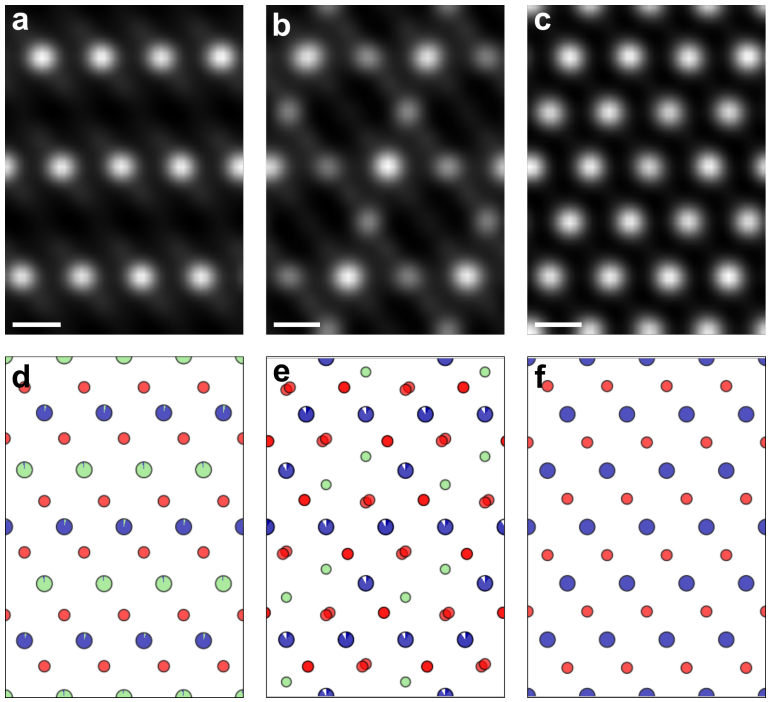

Figure 5.5.: Simulated high resolution HAADF-STEM images of 50 nm thick Ni-rich structures at 200 kV with a convergence angle of 25.4 mrad and a source size of 0.04 nm at HWHM. (a) layered structure in [100] zone axis, (b) spinel structure in [110] zone axis and (c) rock salt structure in [110] zone axis. The simulations were based on the crystallographic information from [41], [145], [75], respectively. The scale bar in (a)-(c) corresponds to 2 Å. (d)-(f) show the corresponding structure models with TM (blue), oxygen (red) and lithium (green).

To obtain a clear picture of spinel in Ni-rich NCM, we performed simulations to visualize how a stable spinel phase in Ni-rich NCM looks like compared to the

layered structure and the rock salt structure in HAADF-STEM images. Figure 5.5a-c show simulated HAADF-STEM images and Figure 5.5d-f show the corresponding structure models of the layered structure [41] along the [100] zone axis, the spinel structure with structure type $MgAl_2O_4$ [145] along the [110] zone axis, and the rock salt structure [75] along the [110] zone axis. The CIF data of the rock salt structure did not provide any Debye-Waller factors (B-factors). Therefore, the B-factors were taken from a NiO-structure model [146], which should be sufficient for qualitative analysis. The images were calculated using Dr.Probe [74] applying a frozen lattice approach to simulate thermal diffuse scattering. The parameters were selected to closely align with those applied in the experiments. The sample thickness was set to 50 nm, the high tension to 200 kV, the convergence angle to 25.4 mrad. The effect of a finite source size of 0.04 nm half width at half maximum (HWHM) was included by convolution with a respective normal distribution. The simulated images show that all three structures are clearly distinguishable in the HAADF-STEM images. Based on the simulations and the available experimental data, we did not find any evidence of a stable intermediate spinel phase in any of the experiments conducted.

5.2. Time-dependent surface degradation of SC-NCM at high potential

In cooperation with the project partners from JLU Gießen, a time-dependent study was conducted focusing on the surface degradation of SC-NCM at a potential of 4.5 V. Although other researchers had already carried out many studies to investigate the degradation mechanisms of Ni-rich NCM, the results of these studies were partially inconsistent or incomplete, as elaborated in Section 2.2. Our goal was to gain insight into the temporal behavior of degradation mechanisms with a focus on the formation of the rock salt structure and CEI layer. This led to the following research questions:

- When does a rock salt or CEI layer form on the surface?
- Does a rock salt or CEI layer grow over time and, if so, how fast?
- Can we determine if any degradation process dominates (to a given point in time) ?

To address these questions, we developed a multiscale study design in which we combined electrochemical measurements with structural and chemical characterization methods, including electrochemical impedance spectroscopy (EIS), STEM, X-ray photoelectron spectroscopy (XPS), and time-of-flight secondary ion mass sepctroscopy (ToF-SIMS). For the study half cells against lithium were fabricated (see Appendix A). We chose a potential of 4.5 V, which corresponds to 80 % of delithiation, to initiate degradation processes. At this potential, the onset of oxygen release has been reached, but electrochemical oxidation of the electrolyte is still negligible [88]. The cells were kept at 4.5 V for several weeks while every 2 days an EIS series was executed. The charge transfer resistance (R_{ct}), an easily accessible indicator for the degree of degradation, was extracted from the EIS data. The relative R_{ct} is represented in Figure 5.6 and shows a non-linear increase over time, suggesting an ongoing degradation during the time period of experiments.

Within the scope of this thesis, the structural degradation at high voltages holds over different time intervals was investigated by conducting HR-STEM experiments and EELS measurements. Therefore, a set of 4 electrodes was chosen: a reference cell and three cells that were kept at 4.5 V for 23 days, 30 days and 37 days, respectively. The reference cell was under open circuit voltage (OCV) conditions for 1 day. The objectives were (i) to identify the rock salt layer on the particle surfaces, (ii) to check for any other phase apart from the initial layered structure and the degraded rock salt structure, and (iii) to measure the thickness of a rock salt layer or any other phase at the surface. A subset of the data has been published previously in [143] and is indicated accordingly.

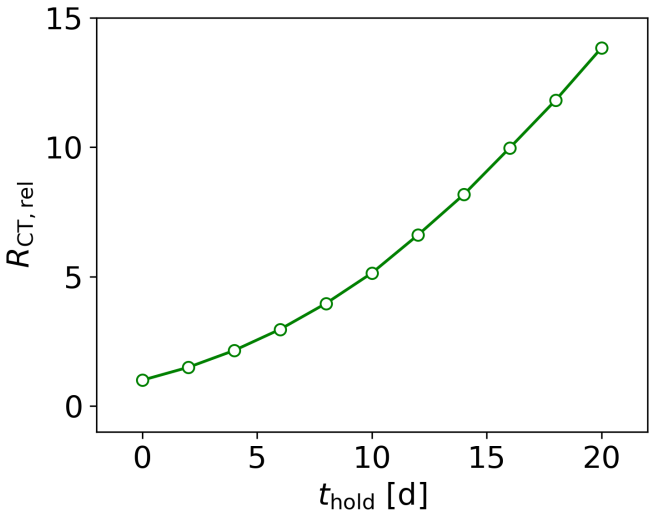

Figure 5.6.: Relative charge transfer resistance (R_{ct}) recorded at 4.5 V over 20 days. A total time of 23 days, 30 days and 37 days corresponds to a holding time of 12 days, 16 days and 20 days, respectively.

5.2.1. Qualitative observations of the surface structure

This section describes the qualitative observations made on the investigated cathodes. To ensure the reliability of the findings, up to ten particles were examined for each period, resulting in a substantial data set. The reference sample, kept in the OCV state for one day, exhibited two different surface scenarios. Figure 5.7a shows a particle which retained its layered structure up to the surface, while the particle presented in Figure 5.7b shows indications of structural surface degradation with the first few atomic layers. This example suggests that surface degradation might have started before any voltage was applied.

One notable finding was that the extent of degradation layers varied depending on the orientation of the lithium channels relative to the surface. Figure 5.8a and b illustrate particles after 23 days and after 37 days at 4.5 V, respectively. The bright, thin line feature parallel to the surface in these images is most likely redeposition of protection layer material. At each particle, two different surfaces were investigated: an open surface and a closed surface. Open surfaces are surface where the lithium intercalation channels end. Often these surfaces were rounded and did not show strong faceting. Closed surface are highly faceted surfaces along the basal plane parallel to the lithium intercalation channels. An open and a closed surface of those particles are analyzed closer in Figure 5.8c-f.

Comparing the open and closed surfaces of the particle after 23 days at 4.5 V revealed that the thicknesses of the rock salt layer were similar at both surface types. Although, the rock salt layer at the open surfaces tended to be slightly thicker,

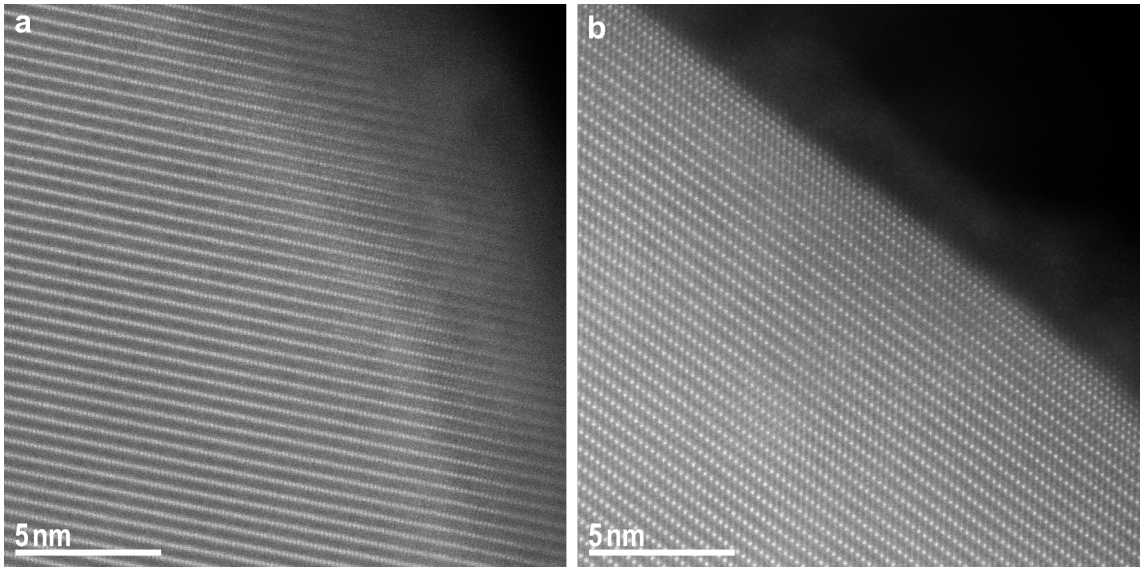

Figure 5.7.: HR-STEM images show the surfaces of two different particles of the reference cell. The reference cell was kept in the OCV state for one day. (a) represents the surface of a particle exhibiting a fully layered structure in [210] zone axis. (b) shows a particle with a layered structure along the [110] zone axis, where the outer atomic layers exhibit indications of cation mixing. Data were previously published in [143].

particularly when considering the entire region until the structure appeared fully layered again. In contrast, the particle after 37 days at 4.5 V exhibited severe degradation on the open surface. Due to the extent of degradation and the prevalence of defects, HR-STEM imaging became more challenging. However, the thickness of the degraded layer parallel to the lithium channels was comparable to that of the first sample after 23 days at 4.5 V. The observed degradation behavior, depending on the orientation of the lithium channels relative to the surface, was observed very frequently.

Figure 5.9 illustrates a typical scenario in which a layer of rock salt was partially present on the surface, but did not form a continuous layer around the entire particle. A rock salt layer formed on the upper surface but was absent on the lower surface. This situation occurred even though both surfaces were open surfaces. As illustrated in Figure 5.9c, contrast and brightness adjustment highlighted that the lower particle side remained encased in a surrounding material, unlike the overview image. This encasing material was presumed to be the organic binder, although this could not be conclusively determined from the available data. This observation suggested that an additional layer surrounding the particle could protect it from transitioning to the rock salt structure.

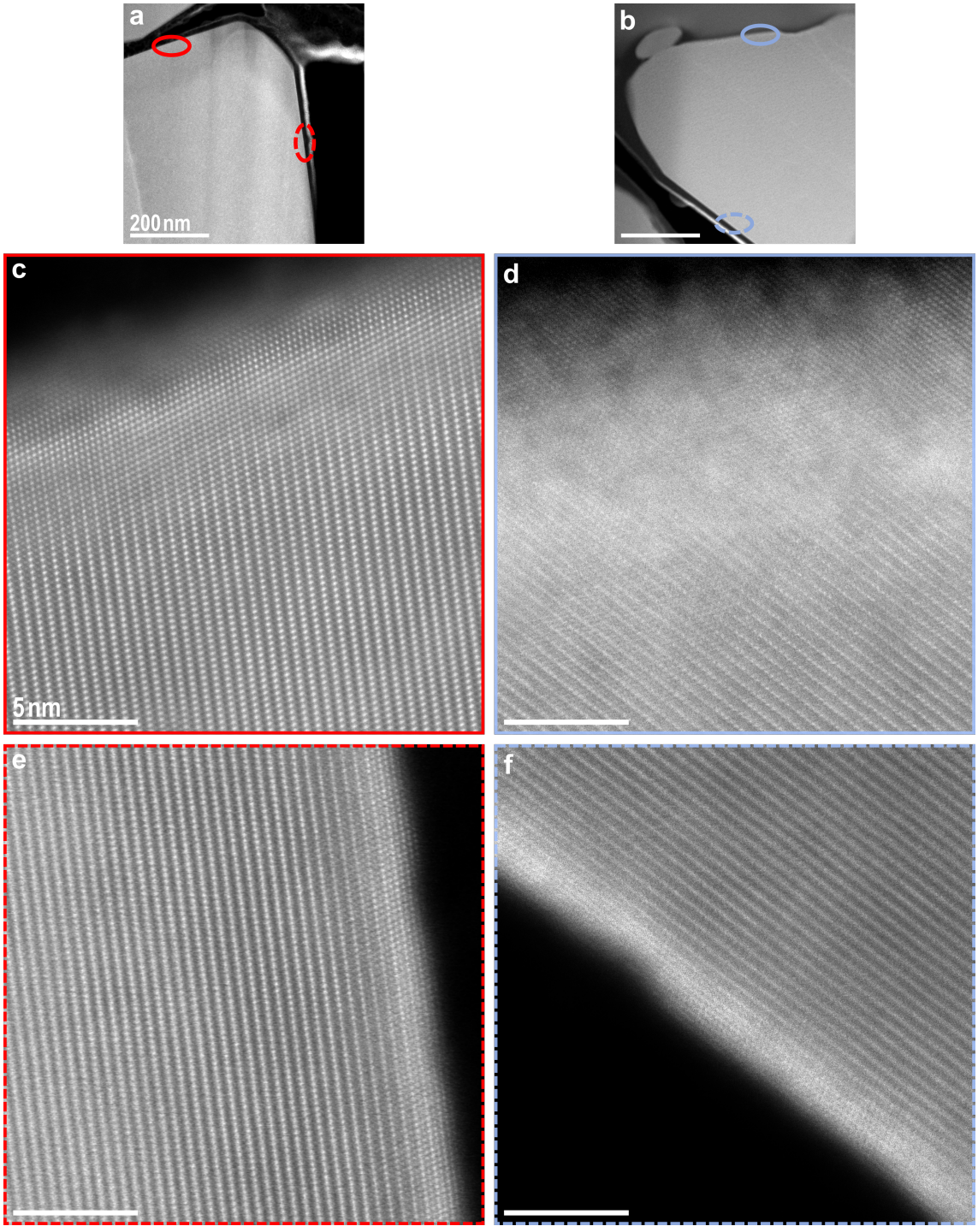

Figure 5.8.: STEM-HAADF images showing two particles (a,c,e) and (b,d,f) after 23 days and 37 days at 4.5V, respectively. The HR-STEM images in (c) and (d) illustrate the degradation at open surfaces where the lithium intercalation channels. The HR-STEM images in (e) and (f) correspond to the situation of basal plane where the lithium channels are parallel to the surface. Lithium channels are exemplarily indicated by white arrows showing the fast lithium diffusion pathway along the basal plane. The layered structure is oriented in [100] zone axis and the occurring rock salt structure at the surface is oriented in [110] zone axis. Data shown in (c) and (e) were previously published in [143].

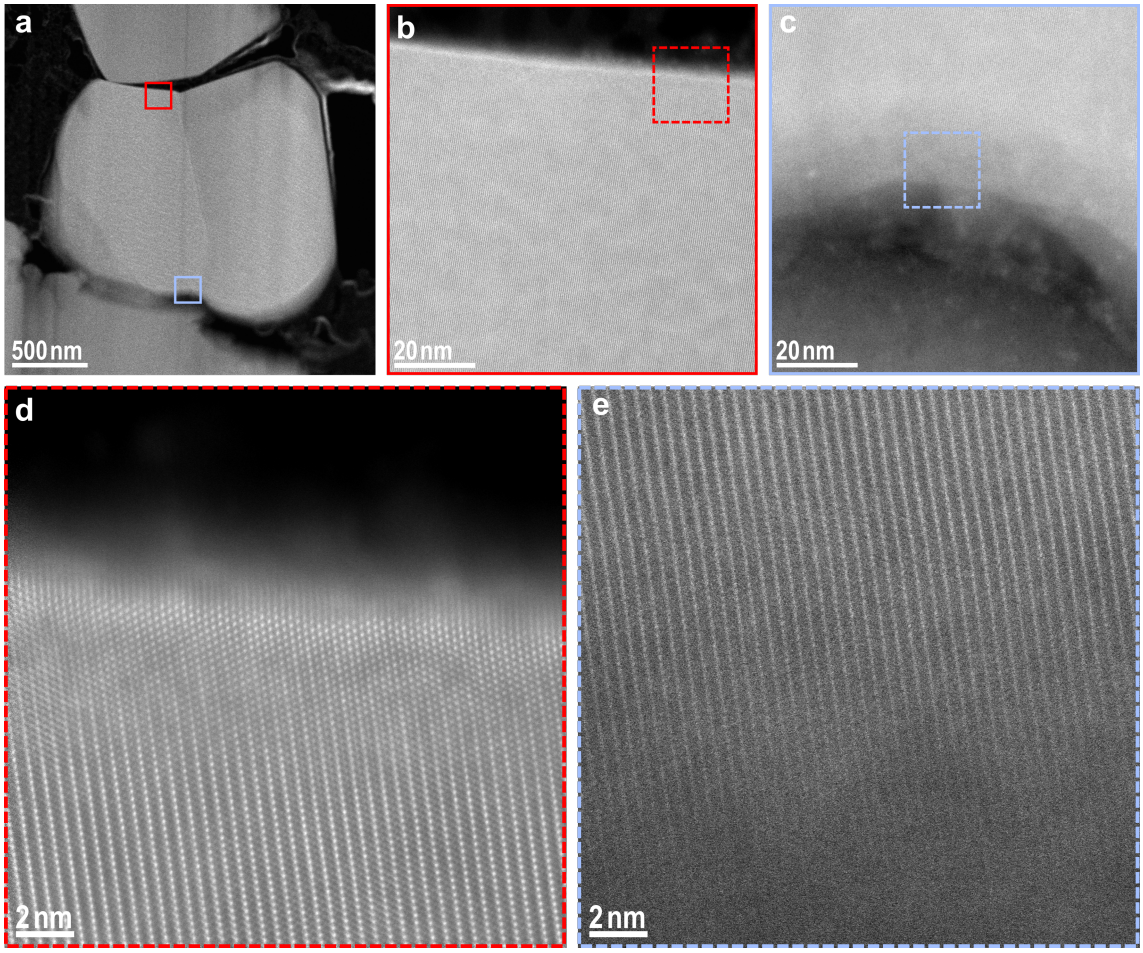

Figure 5.9.: HAADF-STEM images of a particle with a layered structure in [100] zone axis showing a rock salt structure ([110] zone axis) at the upper surface (red square) while the lower surface remained layered (blue square): (a) Overview image, (b) and (c) corresponding enlarged images, (d) and (e) HR-STEM images of the areas indicated by dashed squares in (b) and (c), respectively. Data were previously published in the supplementary of [143].

Furthermore, the position of a particle relative to other particles appeared to be a critical factor in the formation of rock salt layers on the surface. Figure 5.10 shows a particle that partially formed a grain boundary with another particle. The corresponding HR-STEM images, shown in Figure 5.10b-d, illustrate three different situations. First, an open surface (blue square) that was not in contact with another particle showed clear formation of rock salt on the surface. Second, the formation of a grain boundary between two particles (red square) resulted in notable disorder on the particle surface, where TMs occupied lithium sites in the outer layers. The layered structure remained identifiable as a superstructure. It is challenging to determine whether an interface structure formed, as the grain boundary is likely not

viewed edge-on. The disorder layer at the interface was observed to be thinner than the rock salt layer on the open surface. Third, formation of the rock salt structure was also observed on the uncovered, closed surface (green square). The results suggest that structural degradation at the grain boundary interfaces is less severe than at uncovered surfaces.

A detailed examination of the degraded surfaces of the particles revealed that the transition from layered to rock salt was not abrupt; rather, a gradual transition boundary was formed. The gradual transition boundary was characterized by a strong disorder in the layered structure. In the transition region, a significant number of TMs had migrated to lithium positions; yet, the layered structure remained visible. Moreover, the transition region was observed to be larger for degraded open surfaces than for those with closed surfaces. The appearance of transition grain boundaries can, for example, be seen in Figure 5.4b, Figure 5.8c-f, Figure 5.9d and Figure 5.10b and d. In addition, the degraded surfaces not only displayed a transition of the crystallographic structure but also a rough and uneven surface as evident in the these images.

The qualitative analysis demonstrated that the structural degradation in Ni-rich NCM was more complex than suggested by the simplified core-shell model. From the qualitative characterization, the first two TEM-related questions could be answered: First, a rock salt formed on the surface of the particles. Second, no intermediate phase, such as a spinel structure, was observed in the acquired data. However, the question of the layer thickness of the rock salt formed and the transition structure remained unanswered. This topic is discussed in detail in the following section.

5.2.2. Data processing of HR-STEM images

The qualitative characterization of the images shows that the transition from the layered to the rock salt structure was not abrupt but marked by a transition region without sharp interfaces. The absence of sharp interfaces posed a challenge in measuring the thickness of the rock salt layer. To address this challenge, three approaches were applied: (i) measuring the thickness of the bright fringe, (ii) analyzing line scans, and (iii) generating Fourier coefficient maps. Each approach is described detailed in the following.

Measuring thickness of bright fringe

In the first approach, the rock salt layer was identified by measuring the width of the bright fringe as indicated in Figure 5.11a. For NCM, the density of TM atoms in the rock salt structure is approximately twice as high as in the layered structure. In an HAADF-image, a higher density of TM atoms leads to a brighter intensity in the image as more electrons are scattered to high angles. Therefore, the width of the bright fringe was determined by measuring the full width at half maximum

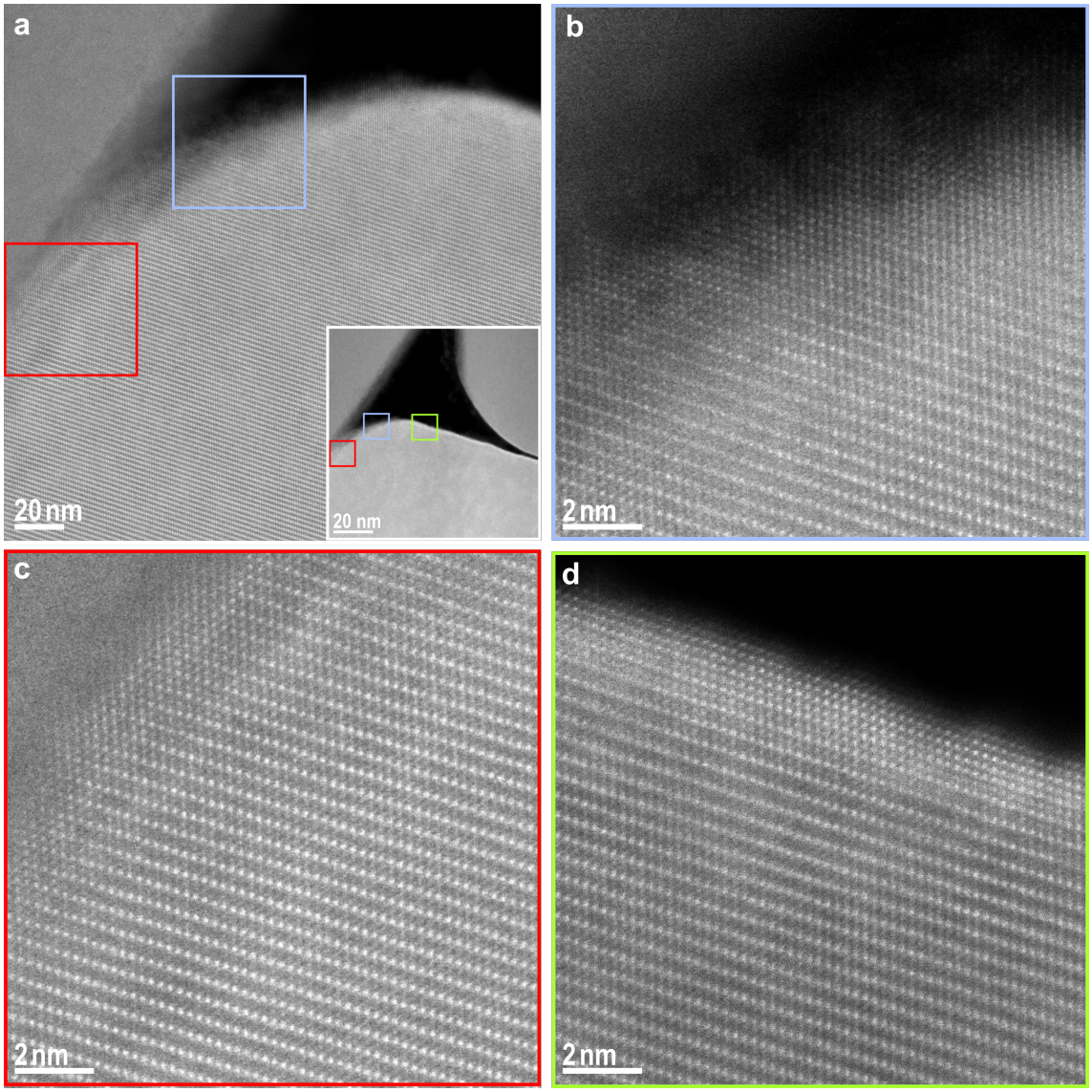

Figure 5.10.: HAADF-STEM images showing a particle that had partial contact with an adjacent grain. (a) Overview image with inset showing entire particle region; squares indicate areas of HR-STEM images presented in (b)-(d) displaying three different scenarios: (b) uncovered, open surface shows rock salt formation, (c) grain boundary interface displays disorder due to TMs occupation on lithium sites over a few atomic layers while the layered structure remained visible and (d) uncovered, closed surface depicts rock salt structure formation. The layered structure is oriented in the [100] zone axis and the rock salt layer in the [110] zone axis correspondingly.

(FWHM) of the increased intensity region. The bright fringe suggests a smooth and well-confined surface layer. Although this method seems simple and does not require an aberration-corrected microscope, it only provides a rough estimate of the structural degradation at the surface. This becomes apparent when analyzing the atomically resolved image shown in Figure 5.11b. The HR-STEM image reveal that the rock salt layer was less homogeneous in thickness than detectable in the medium magnification image. Furthermore, a gradual transition boundary between the rock salt layer at the surface and the layered core structure is visible, highlighting the complexity of the degradation process. Consequently, this approach is suitable if a rough estimation of the degraded surface layer thickness, or being more precise of the rock salt layer thickness, is needed, but not for an in-depth study of surface degradation.

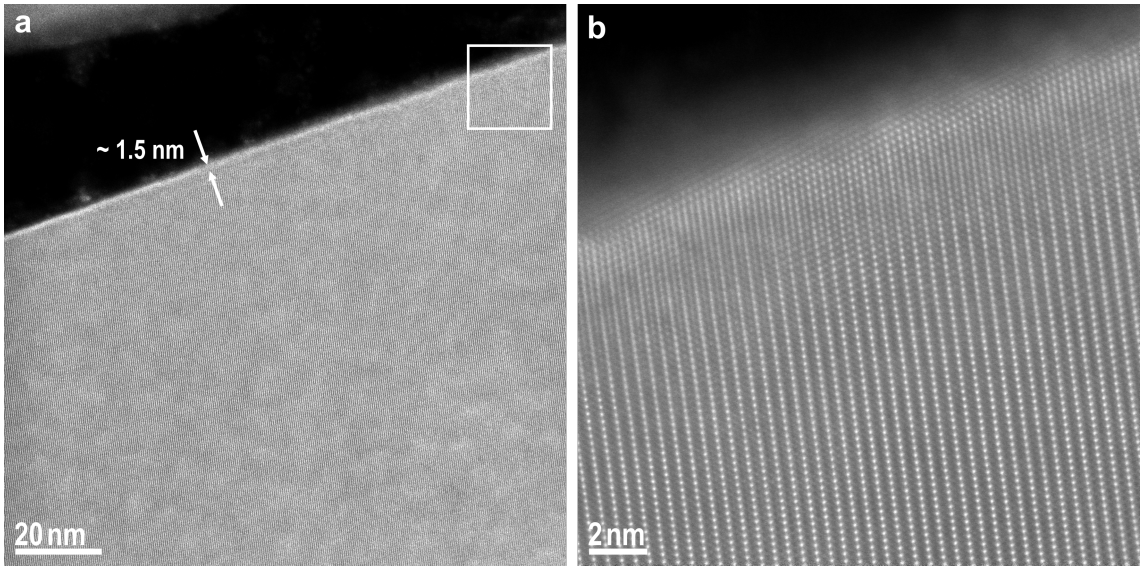

Figure 5.11.: Determining a rock salt layer thickness by measuring the width of the bright fringe at the surface of a particle. (a) HAADF-STEM image at medium magnification showing a homogeneous bright fringe of approximately 1.5 nm thickness. (b) HAADF-STEM image at high magnification (area indicated by a white square in (a) revealing the atomic structure with a bright rock salt layer at the surface, corresponding to the bright fringe in (a), and a gradual transformation into the layered structure.

Analyzing line scans

In the second approach, the surface structure was analyzed by drawing line scans along an initial lithium lattice plane and a TM lattice plane in an HR-STEM image as indicated in Figure 5.12a. The presented HR-STEM image is a cropped version of the image shown in Figure 5.11b. The analysis of the surface structure aims to visu-

alize clearly the dynamic of the phase transition from rock salt to layered structure. This approach again uses the difference in intensity between the layered structure and the rock salt structure apparent in an HAADF-STEM image. In comparison to the first approach, we now analyze an HR-STEM image, which has significantly more structural details and thus allows a more in depth analysis. Considering these factors, the two line scan intensities should be approximately equal at the rock salt structure; whereas in the layered structure, the intensity profile corresponding to the line scan across the lithium lattice plane is anticipated to decrease significantly.

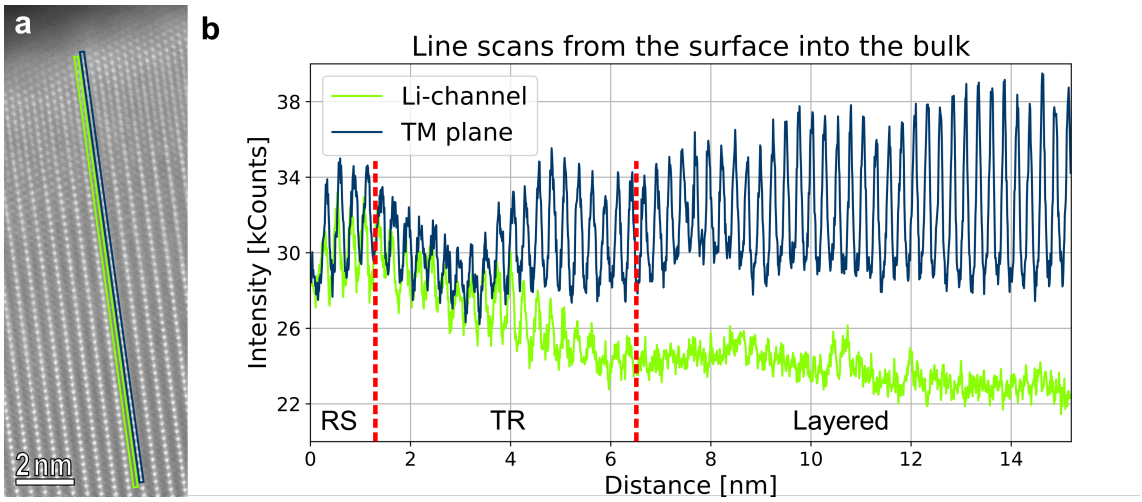

Figure 5.12.: Determining a rock salt layer/defect-rich surface layer thickness by drawing line scans along lattice planes from the surface into the bulk. (a) HR-STEM image showing a rock salt layer at the surface that gradually transitions into the layered structure and two line scans along a lithium lattice plane (green) and along a TM lattice plane (blue) starting from the layered structure as reference. (b) Line scan intensity profiles of the areas marked in (a). The red dashed lines separate the rock salt structure (RS), the transition region (TR) and the layered structure (Layered).

The line scan intensity profiles of the HR-STEM image are presented in Figure 5.12b. The red dashed lines indicate the boundaries between the rock salt layer, the gradual transition boundary and the layered structure based on the analysis. As anticipated, both intensity profiles were very similar in the beginning. In correlation with the HR-STEM image, a rock salt layer of approximately 1.5 nm thickness was determined. The intensity profile along the initial lithium channel subsequently decreased over a span of approximately 5 nm before the lattice contrast disappeared and a noisy intensity signal dominated. This section was assigned to the transition layer visible in the HR-STEM image. After a distance of approximately 11 nm from the surface, a plateau was observed in the intensity profile. This observation suggests that the gradual transition boundary may be more extensive than initially inferred

from the HR-STEM analysis. The intensity profile corresponding to the initial lithium channel did not decrease to zero counts, which indicated the presence of noise and the possible occupation of TMs at lithium sites, which was unresolved in the HR-STEM image.

A further analysis of the intensity profile of the TM lattice plane yielded to the following observations. First, the intensity profile along the TMs lattice plane also showed a slight decrease between a distance of 1.5 nm and 3.5 nm. This phenomenon might be attributed to defects that cannot be fully explained by the current dataset. Second, the overall intensity of the TMs lattice planes in the core was observed to be higher than that at the surface. The difference in intensity can be attributed to factors such as sample thickness and the presence of defects. This observation may differ from the finding in Figure 5.11a, where the intensity on the surface was higher than in the bulk. However, a higher intensity at the surface is consistent with results of intensity profiles, as medium magnification imaging results in the averaging of intensities of the lithium and TM planes. The surface exhibited a higher mean intensity compared to the bulk because both the lithium positions and the TM positions were occupied by heavier TMs which contributed to a higher Z contrast. In conclusion, the line scans highlight the intensity changes in the lithium and TM lattice planes, thereby enhancing the accessibility of the observed information in the HR-STEM image. Due to limited data, future adjustments to the boundaries between the three areas may be necessary.

Generating Fourier coefficient maps

The previous approaches were both based on evaluating the intensity profiles to determine the thickness of the surface layer that deviated from the layered structure. A third approach, the Fourier coefficient mapping, focused on the crystallographic variations between the layered structure and the rock salt structure. Therefore, HR-STEM images were segmented into small patches, each corresponding exactly to one projected unit cell. A fast Fourier transformation was applied to each patch. The resulting FT pattern of these patches were analyzed to determine whether the layered structure, the rock salt structure, or a combination of both structures were apparent within a patch. Based on these results, a Fourier coefficient map was constructed, which visualizes the structural differences of an entire HR-STEM image. An example is shown in Figure 5.13.

The structural differences between the layered structure and the rock structure phase are reflected in their FT pattern. To distinguish between the two phases, it is essential to identify two strong spots: one spot is present in both structures, while the other spot occurs only in one of the two structures. The layered structure shown in the example in Figure 5.13 is oriented in the [100] zone axis and the rock salt layer in the [110] zone axis. In this example, the 003 reflection, which occurs exclusively in the layered structure, and the 006 reflection, seen in both phases, were selected,

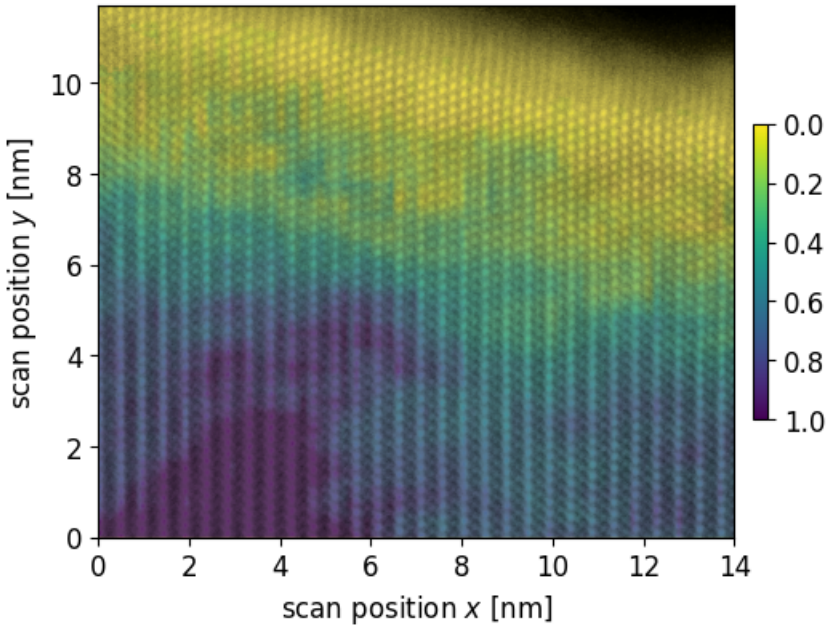

Figure 5.13.: STEM-HAADF image overlaid with the corresponding Fourier coefficient map. A value of zero indicates a pure rock salt structure, while a value of one indicates a pure layered structure. Data were previously published in [143].

as illustrated in Figure 5.14.

The absolute values of the Fourier coefficients depend on many variables, which are either partially unknown or difficult to determine, such as the exact sample thickness. Therefore, the ratio of Fourier coefficients is analyzed to reduce such effects as much as possible. The ratio of F_{003}/F_{006} was calculated, which represents the strength of the two reflections in relation to each other. A ratio equal to zero represents a pure rock salt structure. A ratio equal to one indicates a pure layered structure. The threshold for the layered structure is not one in reality; however, it was normalized to one in order to better ascertain the presence of the pure layered structure. For this purpose, an HAADF-STEM image of the layered structure was simulated using Dr. Probe [74] according to the experimental conditions. The ratio of F_{003}/F_{006} yielded approximately 3.5 for the simulated structure and was used to estimate a normalized threshold value for the layered structure. Values in between represent a mixed phase, assuming a linear dependency of the Fourier coefficients.

The Fourier coefficient mapping was performed using a Python script. This method requires HR-STEM images in which the atomic columns are clearly resolved. The main considerations are briefly presented in the following list. Further details of this approach can be found in annotated script in Appendix B.2.

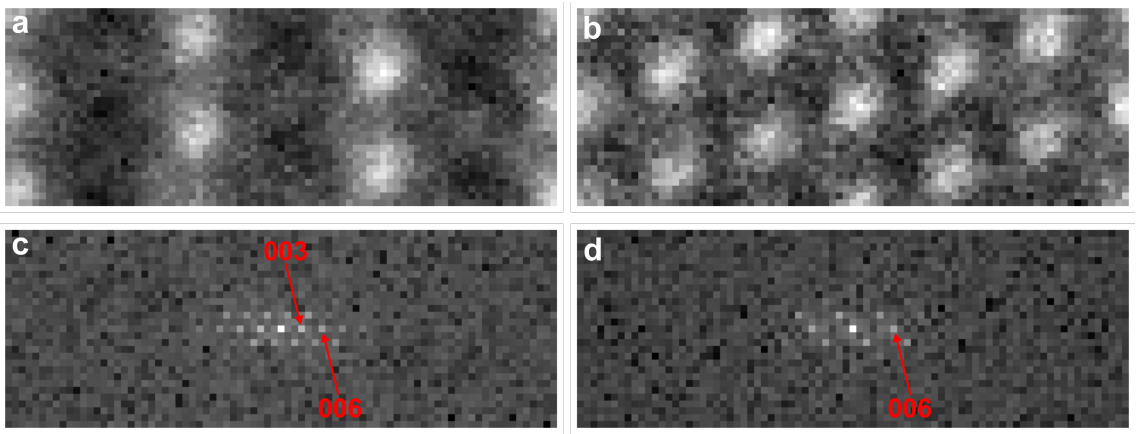

Figure 5.14.: Examples showing a patch of a (a) layered structure and a (b) rock salt structure. The corresponding FT pattern in (c) and (d) highlight the differences in the occurring reflections between both structures. While the 006 reflection occurs in both structures, the 003 reflection occurs exclusively in the layered structure as indicated by red arrows.

- Presets
  - Determine the region of interest by drawing a rectangle in the HR-STEM image.
  - Insert an origin into the image and draw two vectors from this point that define a unit cell.
  - Create a pattern of lattice points and superimpose it on the image. Check if the lattice points fit well; otherwise, adjust the unit cell vectors.
- Interpolation of the image to align the layers vertically
  - Define appropriate sampling rate.
  - Run interpolation.
  - Check if interpolation was successful: Do the y-edges of the interpolated image match with the lattice planes? Does the periodicity of atoms match the edge along the x-axis of the interpolated image?
- Validation
  - Check the quality of a patch: Is the FT pattern free of any streaks?
  - Check the strengths of the Fourier coefficients within a certain patch.
  - In addition to the two spots used to calculate the ratio of Fourier coefficients, a further reflection spot should be checked to confirm 2D-periodicity of the selected patch. This additional reflection spot needs to be in a different plane of refection spots.
- Evaluate Fourier coefficients

- Calculate ratio of Fourier coefficients.
- Subtract background.
- Match Fourier coefficient map with HR-STEM image.
- Estimate the ratio for the layered structure from simulation and determine a normalized threshold value for a purely layered structure.

Figure 5.15 presents Fourier coefficient maps of images showing four distinct situations: (a) an open surface with a rock salt layer on top, (b) a closed surface with a rock salt layer on top, (c) a core area, and (d) a surface of a straight intragranular crack. Areas with yellow speckles within the layered region in Figure 5.15b and d were excluded from the calculation due to a high noise level and can therefore be ignored. The coefficient maps highlight findings previously described in Section 5.2.1 and in the first two approaches presented in this section to measure the thickness of surface layer, together with new insights.

Figure 5.15a showcases the transition phase boundary between the layered structure and the rock salt structure on an open surface. It clearly emphasizes the non-uniformity and the extension of the gradual transition boundary into the core. This result confirms the hypothesis concluded from the line scan analysis that suggests that the mixed layer probably extends further into the core. Only a small area in the lower left quadrant of the image can be assigned to a fully layered structure, as indicated by the violet coloring. Furthermore, the Fourier coefficient map in Figure 5.15b and c compared to Figure 5.15a shows that the transition from the layered structure to the rock salt structure is more rapid on closed surfaces than on open surfaces. So far, a detailed examination of the layered core structure has not been presented in detail, as it often appeared very regular in the HAADF-STEM images. However, the Fourier coefficient map in Figure 5.15c of a uniformly appearing core structure shows a significant amount of mixed phase indicated by the corresponding color map. This result emphasizes that the layered core structure was not defect-free, and that a measurable amount of transition metals had already migrated to the lithium positions.

In conclusion, the Fourier coefficient map is an effective tool for highlighting structural variations in Ni-rich NCM in a 2D-map. This is a great advantage over a line scan, which only represents a single lattice plane. Thus, the Fourier coefficient mapping offers rapid access to previously reported observations. Despite uncertainties in Fourier coefficient mapping due to image quality and thresholds from simulations, it underscores that drawing lines along the interfaces is often an inappropriate approach to defining the different structural regimes. Furthermore, the mapping shows that the transition from the layered to the rock salt structure is often more complex than suggested by the core-shell model. A disadvantage of Fourier coefficient mapping is that it requires high-quality HR-STEM images with a sufficient signal-to-noise ratio to measure the amplitudes of the Fourier coefficients.

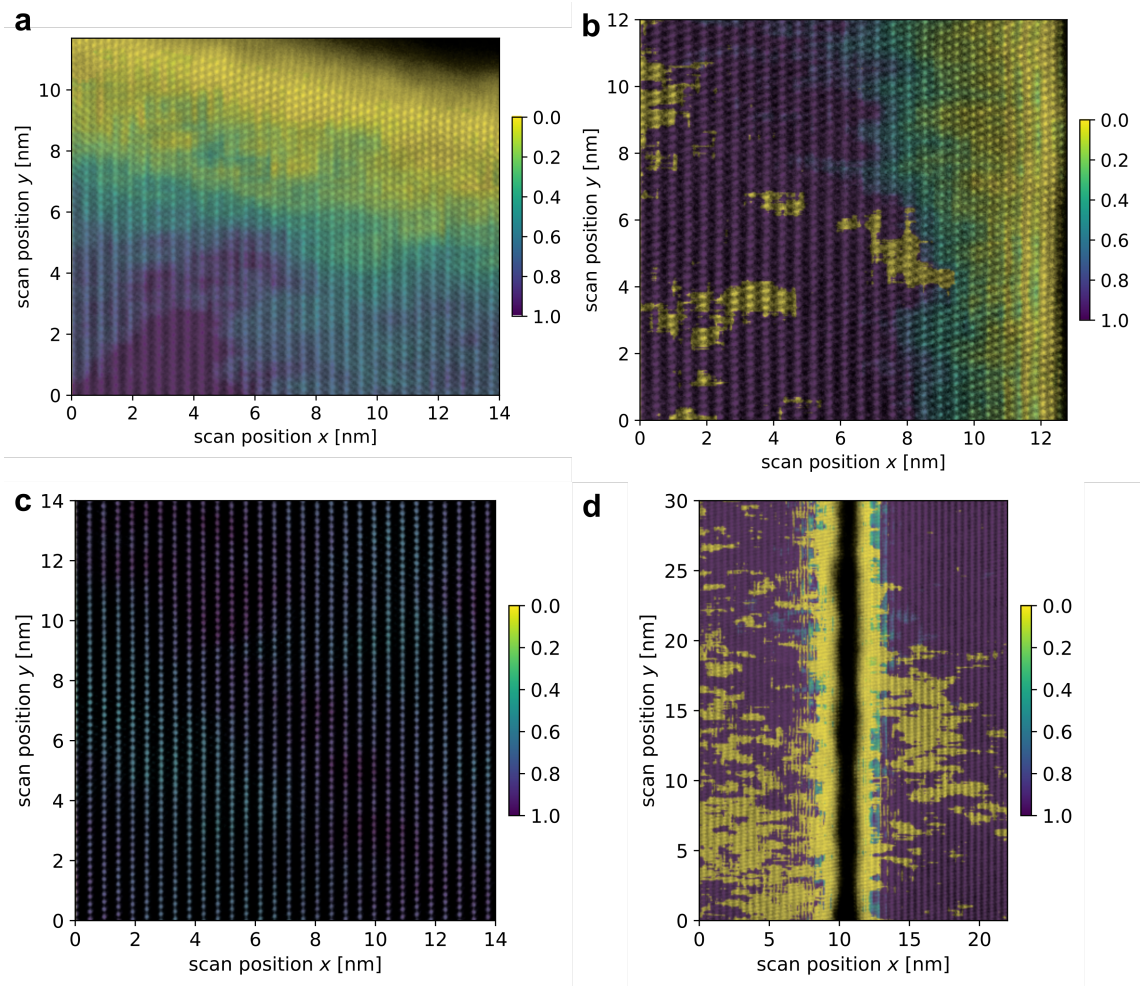

Figure 5.15.: HR-STEM images overlaid with the corresponding Fourier coefficient maps showing different scenarios: (a) Open surface, (b) closed surface, (c) core structure, (d) surface of an intragranular crack. (a)-(c) presents particles kept at 4.5 V for 23 days while (d) presents a particle after 30 days at 4.5 V. The threshold of 0 represents a full rock salt structure, while the threshold of 1 corresponds to the layered structure. This threshold was determined using a simulated HR-STEM image of a layered structure. The simulation parameters were closely align with the experimental conditions. The yellow speckles in (b) and (d) arise when the Fourier coefficient mapping failed due to too much noise in the data. Data in (a) were previously published in [143].

This requires well-prepared samples and an aberration-corrected STEM. Achieving sufficient sample quality was particularly challenging when the material was already severely degraded and the high defect density negatively affected the HR-STEM image quality.

To return to the original motivation of measuring the thickness of the rock salt layer and the transition boundary, it is necessary to define what is considered to be layered and rock salt structure. The limits zero and one are extreme values and represent only a fully intact part of the structure without defects. However, in the material being investigated, defects are present throughout the crystal. It is therefore useful to define thresholds to better distinguish the structural regions. For example, a 10 % deviation from the ideal value could define the structure as still rock salt or layered. While this is not an objective determination, it is necessary to establish a basis for estimating the average layer thickness.

5.2.3. EELS analysis

The transformation from the layered to the rock salt structure alters not only the crystallographic structure but also the electronic configuration. While nickel has a valence state of Ni^{2+}, Ni^{3+} or Ni^{4+} in the layered structure depending on the SOC, nickel is reduced to Ni^{2+} in the rock salt structure. This valence change can be observed through an energy shift in an EEL spectrum. Therefore, EELS mapping was performed to gain additional perspective on the degradation of the the studied NCM material. The data analysis focuses on the behavior of oxygen and nickel, the predominant TM.

The EELS maps were acquired at a high tension of 200 kV with a current of 90 pA, using the Spectra. A camera length of 29 mm and a convergence angle of 21 mrad were employed. A dispersion of 0.3 eV/channel was utilized, resulting in an energy resolution of 1.37 eV. The spectra included the energy-loss range from 420 eV to 1030 eV, which contains the oxygen K-edge and the L-edges of the TMs. EELS maps were acquired by activating the Dual-EELS mode, which acquires the low-loss and the high-loss spectra quasi-simultaneously, with a step size of 5 Å and a pixel time of 0.05 sec for the high loss. The data analysis, including background estimation and subtraction was carried out using Hyperspy-based scripts (Section 3.3.1). The EEL spectra range from the surface equal to 0 nm to 80 nm in the bulk. The signal was binned down to one pixel in the x-direction, which is comparable to a line scan. A map was acquired instead of a line scan to spread the electron dose. To obtain a vertical surface edge for the lower map, the map was rotated.

Figure 5.16 presents HAADF-STEM images and EELS data of a particle from a cell that was kept at 4.5 V for 37 days. The EEL spectra were obtained from the areas indicated in Figure 5.16a by rectangles. The area enclosed by the upper rectangle corresponds to an open-like surface, while the lower rectangle is placed on a closed

surface. The HR-STEM images in Figure 5.16b and c show the atomic structure in the area where the EELS maps were acquired. The HR-STEM images were obtained prior to the acquisition of the EELS maps. The structural surface degradation at the upper area was much more severe than in the bottom part which matches with the observations reported in Section 5.2.1. The EEL spectrum in the red-marked region reveals a collapse of the first peak of the oxygen K-edge fine structure over the first 25 nm suggesting many defects in the oxygen sublattice compared to the layered structure. In the nickel L_3-edge, an energy shift was observed. The maximum of the L_3-edge is at approximately 852.9 eV at the surface. The maximum of the L_3-edge shifts over approximately 42 nm from the surface into the bulk toward higher energies before it fluctuates around 854.2 eV. The properties of the material marked blue exhibited comparable overall behavior, yet notable discrepancies were identified. Although a change in the oxygen K-edge fine structure is evident, the changes are limited to the the first 10 nm at the surface and less pronounced. Furthermore, the energy loss value shifts from approximately 853.1 eV to 854.2 eV over a distance of 35 nm from the surface. While the energies are comparable, especially the upper energies, the distance over which the energy shift occurs differed significantly.

5.2.4. Discussion of the results

The study confirmed that a phase transformation from the layered structure to the rock salt structure is a central degradation phenomenon in Ni-rich NCM when the cathode is exposed to high potential. Local STEM investigations on a wide variety of particles showed that the commonly assumed core-shell model [22] is limited in terms of understanding the structural degradation in Ni-rich NCM in depth. First, the formation of the rock salt structure depends on the orientation of the lithium channels relative to the surface. The open surfaces were shown to degrade significantly more over time than the closed surfaces. Orientation-dependent degradation was also shown by Lin *et al.* [69]. As the open surfaces are the active surface where lithium de-/intercalation takes place, it is plausible that these surfaces degrade more rapidly. Second, the environment of the particle affects whether or not the particle surface comes into direct contact with the electrolyte. A particle with an open surface degraded less severely when the surface was surrounded by a further layer of material or located at a grain boundary compared to the unprotected surface without a further barrier to the electrolyte. Third, the material exhibited defects in a surface layer prior to electrochemical treatment. The data could not determine whether the defects arose from synthesis, storage, or chemical reactions with the electrolytes, but non-uniform aging was evident.

The analysis of the structural data reveals a gradual transition from the rock salt structure to the layered structure. From a thermodynamic perspective, phase boundaries are characterized by a sudden and sharp change in the crystal structure of the material. However, the rock salt structure grew epitaxially and coherently in the layered structure. This is possible due to a low lattice mismatch between these

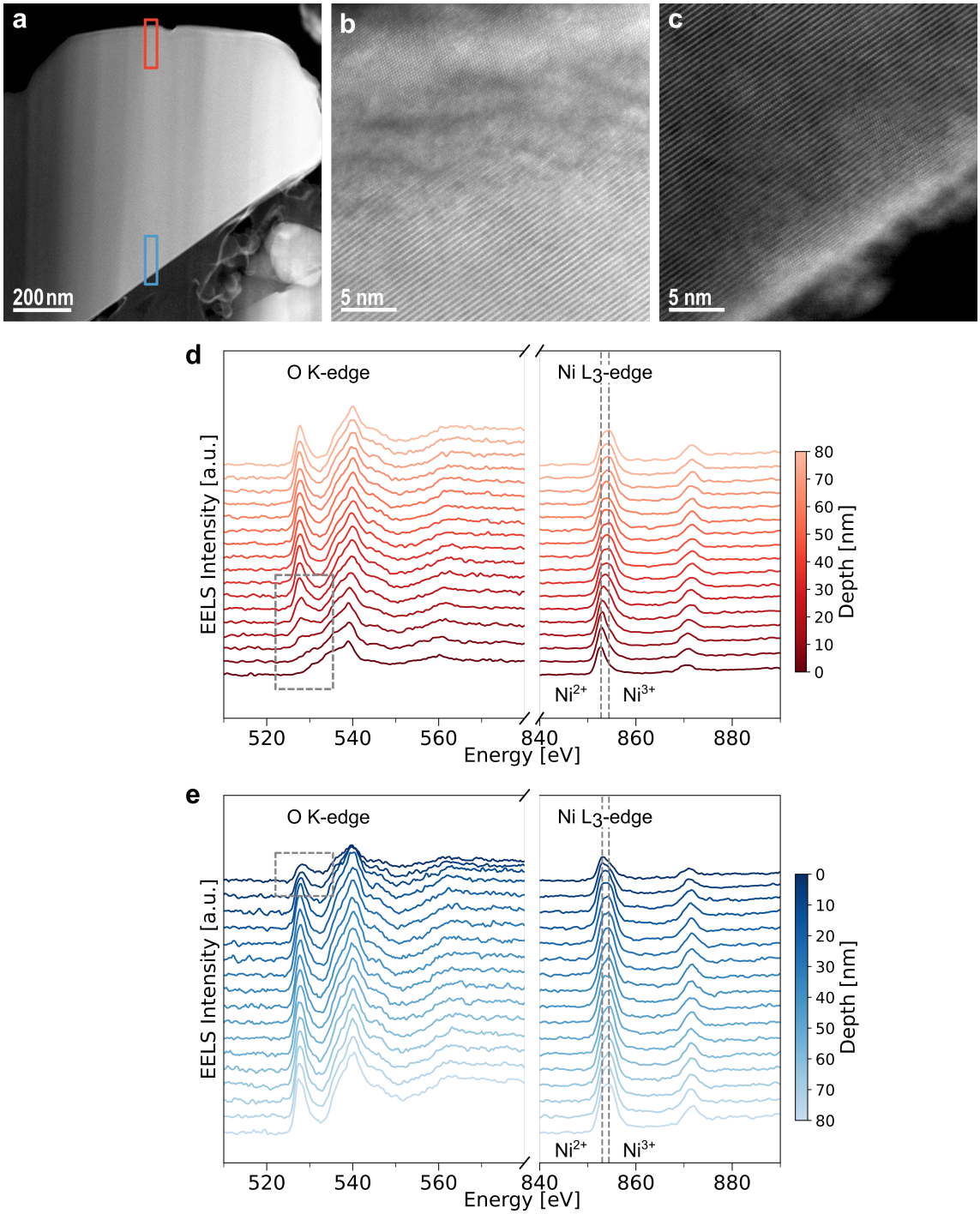

Figure 5.16.: EELS measurements at a particle after 37 days at 4.5 V of two areas indicated by rectangles in the overview HAADF-STEM image in (a). (b) and (c) show HR-STEM images from the indicated regions taken prior EELS measurements whereas (b) refers to the upper region (marked red) with an open surface and (c) to the lower region (marked blue) with a closed surface. (d) and (e) represent EEL spectra showing the oxygen K-edge, where the collapse of the pre-edge is indicated by a dashed rectangle, and the Ni L-edge, where the energy shift of the L_3-edge is indicated by dashed lines. The EEL spectra extend from the surface at 0 nm to a depth of 80 nm into the particle. Data were previously published in the supplementary of [143].

two structures (see Figure 5.5). The gradual transition boundary enables structural adaptation between the layered structure and the rock salt structure [147] which is likely needed to compensate for kinetic constraints and stress gradients at the surface, which prevent the system from reaching equilibrium. The phase transition is driven by the release of oxygen at high SOC, which promotes the reduction of nickel to ensure charge neutrality. The comparable ionic radii allow Ni^{2+} to occupy the lithium sites, thus initiating surface degradation. As already stated in Section 5.1.4, spinel as a stable intermediate phase was not observed in the investigated material. The observation of a gradual transition region with strong cation mixing is in good agreement with other studies [29, 70, 148] published during the time period of this dissertation. However, to the best of our knowledge, the effect of the gradual transition boundary on electrochemical performance has not been further investigated.

The presented EELS data suggest that the defect density extended much further from the surface into the core of the particle than the HAADF-STEM data indicated. The main indicators of extensive structural degradation are represented by the oxygen K-edge and the Ni-L_3-edge. The oxygen pre-edge peak is related to the electronic structure of the TMs and arises from the transition of the O 1s core state to the O 2p state which is hybridized with the TM 3d orbital [147, 149]. The TM3d-O2p-hybridization is strong when TMs with higher oxidation states are present such as Ni^{3+} and Ni^{4+}. A decreased intensity in the oxygen pre-edge suggests a reduction in the nickel state and an increased defect density such as oxygen vacancies [32, 150]. The formation of oxygen vacancies is an indicator for the phase transition from the layered to the rock salt structure, which is accompanied by the release of oxygen, while the oxygen sublattice remains in place. The correlation of EEL spectrum data with the HAADF-STEM image revealed that an oxygen pre-peak is absent in the case of the rock salt structure, which is consistent with other studies [81, 149–151].

The Ni-L_3-edge provides information about the oxidation states of nickel. A shift to higher energies indicates an increasing valence state. EELS data revealed a high concentration of Ni^{2+} at the surface, indicated by the lower energy value of 852.9 eV, which is in good agreement with other studies [81, 149, 150]. With increasing depth from the surface, the concentration of Ni^{3+}, which peaked at 855 eV, [149], and Ni^{4+} increased before reaching equilibrium. At that stage, a layered structure with a minor defect rate was most likely reached. The EELS data showed the far-reaching defect density of the TM valence states. However, the recorded EELS data could not determine the specific location of the Ni^{2+}-ions, whether it was on the TM sites or the lithium-ion sites. However, it is clear that a measurable amount of Ni^{2+}-ions was present 42 nm into the bulk which likely deviated from the equilibrium state.

A comparison of the EEL spectra of a closed surface with that of the EEL spectra of an open surface revealed qualitative very similar result to that obtained with HR-STEM imaging. On the closed surface, the oxygen pre-peak collapsed only at the first atomic layers, which aligns with the observed rock salt formation in the

HAADF-STEM image. The shift of the Ni-L_3-edge extended up to 35 nm into the bulk, which was significantly deeper than suggested by the HAADF-STEM images. However, the defect density was less extensive than on the open surfaces, which qualitatively agrees with the observations from the HAADF-STEM results. In conclusion, the EELS results demonstrate that the layered structure was not fully intact for tens of nanometers. This observation highlights the need for an in-depth analysis to explore complex degradation mechanisms and emphasizes the strength of STEM imaging combined with analytical methods.

Quantifying the thickness of the rock salt layers as a function of time turned out to be impractical. This is mainly due to the complexity of the degradation behavior in Ni-rich NCM, in which the strength of rock salt formation was found to depend on the orientation of the crystal planes to the surface as well as the local conditions surrounding the particle. For these reasons, the usually limited number of TEM studies revealed a variety of different scenarios and did not provide a solid basis for obtaining a coherent quantitative result regarding the thickness of degradation layer. In addition, the transition from the layered structure to the rock salt structure appeared to be gradual and extended deeper into the particle than the apparent thickness of a pure rock salt layer would suggest. However, the experiments performed in this work provided a more detailed picture of the degradation process, which is summarized in a modified anisotropic core-shell model as shown in Figure 5.17. This model describes non-uniform surface degradation that is stronger at surfaces perpendicular to the layer directions and weaker where the surface is aligned to the basal plane or where the NCM particle is in contact with other NCM particles.

Overall, this study showed that for NCM831106, the rock salt layer at the top of the particle surfaces grew steadily, especially on open surfaces. The rock salt structure created a kinetic barrier for lithium diffusion which is supported by other studies [147, 152]. From the results obtained, it can be concluded that the formation of rock salt contributes significantly to the increase in charge transfer resistance. The initially raised question about the contribution of CEI formation to the charge transfer resistance was analyzed by other methods such as XPS and ToF-SIMS. These experiments were conducted by Steffen Schröder (JLU Gießen) and showed that the CEI formed at the beginning after the NCM CAM came into contact with the electrolyte [143]. The organic part of the CEI was observed to decrease over time, while the inorganic part increased slightly. In conclusion, the rock salt formation is very likely to contribute significantly to the increase in charge transfer resistance, while CEI plays a subordinate role in this aspect.

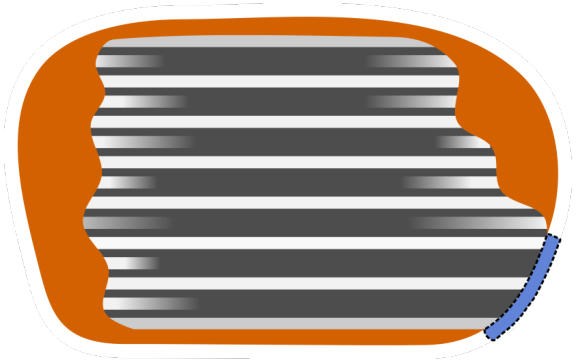

Figure 5.17.: An anisotropic core-shell model with a gradual transition boundary is suggested to visualize the phase transition from the intact layered phase to the rock salt phase at the surface in Ni-rich NCM. The rock salt layer is indicated by the red layer at the particle surface. The continuous light gray layers represent the TM lattice planes of the layered phase, which appear bright in an HAADF-STEM image. The gradual transition boundary, which is characterized by strong cation mixing, where lithium positions are occupied by TMs, which is indicated by light gray layers that smear out towards the core of the particle. The formation of a rock salt layer at the particle surfaces depends on the orientation and the surrounding of the particle (blue), such as a protection layer or another particle.

5.3. Thermal instability of protonated NCM

Washing of NCM powder after synthesis in water is an essential step in industrial manufacturing. Washing removes synthesis residuals and surface contaminants, thus improving the processability, performance, and safety of the battery. However, washing NCM powder in water leads to an ion-exchange of Li^+/H^+ at the surface, and protons from the water solution are incorporated into the layered structure [33]. After the washing step, the material is dried at elevated temperatures. Pritzl *et al.* observed that upon heating oxygen is released from a layered structure, and an oxygen depletion layer forms at the surface, leading to a significant increase in impedance. The oxygen-depletion layer can be partially regenerated by an additional calcination step at elevated temperatures just below the synthesis temperature (approximately 700 °C to 800 °C) under constant oxygen flow. However, this process correlates with high costs and resource demands. In order to achieve an optimized and cost-effective washing and heating procedure, the process parameters need refinement, including the process time, the amount of water, the oxygen partial pressure, and the recalcination temperature. This requires a deeper mechanistic understanding of the washing process, which can only be gained through focused research efforts.

In cooperation with the project partners of TU Munich and the industrial partner BASF, an academic study was designed to investigate the mechanisms and degradation that occur during the washing procedure and the subsequent heating. The main research questions were:

- What level of ion-exchange is reached as a function of water:NCM ratio and wash time?
- Does a rock salt phase form on the surface, and at what temperature?
- If a rock salt phase can be observed, is there also an intermediate transformation via a spinel phase?
- Can the level of exchanged ions be correlated with the thickness of a rock salt layer at the surface?

To address these objectives, a single crystalline, Ni-rich NCM ($LiNi_{0.83}Co_{0.12}Mn_{0.05}O_2$) powder, provided by BASF, was washed under harsher conditions than those used in industry to amplify the effects occurring during the washing procedure and, therefore, allow us to better study structural and chemical changes. The NCM powder was washed in degassed water with a ratio of 25:1 (water:NCM) for 55 hours at 80 °C under constant stirring. A proton concentration of approximately 25 mol% was confirmed. The project partners from TU Munich focused on the quantification of protons, applying different methods such as thermogravimetric analysis (TGA), (time-resolved) XRD, XPS, and titration. More detailed information can be found

in the corresponding publication by Oswald *et al.* [34].

Within the scope of this thesis, (high-resolution) HAADF-STEM measurements and EDX analysis were performed to investigate the phase transition from the layered structure to the rock salt structure and potential intermediate phases. Based on the results of the TGA (Figure 5.18), which indicated the release temperatures of H_2O and O_2 at approximately 140 °C and 230 °C, respectively, a set of four samples was selected. This set of samples included a reference sample, which was the pristine NCM powder after synthesis, as well as samples washed and heated up to 65 °C, 180 °C and 300 °C, respectively. The initial objectives of the TEM study were to address the second to fourth questions previously mentioned by investigating structural changes on the surface and measuring the thickness of the surface degradation layers.

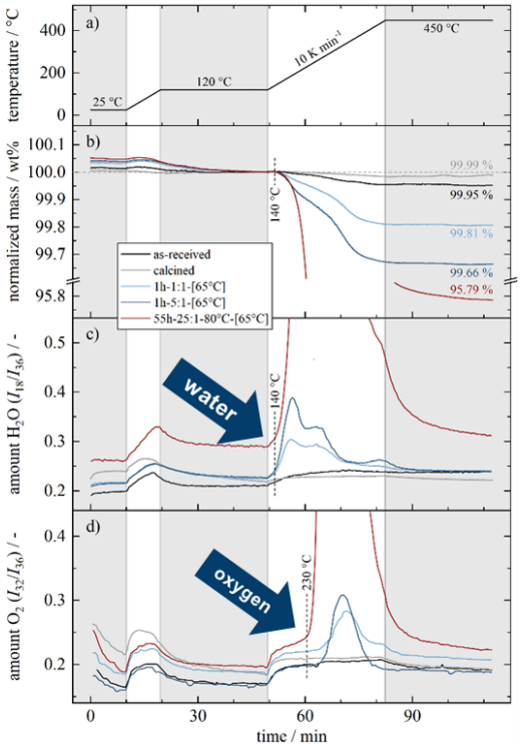

Figure 5.18.: TGA results of as-received (black), calcined (at 525 °C under O_2, gray) and washed Ni-rich NCM samples (dried at 65 °C). The washed samples were treated under different conditions as indicated in the figure (washing time-water:NCM-washing temperature-[drying temperature]. (a) Temperature profile. (b) Relative NCM mass, normalized to the mass at the end of the temperature hold at 120 °C. (c) Amount of water and (d) amount of oxygen normalized to that of argon. The figure was taken from [34].

5.3.1. Nanostructural analysis

Figure 5.19 shows the microstructure of the four investigated samples. The pristine sample and the sample washed and heated to 65 °C displayed similar smooth and uniform cross-section surfaces. In contrast, the washed and heated to 180 °C sample showed first changes at the nanostructure level. While the particle core retained its smooth and even appearance, a notable change in intensity was evident on the surfaces and grain boundaries. Darker regions appeared at the particle surfaces, which exhibited a sponge-like morphology. As discussed in Section 3.2, a lower intensity in an HAADF-STEM image indicates a change in thickness or a change in the composition of materials because the HAADF contrast correlates approximately with the accumulated atomic core charge illuminated by the STEM probe. The degraded areas in the particles reached a thickness of 5 nm to 25 nm. Although most of the investigated particles exhibited alterations in contrast at their surfaces and grain boundaries, this was not universally observed across all particles. Samples washed and heated to 300 °C showed significant changes in the nanostructure, as shown in the examples displayed in Figure 5.19d. Contrast variations were observed not only at the particle surfaces and the grain boundaries but also within the particle core. A more detailed examination revealed two notable findings. First, alterations in nanostructure varied between the particles, as illustrated in the magnified image panels Figure 5.19e and f, corresponding to image Figure 5.19d. Some particles retained smoothly intact regions at the nanoscale, whereas others displayed a sponge-like morphology interspersed with darker zones across the entire particle. Second, various types of defects were identified, including pores, linear features, and repetitive line patterns. While a detailed analysis will be presented later, it is evident that the nanostructure of the washed and heated to 180 °C and 300 °C underwent significant degradation.

To understand the origin of the contrast alteration and thus the effects of washing and subsequent heating, HAADF-STEM imaging was performed at higher magnifications in combination with STEM-EDX analysis on the sample washed and heated to 300 °C. Figure 5.20a shows an HAADF-STEM image revealing the following observations. First, the low contrast and sponge-like morphology resulted from the formation of nanopores and other planar defects, such as the lines visible in the image. Second, the planar defects were additionally surrounded by nanopores. Third, at the edges or surfaces of the nanopores, the intensity increased above average, leading to a bright appearance. This strongly evidenced rock salt formation in Ni-rich NCM, as detailed in Section 5.2.2. However, the proportion of a bright seam around the nanopores was significantly smaller than the area of the nanopores, which can be attributed to two reasons. Reason one: the light seam might not be visible in all areas because of dynamic scattering effects on the HAADF signal. Reason two: previous studies (Section 5.2.2) have shown that only a fully rock salt phase produces a high contrast difference. Consequently, it may be concluded that a mixed form of the layered structure and the rock salt structure was prevalent across large

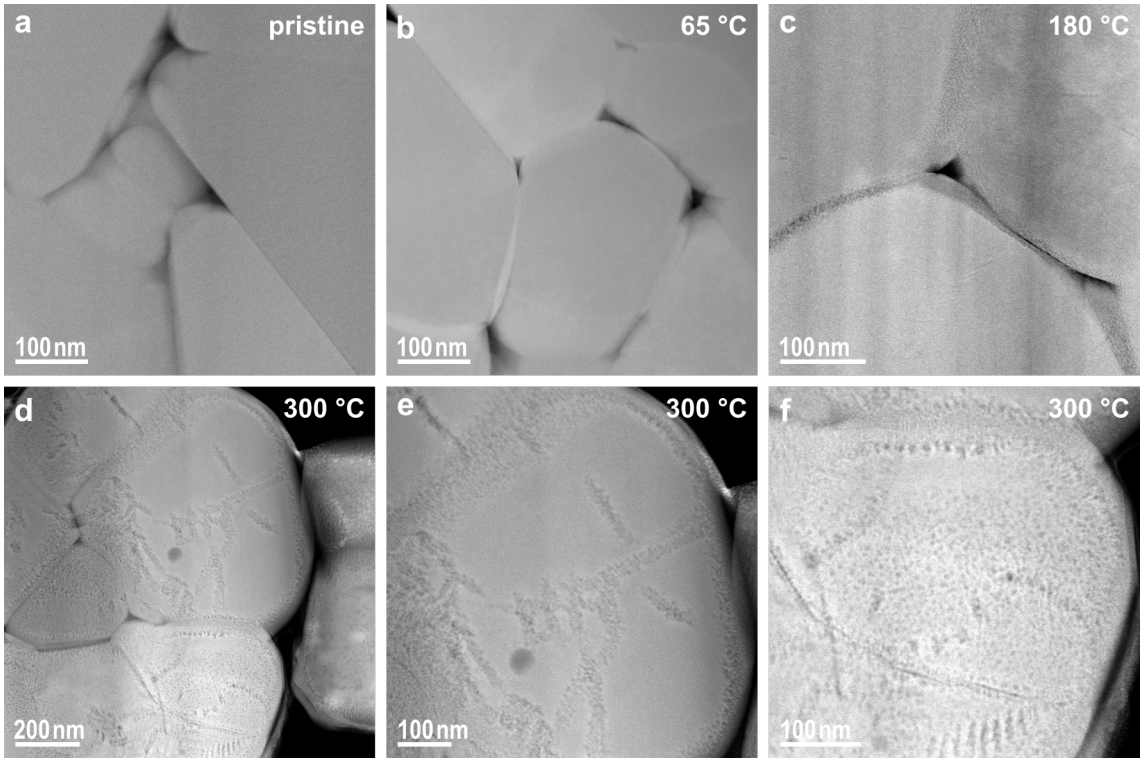

Figure 5.19.: HAADF-STEM images showing Ni-rich SC-NCM before and after different washing and heat treatments. (a) pristine sample. (b)-(f) samples washed for 55 hours in a ratio of 25:1 (water:NCM) at 80 °C and then subsequently heated to (b) 65 °C, (c) 180 °C and (d)-(f) 300 °C. Zones of dark, sponge-like features in (c)-(f) indicate increasing amount of nano-structural defects with rising temperatures.

areas of the sample.

The overlaid EDX maps of nickel and oxygen in Figure 5.20b indicate that the material was absent at locations with low HAADF signal intensity and that the surface of the defect structures was oxygen-depleted. Although absorption of oxygen in the EDX signal might distort the result, the line scan over the area marked on the map clearly demonstrates that the ratio of nickel to oxygen underwent a considerable change across the planar defect as highlighted in the plot in Figure 5.20c. The observed change in the ratio was qualitatively aligned with the intensity fluctuations observed in the HAADF signal.

In summary, the STEM results demonstrate that the degradation of the material after washing and heating to elevated temperatures was not limited to the surface, but also included clear core degradation. The presented data provide substantial evidence for volume reduction at the surface of the particle and within the core, as well as oxygen depletion at the surface of the nanopores. Although the precise

degradation mechanism has not yet been fully elucidated, it is known from the TGA results that water was fully released and oxygen was partially released upon reaching 300 °C. Therefore, it could be hypothesized that the formation of nanopores is closely linked with the release of oxygen, especially considering that the phase transformation from the layered structure to the rock salt structure is usually accompanied by the release of oxygen leading to a reduced volume.

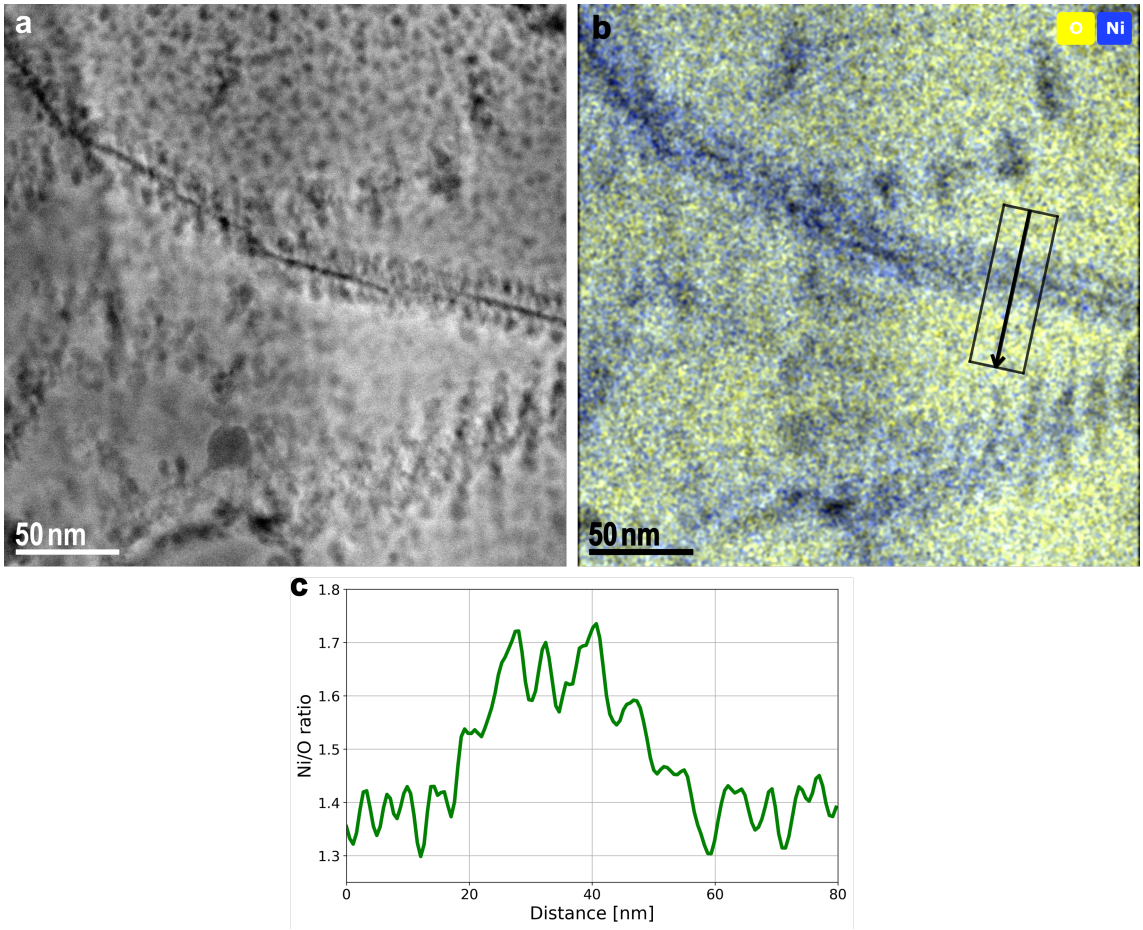

Figure 5.20.: HAADF-imaging combined with EDX-measurements to analyze nanopores. (a) HAADF-STEM image revealing several types of defects including nanopores, repetitive patterns and lines which were closely surrounded by nanopores. The intensity was weak at the nanopores but increased above average at their surface or edge. (b) STEM-EDX confirming a notable increase in the nickel to oxygen ratio (Ni/O) at defect edges, as shown in (c).

5.3.2. HR-STEM analysis

HR-STEM imaging is a further building block in understanding the impact of washing and the induced degradation processes at the atomic scale upon washing and subsequent heating. Figure 5.21 shows the atomic structure of a pristine sample that had not undergone any post-treatment after the synthesis step. Observations on the atomic scale indicated a layered structure; however, the surface exhibited a degradation layer of approximately 2 nm thickness. The formation of the degradation layer was anticipated to some extent due to surface impurities originating from the synthesis process and brief exposure to air, which can lead to the collapse of the layered structure on the outer surface. While the layered substructure was preserved after washing and heating to 65 °C, and looked similar to the pristine sample, significant changes of the atomic structure were observed after heating to 300 °C.

The degradation layer formed partly due to surface impurities from synthesis and brief air exposure, which can collapse the outer surface's layered structure.

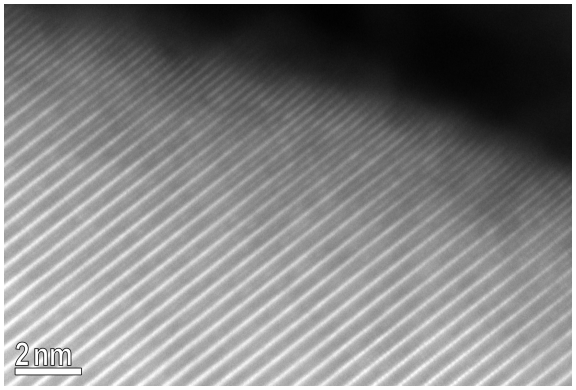

Figure 5.21.: HR-STEM image showing the surface a particle from a pristine sample. A thin degradation layer at the surface was visible, which was anticipated to some extend because after synthesis no further treatment was conducted and surface impurities remained.

As shown in Section 5.3.1, the nanostructure gradually degraded after heating of the washed samples. The severe degradation made atomic resolution imaging of these samples extremely challenging. One reason was that the zone axis was changing over a very small region of a few tens of nanometers, which made it difficult to tilt the particle into a low-index zone axis. The shift of the orientation angle of the zone axis might, for example, result from strain induced by nanopore formation. However, in a few examples, it was possible to tilt a larger area into a low-index zone axis. Constant adjustments of the tilt angle were required to map an entire region.

Figure 5.22a shows the surface of a particle and clearly reveals the degraded nanostructure with the formation of nanopores of different degrees, from a sponge-like

appearance to significant voids. A sponge-like layer formed at the surface followed by a more intact layer towards the core of the particle, which was soon interrupted by further degradation of the nanostructure. The layer at the top of the surface indicated by a brighter contrast was a redeposition layer of the platinum protection layer originating from the FIB preparation. The HR-STEM images presented in Figure 5.22b and c indicate that a rock salt layer formed on the outer surface, followed by a gradual transition boundary that became increasingly layered towards the core of the particle. The presence of rock salt on the surface (red square) was confirmed by analyzing the corresponding Fourier spectrum presented in Figure 5.22d following the description outlined in Section 5.1.3. The rock salt phase was oriented along the [110] zone axis. The Fourier spectrum of the gradual transition boundary region (blue square) clearly shows the overlap of the rock salt structure oriented in the [110] zone axis with the layered structure oriented in the [100] zone axis. No hint of spinel formation was evident.

The rock salt layer at the surface visible in Figure 5.22b was estimated to be $18 \pm 2\,\mathrm{nm}$. However, this is highly localized information and should be treated with caution. For a more general statement, more data are needed. Furthermore, the data analysis presented in Section 5.2.2 emphasizes that the gradual transition boundary is often not linear and it is difficult to determine exact thickness values due to local alternations in the nanometer range. Such alternations can also be seen in those HR-STEM images.

Figure 5.23 shows areas with nanopores in the core of the particle. The images shown aim to provide more insight into the atomic structure around nanopores and to check if the hypotheses made in Section 5.3.1 were confirmed. The images were acquired from a sample that was previously used for computer tomography measurements before a lamella was cut from the pillar which was exposed to air for several days. However, since the sample was already degraded and a layer of rock salt had most likely formed on the surfaces, the inner part of the pillar from which the lamella was cut just prior to the STEM experiment should have been sufficiently protected from the effects of air. Therefore, no significant changes in the TM structure of the examined lamella were expected.

Figure 5.23a and the corresponding magnified area shown in Figure 5.23c show the atomic structure over a nanopore. Significant occupancy of the lithium positions by TM was observed. As an HAADF-imaging is a 2D-projection of the lamella, it was not possible to determine where the signal originated from in the 3D crystal structure. However, it became clear that a highly disordered layered structure was present. The other pair of images shown in Figure 5.23b and d, acquired within the same particle as the first pair of images, revealed that the structure around a nanopore changed to a rock salt structure. The surrounding structure remained in a layered structure with a high disorder of TMs occupying lithium positions. Overall, the data show that no perfect layered structure remained after washing

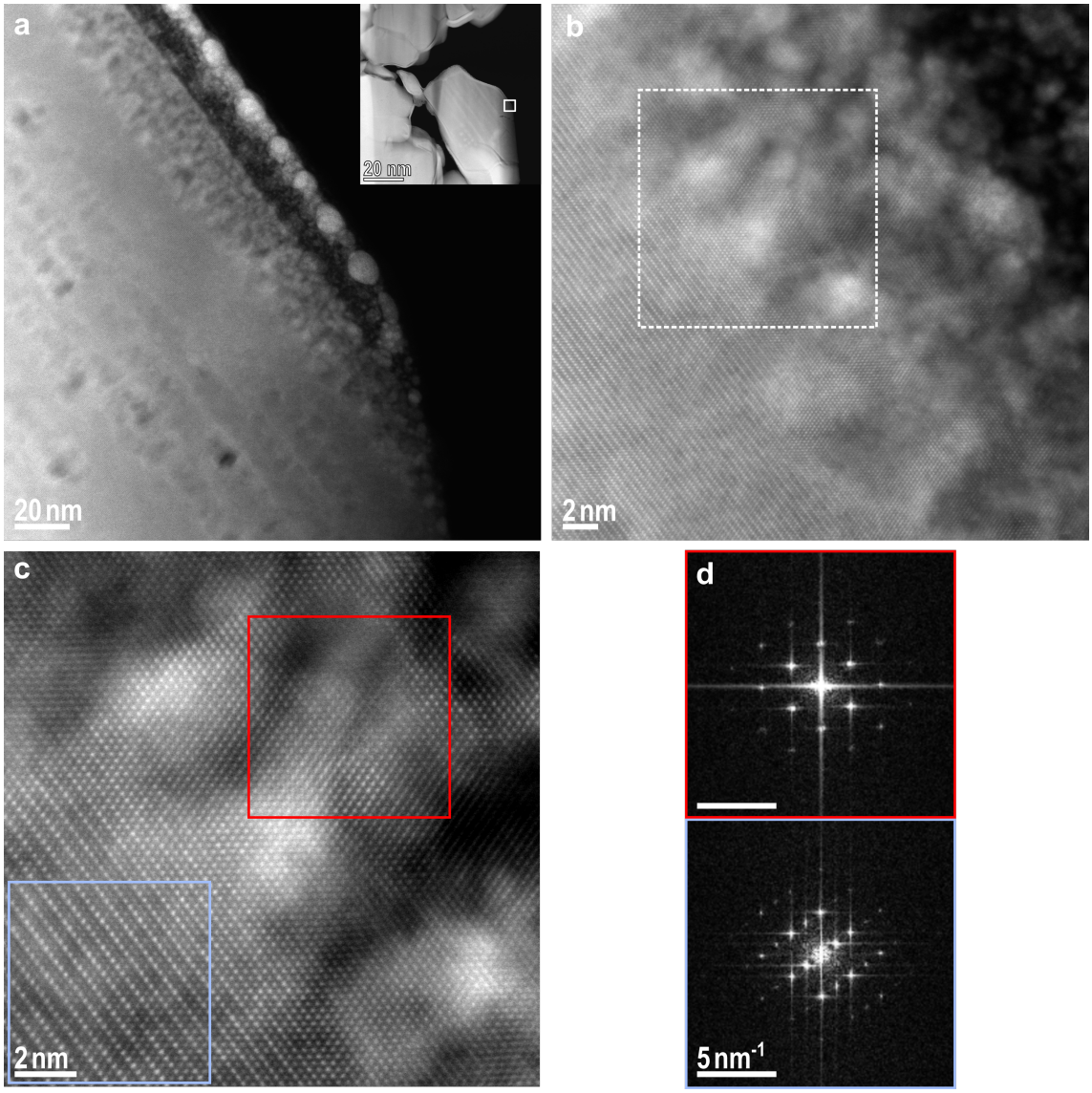

Figure 5.22.: HAADF-STEM images at different magnifications of the washed and heated to 300 °C NCM powder. (a) Particle surface revealing distinct nanopore formation. This area was thin enough for further investigation and is marked by white square in the inset at medium magnification. The inset shows the entire particle and its arrangement in the lamella. (b) HR-STEM image of the surface area. (c) Enlarged image of area indicated by a dashed square in (b). (d) Fourier spectra of the indicated areas in (c) highlighting that a rock salt phase along the [110] zone axis (red square) formed at the surface which transferred to a layered structure along the [100] zone axis via a gradual transition boundary resulting in an Fourier spectrum where two phases overlap (blue square).

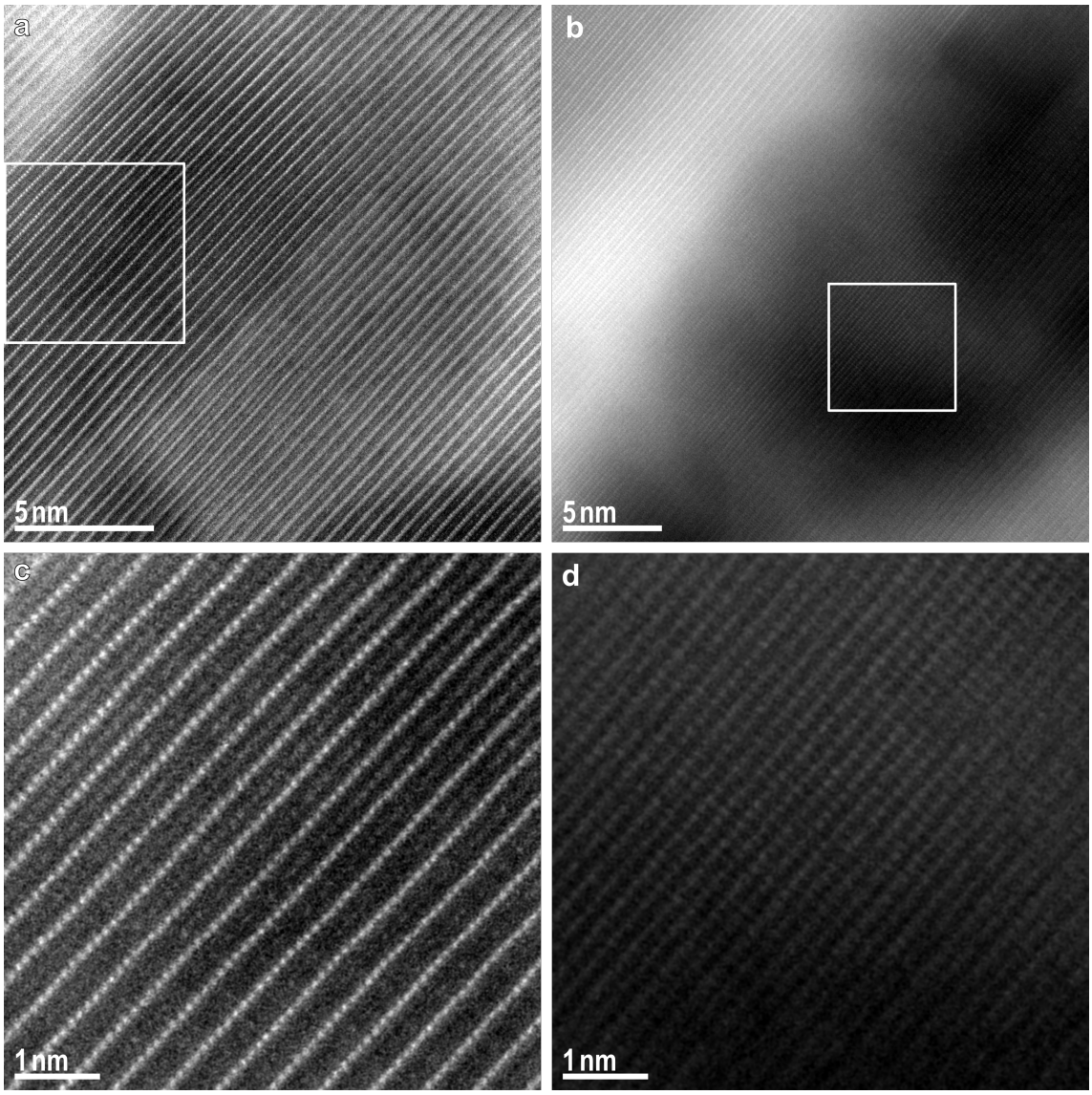

Figure 5.23.: HR-STEM images showing the atomic structure of nanopores in the core of a particle washed and heated to 300 °C. (a) and (b) HAADF-STEM images with white square indicating the enlarged images presented in (c) and (d), respectively.

and subsequent heating to 300 °C in the core of a particle. Furthermore, HR-STEM analysis of the nanopores revealed that a rock salt phase was likely formed around a nanopore, which aligns with the observations and hypothesis made based on data on the nanoscale in Section 5.3.1.

5.3.3. *In situ* heating experiments

Subsequent to the *ex situ* experiments, two *in situ* heating experiments were carried out to further study the volume degradation including nanopore formation. The first *in situ* heating experiment was performed on a washed sample, while the second *in situ* experiment was performed on a pristine sample to assess the influence of washing.

The results of the first *in situ* experiment on the washed sample are presented in Figure 5.24. Figure 5.24a-h illustrate the images captured at the end of each heating stage after the set temperature was reached and kept for 5 min. The defect structure which can be identified at 100 °C, particularly in the large grain on the left, was already observed in the material prior to the start of the heat treatment. The initial subtle modifications in the HAADF contrast were detected at 150 °C, manifesting as small, cloud-like formations. Further notable alterations were observed when the temperature was increased from 400 °C to 450 °C, as the defect structure became more pronounced. This observation is consistent with the results of another *in situ* heating experiment conducted with the same sample using a different microscope. The formation of nanopores was clearly observed at 550 °C and became even more pronounced at 600 °C. At 600 °C temperature, nanopores had formed not only along the defect structures and grain boundaries, but also within the core of the particles. This observation is consistent with the *ex situ* experiments under similar conditions. Figure 5.24i presents an image acquired at 600 °C from an area of the lamella that had been sparsely irradiated before. This control image was acquired to check whether the continuous electron beam exposure of the sample area in Figure 5.24a-h had caused significant damage to the nanostructure. The control area also exhibited strong degradation of the nanostructure, including nanopore formation, due to heating. However, it should be noted that not all particles in the control area showed equally pronounced nanopore formation in the core of the particle as in the area which was exposed to the electron beam during heating. In the *ex situ* experiments some particles showed strong core degradation while others still exhibited smooth cross section surfaces at the nanoscale as evident in Figure 5.19d-f. Therefore, the relatively uniform formation of nanopores, which formed in the long exposed area, could arise from irradiation during the *in situ* experiment, intensifying the effect under investigation. This cannot be conclusively clarified on the basis of the available data.

The results of the second *in situ* experiment on the pristine sample are presented in Figure 5.24.Figure 5.25a-h shows images of each step during the heating process,

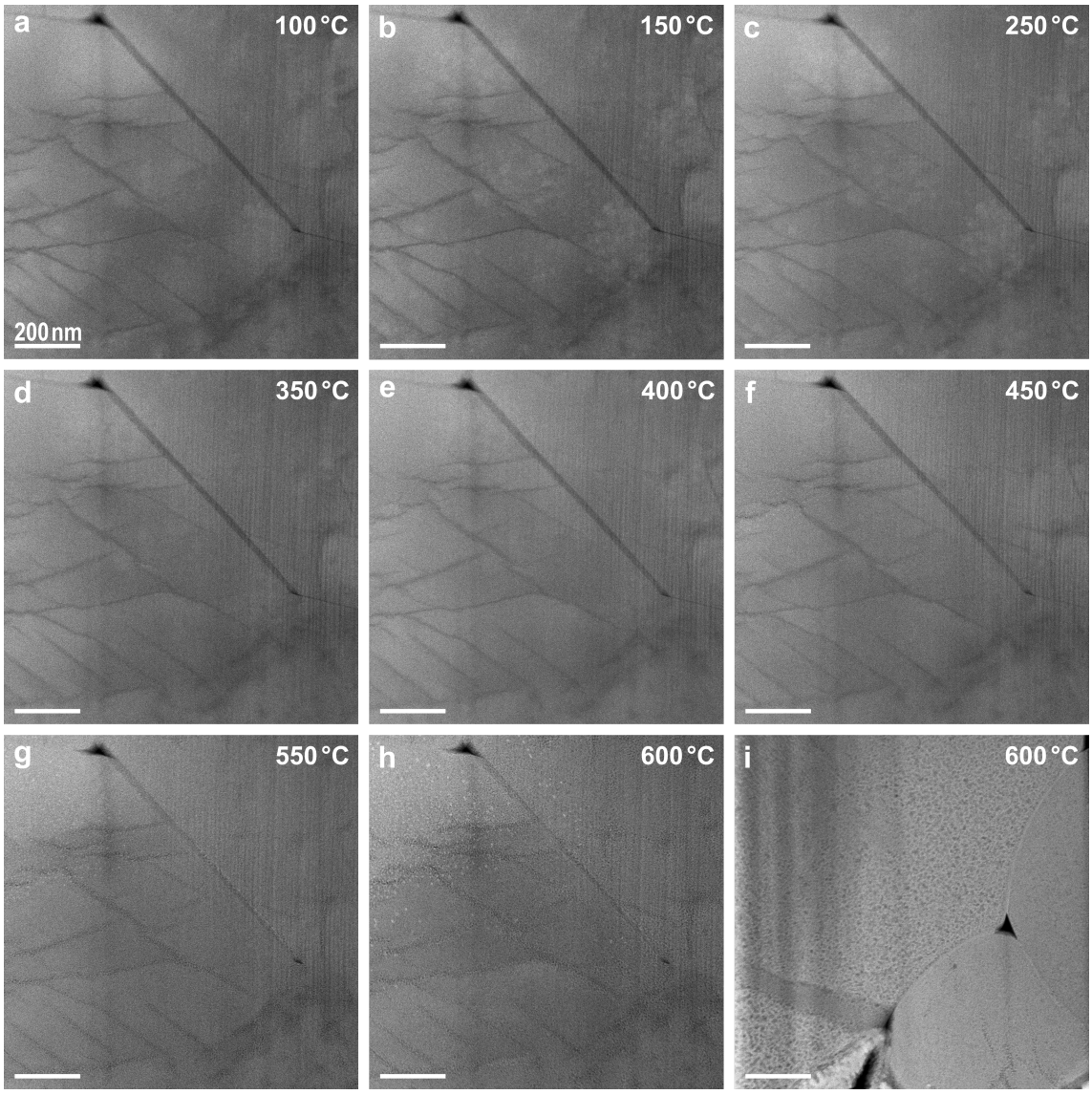

Figure 5.24.: *In situ* heating of a washed sample in a STEM under high vacuum. The heating rate was 1 K/sec with a 5 min temperature hold before proceeding to the next temperature hold. (a)-(h) HAADF-STEM images recorded during heating and thus constantly exposed to the electron beam. (i) HAADF-STEM image of an area which was not constantly exposed to the electron beam showing a similar behavior compared to (h). With increasing temperature, nanopore formation started at the surfaces of particles, grain boundaries and defects before also the cores of the particles were affected by degradation.

after a stabilization period of 5 min once the target temperature was reached. The two pores, which were present from the beginning, were defects that arose from the synthesis. First, slight changes in the nanostructure could be recognized at 350 °C where the appearance of the particle, in particular in the lower left corner, started to become uneven. The formation of nanopores at the grain boundaries was identified at 450 °C. As the temperature increased, the formation of nanopores was also observed at subgrain boundaries, notably in the particle located in the lower right corner, as well as at internal defects, such as the small-angle grain boundary that became more pronounced at 600 °C by the formation of nanopores along the interfaces. Figure 5.25i presents an area which was not illuminated during the recording of images while heating. The image was taken at 300 °C after heating to 600 °C. The presented area showed a behavior similar to that of the constantly illuminated area, where subtle nanopore formation occurred partially at the surfaces and subgrain grain boundaries.

The presented *in situ* heating experiments reveal that both the pristine and the washed samples experienced degradation characterized by nanopore formation. However, the temperature at which the first significant changes occurred differed clearly. Significant changes were observed in the washed sample at 450 °C, while the pristine sample exhibited these changes at 550 °C. Moreover, the extent of nanopore formation varied between the two samples. The pristine sample exhibited nanopore formation predominantly at the particle surfaces and along intrinsic defect structures, such as sub-grain boundaries. In contrast, the washed sample demonstrated more pronounced nanopore formation, extending to the core region of the particle.

The results of the washed and gradually heated sample were found to be qualitatively in agreement with those of the *ex situ* experiments. However, the extent of the observed degradation of the nanostructure at 300 °C in the *ex situ* experiment was only discernible at 450 °C in the *in situ* experiment. Therefore, direct comparison of precise temperature values is not feasible. The discrepancy in the onset temperature may be attributed to the disparate temperature holding times employed in the two experiments. For the *in situ* experiment a holding time of 5 minutes was applied, whereas for the *ex situ* heating process a holding time of 1 hour was utilized. Furthermore, the lamella was exposed to vacuum heating while mounted on a heating MEMS chip, whereas the powder used for the *ex situ* experiments was heated under an argon atmosphere, with the surrounding atmosphere reaching the set temperature.

The *in situ* experiments confirmed that nanopore formation was a direct consequence of heating, rather than a result of FIB preparation. Compared to the *ex situ* experiments, the order of treatments was reversed. For *ex situ* experiments, the samples were first washed and heated before they were prepared by FIB. In contrast, for the *in situ* experiments, the sample was washed, prepared by FIB and then heated. While the quantity of nanopores increased gradually with elevated temperature in the *ex*

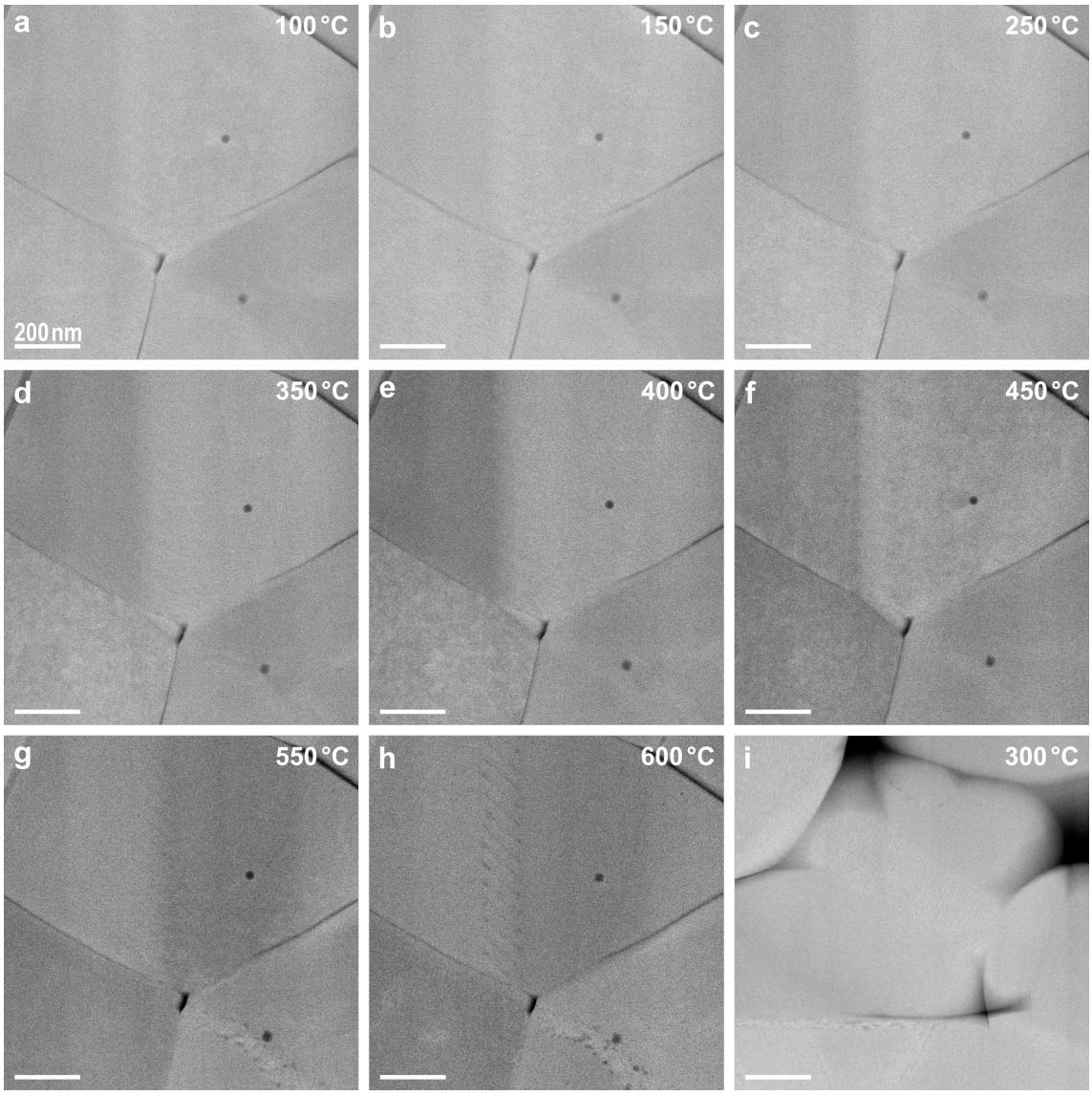

Figure 5.25.: *In situ* heating of a pristine sample in a STEM under high vacuum. The heating rate was 1 K/sec with a 5 min temperature hold before proceeding to the next temperature hold. (a)-(h) HAADF-STEM images representing an image set of the recorded area during gradual heating which was constantly exposed to the electron beam. With increasing temperature nanopores formed at the particle surfaces, grain boundaries and along initial defect structures. Significant changes started to occur at 550 °C. (i) HAADF-STEM image which was not constantly exposed to the electron beam. After heating to 600 °C, it was recorded at 300 °C and shows equivalent nanopore formation at particle surfaces and subgrain boundaries as observed in (h).

situ experiment series, with no indication that FIB was the source, the *in situ* experiments demonstrated unambiguously that nanopore formation was a consequence of heating. However, the lamella shape of the sample altered the experimental setup compared to the shape of the *ex situ* samples as two new, additional large surfaces were created before the sample was heated.

5.3.4. Discussion of the results

In this section, we discuss the results of the STEM investigations and classify them according to the findings presented in Oswald *et al.* [34]. First, washed and heat-treated Ni-rich NCM powder underwent significant structural degradation upon heating in form of phase transition from the layered to the rock salt phase and nanopore formation, which was proven by STEM imaging and spectroscopy. In contrast to the other techniques employed and documented in the publication, TEM measurements demonstrated that degradation occurred not only on the surface, but also significantly affected large regions within the core of the particles. The volume degradation on the surfaces and in the core structure was substantial and was clearly visualized by STEM measurements. This finding presents novel insights that diverge from the previously assumed core-shell model, in which degradation appears only at the surfaces, while the core structure remains in the layered phase.

We hypothesize that the observed nanopore formation which results in volume reduction was caused by the release of water and oxygen. In the *ex situ* STEM experiments, structural changes due to the formation of nanopores at the surface and grain boundaries were observed in the sample heated to 180 °C, which occurred after the release of water had started. At 300 °C, where TGA results indicated a significant release of oxygen from the structure, nanopore formation was observed not only at the surfaces, grain boundaries, and defects within the core, but across whole particles. The diffusion of oxygen typically occurs through oxygen vacancies. Furthermore, oxygen becomes more mobile at elevated temperature. Therefore, nanopore formation extending deeply into the core of the particle, as observed in the *ex situ* sample heat-treated to 300 °C, is a reasonable consequence of the accelerated oxygen diffusion due to increasing temperature and growing number of oxygen vacancies. Although other researchers have investigated thermal degradation and the role of oxygen diffusion in Ni-rich NCM (without focusing on washing) [45,153–155], and observed nanopore formation, the underlying mechanism is not yet clear.

The XPS results presented in the aforementioned publication suggest that the ion-exchange between lithium and hydrogen ions occurs only at the surface. However, the reason for such surface-limited ion-exchange has not yet been fully understood. Assuming that the ion-exchange is limited to the surface of the particles, the pronounced core degradation observed by STEM, which is inherent to the material and not an artifact of sample preparation as previously explained, may result from an escalating number of oxygen vacancies caused by water release. Consequently, these

oxygen vacancies drastically decrease thermal stability. Thus, core degradation may be interpreted as an indirect consequence of the washing process. The STEM results neither confirm nor reject the conclusion drawn from the XPS experiments, as no information about the location of hydrogen ions or a potential lithium gradient can be determined from the available data.

The *in situ* heating STEM experiments support the observations made in the *ex situ* STEM measurements. These experiments clearly visualized that nanopores formed first on surfaces, grain boundaries, and defect structures before the core structure was affected. The *in situ* STEM experiment provided valuable information on the structural degradation on Ni-rich NCM caused by thermal treatment. Qualitatively, the findings regarding the formation and localization of nanopores were comparable to those identified in the washed sample. However, the onset temperature and severity differed distinctly between the pristine and washed materials, which is consistent with the TGA and XRD results. As observed in the cited study and another publication [156], unwashed Ni-rich NCM is thermally stable beyond 600 °C. Nevertheless, nanopore formation was observed in the pristine and heated samples at approximately 550 °C, a temperature at which Ni-rich NCM is expected to remain stable. The lower onset temperature for thermal degradation in a pristine sample may be attributed to the experimental setup. In the *in situ* STEM experiment, a thin lamella was heated, possessing a higher surface-to-volume ratio than bulk particles. Consequently, it could be assumed that oxygen was more readily released from the structure and subsequently evaporated into the vacuum even at lower temperatures. In conclusion, the *in situ* experiments provide further insight into the thermal degradation of Ni-rich NCM and demonstrated that nanopore formation also occurred in the pristine sample and corresponded to that of the washed material. The *in situ* data did not disprove the aforementioned hypothesis that ion-exchange only takes place at the surface but rather support it as they indicated that nanopore formation is a general indicator of thermal degradation in Ni-rich NCM.

Oxygen release not only leads to the formation of nanopores but also plays a crucial role in the formation of the rock salt phase. In response to the initial questions, the atomic structure at the surface of the particle and the nanopores was also investigated. The strong degradation on the nanoscale made HR-STEM imaging immensely challenging. However, the few examples clearly showed that rock salt formed on the inner and outer surfaces of the NCM particles. Since a rock salt phase has been identified at the surface, the third and fourth questions initially raised need to be discussed. Was there an intermediate spinel phase present and how thick was the rock salt layer?

To verify the postulated spinel phase as an intermediate phase that occurs during the phase transition from the layered to the rock salt phase, XRD and TEM measurements were performed. XRD measurements provide global information on the crystal structure and phase transitions of a bulk sample. The XRD results are

presented in detail in the referenced paper and therefore only the key observations are briefly summarized here. *In situ* temperature-resolved XRD was performed up to 450 °C. No evidence for the formation of an intermediate spinel phase could be found in either the washed nor the pristine sample upon heating. However, clear evidence of rock salt formation at 230 °C is indicated in the washed sample by a shift in reflections. To gain more quantitative information on the phases, *ex situ* XRD spectra from samples of critical temperatures were collected, and Rietveld refinement was applied. The results are presented in Figure 5.26. Despite the challenge that the angles at which characteristic reflections occur are very close or even overlap for the layered phase and the rock salt phase of NCM, a rock salt phase could be detected as shown in Figure 5.26a. No evidence of a spinel phase or a separate, stable HMO_2 phase was observed. The amount of rock salt phase increased from 3 % at 180 °C up to 24 % 450 °C as indicated in Figure 5.26c. Although in TEM, minor surface degradation was already observed in the pristine sample, the detection limit of the XRD measurement was too low to capture these small changes in the crystal structure. Nonetheless, the findings of the *in situ* time-resolved XRD and the *ex situ* XRD are in good agreement with the TEM observations because no evidence for spinel formation was observed. Furthermore, an increased Li^+/Ni^{2+} disorder in the washed sample was measured by XRD with increasing temperature. This finding is consistent with the observation made in TEM, in which the sample heated to 300 °C exhibited significant cation mixing across the entire particle and in the gradual transition boundary between the layered and the rock salt phase at the particle surface. The final point to be made in this comparison is that volume degradation was observed in TEM. The XRD results did not preclude the possibility because this method does not provide any local information, making it impossible to distinguish between the core and shell of the particles using XRD.

Finding a clear answer to the fourth question, whether there is a systematic relation between the rock salt layer thickness and the amount of exchanged Li^+/H^+ ions, turned out to be difficult based on the STEM data. For a given exchange volume, a strong local variation of the layer thickness was observed across all samples in this study, meaning thickness measurements depend on the position where they have been performed. As discussed previously in Section 5.2.2, the gradual transition boundary between rock salt structure and layered structure varies greatly in extent and shape. Furthermore, degradation was observed not only at the surface but also within the core of the particle. This means that the microscopic observations deviate strongly from the homogeneous assumption of the model proposed in [34]. A single layer thickness measurement of 18 ± 2 nm agreeing with the model might be coincidental. It may well be that on average over an entire sample there is a correlation between layer thickness and exchange volume. However, in order to support this hypothesis, a systematic study has to be performed in which the exchange volume is varied and the layer thickness is measured at a sufficiently large number of particles to provide a solid statistical basis.

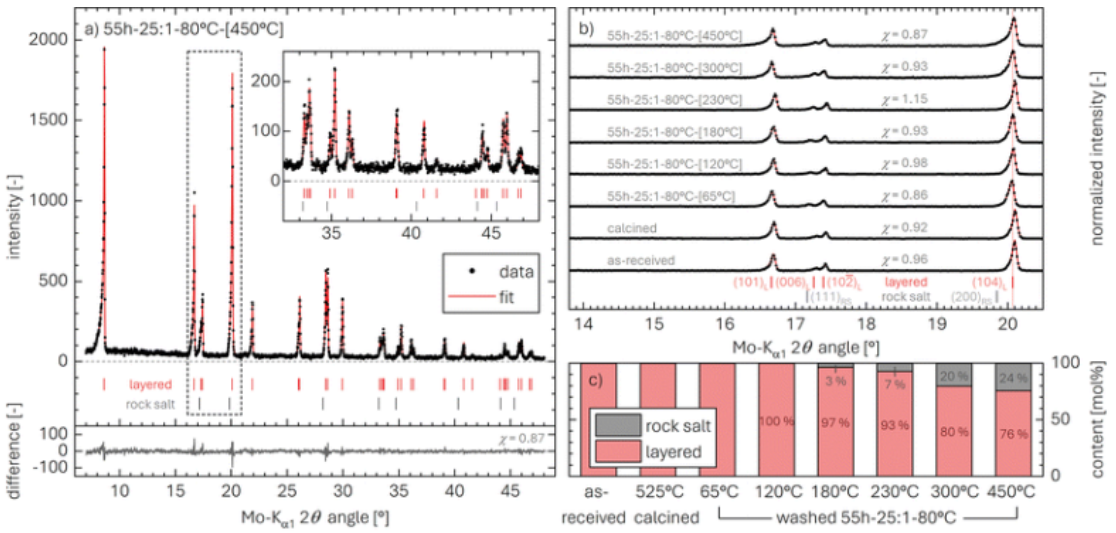

Figure 5.26.: *Ex situ* XRD diffractograms (black data points) and fit of Rietveld refinement (red line) showing the evolution of rock salt formation upon heating. (a) Diffractogram of a washed and heated to 450 °C with indication of the peak positions in the layered and the rock salt structure. (b) Diffractograms with an selected 2Θ angle range of as-received, calcined and various washed and heated samples. (c) Estimation of ratio of layered and rock salt phase. No spile phase was observed. The figure was copied from [34].

5.4. Al_2O_3 surface coating to prevent degradation

The application of coatings on the surface of NCM particles is a common strategy to mitigate surface degradation during battery cycling. Although a coating may lower the initial capacity, it enhances cathode stability, thereby mitigating aging and eventually improving performance over time. Commercial Ni-rich cathode materials are usually coated. Several studies have shown that a homogeneous and thin Al_2O_3 coating (below 2 nm) is essential to achieve a positive impact [157, 158]. However, the structural properties and behavior of applied coatings during cycling remain poorly understood and a few publications have been published on this topic [159]. The anisotropic volume change during cycling and contact with the electrolyte affect the structural stability of coatings. To optimize Ni-rich NCM batteries, especially for long-term applications, closer investigation on coatings and their cycling behavior is needed.

In collaboration with the project partner of JLU Gießen, we investigated PC-NCM and also PC-LNO, a material with similar expansion behavior, both coated with Al_2O_3. The cathode particles were coated with a variety of thicknesses of Al_2O_3 layer deposited by atomic layer deposition (ALD). The TEM work focused on the following three objectives:

- Validation of coating thickness and homogeneity by STEM-EDX, which is essential for the interpretation of electrochemical data.
- Investigation of structural integrity before and after cycling by STEM-EDX.
- First test of *in situ* biasing setup to study dynamical changes of the coating structure during cycling.

The following sections address the aforementioned objectives and present representative data for PC-NCM or PC-LNO coated with 15 ALD cycles. Each ALD cycle was expected to deposit a layer of Al_2O_3 with a mean thickness of 0.1 nm, resulting in a coating layer with a total thickness of 1.5 nm.

5.4.1. Verifying the quality and thickness of the Al_2O_3 coating

As mentioned in the introduction, the thickness of the layer is a crucial parameter that affects the electrochemical behavior. Therefore, it is crucial to verify the thickness and homogeneity of the coating layer, as exemplarily shown in Figure 5.27. The HAADF-STEM image in Figure 5.27a displays a coated surface of PC-NCM, where the Al_2O_3 coating is identified as the thin dark layer on the particle surface. This can be clearly seen by comparing the HAADF-STEM image in Figure 5.27b with the Al-K map in Figure 5.27c. The thick and brighter layer on top of the coated PC-NCM surface is the platinum protection layer remaining from the FIB preparation. Despite the rough surface, the coating layers appear homogeneously deposited

by the ALD process and tightly bonded to the particle surface. The Al_2O_3 layer exhibited a projected thickness of approximately 10 nm, measured on several particles, which differs significantly from the presumed thickness of 1.5 nm. The tendency of underestimating the layer thickness based on the ALD process parameters was observed across several samples. This indicates that layer thickness measurements should be performed before correlating coating thickness with electrochemical data.

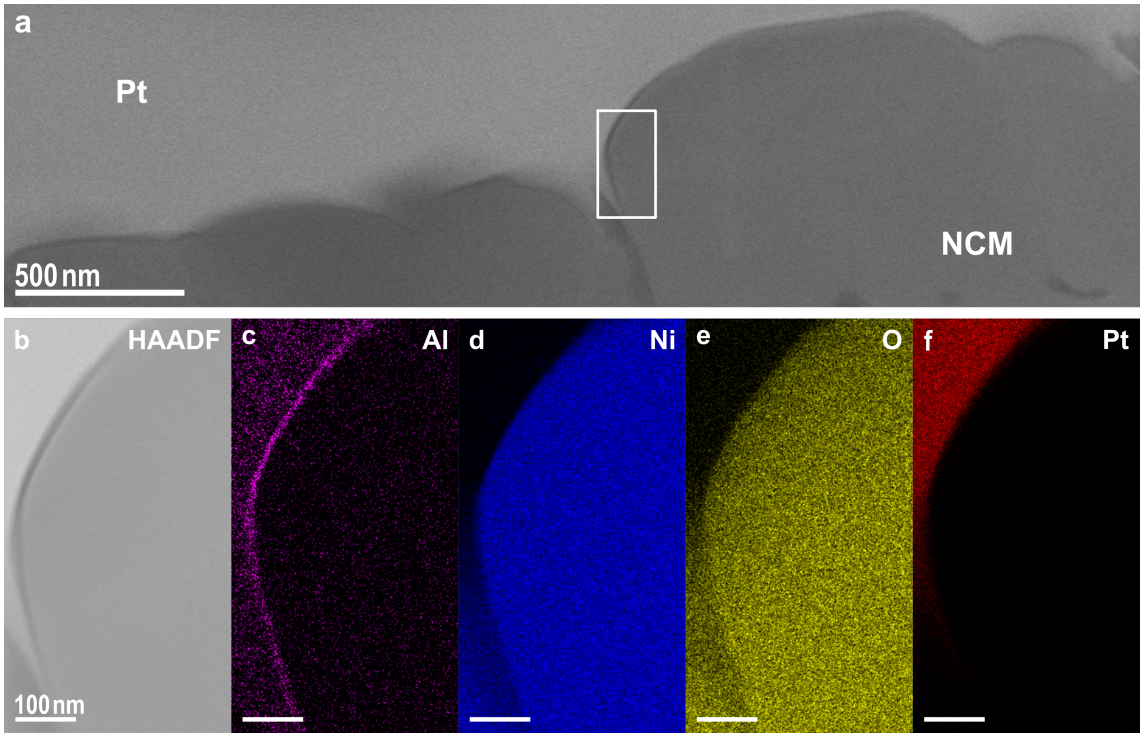

Figure 5.27.: HAADF-STEM imaging and STEM-EDX measurements displaying the homogeneity and thickness of a Al_2O_3 coating on a PC-NCM. (a) HAADF-STEM image with a white rectangle indicating the EDX-scanning area. (b) HAADF-STEM image of the EDX-scanning area. (c)-(f) EDX elemental maps of aluminum, nickel, oxygen and platinum, respectively.

5.4.2. Studying of coating before and after cycling

In the next step, we investigated and compared the structural stability of an Al_2O_3 coating before and after cycling. In the context of a master thesis [160], Shriya Agarwal investigated an Al_2O_3 coating deposited on PC-LNO before cycling (pristine) and after 150 cycles, reaching up to 4.5 V against lithium. This section presents selected results with slight formatting changes. The data were obtained with the conventional JEM F200 (Jeol, Japan), which was equipped with an AZtecEnergy TEM Advanced EDX 100 mm^2 detector (Oxford Instruments, UK). More details on

the setup can be found in the cited master thesis.

The particles of the pristine electrode sheet exhibited a homogeneous Al_2O_3 coating despite the rough surface topography as illustrated in the HAADF-STEM image in Figure 5.28a and the corresponding EDX-map in Figure 5.28c. The coating thickness varied between 8 nm and 40 nm across multiple particles. However, since the lamellae were relatively thick (above 150 nm), and the particle surfaces were not consistently aligned edge-on, these values might be distorted. Figure 5.28b and Figure 5.28d show a sample after cycling. Two aspects are notable. First, the coating appeared less uniform than that in the pristine sample, with the presence of a dispersed layer indicated by the solid ellipse in Figure 5.28d. The dispersed coating layer might result from the cycling process; however, since it was a post-mortem analysis, that could not be confirmed by the available data. Second, a fluorine signal appeared in the cycled sample presumably originating from the lithium salt ($LiPF_6$) of the electrolyte. The elemental EDX mapping demonstrated that the electrolyte not only reached the coated surface of the secondary particles, but also penetrated into the polycrystalline structure. The electrolyte was dispersed along the uncoated surfaces of the primary particles, at least those that were close to the secondary particle surface, as indicated by the dashed ellipse. This observation indicates that the coating did not completely prevent direct contact between the particle and the electrolyte. However, there were pathways through which electrolytes could diffuse. Although these findings offer preliminary evidence for a change in the Al_2O_3 coating, the use of STEM-EDX alone does not provide sufficient information on the dynamics of the coating during the cycling process.

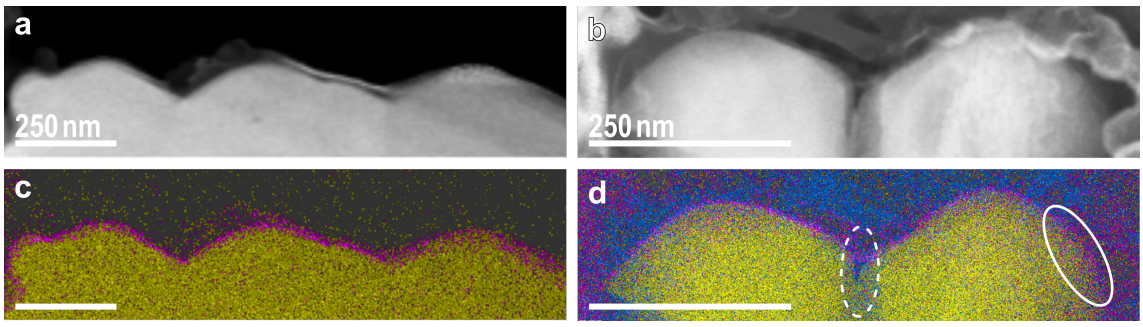

Figure 5.28.: PC-LNO coated with an approximately 10 nm thick Al_2O_3 coating. (a) and (b) HAADF-STEM images showing a pristine and cycled cathode sheet, respectively. (c) and (d) corresponding mixed EDX elemental maps nickel (yellow), aluminum (pink) and fluorine (blue). Fluorine-containing species were observed on particle surfaces, even in uncoated regions (dashed ellipse). The coating may have dispersed during cycling (solid ellipse).

5.4.3. *In situ* biasing experiments of coated PC-NCM

The *ex situ* study presented in Section 5.4.2 shows that cycling leads to structural changes of the coating. However, these data could not provide information on the origins and dynamics of structural changes. Therefore, an initial attempt was made to visually examine the structural stability of the coating during cycling by *in situ* biasing TEM. The basis for this *in situ* biasing experiment was an article published by Basak *et al.* [161], in which they used an *in situ* biasing setup with a solid-state electrolyte to investigate coating thickness dependencies. The authors used Si/SiO_2 nanoparticles coated with TiO_2. In contrast, we tested this setup with a PC-NCM lamella with an Al_2O_3 coated surface. Although the volume change upon cycling is much less in Ni-rich NCM than in silicon, a volume change of approximately 6 %, which was found for Ni-rich NCM [162], should be clearly visible.

For the first experiment, a voltage was applied from 0 V to 5 V and back to 0 V to stimulate lithium intercalation and deintercalation in the NCM cathode. After a voltage hold at 0 V for 3 sec at the beginning, the voltage was changed by $\Delta V = 0.1\,\mathrm{V/sec}$. A low TEM magnification was chosen to compromise between resolution and the field of view. To first test the feasibility on a NCM lamella, we chose a field of view in which both the needle and individual grains of the sample were visible. Since the needle should not come into contact with the platinum layer remaining from the FIB preparation to avoid a short circuit, the coated surface directly under the platinum layer was not visible in the selected field of view.

An IV-curve was recorded during the experiment which is shown in Figure 5.29. The IV-curve illustrates the sensitivity of the sample to the applied voltage. Figure 5.30 displays the corresponding TEM image series showing a few NCM grains and the tungsten needle which is surrounded by the Li/Li_xO cloud. During voltage application, a constant change in the bending contrast of the NCM lamella was observed. At approximately 4.6 V, a break down in the IV-curve was identified which was accompanied by a detachment of the needle and the NCM lamella as evident in Figure 5.30h. A possible explanation is that the Li/Li_xO cloud touched the platinum layer and caused a short circuit which led to high local stress induction causing the lamella to break. The pictures of the fluorescence screen before any voltage was applied and after the breakdown in Figure 5.31 demonstrate that the space between the Li/Li_xO cloud and platinum layer was limited. This makes it plausible that the cloud likely contacted the platinum layer due to slight movement. Furthermore, no volume changes of the NCM grains were observed upon this point. As the NCM particle should be almost fully lithiated at the beginning, an observable change was not anticipated during lithiation.

The experiment presented shows that microstructural changes due to an applied electrical voltage can be visually observed in the TEM images and correlated with the values of the IV curve. However, some limitations in the experimental setup

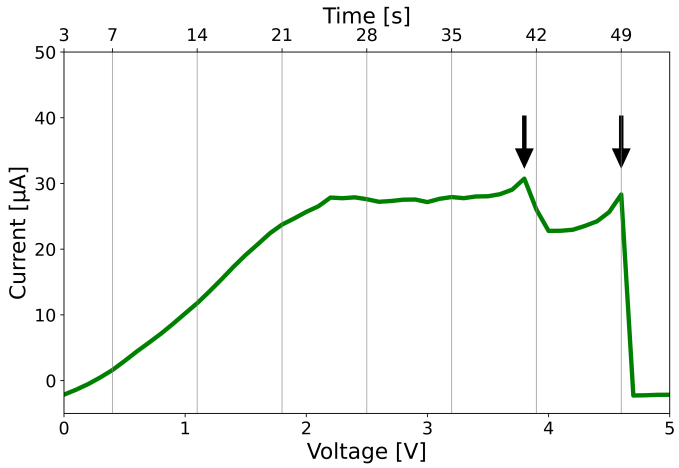

Figure 5.29.: IV-curve recorded during the *in situ* biasing experiment. The marked peaks at 3.8 V and 4.6 V highlight the sensitivity of the sample to the applied voltage. Shortly after 4.6 V an electrical breakdown occured. The time-axis at the top of the plot marks the time stamps corresponding to the images presented in Figure 5.30.

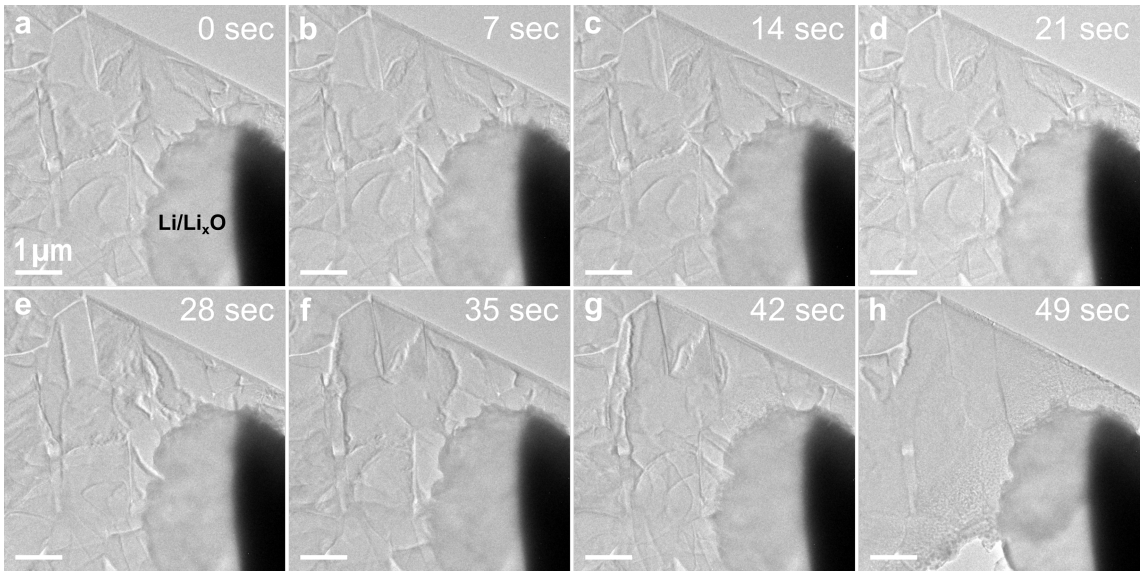

Figure 5.30.: TEM images were continuously recorded during the delithiation of the NCM sample. (a)-(g) TEM images showing constantly change in bending contrast with increasing voltage. The applied voltages at the individual time stamps are displayed in Figure 5.29. (h) TEM image after the current breakdown, which resulted in a subtle shift in the height of the sample, leading to a defocused image compared to images (a)-(g). The scale bar is 1 μm for all image.

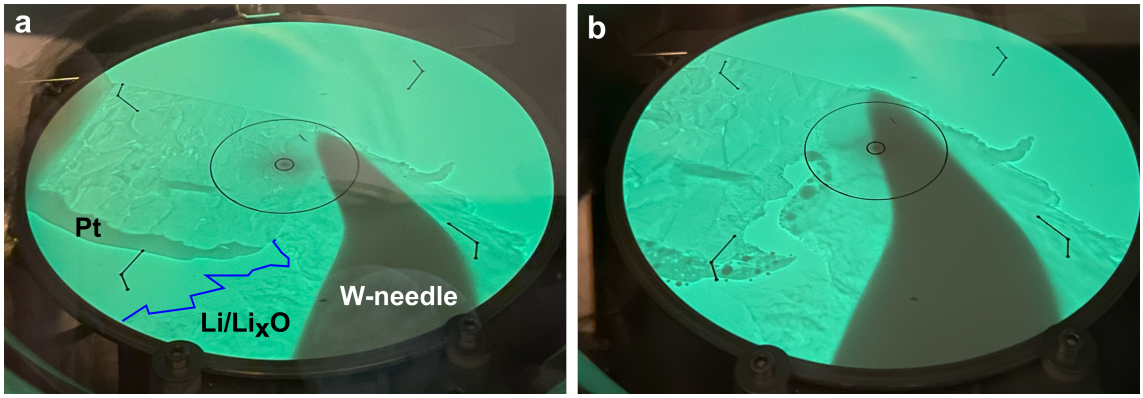

Figure 5.31.: Pictures of a fluorescence screen showing the lamella-needle situation: (a) before a potential was applied and (b) after the the breakdown. The blue line in (a) marks the surface of the Li/Li$_x$O chunk.

currently restrict the *in situ* investigation of the structural behavior of the coating during cycling. The main limitations are listed below.

- **Sample preparation:** The size and shape of the sample allowed only FIB preparation, which led to two issues. First, the coating no longer covered the entire particle, as only a part of the particle could be used for the lamella. Second, due to FIB preparation, the coating layer was covered by a platinum layer, which tended to cause short circuits when touching the Li/Li$_x$O cloud when a voltage was applied.

- **Electrolyte preparation:** While scratching the tungsten needle over the lithium foil, it was difficult to control the amount and the shape of the Li/Li$_x$O cloud. However, both are important for a successful experiment. The Li/Li$_x$O cloud should be as large as possible to contact a large area of the sample and thus provide good ionic conductivity. However, it should be shaped so that it does not touch the platinum layer.

- **Contact between NCM lamella and needle:** Adjusting the needle position required small movements of the needle to avoid breaking the fragile lamella. Therefore, it was difficult and time-consuming to establish good physical contact between the lamella and the Li/Li$_x$O cloud or tungsten needle to ensure electrical current flow. Additionally, due to the small contact area, sufficient charge transport across the entire lamella could not be guaranteed.

Furthermore, it should be noted that the experimental setup deviated from a real-world battery and the following aspects should be considered as potential limitations. First, instead of a liquid electrolyte, a solid-state electrolyte was used in the setup. This might heavily impact the ionic conductivity during cycling, as it has a different diffusion kinetics than that of a liquid electrolyte. Second, a lamella is very thin and might behave differently from a bulk cathode. Therefore, the applied voltages

might need adjustment to meet the conditions of a conventional NCM battery.

In summary, the presented example highlights the challenges of *in situ* biasing TEM experiments to study coated NCM materials. Further efforts are needed, requiring more time and money, to overcome the limitations and refine the approach. This experiment is a first building block to study electrochemical dynamics of NCM batteries via *in situ* TEM.

6. Discussion

6.1. Phase transition on the particle surface in Ni-rich NCM at high potential holds

The results presented in Section 5.2 show anisotropic degradation behavior of the surface at high potential holds. The phase transition from the intact layered structure to a gradual transition boundary with strong cation mixing in the rock salt structure was observed, particularly at surfaces with open lithium channels. At these open surfaces, a significant increase in surface degradation over time was seen, while the changes along the basal plane were moderate, and the change over time was subtle. The newly implemented image processing, the Fourier coefficient mapping, revealed that the transition boundary penetrated deeply into the material. The EELS data collected support this interpretation and demonstrate that the cation mixing extended even further into the material than previously suggested on the basis of the HAADF-STEM images. These results emphasize the strength of the combination of local imaging and spectroscopic analysis.

The degradation mechanisms in nickel-rich NCM are complex and challenging to delineate individually. Comparing the evolution of the rock salt layer with CEI formation at the surface, it seems that the physical driving force of high potentials has a larger effect on the charge transfer resistance, and thus finally on capacity retention than chemical reactions between the cathode and the electrolyte. However, chemical reactions should still be thoroughly considered. Assuming that structural transformation is the most server degradation mechanism in the tested battery configuration, optimizing structural integrity and stability is key in order to design high-quality LIBs with Ni-rich NCM cathodes. Common mitigation strategies are to optimize synthesis protocols, for example, to keep the initial defect concentration low, and to apply coating and doping (Section 2.4) [163]. The aim is to stabilize the TM-O bonds to prevent oxygen release and to hinder TM migration to lithium, sites, and thus to preserve fast lithium diffusion pathways and not permanently bind any active material. [20, 164].

The work contributes to the understanding of structural degradation in Ni-rich NCM. However, some limitations persist. First, due to the inhomogeneous growth of the rock salt layer, it is difficult to determine a growth rate and to estimate the exact effect of the rock salt layer on the increase in charge transfer resistance. Second, the impact of the gradual transition boundary on the electrochemistry could not be

quantified. Since the possibilities for investigating phase transitions at the atomic level beyond transmission electron microscopy are limited, a precise determination of the exact correlation between the rock salt layer, the gradual transition boundary, and the electrochemical data remains a challenge.

To gain a refined picture of the evolution of phase transition surface across many particles, two aspects should be considered for future experiments. First, 4D-STEM with nanobeam precession diffraction should be used to simultaneously acquire 2D-data sets of real-space STEM images and diffraction patterns. This approach allows to map entire particles and to investigate the extent of rock salt formation and cation mixing into the core of the particle. The diffraction pattern allow to obtain crystallographic information of a much broader field of view than with HR-STEM imaging. Not all TEMs are equipped with a precession unit and dedicated detectors. Therefore, a TEM with a resolution lower than that achieved in this study might be utilized. Nevertheless, any TEM used should have enough resolution to study the rock salt layer, expected to be several nanometers thick. The precession of the electron probe balances small deviations from the zone axis and accommodates for mistilt or strain in the sample. The 4D-STEM approach requires a dedicated setup. The acquired data sets are large and need advanced software to analyze the data which should be taken into consideration. Second, in combination with 4D-STEM analysis, the set of samples should be extended by samples that were kept at high potential for a couple of months to investigate the long-term effects on the rock salt evolution better. Alternatively, cycled electrodes could be investigated. In principle, similar behavior at the surface is expected for cycled electrodes, including the formation of a rock salt layer and most likely a gradual transition boundary. However, during cycling the electrode is exposed significantly more voltage changes than during long potential holds, which might change the dynamics of the phase transition.

6.2. Impact of protonated Ni-rich NCM on the structural and thermal stability

Washing of Ni-rich NCM cathode active material is a critical step in manufacturing Ni-rich LIBs and has a significant impact on material quality, cost and time on an industrial scale [34]. In order to gain a deeper mechanistic understanding of the washing process, the samples analyzed in this study were washed under more extreme conditions, with longer durations and a higher water:CAM ratio than typically applied in industry. Elevated temperatures during the drying process result in the release of water and oxygen [34]. As a consequence, structural changes in the material were observed including nanopore formation at the nanoscale and rock salt formation at inner surfaces of the nanopores and outer surfaces of the particles. The phase transition from the layered structure to the rock salt structure was ac-

companied by a gradual transition region as observed in the study of high potential holds (Section 5.2). No evidence of a stable intermediate spinel phase was found, as postulated previously in the literature [33, 34]. *In situ* experiments confirmed the decrease in thermal stability and the detrimental effects on structural stability subsequent to washing.

The TEM results show the dimensions of structural degradation due to washing and subsequent heating, which were not limited to the surface structure but also affected the core structure. The core structure was disrupted by nanopores with oxygen-depleted surfaces and defected-rich layered structures. Formation of nanopores were observed in recent studies as a result of oxygen release under harsh cycling conditions [153–155, 165, 166]. However, to our best knowledge, the connection to the washing procedure was not made before. The results show two central aspects. First, different treatments on Ni-rich NCM lead to, at least at a first glance, same consequence, as for example the formation of nanopores or rock salt. The reason for this is that structural degradation is very closely linked to the release of oxygen, which is triggered by various processes [163,164,167]. Second, the results underscore the necessity to carefully examine each process step to identify the weaknesses in the material. Post-mortem examinations alone are insufficient if the source of the final outcome cannot be distinguished clearly. For the development of long-lasting, well-performing and safe materials, it is very important to investigate the introduction of defects along the entire manufacturing chain and operation cycles, and to systematically minimize the sources of defects.
The effects of the washing process and the associated Li^+/H^+-ion exchange are becoming increasingly important beyond conventional manufacturing. In recent studies, water-based coatings have been developed and tested [168–170]. This is an exciting approach because it can combine process steps, thus saving resources. It is essential to incorporate existing knowledge on washing and its impact on structural and thermal stability in designing water-based coatings.

The combination of various methods [34] including high-end analytics like TEM measurements has provided important building blocks for understanding the washing and heating of structural and thermal stability. However, two key points remain unresolved. First, the distribution of protons within the material remains unclear. Thus, the exact ion exchange mechanism has not yet been conclusively clarified. Second, a close link between structural degradation and precise electrochemical data from the same material system is needed to assess the effects of washing on material quality. A comprehensive study that examines both structural degradation and electrochemical data under real washing conditions would be desirable. The data obtained could be used to characterize after how many cycles a critical threshold for capacity loss or material failure is reached and which structural changes have led to this behavior. These data are vital for material development.

For a deeper understanding of the ion-exchange mechanisms, we suggest atom probe

tomography (APT), which is a technique that can resolve chemical elements locally at the atomic scale [171] and has been successfully applied to NCM cathode materials before [172–175]. APT can detect very light elements, such as lithium and hydrogen, which is a great advantage over TEM. Consequently, APT is an approach to analyze diffusion paths and potential concentration gradients of lithium and hydrogen. To improve the signal-to-noise ratio and to avoid measuring artifacts in the hydrogen signal, we recommend washing the powder in heavy water (D_2O) [176]. The proposed experiment is very challenging, especially considering sample preparation. It requires the preparation of a needle with a very fine tip from the brittle Ni-rich NCM powders. Nevertheless, it is a promising approach to gain a deep understanding of the Li^+/H^+-ion exchange mechanism.
A profound understanding of the Li^+/H^+-ion exchange mechanism and its impact on thermal and structural stability is needed to develop an efficient, gentle and cost-effective solution. Optimizing the washing parameters, including washing time and CAM:water ratio, drying temperature and atmosphere, are needed for resource-efficient production. To investigate the influence of the drying atmosphere, we suggest *ex situ* STEM experiments of samples heated under oxygen-containing atmospheres. For a deeper understanding of the effect of heating under oxygen on the structural level, we recommend *in situ* heating under oxygen flow to study the behavior of the materials with respect to nanopore formation.

6.3. Experimental limitations

6.3.1. HAADF-STEM imaging and other imaging techniques

HAADF-STEM imaging is a suitable technique to investigate structural degradation in Ni-rich NCM locally. The layered structure and the rock salt structure can be clearly distinguished due to the changes in the TM sublattice. The main advantages of HAADF-STEM imaging are straightforward image interpretation due to Z-contrast and the robustness against variations in sample thickness, small mistilt, and small defocus. However, HAADF-STEM imaging is not sensitive to the lighter oxygen and lithium atoms. The precise determination of the oxygen positions and the quantification of the oxygen vacancy concentration in the samples are of potential interest, as the release of oxygen is closely linked to the phase transformation from the layered to the rock salt structure. Furthermore, imaging lithium could assist in providing more insight into the structural degradation of Ni-rich NCM. STEM techniques like ABF imaging and offer better sensitivity to image light elements in the vicinity of heaver elements (see also Section 3.2.2).

At this point, the question arises as to why neither of the two methods was used, as both have strong advantages for imaging light elements. In addition, both modes need less electron dose which is attractive for investigating beam sensitive materials such as Ni-rich NCM. The explanation for this choice is attributed to the sample

thickness and the primary research questions focused on the surface degradation of Ni-rich NCM. As described in detail in Chapter 4, the preparation of high-quality samples of Ni-rich NCM powder or electrodes was very challenging. Both ABF and iDPC require much cleaner and significantly thinner samples than acceptable for HAADF-STEM imaging. In principle, this would be possible with conventional preparation techniques. However, grinding the sample does not allow to later assess which of the particle surfaces were primary outer surfaces. Therefore, samples prepared through grinding are not suitable to address the primary research questions. Dimpling would have been an option if enough sample material would have been available. However, preparation via dimpling would have introduced additional concerns, such as potential reactions due to contact with water-based lubricants or exposure to air as long as the devices are not stored in a glovebox. Finally, TEM sample preparation using FIB best met the sample preparation requirements for the research questions, albeit at the expense of limited minimum achievable sample thicknesses.

Figure 6.1 shows simulated images of HAADF-STEM, ABF-STEM and iDPC-STEM with varying thickness of 2 nm, 10 nm, 25 nm, 50 nm and 75 nm, respectively. The images show the layered structure in the [100] zone axis corresponding to the structure model presented in Figure 5.5d. The HAADF-STEM images, presented in the first row, show bright spots which correspond to the TM of the layered structure. Despite the large thickness variations, the HAADF-STEM image contrast is robust and essentially the background level increases with increasing thickness while the qualitative information remains.

The ABF-STEM image simulation series, shown in the middle row, presents the TM, oxygen and lithium-ions appearing as dark to bright spots, respectively. The image at 2 nm thickness shows a very clear image contrast and the individual columns are visible. The image at 10 nm thickness is already a bit more blurred, but the individual columns appear clearly. With increasing thickness, the dark spots corresponding to the TMs become more pronounced, while the signal originating from scattering at columns of light elements smears out. Also, the signal ratio between columns of heavy and light elements found for thin samples changes significantly with increasing thickness.

The iDPC images, illustrated in the third row, highlight that iDPC-STEM imaging is very sensitive to thickness. Only at very thin samples a directly interpretable contrast is produced. With increasing thickness, contrast changes occur, resulting in non-intuitive patterns. In order to evaluate these images, precise knowledge of the sample thickness and a comparison with simulated images is required.

What has not been discussed yet is potential cross talk between the atomic columns which should be considered in particular for ABF-STEM and iDPC-STEM imaging where the contrast is obtained by scattering at light and heavy elements. Cross talk

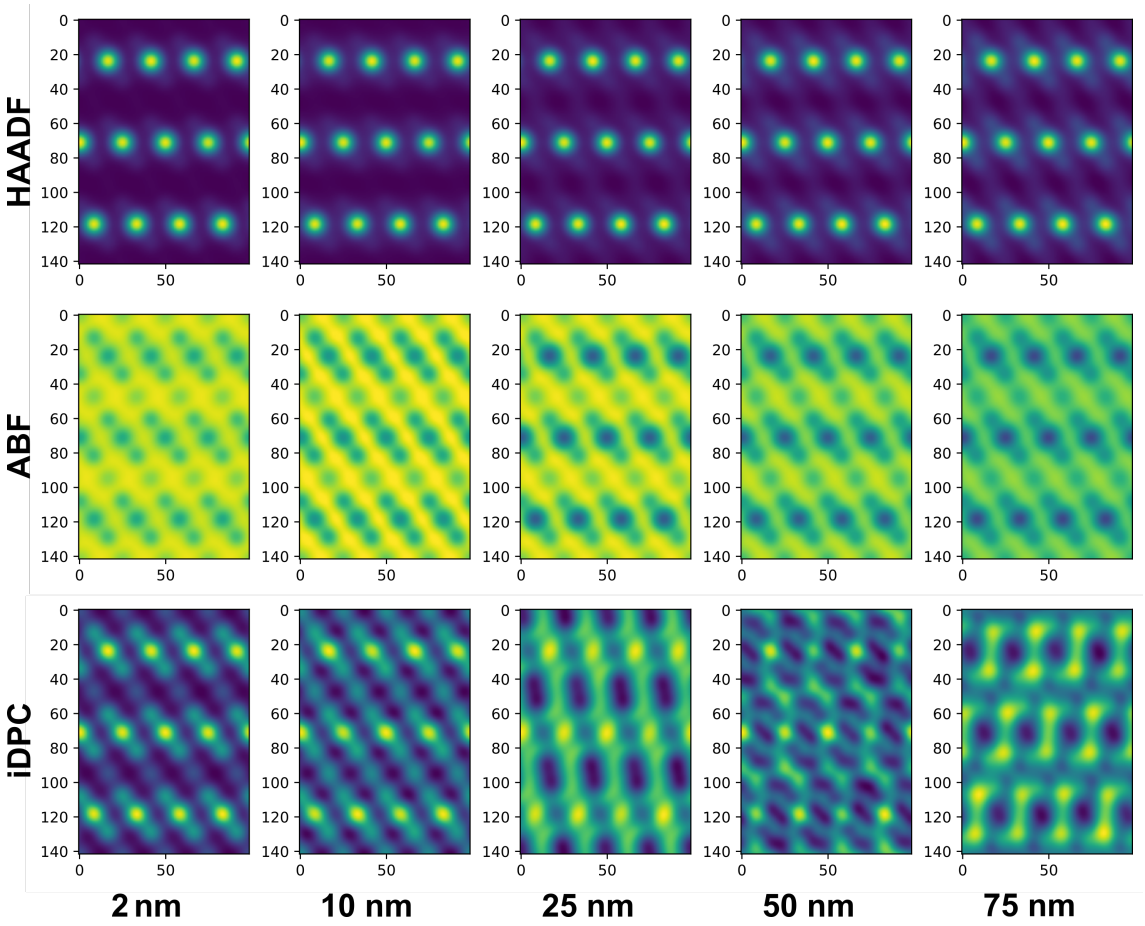

Figure 6.1.: Image simulation [74] showing the thickness dependence of the sample to the signal formation for HAADF-STEM image (upper row), ABF-STEM image (middle row) and ABF-STEM (lower row) with thicknesses from 2 nm, 10 nm, 25 nm, 50 nm and 75 nm from left to right, respectively. The underlying structure model is Ni-rich NCM layered structure [41] in the [100] zone axis.

describes the phenomenon where the electron probe initially focused on an atomic column interacts with nearby columns when propagation through the crystal. The generated intensities then stem not only from the initial atomic column but also from neighboring columns, which may lead to ambiguous result.

In literature, ABF-STEM imaging of Ni-rich NCM was mostly used to confirm the layered structure or to support structural changes observed in HAADF-images [62,82,177–179]. Studies in which ABF-STEM was applied to Ni-rich NCM were not found, just a few studies on other layered lithium oxide battery materials [180,181]. These studies show that, on a qualitative level, iDPC-STEM imaging is possible on Ni-rich NCM. However, the additional information gained on phase transition from the layered to the rock salt structure compared to the HAADF-STEM images is lim-

ited. Furthermore, it should be considered that the sample preparation requirements for ABF-STEM imaging are significantly higher than for HAADF-STEM imaging. The samples need to be much thinner to obtain a clear contrast.

Based on the simulated images, we recommend ABF-STEM for imaging light elements in Ni-rich NCM when this is of great interest in future studies. In order to quantitatively analyze defects such as vacancies, high-quality samples and a systematic approach with the addition of simulations are required to clearly identify the defects based on intensity differences. When the focus is on analyzing the phase transformation as in this work, HAADF-STEM is the method of choice.

6.3.2. *In situ* transmission electron microscopy

In situ TEM techniques enable the study of dynamic processes with local resolution, constituting an important building block to achieve a deep understanding of dynamical processes in materials using imaging methods. Recent progress in *in situ* TEM holders and detector development made *in situ* TEM more popular [182]. However, *in situ* TEM experiments still encounter some major constraints which can limit the outcome of the investigations [183, 184]. For both types of conducted *in situ* experiments the following limitations occurred. First, *in situ* experiments are always a compromise between imitations of the real world and feasible realization in a TEM. For TEM investigations, the sample has to be electron-transparent and has also a limited size in the lateral directions. Due to the microscopic sample size, the measured value, such as temperature dependencies or currents, and the observed phenomena cannot always be directly transferred to the macroscopic world. Second, the field of view is limited. Consequently, a sample area must be selected for experiments at higher magnifications. This may result in missing significant events outside the chosen area. Third, the acquisition speed of the detectors and the scan speed of a STEM are limited. In comparison, structural changes in a material occur on much smaller time scales. Therefore, not all details might be captured.

The major practical limitation of the *in situ* heating experiments conducted was the drift of the sample in all three spatial directions, in particular during temperature ramps. The movement in z-direction was particularly worse beyond 500 °C and the focus was lost. Consequently, the recorded image series between temperature plateaus could not be analyzed, thereby minimizing the advantage of *in situ* studying dynamic effects. Because the experiments were conducted at medium magnification, the drift at elevated temperatures was manageable because the focus could be adjusted during temperature holding. The alterations in structure could be consistently compared across different holding temperatures. The problem would be exacerbated if the experiment had been conducted at atomic resolution, as it would become considerably more difficult to identify the same position again. This was ultimately a decisive reason not to carry out atomically resolved *in situ* experiments.

Another aspect that should be considered in future *in situ* heating experiments on Ni-rich NCM is potential irradiation damage due to the long electron beam exposure during the acquisition of an image series. In order to check how strongly the radiation exposure affects the sample, it is advisable to acquire a single image, for example, at 30-second intervals while employing the pre-sample shutter between exposures. If a significant difference between constant irradiation and reduced irradiation can be recognized, the electron dose should be reduced in future experiments by changing the beam current, the dwell time or the imaging intervals. However, longer intervals between exposures may risk to miss critical changes.

In case of the *in situ* biasing experiment, presenting a first building block to study coated NCM particles during cycling, the experimental obstacles are already outlined in Section 5.4.3. An approach to simplify the requirements of the experiment might be to change from PC-NCM particles with a large diameter to SC-NCM particles with a smaller diameter of e.g. 5 µm. A smaller particle would allow to (i) cut al lamella of an entire, fully coated particle, (ii) ensure larger contact areas between the lamella and the $LiLi_xO$ cloud and (iii) use higher magnifications as a smaller FOV is needed. In addition, a carbon protection layer could be tried to minimize the potential of short circuits between the protection layer remaining from FIB and the $LiLi_xO$ cloud or needle.

In summary, *in situ* experiments are a very valuable addition to the toolbox of TEM methods, as they enable the investigation of dynamic processes. However, despite the rapid development of *in situ* TEM in recent years, they still suffer from experimental limitations that can minimize the scientific outcome. The more complex the system, the more restrictions are added and the more compromises have to be made in order to carry out the experiments. Therefore, a well-organized experimental plan that combines *ex situ* and *in situ* TEM is key to utilizing the strengths of both approaches and solving unanswered questions in materials science.

7. Conclusion

Ni-rich NCM cathodes are promising materials for high-energy LIBs, which are needed, for example, to increase the mileage of electric vehicles, due to their high theoretical capacity. However, the theoretical capacity cannot be achieved in a real battery cell, as Ni-rich NCM suffers from structural and thermal instabilities at high SOC. Although other NCM compositions are subject to structural instability, a high nickel content exacerbates the situation. A primary degradation phenomenon in Ni-rich NCM is the phase transition from its intact layered structure to a rock salt structure, where TM ions occupy lithium sites. This phase transition is triggered by the release of lattice oxygen and the migration of Ni^{2+} ions to lithium positions, which leads to kinetic hindrance of lithium diffusion pathways and ultimately to a loss of capacity. In addition to the phase transition of the surface, other degradation phenomena can occur in Ni-rich NCM, such as cation mixing, TM dissolution, cracking and electrolyte decomposition that leads to the formation of a CEI which can potentially behave like a passivation layer at the particle surface.

This work focuses on three topics: (i) time-dependent structural surface degradation at high potential holds, (ii) thermally induced structural degradation of protonated NCM, and (iii) Al_2O_3 coatings and their behavior during de-/lithiation. The aim is to better understand the degradation behavior in Ni-rich NCM in order to find targeted material solutions that enable long-lasting and high-performance cathode materials. High-resolution HAADF-STEM imaging, EDX, EELS and *in situ* TEM were employed to investigate the structural degradation of Ni-rich NCM locally at the nanoscale and atomic scale. HAADF-STEM imaging provides a straightforward way to interpret image contrast by recording inelastic scattering signals proportional to the atomic number Z. In Ni-rich NCM, the Z contrast essentially captures the position of heavy TM atoms, while the lighter elements, oxygen and lithium, are not visible. Studying the positions of TMs provides substantial insight into structural degradation processes in Ni-rich NCM.

To better study surface degradation in (i) and (ii), we chose single crystalline NCM particles to keep the surface situation as simple as possible. Polycrystalline powder was selected for the analysis of the coating in (iii). For TEM investigations, electron-transparent samples are required. As most of the work focused on structural degradation at the surface, it was inherent to preserve the original particle surfaces. To meet these requirements, FIB lamella preparation was applied. Due to the morphology and shape of the samples, FIB preparation was challenging. Since the sample quality massively determines the outcome of a TEM experiment, it was necessary to

optimize the FIB sample preparation on NCM powder and electrodes. As a result, this work provides practical guidance for TEM sample preparation.

The time-dependent study of Ni-rich NCM at high potential holds of 4.5 V aimed to trigger structural degradation while the electrolyte decomposition was still negligible. A reference sample kept at OCV for one day and three samples kept at 4.5 V for 23, 30 and 37 days, with impedance measured every two days, were examined using atomically resolved HAADF-STEM. The investigations revealed that a rock salt layer grew epitaxially and coherently on particle surfaces at high potentials. However, the formation of the rock salt layer was anisotropic and diverged from the often proposed core-shell model. Open surfaces, where lithium channels terminate, were more prone to phase transition from the layered to the rock salt structure than surfaces parallel to lithium channels. The particle surroundings significantly influenced structural degradation. Furthermore, no sharp interfaces were observed between the rock salt layer and the layered structure, but the transition region was characterized by a gradual transition boundary with substantial cation mixing. This observation highlights that a stable intermediate spinel phase did not form in Ni-rich NCM, distinguishing it from NCM compounds with higher manganese concentrations.

Due to the anisotropic degradation behavior, it was challenging to measure the thickness of the reconstructed surface. Three different approaches were applied to estimate the thickness: measuring image intensities at medium magnification and atomic resolution, and mapping Fourier coefficient ratios. The first two approaches used that the density of TMs is approximately twice as high in the rock salt structure than in the layered structure. Measuring intensities at medium magnification provided a quick and rough estimate of the rock salt layer. Measuring intensities at atomic resolution yielded highly localized and detailed information of the intensities and thus offered additional information of the gradual transition boundary. The third approach, Fourier coefficient mapping, is a novel image processing method that we developed as part of this work. This method utilizes the crystallographic differences between the layer and rock salt structures to clearly visualize these structures and the gradual transition boundary in a high-resolution HAADF-STEM image at a glance. EELS data indicate that the phase transition extends much further into the particle than suggested by the HAADF-STEM images.

The anisotropic and inhomogeneous behavior of the phase transition on the surface did not allow to estimate a universal thickness value for the rock salt structure or the reconstructed surface. However, an increase in rock salt layer over time at uncovered open surfaces was found, which is likely contributing to the measured increase in the relative charge transfer resistance. To further investigate the rock salt evolution over time at high potential holds, we suggest to conduct 4D-STEM nanobeam diffraction at samples kept at high potentials for a couple of months to even better study the long-term effects on structural degradation and to mapping

entire particle structures within an image.

Washing of freshly synthesized powder is an important step in industry to remove harmful lithium residuals from the surface. These residuals remain from the synthesis due to a slight lithium excess which is needed, in particular, for Ni-rich NCMs. However, washing leads to a lithium/proton-exchange at the surface resulting in a destabilization of the layered structure. When heated, water and oxygen are released, which occurs at significantly lower temperatures than in unwashed Ni-rich NCM, and leads to a partial collapse of the layered structure into a rock salt structure. A set of four samples, consisting of a pristine sample and three washed samples heated at 65 °C, 180 °C and 300 °C, were studied. The powders were washed under harsher conditions than in industry to accelerate degradation.

As anticipated, the HAADF-STEM measurements showed that a relatively thick rock salt layer formed at the top of the particle surface. In addition, HAADF-STEM images and EDX measurements revealed that at the surface, but also along defects and in the core of the particles, nanopores with oxygen-depleted surfaces formed, which was confirmed by *in situ* heating STEM experiments. These findings present new insight into structural degradation due to washing. Nanopore formation was observed already in other studies due to the release of oxygen, but to the best of our knowledge, it had not been linked to washed samples before. Furthermore, no stable intermediate spinel phase was found as proposed in the literature [33], which is in good agreement with recent XRD measurements [34]. Instead, a gradual transition boundary was observed. The results emphasize the importance of local investigation of the structure at the nano- and atomic scale. The diffusion of protons within the layered structure remains unclear and cannot be answered by TEM methods as protons are too light to be visualized in TEM. Therefore, we recommend using atom probe tomography to identify proton locations, whether confined to the surface or distributed within the layered structure.

Various mitigation strategies such as adjusting the synthesis conditions, applying a coating, or introducing dopants to stabilize the structure in Ni-rich NCMs This work focused on Al_2O_3 coating on PC-NCM and its behavior during cycling. First, the thickness and homogeneity of the Al_2O_3 coating, which was deposit by ALD, was investigated using HAADF-STEM. The results showed that the coating thickness was approximately 10 nm and much thicker than the anticipated thickness of 1.5 nm. This finding highlights the need for precise thickness measurements to accurately classify electrochemical results. *Ex situ* STEM-EDX experiments showed that the homogeneous coating became more diffuse after cycling. However, these data could not explain the origins, which is necessary to develop targeted and resource-efficient coatings. An *in situ* biasing TEM setup was tested to examine the dynamic behavior of the coating during cycling, which induces an anisotropic volume change due to de-/lithiation. A lamella was prepared from a coated particle and a tungsten needle covered by a Li/Li_xO cloud served as electrode with a solid electrolyte. Dur-

ing voltage application, which stimulates lithium de-/intercalation, the recorded IV-curve and image series were sensitive to the applied potential and correlated. However, the experimental design and sample choice demonstrated some fundamental issues that need to be solved in order to study the coating dynamics during cycling in PC-NCM in detail. This work provides a first building block and ideas for improvements such as the modification of the sample system.

In conclusion, in (i) and (ii) in this work we analyzed Ni-rich NCM cathode materials under different aspects and showed the that the extent of structural degradation is more complex and pronounced than initially assumed. The significant contribution of the reconstructed surface in (i) to an increase in the charge transfer resistance over time demonstrates the need to stabilize the layered structure at high SOC. The findings in (ii) visualize the impact of washing and heating on structural and thermal stability. Since washing is currently still an unavoidable process step in the production of Ni-rich NCMs, this work motivates the optimization of the process parameters to minimize structural degradation. To estimate the structural degradation on the performance of the cathode material, it would be important to correlate the STEM data with electrochemical cycling data to optimize industrial cathode materials. In addition, the results on the structural degradation of protonated Ni-rich NCMs are increasingly relevant for the development of e.g. new water-based coatings, where structural degradation by protonated layered structures should be taken into account. Future experimental approaches such as 4D-STEM and *in situ* experiments under gas flow were proposed to address the remaining questions. However, some open aspects are beyond the capabilities of TEM methods. Therefore, we have recommended further high-analytical techniques such as atom probe tomography.

Bibliography

[1] Organization, W. M. State of the climate 2024 (12/9/2024). URL https://library.wmo.int/records/item/69075-state-of-the-climate-2024.

[2] World Meteorological Organization. Wmo confirms 2024 as warmest year on record at about 1.55°c above pre-industrial level (2025). URL https://wmo.int/news/media-centre/wmo-confirms-2024-warmest-year-record-about-155degc-above-pre-industrial-leve

[3] IEA. Net zero roadmap: A global pathway to keep the 1.5 °c goal in reach – analysis - iea (12/19/2024). URL https://www.iea.org/reports/net-zero-roadmap-a-global-pathway-to-keep-the-15-0c-goal-in-reach.

[4] IEA. Outlook for emissions reductions – global ev outlook 2024 – analysis - iea (27.12.2024). URL https://www.iea.org/reports/global-ev-outlook-2024/outlook-for-emissions-reductions.

[5] IEA. Batteries and secure energy transitions (3/23/2025). URL https://www.iea.org/reports/batteries-and-secure-energy-transitions.

[6] Solyali, D., Safaei, B., Zargar, O. & Aytac, G. A comprehensive state–of–the–art review of electrochemical battery storage systems for power grids. *International Journal of Energy Research* **46**, 17786–17812 (2022). URL https://onlinelibrary.wiley.com/doi/full/10.1002/er.8451.

[7] Olabi, A. G., Abbas, Q., Shinde, P. A. & Abdelkareem, M. A. Rechargeable batteries: Technological advancement, challenges, current and emerging applications. *Energy* **266**, 126408 (2023). URL https://www.sciencedirect.com/science/article/pii/S0360544222032947.

[8] Patel, M. *et al.* Fundamentals, recent developments and prospects of lithium and non-lithium electrochemical rechargeable battery systems. *Journal of Energy Chemistry* **81**, 221–259 (2023). URL https://www.sciencedirect.com/science/article/pii/S2095495623001158.

[9] Nishi, Y. The development of lithium ion secondary batteries. *Chemical record (New York, N.Y.)* **1**, 406–413 (2001). URL https://onlinelibrary.wiley.com/doi/full/10.1002/tcr.1024.

[10] Battery market size, share & growth | industry report, 2030 (12/27/2024). URL https://www.grandviewresearch.com/industry-analysis/battery-market.

[11] Armand, M. *et al.* Lithium-ion batteries – current state of the art and anticipated developments. *Journal of Power Sources* **479**, 228708 (2020). URL https://www.sciencedirect.com/science/article/pii/S0378775320310120.

[12] Khan, F. M. N. U., Rasul, M. G., Sayem, A. & Mandal, N. K. Design and optimization of lithium-ion battery as an efficient energy storage device for electric vehicles: A comprehensive review. *Journal of Energy Storage* **71**, 108033 (2023). URL https://www.sciencedirect.com/science/article/pii/S2352152X23014305.

[13] Deng, J., Bae, C., Denlinger, A. & Miller, T. Electric vehicles batteries: Requirements and challenges. *Joule* **4**, 511–515 (2020). URL https://www.sciencedirect.com/science/article/pii/S254243512030043X.

[14] Hesse, H., Schimpe, M., Kucevic, D. & Jossen, A. Lithium-ion battery storage for the grid—a review of stationary battery storage system design tailored for applications in modern power grids. *Energies* **10**, 2107 (2017). URL https://www.mdpi.com/1996-1073/10/12/2107.

[15] Koech, A. K., Mwandila, G., Mulolani, F. & Mwaanga, P. Lithium-ion battery fundamentals and exploration of cathode materials: A review. *South African Journal of Chemical Engineering* **50**, 321–339 (2024). URL https://www.sciencedirect.com/science/article/pii/S1026918524001100.

[16] Oswald, S. & Gasteiger, H. A. The structural stability limit of layered lithium transition metal oxides due to oxygen release at high state of charge and its dependence on the nickel content. *Journal of The Electrochemical Society* **170**, 030506 (2023).

[17] Wang, J. & Sun, X. Olivine lifepo 4 : the remaining challenges for future energy storage. *Energy & Environmental Science* **8**, 1110–1138 (2015). URL https://pubs.rsc.org/en/content/articlelanding/2015/ee/c4ee04016c.

[18] Sovacool, B. K. The precarious political economy of cobalt: Balancing prosperity, poverty, and brutality in artisanal and industrial mining in the democratic republic of the congo. *The Extractive Industries and Society* **6**, 915–939 (2019). URL https://www.sciencedirect.com/science/article/pii/S2214790X1930084X.

[19] Noh, H.-J., Youn, S., Yoon, C. S. & Sun, Y.-K. Comparison of the structural and electrochemical properties of layered li[nixcoymnz]o2 (x = 1/3, 0.5,

0.6, 0.7, 0.8 and 0.85) cathode material for lithium-ion batteries. *Journal of Power Sources* **233**, 121–130 (2013). URL https://www.sciencedirect.com/science/article/pii/S0378775313001110.

[20] Britala, L., Marinaro, M. & Kucinskis, G. A review of the degradation mechanisms of ncm cathodes and corresponding mitigation strategies. *Journal of Energy Storage* **73**, 108875 (2023). URL https://www.sciencedirect.com/science/article/pii/S2352152X23022727.

[21] Myung, S.-T. *et al.* Nickel-rich layered cathode materials for automotive lithium-ion batteries: Achievements and perspectives. *ACS Energy Letters* **2**, 196–223 (2017).

[22] Li, T. *et al.* Degradation mechanisms and mitigation strategies of nickel-rich nmc-based lithium-ion batteries. *Electrochemical Energy Reviews* **3**, 43–80 (2020).

[23] Gan, Q. *et al.* Critical review on the degradation mechanisms and recent progress of ni-rich layered oxide cathodes for lithium-ion batteries. *EnergyChem* **5**, 100103 (2023). URL https://www.sciencedirect.com/science/article/pii/S2589778023000064.

[24] Li, D., Liu, W., Liang, W. & Xu, R. Degradation mechanisms and modification strategies of nickel-rich ncm cathode in lithium-ion batteries. *Materials Research Express* **11**, 012006 (2024).

[25] Jiang, M., Danilov, D. L., Eichel, R.-A. & Notten, P. H. L. A review of degradation mechanisms and recent achievements for ni–rich cathode–based li–ion batteries. *Advanced Energy Materials* **11**, 2103005 (2021).

[26] Zhang, S. S. Problems and their origins of ni-rich layered oxide cathode materials. *Energy Storage Materials* **24**, 247–254 (2020). URL https://www.sciencedirect.com/science/article/pii/S2405829719309262.

[27] Choi, J. *et al.* The role of zr doping in stabilizing lini0.6 co0.2 mn0.2 o2 as a cathode material for lithium-ion batteries. *ChemSusChem* **12**, 2439–2446 (2019).

[28] Dose, W. M. *et al.* Electrolyte reactivity at the charged ni-rich cathode interface and degradation in li-ion batteries. *ACS Applied Materials & Interfaces* **14**, 13206–13222 (2022).

[29] Tanim, T. R. *et al.* A comprehensive understanding of the aging effects of extreme fast charging on high ni nmc cathode. *Advanced Energy Materials* **12** (2022).

[30] Wu, Y. *et al.* Thermal runaway of nonflammable localized high-concentration electrolytes for practical lini0.8 mn0.1 co0.1 o2 |graphite-sio pouch cells. *Advanced science (Weinheim, Baden-Wurttemberg, Germany)* **9**, e2204059 (2022).

[31] Chang, B. *et al.* Highly elastic binder for improved cyclability of nickel–rich layered cathode materials in lithium–ion batteries. *Advanced Energy Materials* **10**, 2001069 (2020). URL `https://onlinelibrary.wiley.com/doi/full/10.1002/aenm.202001069`.

[32] Wang, L. *et al.* Unraveling the degradation mechanism of lini0.8co0.1mn0.1o2 at the high cut-off voltage for lithium ion batteries. *Journal of Energy Chemistry* **77**, 428–437 (2023). URL `https://www.sciencedirect.com/science/article/pii/S2095495622006167`.

[33] Pritzl, D. *et al.* Editors' choice—washing of nickel-rich cathode materials for lithium-ion batteries: Towards a mechanistic understanding. *Journal of The Electrochemical Society* **166**, A4056–A4066 (2019).

[34] Oswald, S. *et al.* Effect of washing on nickel-rich ncms: methodology to quantify the lithium/proton-exchange kinetics, the inserted protons, and the structural changes. *Journal of Materials Chemistry A* (2024). URL `https://pubs.rsc.org/en/content/articlelanding/2024/ta/d4ta03319a`.

[35] Akhilash, M., Salini, P. S., John, B., Sujatha, S. & Mercy, T. D. Surface modification on nickel rich cathode materials for lithium-ion cells: A mini review. *The Chemical Record* **23**, e202300132 (2023). URL `https://onlinelibrary.wiley.com/doi/10.1002/tcr.202300132`.

[36] Kaur, G. & Gates, B. D. Review—surface coatings for cathodes in lithium ion batteries: From crystal structures to electrochemical performance. *Journal of The Electrochemical Society* **169**, 043504 (2022). URL `https://iopscience.iop.org/article/10.1149/1945-7111/ac60f3`.

[37] Dang, R. *et al.* The effect of elemental doping on nickel-rich ncm cathode materials of lithium ion batteries. *The Journal of Physical Chemistry C* **126**, 151–159 (2022).

[38] Sun, H. H. *et al.* Transition metal-doped ni-rich layered cathode materials for durable li-ion batteries. *Nature Communications* **12**, 6552 (2021). URL `https://www.nature.com/articles/s41467-021-26815-6`.

[39] Park, K.-J. *et al.* Improved cycling stability of li[ni 0.90 co 0.05 mn 0.05]o 2 through microstructure modification by boron doping for li-ion batteries. *Advanced Energy Materials* **8**, 1801202 (2018). URL `https://onlinelibrary.wiley.com/doi/full/10.1002/aenm.201801202`.

[40] Yin, S.-C., Rho, Y.-H., Swainson, I. & Nazar, L. F. X-ray/neutron diffraction and electrochemical studies of lithium de/re-intercalation in li 1-x co 1/3 ni 1/3 mn 1/3 o 2 (x = 0 → 1). *Chemistry of Materials* **18**, 1901–1910 (2006).

[41] Friedrich, F. *et al.* Editors' choice—capacity fading mechanisms of ncm-811 cathodes in lithium-ion batteries studied by x-ray diffraction and other diagnostics. *Journal of The Electrochemical Society* **166**, A3760–A3774 (2019).

[42] Momma, K. & Izumi, F. Vesta 3 for three-dimensional visualization of crystal, volumetric and morphology data. *Journal of Applied Crystallography* **44**, 1272–1276 (2011).

[43] Märker, K., Reeves, P. J., Xu, C., Griffith, K. J. & Grey, C. P. Evolution of structure and lithium dynamics in lini 0.8 mn 0.1 co 0.1 o 2 (nmc811) cathodes during electrochemical cycling. *Chemistry of Materials* **31**, 2545–2554 (2019).

[44] Xu, C., Reeves, P. J., Jacquet, Q. & Grey, C. P. Phase behavior during electrochemical cycling of ni–rich cathode materials for li–ion batteries. *Advanced Energy Materials* **11**, 2003404 (2021).

[45] Dai, Z., Li, Z., Chen, R., Wu, F. & Li, L. Defective oxygen inert phase stabilized high-voltage nickel-rich cathode for high-energy lithium-ion batteries. *Nature Communications* **14**, 8087 (2023). URL `https://www.nature.com/articles/s41467-023-43792-0`.

[46] Ko, D.-S. *et al.* Degradation of high–nickel–layered oxide cathodes from surface to bulk: A comprehensive structural, chemical, and electrical analysis. *Advanced Energy Materials* **10** (2020).

[47] Jung, C.-H., Shim, H., Eum, D. & Hong, S.-H. Challenges and recent progress in linixcoymn1−x−yo2 (ncm) cathodes for lithium ion batteries. *Journal of the Korean Ceramic Society* **58**, 1–27 (2021). URL `https://link.springer.com/article/10.1007/s43207-020-00098-x`.

[48] Manthiram, A. A reflection on lithium-ion battery cathode chemistry. *Nature Communications* **11**, 1550 (2020). URL `https://www.nature.com/articles/s41467-020-15355-0`.

[49] Lu, S.-j. *et al.* Single-crystal nickel-based cathodes: Fundamentals and recent advances. *Electrochemical Energy Reviews* **5**, 1–41 (2022). URL `https://link.springer.com/article/10.1007/s41918-022-00166-2`.

[50] Zhu, J. & Chen, G. Single-crystal based studies for correlating the properties and high-voltage performance of li[ni x mn y co 1−x−y]o 2 cathodes. *Journal of Materials Chemistry A* **7**, 5463–5474 (2019).

[51] Gent, W. E., Busse, G. M. & House, K. Z. The predicted persistence of cobalt in lithium-ion batteries. *Nature Energy* **7**, 1132–1143 (2022). URL `https://www.nature.com/articles/s41560-022-01129-z`.

[52] Saaid, F. I. *et al.* Ni-rich lithium nickel manganese cobalt oxide cathode materials: A review on the synthesis methods and their electrochemical performances. *Heliyon* **10**, e23968 (2024). URL `https://www.sciencedirect.com/science/article/pii/S2405844023111765`.

[53] Ruess, R. *et al.* Transition metal oxides and li 2 co 3 as precursors for the synthesis of ni-rich single-crystalline ncm for sustainable lithium-ion battery production. *Journal of The Electrochemical Society* **169**, 070531 (2022).

[54] Li, H. *et al.* An unavoidable challenge for ni-rich positive electrode materials for lithium-ion batteries. *Chemistry of Materials* **31**, 7574–7583 (2019).

[55] Trevisanello, E., Ruess, R., Conforto, G., Richter, F. H. & Janek, J. Polycrystalline and single crystalline ncm cathode materials—quantifying particle cracking, active surface area, and lithium diffusion. *Advanced Energy Materials* **11** (2021).

[56] Deng, X. *et al.* A comparative investigation of single crystal and polycrystalline ni–rich ncms as cathodes for lithium–ion batteries. *ENERGY & ENVIRONMENTAL MATERIALS* **6** (2023).

[57] Kondrakov, A. O. *et al.* Anisotropic lattice strain and mechanical degradation of high- and low-nickel ncm cathode materials for li-ion batteries. *The Journal of Physical Chemistry C* **121**, 3286–3294 (2017).

[58] Ryu, H.-H. *et al.* Capacity fading mechanisms in ni-rich single-crystal ncm cathodes. *ACS Energy Letters* **6**, 2726–2734 (2021).

[59] Abdollahifar, M. *et al.* Insights into influencing electrode calendering on the battery performance. *Advanced Energy Materials* **13** (2023).

[60] Mu, L. *et al.* Oxygen release induced chemomechanical breakdown of layered cathode materials. *Nano Letters* **18**, 3241–3249 (2018).

[61] Ahmed, S. *et al.* The role of intragranular nanopores in capacity fade of nickel-rich layered li(ni1-x-ycoxmny)o2 cathode materials. *ACS Nano* **13**, 10694–10704 (2019).

[62] Yan, P. *et al.* Intragranular cracking as a critical barrier for high-voltage usage of layer-structured cathode for lithium-ion batteries. *Nature Communications* **8**, 14101 (2017). URL `https://www.nature.com/articles/ncomms14101`.

[63] Mao, K. *et al.* Fracture mechanisms of ncm polycrystalline particles in lithium-ion batteries: A review. *Journal of Energy Storage* **84**, 110807 (2024). URL https://www.sciencedirect.com/science/article/pii/S2352152X24003918.

[64] Morzy, J. K. *et al.* Origins and importance of intragranular cracking in layered lithium transition metal oxide cathodes. *ACS Applied Energy Materials* **7**, 3945–3956 (2024).

[65] Yan, P. *et al.* Injection of oxygen vacancies in the bulk lattice of layered cathodes. *Nature Nanotechnology* **14**, 602–608 (2019). URL https://www.nature.com/articles/s41565-019-0428-8?utm_source=acs&getft_integrator=acs.

[66] Li, J. *et al.* Addressing cation mixing in layered structured cathodes for lithium-ion batteries: A critical review. *Nano Materials Science* **5**, 404–420 (2023). URL https://www.sciencedirect.com/science/article/pii/S2589965122000496.

[67] Wei, H.-x. *et al.* Comprehensive understanding of li/ni intermixing in layered transition metal oxides. *Materials Today* **51**, 365–392 (2021).

[68] Cho, H. *et al.* A review of problems and solutions in ni-rich cathode-based li-ion batteries from two research aspects: Experimental studies and computational insights. *Journal of Power Sources* **597**, 234132 (2024). URL https://www.sciencedirect.com/science/article/pii/S0378775324000831.

[69] Lin, F. *et al.* Surface reconstruction and chemical evolution of stoichiometric layered cathode materials for lithium-ion batteries. *Nature Communications* **5**, 3529 (2014). URL https://www.nature.com/articles/ncomms4529.

[70] Zhu, J. *et al.* Atomic-level understanding of surface reconstruction based on li[ni x mn y co 1– x – y]o 2 single-crystal studies. *ACS Applied Energy Materials* **3**, 4799–4811 (2020).

[71] Xu, C. *et al.* Bulk fatigue induced by surface reconstruction in layered ni-rich cathodes for li-ion batteries. *Nature Materials* **20**, 84–92 (2021). URL https://www.nature.com/articles/s41563-020-0767-8.

[72] Ryu, H.-H., Lim, H.-W., Lee, S. G. & Sun, Y.-K. Near-surface reconstruction in ni-rich layered cathodes for high-performance lithium-ion batteries. *Nature Energy* 1–10 (2023). URL https://www.nature.com/articles/s41560-023-01403-8.

[73] Orlova, E. D., Savina, A. A., Abakumov, S. A., Morozov, A. V. & Abakumov, A. M. Comprehensive study of li+/ni2+ disorder in ni-rich nmcs cathodes for li-ion batteries. *Symmetry* **13**, 1628 (2021). URL https://www.mdpi.com/2073-8994/13/9/1628#B5-symmetry-13-01628.

[74] Barthel, J. Dr. probe: A software for high-resolution stem image simulation. *Ultramicroscopy* **193**, 1–11 (2018). URL `https://www.sciencedirect.com/science/article/pii/S0304399118301402`.

[75] Hua, W. *et al.* Chemical and structural evolution during the synthesis of layered li(ni,co,mn)o 2 oxides. *Chemistry of Materials* **32**, 4984–4997 (2020).

[76] Bak, S.-M. *et al.* Structural changes and thermal stability of charged linixmnycozo$_2$ cathode materials studied by combined in situ time-resolved xrd and mass spectroscopy. *ACS Applied Materials & Interfaces* **6**, 22594–22601 (2014).

[77] Liu, W. *et al.* Nickel-rich layered lithium transition-metal oxide for high-energy lithium-ion batteries. *Angewandte Chemie International Edition* **54**, 4440–4457 (2015).

[78] Quintelier, M. *et al.* Determination of spinel content in cycled li1.2ni0.13mn0.54co0.13o2 using three-dimensional electron diffraction and precession electron diffraction. *Symmetry* **13**, 1989 (2021).

[79] Monge, M. Á., Amarilla, J. M., Gutiérrez-Puebla, E., Campa, J. A. & Rasines, I. Atomic level study of limn2o4 as electrode in lithium batteries. *ChemPhysChem* **3**, 367–370 (2002).

[80] Korthauer, R. (ed.) *Lithium-ion batteries: Basics and applications*. SpringerLink Bücher (Springer, Berlin, 2019).

[81] Abraham, D. P. *et al.* Microscopy and spectroscopy of lithium nickel oxide-based particles used in high power lithium-ion cells. *Journal of The Electrochemical Society* **150**, A1450 (2003).

[82] Lin, Q. *et al.* A new insight into continuous performance decay mechanism of ni-rich layered oxide cathode for high energy lithium ion batteries. *Nano Energy* **54**, 313–321 (2018). URL `https://www.sciencedirect.com/science/article/pii/S2211285518307092`.

[83] Li, J. *et al.* The impact of electrolyte additives and upper cut-off voltage on the formation of a rocksalt surface layer in lini 0.8 mn 0.1 co 0.1 o 2 electrodes. *Journal of The Electrochemical Society* **164**, A655–A665 (2017). URL `https://iopscience.iop.org/article/10.1149/2.0651704jes/meta`.

[84] Sun, H.-H. & Manthiram, A. Impact of microcrack generation and surface degradation on a nickel-rich layered li[ni 0.9 co 0.05 mn 0.05]o 2 cathode for lithium-ion batteries. *Chemistry of Materials* **29**, 8486–8493 (2017).

[85] Jung, S.-K. *et al.* Understanding the degradation mechanisms of lini 0.5 co 0.2 mn 0.3 o 2 cathode material in lithium ion batteries. *Advanced Energy*

Materials **4**, 1300787 (2014). URL https://onlinelibrary.wiley.com/doi/10.1002/aenm.201300787.

[86] Stich, M., Göttlinger, M., Kurniawan, M., Schmidt, U. & Bund, A. Hydrolysis of lipf 6 in carbonate-based electrolytes for lithium-ion batteries and in aqueous media. *The Journal of Physical Chemistry C* **122**, 8836–8842 (2018).

[87] Wandt, J., Freiberg, A. T., Ogrodnik, A. & Gasteiger, H. A. Singlet oxygen evolution from layered transition metal oxide cathode materials and its implications for lithium-ion batteries. *Materials Today* **21**, 825–833 (2018). URL https://www.sciencedirect.com/science/article/pii/S1369702118300737.

[88] Dose, W. M. *et al.* Onset potential for electrolyte oxidation and ni-rich cathode degradation in lithium-ion batteries. *ACS Energy Letters* **7**, 3524–3530 (2022).

[89] Jung, R., Metzger, M., Maglia, F., Stinner, C. & Gasteiger, H. A. Oxygen release and its effect on the cycling stability of lini x mn y co z o 2 (nmc) cathode materials for li-ion batteries. *Journal of The Electrochemical Society* **164**, A1361–A1377 (2017).

[90] Rinkel, B. L. D., Vivek, J. P., Garcia-Araez, N. & Grey, C. P. Two electrolyte decomposition pathways at nickel-rich cathode surfaces in lithium-ion batteries. *Energy & Environmental Science* **15**, 3416–3438 (2022). URL https://pubs.rsc.org/en/content/articlelanding/2022/ee/d1ee04053g.

[91] Phelan, C. M. E. *et al.* Role of salt concentration in stabilizing charged ni-rich cathode interfaces in li-ion batteries. *Chemistry of Materials* **36**, 3334–3344 (2024).

[92] Xue, W. *et al.* Ultra-high-voltage ni-rich layered cathodes in practical li metal batteries enabled by a sulfonamide-based electrolyte. *Nature Energy* **6**, 495–505 (2021). URL https://www.nature.com/articles/s41560-021-00792-y.

[93] Ruff, Z., Xu, C. & Grey, C. P. Transition metal dissolution and degradation in nmc811-graphite electrochemical cells. *Journal of The Electrochemical Society* **168**, 060518 (2021).

[94] Ko, D.-S. *et al.* Microstructural visualization of compositional changes induced by transition metal dissolution in ni-rich layered cathode materials by high-resolution particle analysis. *Nano Energy* **56**, 434–442 (2019). URL https://www.sciencedirect.com/science/article/pii/S2211285518308589.

[95] Hestenes, J. C., Sadowski, J. T., May, R. & Marbella, L. E. Transition metal dissolution mechanisms and impacts on electronic conductivity in composite lini0.5mn1.5o4 cathode films. *ACS materials Au* **3**, 88–101 (2023).

[96] Schipper, F. *et al.* Review—recent advances and remaining challenges for lithium ion battery cathodes. *Journal of The Electrochemical Society* **164**, A6220–A6228 (2017).

[97] Jung, R. *et al.* Effect of ambient storage on the degradation of ni-rich positive electrode materials (nmc811) for li-ion batteries. *Journal of The Electrochemical Society* **165**, A132–A141 (2018).

[98] Faenza, N. V. *et al.* Editors' choice—growth of ambient induced surface impurity species on layered positive electrode materials and impact on electrochemical performance. *Journal of The Electrochemical Society* **164**, A3727–A3741 (2017).

[99] Sicklinger, J., Metzger, M., Beyer, H., Pritzl, D. & Gasteiger, H. A. Ambient storage derived surface contamination of ncm811 and ncm111: Performance implications and mitigation strategies. *Journal of The Electrochemical Society* **166**, A2322–A2335 (2019).

[100] Shkrob, I. A. *et al.* Chemical weathering of layered ni-rich oxide electrode materials: Evidence for cation exchange. *Journal of The Electrochemical Society* **164**, A1489–A1498 (2017).

[101] Kim, Y., Park, H., Warner, J. H. & Manthiram, A. Unraveling the intricacies of residual lithium in high-ni cathodes for lithium-ion batteries. *ACS Energy Letters* **6**, 941–948 (2021).

[102] Renfrew, S. E. & McCloskey, B. D. Residual lithium carbonate predominantly accounts for first cycle co2 and co outgassing of li-stoichiometric and li-rich layered transition-metal oxides. *Journal of the American Chemical Society* **139**, 17853–17860 (2017).

[103] Freiberg, A. T., Sicklinger, J., Solchenbach, S. & Gasteiger, H. A. Li2co3 decomposition in li-ion batteries induced by the electrochemical oxidation of the electrolyte and of electrolyte impurities. *Electrochimica Acta* **346**, 136271 (2020). URL `https://www.sciencedirect.com/science/article/pii/S0013468620306630`.

[104] Chen, Z. *et al.* The high-temperature and high-humidity storage behaviors and electrochemical degradation mechanism of lini0.6co0.2mn0.2o2 cathode material for lithium ion batteries. *Journal of Power Sources* **363**, 168–176 (2017). URL `https://www.sciencedirect.com/science/article/pii/S0378775317309734`.

[105] Hartmann, L., Pritzl, D., Beyer, H. & Gasteiger, H. A. Evidence for li + /h + exchange during ambient storage of ni-rich cathode active materials. *Journal of The Electrochemical Society* **168**, 070507 (2021). URL `https://iopscience.iop.org/article/10.1149/1945-7111/ac0d3a`.

[106] Xu, S. *et al.* The effects of washing on lini0.83co0.13mn0.04o2 cathode materials. *Solid State Ionics* **334**, 105–110 (2019). URL `https://www.sciencedirect.com/science/article/pii/S0167273818309299`.

[107] Beyer, H. *et al.* (invited) ambient storage and washing of ncms: Formation/removal of surface contaminants and ncm structural changes upon heating of washed/stored ncms. *ECS Meeting Abstracts* **MA2021-02**, 389 (2021).

[108] Sun, Y.-K. *et al.* Nanostructured high-energy cathode materials for advanced lithium batteries. *Nature Materials* **11**, 942–947 (2012). URL `https://www.nature.com/articles/nmat3435`.

[109] Lin, R. *et al.* Hierarchical nickel valence gradient stabilizes high-nickel content layered cathode materials. *Nature Communications* **12**, 2350 (2021). URL `https://www.nature.com/articles/s41467-021-22635-w`.

[110] Yan, W., Yang, S., Huang, Y., Yang, Y. & Yuan, G. A review on doping/coating of nickel-rich cathode materials for lithium-ion batteries. *Journal of Alloys and Compounds* **819**, 153048 (2020). URL `https://www.sciencedirect.com/science/article/pii/S092583881934294X`.

[111] Wang, L. *et al.* Optimized structure stability and cycling performance of lini0.8co0.1mn0.1o2 through homogeneous nano-thickness al2o3 coating. *Electrochimica Acta* **435**, 141411 (2022). URL `https://www.sciencedirect.com/science/article/pii/S0013468622015687`.

[112] Zhao, W. *et al.* Optimized al doping improves both interphase stability and bulk structural integrity of ni-rich nmc cathode materials. *ACS Applied Energy Materials* **3**, 3369–3377 (2020).

[113] Li, L. *et al.* Effect of al substitution sites on li 1−x al x (ni 0.5 co 0.2 mn 0.3) 1−y al y o 2 cathode materials for lithium ion batteries. *Journal of Alloys and Compounds* **686**, 30–37 (2016). URL `https://www.sciencedirect.com/science/article/pii/S0925838816316942`.

[114] Dixit, M., Markovsky, B., Aurbach, D. & Major, D. T. Unraveling the effects of al doping on the electrochemical properties of lini 0.5 co 0.2 mn 0.3 o 2 using first principles. *Journal of The Electrochemical Society* **164**, A6359–A6365 (2017).

[115] Reimer, L. & Kohl, H. *Transmission electron microscopy: Physics of image formation*, vol. 36 of *Springer Series in Optical Sciences* (Springer, New York, NY, 2008), 5. ed. edn.

[116] Reimer, L. *Scanning electron microscopy: Physics of image formation and microanalysis*, vol. 45 of *Springer Series in Optical Sciences* (Springer, Berlin and Heidelberg, 1998), 2., completely rev. and updated ed. edn.

[117] Williams, D. B. & Carter, C. B. *Transmission Electron Microscopy: A Textbook for Materials Science* (Springer US, Boston, MA, 2009), 2. ed. edn.

[118] Pennycook, S. J. *Scanning Transmission Electron Microscopy: Imaging and Analysis* (Springer New York, New York, NY, 2011). URL https://ebookcentral.proquest.com/lib/kxp/detail.action?docID=691040.

[119] Egerton, R. F. *Electron Energy-Loss Spectroscopy in the Electron Microscope*. SpringerLink Bücher (Springer US, Boston, MA, 2011).

[120] Giannuzzi, L. A. & Stevie, F. A. (eds.) *Introduction to focused ion beams: Instrumentation, theory, techniques and practice* (Springer, New York, NY, 2005). URL https://ebookcentral.proquest.com/lib/kxp/detail.action?docID=226458.

[121] Scherzer, O. The theoretical resolution limit of the electron microscope. *Journal of Applied Physics* **20**, 20–29 (1949).

[122] Cowley, J. M. Image contrast in a transmission scanning electron microscope. *Applied Physics Letters* **15**, 58–59 (1969).

[123] Pennycook, S. J. & Boatner, L. A. Chemically sensitive structure-imaging with a scanning transmission electron microscope. *Nature* **336**, 565–567 (1988). URL https://www.nature.com/articles/336565a0.

[124] Findlay, S. D. *et al.* Dynamics of annular bright field imaging in scanning transmission electron microscopy. *Ultramicroscopy* **110**, 903–923 (2010). URL https://www.sciencedirect.com/science/article/pii/S0304399110001129.

[125] Findlay, S. D. *et al.* Annular bright-field scanning transmission electron microscopy: Direct and robust atomic-resolution imaging of light elements in crystalline materials. *Microscopy Today* **25**, 36–41 (2017). URL https://academic.oup.com/mt/article/25/6/36/6815498.

[126] Lazić, I., Bosch, E. G. T. & Lazar, S. Phase contrast stem for thin samples: Integrated differential phase contrast. *Ultramicroscopy* **160**, 265–280 (2016). URL https://www.sciencedirect.com/science/article/pii/S0304399115300449.

[127] Ophus, C. Four-dimensional scanning transmission electron microscopy (4d-stem): From scanning nanodiffraction to ptychography and beyond. *Microscopy and Microanalysis* **25**, 563–582 (2019). URL https://academic.oup.com/mam/article/25/3/563/6887544.

[128] Jones, L. Scan-noise and drift correction in the stem. *Microscopy Today* **22**, 40–41 (2014).

[129] Scherzer, O. Über einige fehler von elektronenlinsen. *Zeitschrift für Physik* **101**, 593–603 (1936). URL https://link.springer.com/article/10.1007/BF01349606.

[130] Scherzer, O. Sphärische und chromatische korrektur von elektronen-linsen. *Optik* 114–132 (1947).

[131] Rose, H. Outline of a spherically corrected semiaplanatic medium-voltage transmission electron microscope. *Optik* 19–24 (1990).

[132] Rose, H. H. Optics of high-performance electron microscopes. *Science and Technology of Advanced Materials* **9**, 014107 (2008).

[133] Haider, M. *et al.* A spherical-aberration-corrected 200kv transmission electron microscope. *Ultramicroscopy* **75**, 53–60 (1998). URL https://www.sciencedirect.com/science/article/pii/S0304399198000485.

[134] Krivanek, O. L., Dellby, N. & Lupini, A. R. Towards sub-å electron beams. *Ultramicroscopy* **78**, 1–11 (1999). URL https://www.sciencedirect.com/science/article/pii/S0304399199000133.

[135] Krivanek, O. L. *et al.* Vibrational spectroscopy in the electron microscope. *Nature* **514**, 209–212 (2014). URL https://www.nature.com/articles/nature13870.

[136] What is eels? | eels.info (1/7/2025). URL https://eels.info/about/overview.

[137] Francisco de la Peña *et al. hyperspy/hyperspy: v2.1.0* (Zenodo, 2024). URL https://zenodo.org/records/11148112.

[138] Francisco de la Peña *et al. hyperspy/exspy: v0.2* (Zenodo, 2024). URL https://zenodo.org/records/10953535.

[139] Lin, F., Markus, I. M., Doeff, M. M. & Xin, H. L. Chemical and structural stability of lithium-ion battery electrode materials under electron beam. *Scientific Reports* **4**, 5694 (2014). URL https://www.nature.com/articles/srep05694.

[140] Seo.2024Seo, J. H. *et al.* Electron beam-induced effects on a ni-rich layered cathode material: A comprehensive investigation using stem and eels. *The Journal of Physical Chemistry C* **128**, 9099–9104 (2024).

[141] User manual wildfire h+ dt: Compatible with thermo fischer /fei microscopes.

[142] Basak, S. *et al.* Screening of coatings for an all-solid-state battery using in situ transmission electron microscopy. *Journal of Visualized Experiments (JoVE)* e64316 (2023). URL https://app.jove.com/t/64316.

[143] Vettori, K. *et al.* Chemical and structural degradation of single crystalline high–nickel cathode materials during high–voltage holds. *Advanced Energy Materials* **15** (2025).

[144] Jems-swiss (10/30/2024). URL `https://www.jems-swiss.ch/`.

[145] Chang, Z. *et al.* Sustainable lithium-metal battery achieved by a safe electrolyte based on recyclable and low-cost molecular sieve. *Angewandte Chemie International Edition* **60**, 15572–15581 (2021). URL `https://onlinelibrary.wiley.com/doi/10.1002/anie.202104124`.

[146] SASAKI, S., FUJINO, K. & TAKÉUCHI, Y. X-ray determination of electron-density distributions in oxides, mgo, mno, coo, and nio, and atomic scattering factors of their constituent atoms. *Proceedings of the Japan Academy, Series B* **55**, 43–48 (1979).

[147] Lin, F. *et al.* Profiling the nanoscale gradient in stoichiometric layered cathode particles for lithium-ion batteries. *Energy & Environmental Science* **7**, 3077 (2014). URL `https://pubs.rsc.org/en/content/articlelanding/2014/ee/c4ee01400f`.

[148] Kang, Y.-S. *et al.* Revealing the structural degradation mechanism of the ni-rich cathode surface: How thick is the surface? *Journal of Power Sources* **490**, 229542 (2021). URL `https://www.sciencedirect.com/science/article/pii/S0378775321000896`.

[149] Koyama, Y., Mizoguchi, T., Ikeno, H. & Tanaka, I. Electronic structure of lithium nickel oxides by electron energy loss spectroscopy. *The journal of physical chemistry. B* **109**, 10749–10755 (2005).

[150] Yoon, M. *et al.* Reactive boride infusion stabilizes ni-rich cathodes for lithium-ion batteries. *Nature Energy* **6**, 362–371 (2021). URL `https://www.nature.com/articles/s41560-021-00782-0`.

[151] Liu, H. *et al.* Spatially resolved surface valence gradient and structural transformation of lithium transition metal oxides in lithium-ion batteries. *Physical chemistry chemical physics : PCCP* **18**, 29064–29075 (2016).

[152] Shah, N. A. *et al.* Nature of the oxygen-loss-induced rocksalt layer and its impact on capacity fade in ni-rich layered oxide cathodes. *ACS Energy Letters* 1313–1320 (2025).

[153] Wei, Z. *et al.* In-depth study on diffusion of oxygen vacancies in li(nixcoymnz)o2 cathode materials under thermal induction. *Energy Storage Materials* **47**, 51–60 (2022). URL `https://www.sciencedirect.com/science/article/pii/S2405829722000629`.

[154] Wei, Z. *et al.* Probing the thermal degradation mechanism of polycrystalline and single-crystal li(ni0.8co0.1mn0.1)o2 cathodes from the perspective of oxygen vacancy diffusion. *Energy Storage Materials* **56**, 495–505 (2023). URL https://www.sciencedirect.com/science/article/pii/S2405829723000399.

[155] Song, Y. *et al.* Revealing the origin of high-thermal-stability of single-crystal ni-rich cathodes toward higher-safety batteries. *Nano Energy* **116**, 108846 (2023). URL https://www.sciencedirect.com/science/article/pii/S2211285523006833.

[156] Martinez, A. C. *et al.* High reactivity of the nickel-rich lini1-x-ymnxcoyo2 layered materials surface towards h2o/co2 atmosphere and lipf6-based electrolyte. *Journal of Power Sources* **468**, 228204 (2020). URL https://www.sciencedirect.com/science/article/pii/S0378775320305073.

[157] Zhu, W. *et al.* Ultrathin al2o3 coating on lini0.8co0.1mn0.1o2 cathode material for enhanced cycleability at extended voltage ranges. *Coatings* **9**, 92 (2019).

[158] Hu, D. *et al.* An effective strategy to control thickness of al2o3 coating layer on nickel-rich cathode materials. *Journal of Electroanalytical Chemistry* **880**, 114910 (2021). URL https://www.sciencedirect.com/science/article/pii/S1572665720311395.

[159] Herzog, M. J., Gauquelin, N., Esken, D., Verbeeck, J. & Janek, J. Facile dry coating method of high–nickel cathode material by nanostructured fumed alumina (al 2 o 3) improving the performance of lithium–ion batteries. *Energy Technology* **9** (2021).

[160] Shriya Agarwal. *Structural Analysis of Li-ion Battery Electrodes using Electron Microscopy: Master thesis* (2024).

[161] Basak, S. *et al.* Operando transmission electron microscopy of battery cycling: thickness dependent breaking of tio2 coating on si/sio2 nanoparticles. *Chemical communications (Cambridge, England)* **58**, 3130–3133 (2022).

[162] Ishidzu, K., Oka, Y. & Nakamura, T. Lattice volume change during charge/discharge reaction and cycle performance of li[nixcoymnz]o2. *Solid State Ionics* **288**, 176–179 (2016). URL https://www.sciencedirect.com/science/article/pii/S0167273816000126.

[163] Chu, Y. *et al.* Oxygen release in ni–rich layered cathode for lithium–ion batteries: Mechanisms and mitigating strategies. *ChemElectroChem* **11**, e202300653 (2024). URL https://chemistry-europe.onlinelibrary.wiley.com/doi/10.1002/celc.202300653.

[164] Duan, Y., Chen, S.-P., Zhang, L., Guo, L. & Shi, F.-N. Review on oxygen release mechanism and modification strategy of nickel-rich ncm cathode materials for lithium-ion batteries: Recent advances and future directions. *Energy & Fuels* **38**, 5607–5631 (2024).

[165] Na, S. *et al.* Formation cycle control for enhanced structural stability of ni-rich linixcoymn1-x-yo2 cathodes. *ACS Nano* **19**, 2136–2147 (2025).

[166] Zhang, L. *et al.* Heterogeneous degradation in thick nickel-rich cathodes during high-temperature storage and mitigation of thermal instability by regulating cationic disordering. *Small (Weinheim an der Bergstrasse, Germany)* **17**, e2102055 (2021).

[167] Sharifi-Asl, S., Lu, J., Amine, K. & Shahbazian-Yassar, R. Oxygen release degradation in li–ion battery cathode materials: Mechanisms and mitigating approaches. *Advanced Energy Materials* **9** (2019).

[168] Memm, M., Hoffmann, A. & Wohlfahrt-Mehrens, M. Water-based lini1/3mn1/3co1/3o2-cathodes with good electrochemical performance by use of additives. *Electrochimica Acta* **260**, 664–673 (2018).

[169] Radloff, S., Scurtu, R.-G., Hölzle, M. & Wohlfahrt-Mehrens, M. Water-based lini 0.83 co 0.12 mn 0.05 o 2 electrodes with excellent cycling stability fabricated using unconventional binders. *Journal of The Electrochemical Society* **169**, 040514 (2022).

[170] Radloff, S. *et al.* Mitigating water-induced surface degradation in water-based ni-rich li-ion battery electrodes. *Journal of Power Sources* **580**, 233314 (2023). URL `https://www.sciencedirect.com/science/article/pii/S0378775323006900`.

[171] Gault, B. *et al.* Atom probe tomography. *Nature Reviews Methods Primers* **1**, 1–30 (2021). URL `https://www.nature.com/articles/s43586-021-00047-w`.

[172] Kim, S.-H. *et al.* Atom probe analysis of electrode materials for li-ion batteries: challenges and ways forward. *Journal of Materials Chemistry A* **10**, 4926–4935 (2022).

[173] Lee, J. Y. *et al.* Three-dimensional evaluation of compositional and structural changes in cycled lini1/3co1/3mn1/3o2 by atom probe tomography. *Journal of Power Sources* **379**, 160–166 (2018).

[174] Singh, M. P. *et al.* Near–atomic–scale evolution of the surface chemistry in li[ni,mn,co]o 2 cathode for li–ion batteries stored in air. *Advanced Energy and Sustainability Research* **4** (2023).

[175] Singh, M. P. *et al.* Facilitating the systematic nanoscale study of battery materials by atom probe tomography through in–situ metal coating. *Batteries & Supercaps* **7** (2024).

[176] Chen, Y.-S. *et al.* Atom probe tomography for the observation of hydrogen in materials: A review. *Microscopy and Microanalysis* **29**, 1–15 (2023).

[177] Ahmed, S. *et al.* Visualization of light elements using 4d stem: The layered–to–rock salt phase transition in linio 2 cathode material. *Advanced Energy Materials* **10**, 2001026 (2020).

[178] Lee, S.-Y. *et al.* Revisiting primary particles in layered lithium transition-metal oxides and their impact on structural degradation. *Advanced Science* **6**, 1800843 (2019). URL `https://advanced.onlinelibrary.wiley.com/doi/10.1002/advs.201800843`.

[179] Zhou, Y.-N. *et al.* High–rate charging induced intermediate phases and structural changes of layer–structured cathode for lithium–ion batteries. *Advanced Energy Materials* **6**, 1600597 (2016). URL `https://advanced.onlinelibrary.wiley.com/doi/full/10.1002/aenm.201600597`.

[180] Yang, Y. *et al.* Unlocking the potential of li-rich mn-based oxides for high-rate rechargeable lithium-ion batteries. *Advanced Materials* **35**, e2307138 (2023).

[181] Liu, Z. *et al.* Revealing the degradation pathways of layered li-rich oxide cathodes. *Nature Nanotechnology* **19**, 1821–1830 (2024). URL `https://www.nature.com/articles/s41565-024-01773-4`.

[182] Zhang, C. *et al.* Recent progress of in situ transmission electron microscopy for energy materials. *Advanced Materials* **32**, e1904094 (2020).

[183] Xie, Z.-H., Jiang, Z. & Zhang, X. Review—promises and challenges of in situ transmission electron microscopy electrochemical techniques in the studies of lithium ion batteries. *Journal of The Electrochemical Society* **164**, A2110–A2123 (2017). URL `https://iopscience.iop.org/article/10.1149/2.1451709jes`.

[184] Basak, S. *et al.* Characterizing battery materials and electrodes via in situ / operando transmission electron microscopy. *Chemical Physics Reviews* **3**, 031303 (2022). URL `https://aip.scitation.org/doi/full/10.1063/5.0075430`.

List of Figures

1.1. Schematic of the working principle of a battery. 2

2.1. Crystal structure of Ni-rich NCM 8
2.2. Crystal structures in Ni-rich NCM depends on SOC 9
2.3. Electronic band structure of NCM 10
2.4. Schematic of PC and single crystalline NCM powder 11
2.5. Degradation mechanisms in Ni-rich NCM 12
2.6. Phase transition from layered to rock salt structure 14
2.7. Li^+/H^+ ion-exchange 20

3.1. Simplified ray diagram TEM 26
3.2. Amplitude contrast 27
3.3. Phase contrast in HR-TEM 28
3.4. Schematic ray diagram STEM 30
3.5. Imaging modes in STEM 31
3.6. Schematic showing different STEM detectors 33
3.7. Spherical aberration 34
3.8. Inelastic scattering and secondary processes used in analytical TEM . 36
3.9. Schematic of EEL spectrometer 37
3.10. EEL spectrum 38
3.11. EDX spectrum 39
3.12. *In situ* heating: holder and setup 42
3.13. *In situ* biasing: holder and setup 43
3.14. Schematic of an SEM 44
3.15. Schematic of a FIB 45

4.1. Schematic of sample requirements: edge-on and thin samples 48
4.2. Embedding powder in epoxy 50
4.3. Standard FIB procedure 52
4.4. Failures of FIB sample preparation 56
4.5. Improvements of FIB sample preparation 57
4.6. *In situ* chip preparation 60
4.7. Schematic of NCM powder particles before and after crushing with mortar and pestle. 62
4.8. STEM images showing crushed particles on a carbon hole grid. 62

5.1. Representative XRD-spectrum of layered NCM. 64
5.2. Morphology single crystalline Ni-rich NCM powder 64

5.3. Morphology polycrystalline Ni-rich NCM powder 65
5.4. Example HAADF-STEM images of layered and rock-salt NCM 66
5.5. Simulated HAADF-images of layered, spinel and rock salt structure and the corresponding structure models 68
5.6. Relative R_{ct} curve 71
5.7. Reference sample of high potential study. 72
5.8. Severity of surface degradation depended on the direction of the lithium channels. 73
5.9. Inhomogeneous degradation within a single particle depending on the surrounding of the particle 74
5.10. Inhomogeneous degradation along grain boundary interfaces 76
5.11. Measuring thickness of rock salt layer: bright fringes 77
5.12. Measuring thickness of rock salt layer: line scan 78
5.13. Measuring thickness of rock salt layer: Fourier coefficient map 80
5.14. Examples of patches of the layered and the rock salt structure used for Fourier coefficient mapping and the corresponding FT pattern. . . 81
5.15. Fourier coefficient maps 83
5.16. EEL spectra showing structural surface degradation after high potential holds 86
5.17. Anisotropic core-shell model with gradual transition boundary. 89
5.18. TGA results of protonated NCM. 91
5.19. Overview of pristine and washed samples indicating nano-structural defects formation. 93
5.20. HAADF-imaging and EDX-analysis of sample washed and heated to 300 °C. 94
5.21. HR-STEM image of particle surface of a pristine sample. 95
5.22. HR-STEM images of the particle surface of a sample washed and heated to 300 °C. 97
5.23. HR-STEM images of the particle core of a sample washed and heated to 300 °C. 98
5.24. Images of an *in situ* heating experiment of a washed sample. 100
5.25. Images of an *in situ* heating experiment of a pristine sample. 102
5.26. *Ex situ* XRD results of pristine and washed samples [34] 106
5.27. HAADF-STEM and EDX results showing a Al_2O_3 coating layer on top of a PC-NCM particle 108
5.29. IV-curve recorded during *in situ* biasing experiment. 111
5.30. TEM image set recorded during *in situ* biasing experiment. 111
5.31. Pictures of fluorescence screen showing sample before and after biasing 112

6.1. Image simulation showing thickness series of HAADF-STEM, ABF-STEM and iDPC-STEM imaging. 120

List of Tables

2.1. Literature overview about phase transition on the surface in Ni-rich NCM. 17

4.1. FIB Process Steps 54

A. Synthesis protocols

The synthesis procedure and further treatments of the material used in Section 5.2 can be found in [143] and for the material used in Section 5.3 can be foudn in [34].

A.1. PC-NCM coated with Al_2O_3

The NCM powder synthesis was carried out by Kilian Vettori at JLU Gießen. The commercial NCM hydroxid precursor (Shandong Gelon Lib Co., Ltd) with a Li/TM ratio of 1.069 was mixed. The powder was calcined after the following heating scheme under oxygen flow of 100 sccm. First, the material was heated with 100 °C/h up to 550 °C, where the temperature was kept for 3 h. Subsequently, the temperature was again increased with a heat ramp of 100 °C/h up to 850 °C, where the temperature was 12 h before it was reduced to room temperature with 100 °C/h. The calcined powder was ground with mortar and pestle. The powder was washed twice in water with a H_2O:CAM ratio of 10:1. To remove the water, the powder was washed in ethanol with a mass ratio 1 : 1. During each washing step, the powder was stirred for 1 min, then centrifuged and decanted. For post-annealing, the material was heated with a temperature ramp of 100 °C/h to 750 °C, where the temperature was kept for 3 h. Subsequently, the powder was sieved in an ambient atmosphere and dried in a Büchi 120 °C for 12 h before being transferred to a glovebox.

B. Python scripts

In the following the python scripts used for EELS data analysis and Fourier coefficient mapping are presented. The notebooks are also available on GitHub https://github.com/laraahr/Dissertation.

B.1. EELS analysis

```
#!/usr/bin/env python
# coding: utf-8

# In[1]:


#EELS data analysis using hyperspy
#input from the public notebook written by Magnus Nord (https://github.com/ePSIC-DLS/Hyperspy_Workshop_2024/blob/main/EELS/EELS_finestructure_analysis_full.ipynb)
#goal: fit oxygen and Ni edge
#mateial: Ni-rich NCM cathode material for LIBs


# ## General/Loading data

# In[2]:


get_ipython().run_line_magic('matplotlib', 'qt5')


# In[3]:


import hyperspy.api as hs
import numpy as np
import matplotlib.pyplot as plt
from mpl_toolkits.axes_grid1.anchored_artists import AnchoredSizeBar
import matplotlib.font_manager as fm
import matplotlib.patheffects as patheffects
from matplotlib import cm
from matplotlib.colors import LinearSegmentedColormap


```

```
# In[4]:


#load signal
signals = hs.load(r"240302_CAM-Deg_4.5V_37d_L3_P4_top\STEM SI.dm4")


# In[5]:


# ckeck what kind of signals is included
signals

#check metadata
signals[3].metadata


# In[6]:


#define low loss peak
s_ll = signals[2]
s_ll


# In[7]:


#define high loss peak
s_hl = signals[3]
s_hl
s_hl.plot()


# In[8]:


#align hl to ZLP
s_ll.align_zero_loss_peak(also_align = [s_hl], crop=False)


# In[9]:


# check if ZLP alignment worked
s_ll.plot()


# ## Fine structure Ni-edge

# In[10]:

```

```
86
87 #Bin data --> specify the new:old pixel ratio for each dimension
88 #1 = no binning, 2 = each pixel in the new spectrum is twice the
      size of the pixels in the old spectrum
89 s_hl_binned_ni = s_hl.rebin(scale = (50,1,1)) # old dimensions:
      (50, 360|2048)
90 s_hl_binned_ni.plot()
91
92
93 # In[11]:
94
95
96 #crop signal
97 s_hl_binned_ni.plot()
98 s_hl_binned_ni.crop_signal()
99
100
101 # In[12]:
102
103
104 s_hl_binned_ni.axes_manager.signal_axes[0].offset, s_hl_binned_ni.
      axes_manager.signal_axes[0].scale
105
106
107 # In[13]:
108
109
110 #remove background
111 s_hl_binned_ni.plot()
112 s_hl_binned_ni.remove_background()
113
114
115 # In[14]:
116
117
118 s_hl_binned_ni.plot()
119
120
121 # ## Line plot
122
123 # In[15]:
124
125
126 # Bin data for line plot and exclude artefacts
127
128 #Bin data --> specify the new:old pixel ratio for each dimension
129 #1 = no binning, 2 = each pixel in the new spectrum is twice the
      size of the pixels in the old spectrum
130 s_hl_binned_ni_2 = s_hl.rebin(scale = (50,4,1)) # old dimensions:
      (50, 360|2048)
131 s_hl_binned_ni_2.plot()
132
```

```
133
134 # In[16]:
135
136
137 #crop signal
138 s_hl_binned_ni_2.plot()
139 s_hl_binned_ni_2.crop_signal()
140
141
142 # In[17]:
143
144
145 #remove background
146 s_hl_binned_ni_2.plot()
147 s_hl_binned_ni_2.remove_background()
148
149
150 # In[18]:
151
152
153 # 1. created model without any conent
154 m = s_hl_binned_ni_2.create_model(auto_background = False)
155
156
157 # In[19]:
158
159
160 # 2. create components for each edge
161 ni_1 = hs.model.components1D.Gaussian()
162 ni_2 = hs.model.components1D.Gaussian()
163
164 # 3. load components into model
165 m.append(ni_1)
166 m.fit_component(ni_1, signal_range = (845., 863.), only_current =
    False)
167
168 m.plot(plot_components=True)
169
170
171 # In[20]:
172
173
174 m[0].plot()
175
176
177 # In[21]:
178
179
180 #center of gaussian
181 gaussian_center = ni_1.centre.as_signal()
182 gaussian_center
183
```

```
184
185
186 # In[22]:
187
188
189 gaussian_center.axes_manager
190
191
192 # In[23]:
193
194
195 #### making a line plot
196
197 # need to match the scale and pixel --> check ut axes.manager
198 x = np.linspace(0, 175, 90)
199 y = np.median(gaussian_center, axis=1)
200 y = y[0:90]
201 fig, ax1 = plt.subplots(1, 1)
202
203 # only the actual sample and exclude noise
204 ax1.set_xlim(30, 175)
205
206
207 plt.xlabel('Distance [nm]', fontsize = 12)
208 plt.ylabel('Maximum value of the Ni-L3 edge [eV]', fontsize = 12)
209
210 ax1.plot(x, y)
211
212
213 # In[24]:
214
215
216 # Find energy values for dashed lines later
217 x_min = 30
218 x_max = 120
219
220 # Find the index of the closest x-value
221 closest_index_min = np.abs(x - x_min).argmin()
222 closest_index_max = np.abs(x - x_max).argmin()
223 # Get the corresponding y-value
224 y_min = y[closest_index_min]
225 y_max = y[closest_index_max]
226 #print(f"The y-value at x = {specific_x} is approximately {
       y_value_at_specific_x}")
227
228
229 # In[25]:
230
231
232 y_min
233
234
```

```
# In[26]:


y_max


# In[27]:


s_hl_binned_ni.axes_manager


# In[28]:


shape = s_hl_binned_ni.data.shape
shape


# ## Fine-structure oxygen-edge

# In[29]:


get_ipython().run_line_magic('matplotlib', 'qt5')
s_hl_binned_ox = s_hl.rebin(scale=(50,1,1))
s_hl_binned_ox.plot()


# In[30]:


s_hl_binned_ox.plot()
s_hl_binned_ox.remove_background()


# In[31]:


#check if background substraction worked
s_hl_binned_ox.plot()


# In[32]:


s_hl_binned_ox.plot()
s_hl_binned_ox.crop_signal()


# ## Plot oxygen and Ni-edge

```

```
# In[36]:


get_ipython().run_line_magic('matplotlib', 'inline')

# Assuming s_hl_binned_ox and s_hl_binned_ni are defined
# Define the datasets
offset_ox = s_hl_binned_ox.axes_manager.signal_axes[0].offset
scale_ox = s_hl_binned_ox.axes_manager.signal_axes[0].scale
x1 = [offset_ox + i * scale_ox for i in range(558)]
offset_ni = s_hl_binned_ni.axes_manager.signal_axes[0].offset
scale_ni = s_hl_binned_ni.axes_manager.signal_axes[0].scale
x2 = [offset_ni + i * scale_ni for i in range(541)]
# Create a figure with two subplots
fig, (ax1, ax2) = plt.subplots(1, 2, figsize=(10, 6), dpi=500,
    gridspec_kw={'width_ratios': [1, 1]})
fig.subplots_adjust(wspace=0.05)  # Adjust space between subplots


# Create a truncated colormap
def truncate_colormap(cmap, minval=0.0, maxval=0.75, n=100):
    new_cmap = LinearSegmentedColormap.from_list(
        'truncated', cmap(np.linspace(minval, maxval, n)))
    return new_cmap

# Use the truncated colormap
cmap = truncate_colormap(cm.get_cmap('Reds_r'), 0.0, 0.75)


# Plot the first dataset on the first axis
num_lines = len(range(60, 230, 10))
offsets = 7500
for idx, i in enumerate(range(60, 230, 10)):
    ax1.plot(x1, s_hl_binned_ox.data[i, 0] + (offsets * i), color=
    cmap(idx / (num_lines - 1)))

# Plot the second dataset on the second axis
for idx, i in enumerate(range(60, 230, 10)):
    ax2.plot(x2, s_hl_binned_ni.data[i, 0] + (offsets * i), color=
    cmap(idx / (num_lines - 1)))

#lowest_line_max = x2[np.argmax(s_hl_binned_ni[60])]
#highest_line_max = x2[np.argmax(s_hl_binned_ni[240])]

# Add dashed vertical lines
#ax2.axvline(lowest_line_max, color='gray', linestyle='--')
#ax2.axvline(highest_line_max, color='gray', linestyle='--')



# Set limits and labels
ax1.set_xlim(510, 580)
```

```
ax2.set_xlim(840, 890)
ax1.set_ylim(0.2*10**6, 2.3*10**6)
ax2.set_ylim(0.2*10**6, 2.3*10**6)
#ax1.set_xlabel('Energy (eV)')
#ax2.set_xlabel('Energy (eV)')
fig.supxlabel ('Energy [eV]',  fontsize = 12)
#set_xlabel('Energy (eV)')
ax1.set_ylabel('EELS Intensity [a.u.]', fontsize = 12)

# Customize x-ticks for ax1 and ax2
ax1.set_xticks([520, 540, 560])
ax1.set_xticks(np.arange(510, 579, 10), minor=True)
ax2.set_xticks([840, 860, 880])
ax2.set_xticks(np.arange(840, 891, 10), minor=True)
ax1.tick_params(axis='x', which='major', length=7, labelsize=12)
ax1.tick_params(axis='x', which='minor', length=4, labelsize=12)
ax2.tick_params(axis='x', which='major', length=7, labelsize=12)
ax2.tick_params(axis='x', which='minor', length=4, labelsize=12)
ax1.set_yticks([])
ax2.set_yticks([])
#ax.tick_params(axis='both', which='major', labelsize=12)


# Hide the spines between the subplots
ax1.spines['right'].set_visible(False)
ax2.spines['left'].set_visible(False)
ax1.yaxis.tick_left()
ax2.yaxis.tick_right()

# Add diagonal lines to indicate the break
d = .015  # Size of diagonal lines
kwargs = dict(transform=ax1.transAxes, color='k', clip_on=False)
ax1.plot((1-d, 1+d), (-d, +d), **kwargs)
ax1.plot((1-d, 1+d), (1-d, 1+d), **kwargs)

kwargs.update(transform=ax2.transAxes)
ax2.plot((-d, +d), (-d, +d), **kwargs)
ax2.plot((-d, +d), (1-d, 1+d), **kwargs)

#Dashed lines
ax2.axvline(x=852.75, color='gray', linestyle='--', linewidth=1)
ax2.axvline(x=854.4, color='gray', linestyle='--', linewidth=1)

# Add a color bar
sm = plt.cm.ScalarMappable(cmap=cmap, norm=plt.Normalize(vmin=0,
    vmax=80))
sm.set_array([])
cbar = fig.colorbar(sm, ax=ax2, orientation='vertical', anchor
    =(-0.0, 0.315), shrink=0.60)
cbar.set_ticks([0, 10, 20, 30, 40, 50, 60, 70, 80])
cbar.set_label('Depth [nm]', fontsize = 12)
cbar.ax.tick_params(labelsize=12)
```

```
386
387
388 plt.show()
389 #plt.savefig('240302_CAM-Deg_4.5V_37d_L3_P4_top_spectrum.svg')
390
391
392 # In[ ]:
```

Listing B.1: Python scrip to analyze EELS data.

B.2. Fourier coefficient mapping

```
1  #!/usr/bin/env python
2  # coding: utf-8
3
4  # In[1]:
5
6
7  # ----------------------------------------------------------------
8  # image contrast analysis  - mix factor between layered and
9  # rock-salt structure at the grain surface
10 #
11 # L. Ahrens, J. Barthel
12 # ER-C 2, Forschungszentrum J lich GmbH, J lich 52425, Germany
13 # ----------------------------------------------------------------
14
15
16 # In[2]:
17
18
19 import os
20 import ncempy
21 import numpy as np
22 from emilys.image.arrayplot import arrayplot2d
23 #import emilys.image.kernels as ek
24 import emilys.image.imagedata as ed
25 #import emilys.image.peakfit as pfit
26 import matplotlib.pyplot as plt
27 from scipy.optimize import curve_fit
28 from matplotlib.patches import Circle, Rectangle, Arrow
29
30
31 # In[3]:
32
33
34 swd = r'' #set file path
35 sfn0 = '0039 - 20231116_CAM-Deg_4.5V_23d_L1_STEM_HAADF_5.10_Mx DCFI
       (HAADF).dm4'
36 #sfn0 = 'Plane 19 of 0039 - 20231116_CAM-Deg_4.5
       V_23d_L1_STEM_HAADF_5.10_Mx DCFI(HAADF)_avg.dm3'
37 din0 = ncempy.io.dm.dmReader(os.path.join(swd, sfn0))
38
```

```
flipped_data = np.flipud(din0['data'])

# Update the data in din0 with the flipped image
din0['data'] = flipped_data

arrayplot2d(din0['data'],0.25,'gray');
ndim0 = np.array(din0['data'].shape)
sa0 = din0['pixelSize']


# In[4]:


sa0


# In[5]:


# from the radius decide the kernel size 0.2 -> 5 pixels

fig, ax = arrayplot2d(din0['data'],0.5,'inferno');
# mark a region of interest (to exclude edges and areas not of
    interest)
roi = np.array([[260,200],[2000,1250]])
rc_roi = Rectangle(roi[0], roi[1,0] - roi[0,0], roi[1,1] - roi
    [0,1], ec='r', fc=None, fill=False)
ax.add_patch(rc_roi);
# mark 3 points to identify a start for the search of lattice
    vectors
cc_rad = 14. # approximate peak radius
lt_pt0 = np.array([523,489]) # position of one cell corner
lt_pt1 = np.array([673.5,512.5]) # position of another cell corner
    defining vector 1
lt_pt2 = np.array([515.5,543]) # position of another cell corner
    defining vector 2
v1 = lt_pt1 - lt_pt0; v2 = lt_pt2 - lt_pt0; # lattice vectors
cc_pt0 = Circle(lt_pt0, cc_rad, ec='b', fc=None, fill=False)
cc_pt1 = Circle(lt_pt1, cc_rad, ec='r', fc=None, fill=False)
cc_pt2 = Circle(lt_pt2, cc_rad, ec='g', fc=None, fill=False)
ar_1 = Arrow(lt_pt0[0], lt_pt0[1], v1[0], v1[1], width=10, ec='r',
    fc='r', fill=True)
ar_2 = Arrow(lt_pt0[0], lt_pt0[1], v2[0], v2[1], width=10, ec='g',
    fc='g', fill=True)
ax.add_patch(cc_pt0); ax.add_patch(cc_pt1); ax.add_patch(cc_pt2);
ax.add_patch(ar_1); ax.add_patch(ar_2);
# generate a set of lattice points
nmax = 25
l_ltpt = []; l_ltpti = [];
for j in range(-nmax, nmax+1):
    for i in range(-nmax, nmax+1):
        p = lt_pt0 + i * v1 + j * v2
```

```
84          if (p[0] > roi[0,0]) and (p[0] < roi[1,0]) and (p[1] > roi
    [0,1]) and (p[1] < roi[1,1]):
85              l_ltpt.append(p)
86              l_ltpti.append([i,j])
87 a_ltpt = np.array(l_ltpt)
88 a_ltpti = np.array(l_ltpti)
89 ax.plot(a_ltpt.T[0], a_ltpt.T[1], 'w.');
90
91
92 # In[6]:
93
94
95 np.dot(v1,v2)/np.sqrt(np.dot(v1,v1) * np.dot(v2,v2)) #
    perpendicular ? if close to zero
96
97
98 # In[7]:
99
100
101 #lt_pt0 + i * v1 + j * v2; redefinition of vectors and lattice
    points
102 lt_pt0_fit = lt_pt0
103 lt_v1_fit = v1
104 lt_v2_fit = v2
105
106
107 # In[8]:
108
109
110 # get length of lattice vectors
111 lv1 = np.sqrt(np.dot(lt_v1_fit,lt_v1_fit))
112 lv2 = np.sqrt(np.dot(lt_v2_fit,lt_v2_fit))
113 [lv1,lv2]
114
115
116 # In[9]:
117
118
119 # check which sampling would fit with n > 24 along v1 (need refelx
    006 and don't want 006 at Nyquist frequence)
120 # and isotropic sampling along v1 and v2
121 for i in range(24, 240):
122     num_long = i # number of pixel on long cell axis
123     test = lv2/lv1 * num_long # number of pixels (fractional) along
     short axis
124     testr = int(np.round(test)) # integer number of pixels along
    short axis (target)
125     testif = np.round(test) - test # fractional rest (digitization
    error)
126     if np.abs(testif) < 0.05: # ? small fractional rest ?
127         print(i, int(np.round(test))) # yes
128
```

```
129 #choose close to 29, 81 because it is just a bit samller than
    original size ad fits with simulation
130
131
132 # In[10]:
133
134
135 # setup interpolation sampling
136 ncdim = np.array([29, 81]) # set cell sampling (y,x) !take same
    values if compare!
137 ncrng = np.array([[-8, -2],[15, 9]]) # range of cells to include:
    count manually, image edge limitation
138 nodim = np.array([ncdim[0]*(ncrng[1][0]-ncrng[0][0]), ncdim[1]*(
    ncrng[1][1]-ncrng[0][1])]) # output size
139 print(nodim)
140
141
142 # In[11]:
143
144
145 # interpolate from input to output where each cell is on a
    commensurate sampling
146 img1 = np.zeros(nodim, dtype=float)
147 for j in range(0, nodim[0]):
148     f2 = ncrng[0,0] + j / ncdim[0]
149     for i in range(0, nodim[1]):
150         f1 = ncrng[0,1] + i / ncdim[1]
151         p = lt_pt0_fit + f1 * lt_v1_fit + f2 * lt_v2_fit
152         img1[j,i] = ed.image_at_bilin(din0['data'], p)
153 fig, ax = arrayplot2d(img1,1,'inferno');
154
155
156 #does interpolation fit? --> check!
157
158
159 # In[12]:
160
161
162 # test a random partition of one cell size
163 # the FT should show clear peaks, no streaks
164 i0 = [19*ncdim[0],2*ncdim[1]] #nc= size of cell
165 imgp = img1[i0[0]:i0[0]+ncdim[0],i0[1]:i0[1]+ncdim[1]]
166 imgpft = np.fft.fft2(imgp)
167 fig, ax = arrayplot2d(imgp,4,'gray');
168 fig, ax = arrayplot2d(np.log(np.fft.fftshift(np.abs(imgpft))),4,'
    gray');
169 print('Ratio |FT(3,0)/FT(6,0)|: {:.2f}'.format(np.abs(imgpft[0,3]/
    imgpft[0,6])))
170
171
172 # In[13]:
173
```

```
174
175 # optional check: some tests to check FT coefficient strengths
176 # check critical areas
177 i0 = np.round([17.5*ncdim[0],8.0*ncdim[1]]).astype(int)
178 print(i0)
179 imgp = img1[i0[0]:i0[0]+ncdim[0],i0[1]:i0[1]+ncdim[1]]
180 imgpft = np.fft.fft2(imgp)
181 arrayplot2d(imgp,4,'gray');plt.show();
182 imgpft2 = np.abs(imgpft)
183 arrayplot2d(np.fft.fftshift(imgpft2)**0.1,4,'gray');plt.show();
184 plt.plot(np.arange(1,9),imgpft2[2,1:9],'k-')
185 plt.plot(np.arange(1,9),imgpft2[0,1:9],'b-')
186 v1 = imgpft2[0, 3]; v2 = imgpft2[0, 6];
187 #v3 = imgpft2[2, 4]
188 v3 = imgpft2[2, 2]
189 # we choose 6 times over background as threshold to accept the
    pattern
190 vthr2 = 6 * np.sqrt((np.sum(imgpft2[0:2,5:8]**2) - v2**2) / 5)
191 #vthr3 = 6 * np.sqrt((np.sum(imgpft2[1:4,3:6]**2) - v3**2) / 8)
192 vthr3 = 6 * np.sqrt((np.sum(imgpft2[1:4,1:4]**2) - v3**2) / 8)
193 [v2/vthr2, v3/vthr3, v1/v2]
194
195
196 # In[14]:
197
198
199 # evaluate Fourier coefficients of the horizontal modes 3 and 6
200 #creating maps & background --> generate arrays
201 img2v1 = np.zeros(nodim, dtype=float)
202 img2v2 = np.zeros(nodim, dtype=float)
203 img2v3 = np.zeros(nodim, dtype=float)
204 bkg1 = np.ones(nodim, dtype=float)
205 bkg2 = np.ones(nodim, dtype=float)
206 bkg3 = np.ones(nodim, dtype=float)
207 ncdim2 = ncdim >> 1
208 for j in range(0, nodim[0] - ncdim[0]):
209     j1 = ncdim2[0] + j
210     for i in range(0, nodim[1] - ncdim[1]):
211         i1 = ncdim2[1] + i
212         img1cft = np.abs(np.fft.fft2(img1[j:j+ncdim[0],i:i+ncdim
    [1]]))
213         # maps of selected beam Fourier coeff
214         img2v1[j1,i1] = img1cft[0, 3]
215         img2v2[j1,i1] = img1cft[0, 6]
216         img2v3[j1,i1] = img1cft[2, 4]
217         # estimation of noise of Fourier coeff
218         bkg1[j1,i1] = np.sqrt((np.sum(img1cft[0:2,2:5]**2) - img2v1
    [j1,i1]**2) / 5)
219         bkg2[j1,i1] = np.sqrt((np.sum(img1cft[0:2,5:8]**2) - img2v2
    [j1,i1]**2) / 5)
220         bkg3[j1,i1] = np.sqrt((np.sum(img1cft[1:4,3:6]**2) - img2v3
    [j1,i1]**2) / 8)
```

```
221
222
223 # In[15]:
224
225
226 # determine threshold for contribution to final map
227 arrayplot2d(img2v3/bkg3, 0.5, 'inferno', vrangetype='direct',
    vrange=[0,4]); #threshold: vrange=[0,4]
228
229
230 # In[16]:
231
232
233 arrayplot2d(img2v2/bkg2, 0.5, 'inferno', vrangetype='direct',
    vrange=[0,4]);
234
235
236 # In[17]:
237
238
239 # Calc final coeff map
240 # Generate ratio of coeff ratio 003/006
241 # Deactivate insiginficant contributions
242 img2 = np.zeros(nodim, dtype=float)
243 rthr2 = 4. # SET threshold for the [0,6] peak against its
    background estimate
244 rthr3 = 4. # SET threshold for the [0,6] peak against its
    background estimate
245 for j in range(0, nodim[0] - ncdim[0]):    #predefine target array
    for coeff map
246     j1 = ncdim2[0] + j                     # output px index y
247     for i in range(0, nodim[1] - ncdim[1]):
248         i1 = ncdim2[1] + i                 # output px index x
249         if (img2v2[j1,i1] > rthr2*bkg2[j1,i1]) and (img2v3[j1,i1] >
     rthr3*bkg3[j1,i1]):       #set threshold
250             #ratio |FT[0,6] background sutracted
251             img2[j1,i1] = (img2v1[j1,i1] - bkg1[j1,i1])/(img2v2[j1,
    i1] - bkg2[j1,i1])
252
253
254 # In[18]:
255
256
257 arrayplot2d(img2, 0.5, 'ocean_r');
258
259
260 # In[19]:
261
262
263 # make a combined image/map on scale
264 sr = 1.42 / ncdim[1]
265 fig, ax = plt.subplots()
```

```
i1max = np.amax(img1); i1min = np.amin(img1); i1rng = i1max - i1min
    ;
alphas = np.clip(1.0 - (img1 - i1min - 0.2*i1rng) / (0.8 * i1rng),
    0., 1.)

pos = ax.imshow(img2 / 3.5, origin='lower', extent=(-0.75, nodim[1]
     * sr+0.75, -0.25, nodim[0] * sr+0.25), cmap='viridis_r', vmin
    =0, vmax=1) #3.5 simulation reference value for layered
    structure
ax.imshow(img1, alpha=alphas, cmap='gray', origin='lower', extent
    =(0, nodim[1] * sr, 0, nodim[0] * sr), vmin=i1min+0.3*i1rng,
    vmax=i1max)
ax.set_xlabel(r'scan position $x$ [nm]',  fontsize = 12)
ax.set_ylabel(r'scan position $y$ [nm]',  fontsize = 12)
ax.tick_params(axis='both', which='major', labelsize=12)
cb = fig.colorbar(pos, location='right', anchor=(-0.2, 0.5), shrink
    =0.5)
cb.ax.tick_params(labelsize=12)
ax.set_xlim(0, 14)
ax.set_ylim(0, nodim[0] * sr)
ax.set_xticks(np.arange(0, nodim[1] * sr, step=2))
ax.set_yticks(np.arange(0, nodim[0] * sr, step=2))
cb.ax.invert_yaxis()
plt.savefig(r'', bbox_inches='tight', format='svg') #set file path
plt.savefig(r'', bbox_inches='tight', format='png') #set file path
plt.show()


# In[20]:


#check transparancy of combined map
arrayplot2d(1-alphas)
```

Listing B.2: Python script for Fourier coefficient mapping used in Section 5.2.